

Model-Based Sensor Placement for Component Condition Monitoring and Fault Detection in an  
Integrated Gasification Combined Cycle Plant

by

Parham Mobed, B.Sc.

A Thesis/Dissertation

In

CHEMICAL ENGINEERING

Submitted to the Graduate Faculty  
Of Texas Tech University in  
Partial Fulfillment of  
the Requirements for  
The Degree of

DOCTOR OF PHILOSOPHY

Approved by:

Raghunathan Rengaswamy  
Chair of Committee

Chau-Chyun Chen

Rajesh Khare

Ted Wiesner

Akif Ibraguimov

Mark Sheridan  
Dean of the Graduate School

May, 2016

Copyright 2016, Parham Mobed

## Acknowledgements

First and foremost, I would like to express my deepest sense of gratitude and profound respect to my advisor Dr. Raghunathan Rengaswamy who offered his continuous support, encouragement and advice throughout my PhD experience and the course of this thesis. He has been supportive ever since the day I expressed my interest in his research group. I thank him for inviting me to Indian Institute of Technology, Madras in India, it was a wonderful experience.

I would like to thank my thesis committee, Dr. Ted Wiesner, Dr. Rajesh Khare, Dr. Chau-Chyun Chen and Dr. Akif Ibragimov for serving on my doctoral committee as well as providing valuable interests and comments on my work. I would also like to thank Dr. Debangsu Bhattacharyya from West Virginia University for being a mentor, providing me with direction and technical support, and sharing his knowledge and experience throughout my work. I am also grateful to Dr. Richard Turton from West Virginia University for his kind consultations in this work.

I would like to express my deep appreciation to our group members, Dr. Jeevan Maddala, Dr. Timothy Spinner, Srinivasan Raman, Md Islam, and Dr. Sudhakar Munusamy whom I share many memories. I would also thank my friends at IIT Madras, whom made my visit to India a wonderful and memorable experience.

I owe a great deal to the kindness of friends in Iran and USA whom this journey would not have been possible without their support. My special thanks to Masoud Mohammadi Panah, a true caring and supportive friend that I am blessed to have.

Finally, I wish to dedicate this dissertation to my parents, Mahmoud and Mahin Mobed, and my brothers, Pedram Mobed and Payam Mobed and their families for their constant support and unconditional love.

## Table of Contents

Acknowledgements .....	ii
Abstract .....	vii
List of Tables .....	ix
List of Figures .....	xi
<b>Chapter 1 - Introduction .....</b>	<b>1</b>
1.1    Approach .....	2
1.1.1    Scientific Review .....	2
1.1.2    2-Tier Sensor Placement .....	3
1.1.3    Problem Tractability .....	6
1.2    IGCC Power plant .....	8
1.3    Computation Tools .....	10
1.4    Thesis Organization .....	11
<b>Chapter 2 - Process and Model Descriptions .....</b>	<b>13</b>
2.1    Sour Water Gas Shift Reactor .....	13
2.1.1    Process Description .....	16
2.1.2    Model Description .....	17
2.1.3    Solution Approach .....	24
2.1.4    Data Reconciliation .....	25
2.1.5    Results and Discussions .....	30
2.1.6    Conclusion .....	40
2.2    Acid Gas Removal Plant – SELEXOL Unit .....	41
2.2.1    Process Description .....	41
2.2.2    Model Description .....	42

2.3	Gasification Island.....	43
2.3.1	Process Description.....	43
2.3.2	Model Description .....	43
2.4	Combined Cycle Unit.....	46
2.4.1	Process Description.....	46
2.4.2	Model Description .....	47
Chapter 3 - Scaling Analysis and Simplification of sour WGS Model .....		49
3.1	Introduction .....	49
3.1.1	Model Simplification Using Current Scaling Analysis .....	50
3.1.2	Improvements to the Method of Scaling Analysis.....	54
3.1.3	Illustrative Examples .....	56
3.1.4	Numerical Results for Sour WGS Example.....	65
3.2	Conclusion.....	79
Chapter 4 - System-Level Sensor Placement .....		80
4.1	Introduction .....	80
4.2	Sensor Placement Approach.....	83
4.3	SDG and FES Algorithms in the Presence of Numerical Simulations .....	84
4.4	Sensor Placement Using Magnitude Ratio.....	87
4.5	Constraint Matrix for FES and MR.....	91
4.6	Formulation Summary.....	92
4.6.1	Optimization Problem.....	92
4.6.2	Solution Approach .....	92
4.7	Results .....	92
4.7.1	CSTR Case Study .....	93
4.7.2	Five-Tank Case Study.....	99

4.7.3	Tennessee Eastman Case Study .....	104
4.7.4	SELEXOL Process Case Study .....	107
4.7.5	Combined Cycle Case Study .....	111
4.8	Conclusion.....	115
Chapter 5 - Network Decomposition.....		117
5.1	Introduction.....	117
5.1.1	Method .....	119
5.1.2	Fault Detection in Decomposed System .....	123
5.2	Results .....	124
5.3	Conclusion.....	130
Chapter 6 - Component-Level Sensor Placement .....		132
6.1	State Estimation Development .....	132
6.1.1	Introduction.....	132
6.1.2	State Estimation of DAE Systems .....	134
6.1.3	Equality Constrained State Estimation of Uncertain Nonlinear DAEs ....	136
6.2	Problem Formulation.....	144
6.2.1	Introduction.....	144
6.2.2	Summary of Simplified WGS Model .....	146
6.2.3	EKF for Simplified Model .....	147
6.2.4	Genetic Algorithm .....	150
6.2.5	State Estimation Validation .....	150
6.2.6	Optimal Distributed Sensor Placement.....	162
6.3	Conclusion.....	172
Chapter 7 - Implementation of 2-Tier Sensor Placement on Gasification Island .....		175

7.1	Fault Simulation .....	175
7.1.1	Study of Fault Effects .....	178
7.2	Results .....	184
7.2.1	System-Level: Gasification Island .....	184
7.2.2	Component-Level: First-Stage Sour Water Gas Shift Reactor .....	186
7.3	Conclusion.....	189
Chapter 8 - Summary and Future Work .....		198
8.1	Summary .....	198
8.2	Future Work .....	198
References.....		200

## Abstract

The goal of this thesis is to establish a comprehensive methodology to determine the type, location, and cost/number of sensors required for component condition monitoring and fault detection in fossil energy systems. The root cause for productivity losses and shut-downs are called “faults”. Through a transformative two-tier framework, the thesis seeks to develop a model-based sensor placement methodology that addresses: (i) sensor placement for fault detection based on tractable models that are developed from the system-level dynamic model, (ii) identification of precise locations for component condition monitoring based on distributed component-level models. With these objectives in mind, algorithms are developed for maximizing the effectiveness of the sensor network for system-level fault detection and component-level condition monitoring. Integrating the networks identified at each level, the 2-tier sensor network is obtained. The algorithms are developed for and tested on a high fidelity model of the gasification island of an integrated gasification combined cycle (IGCC) plant.

For the identification of the system-level fault detection network, the problem is approached through qualitative reasoning using a cause and effect model (graph model) to identify an optimal cost network. This well-studied approach avoids solving thousands of partial differential equations in an optimization loop and reduces the problem to solving an integer linear programming problem. The classical algorithms for fault detection using graph models are enhanced through the use of numerical simulations and introduction of quantitative features.

For a condition monitoring network, whether equipment should be considered at a component-level or a system-level depends upon the criticality of the process equipment, its likeliness to fail, and the level of resolution desired for any specific failure. Because of the presence of a higher fidelity model at the component-level, a sensor network can be designed to monitor the spatial profile of the states and estimate fault severity levels. The state estimation is performed using an extended Kalman filter (EKF) that estimates the states, including faults, at the component level. A genetic algorithm is used in consort with the EKF to find the optimal measurement model for highest accuracy of the estimates with

a fixed number/budget of the sensors. The identified measurement model represents the optimal sensor network for component condition monitoring.

In an IGCC plant, besides the gasifier, the sour water gas shift (WGS) reactor plays an important role. Yet, it is one of the equipment with a high likelihood of failure because of the harsh conditions that it is subjected to. In view of this, we have considered condition monitoring of the sour WGS reactor at the component-level, while a detailed plant-wide model of gasification island (including sour WGS reactor and the SELEXOL process) is considered for fault detection at the system-level. SELEXOL process is a unit of acid gas removal process in an IGCC for removing carbon dioxide and other impurities. Finally, the developed algorithms unify the two levels and identify an optimal sensor network that maximizes the effectiveness of the overall system-level fault diagnosis and component-level condition monitoring in gasification island. Measurement and model uncertainties are naturally handled in the solution approach while sensor failure probabilities and failure occurrence probabilities can be easily included, if required. In addition, the same algorithms developed in this thesis can be further enhanced to be used in retrofits, where the objectives could be upgrade (addition of more sensors) and/or relocation of existing sensors.

## List of Tables

Table 2.1. Properties of Catalyst Q <sup>56</sup> .....	25
Table 2.2. Standard deviation of different variables <sup>76-77</sup> .....	28
Table 2.3. Comparison of the reconciled and original mole fractions <sup>56</sup> .....	29
Table 2.4. Simulation condition <sup>16</sup> .....	30
Table 3.1. Parameters and inlet conditions for the sour WGS reactor.....	66
Table 3.2. Scale values for the variables in sour WGS reactor.....	67
Table 3.3. Values of dimensionless groups for species balance equation of WGS reactor model.....	72
Table 3.4. Values of dimensionless groups for energy balance equations of sour WGS reactor model .....	74
Table 3.5. Values of dimensionless groups for new energy balance equation and pressure drop equation .....	75
Table 3.6. Comparison of the reduced model vs the detailed model.....	78
Table 4.1. SDG example .....	88
Table 4.2. Type and cost of each sensor used in all case studies <sup>190</sup> .....	93
Table 4.3. List of measured variables in CSTR system.....	94
Table 4.4. List of simulated faults and the corresponding affected sensors in CSTR system .....	94
Table 4.5. Results of applying different algorithms to CSTR system .....	95
Table 4.6. Fault resolution by SDG, FES and MR in CSTR system .....	96
Table 4.7. List of measured variables in five-tank case-study.....	99
Table 4.8. List of simulated faults and the corresponding affected sensors in five-tank case-study .....	99
Table 4.9. Results of applying different algorithms to five-tank case-study .....	101
Table 4.10. Fault resolution by SDG, FES and MR in five-tank case-study .....	101
Table 4.11. List of measured variables in TE process <sup>102</sup> .....	105
Table 4.12. List of simulated faults in TE process <sup>102</sup> .....	105
Table 4.13. Results of applying different algorithms to TE process .....	106
Table 4.14. Fault resolution by SDG, FES and MR in TE process .....	107
Table 4.15. List of measured variables in SELEXOL process .....	109

Table 4.16. List of simulated faults in SELEXOL process.....	110
Table 4.17. Results of applying different algorithms to SELEXOL process.....	110
Table 4.18. Faults at different severity level simulated in the combined cycle model...	113
Table 4.19. SDG and FES algorithms results .....	114
Table 4.20. MR algorithm results .....	115
Table 5.1. Sensitivity analysis of number of sub-systems .....	126
Table 5.2. Sensitivity analysis of number of nodes and fault nodes.....	128
Table 5.3. Sensitivity analysis of number of cross-connections.....	129
Table 6.1. Comparison of RMSE and SSE values for measured and estimated values .	155
Table 6.2. Summary of equations of water gas shift reactor .....	156
Table 6.3. Summary of the parameters of the WGSR model used in this work .....	156
Table 6.4. Sum of squared errors value when fixed points measure the same type of states .....	161
Table 6.5. Sum of squared errors with one missing measurement .....	162
Table 6.6. SSE values with measurement combination .....	162
Table 6.7. Water gas shift reactor model parameters.....	163
Table 6.8. Process noise variance values for different models .....	165
Table 6.9. Sensor placement results and computation time for each model.....	168
Table 6.10. Sensor placement results comparison of <i>Model I</i> and <i>Model V</i> for different number of sensors .....	169
Table 6.11. Effect of process noise covariance on the sensor placement results.....	170
Table 6.12. Effect of initial error covariance on the sensor placement results .....	172
Table 7.1. Faults simulated on the SELEXOL side of the integrated model.....	176
Table 7.2. Faults simulated on the sour WGS reactor side of the integrated model.....	178
Table 7.3. System-level sensor placement results of gasification island.....	185
Table 7.4. List of sensors for FES & MR algorithm with low MR threshold level.....	185
Table 7.5. Reactor and state estimation parameters.....	187
Table 7.6. Optimal location and type of sensors for different faults .....	188
Table 7.7. Comparison of normalized fitness values for GA solution and final sensor network .....	191

## List of Figures

Figure 1-1. Schematic of the 2-tier sensor placement approach .....	3
Figure 1-2. Genetic algorithm approach .....	5
Figure 1-3. Diagnostic approach for fault detection and condition monitoring .....	6
Figure 1-4. Schematic of the IGCC plant <sup>3</sup> .....	8
Figure 2-1. Diagram of the data reconciliation procedure .....	27
Figure 2-2. Arrhenius plot for the water gas shift reaction .....	29
Figure 2-3. CO mole fraction profile along the reactor when length is increased to 40 m .....	31
Figure 2-4. (a) COS mole fraction (b) Gas temperature profile along the reactor when length is increased to 40 m .....	32
Figure 2-5. CO mole fraction profile for different reactor diameters .....	33
Figure 2-6. Pressure profile for different reactor diameters .....	33
Figure 2-7. Pressure drop vs. L/D ratio of the reactor .....	34
Figure 2-8. CO conversion profiles for different inlet gas temperatures .....	35
Figure 2-9. COS conversion profiles for different inlet gas temperatures .....	35
Figure 2-10. CO conversion transient for a step change in inlet temperature from 620 to 640 K .....	36
Figure 2-11. Temperature transient at the outlet of the reactor for a step change in inlet temperature from 620 to 640 K .....	37
Figure 2-12. CO conversion profile for different steam/CO molar ratio .....	38
Figure 2-13. Required (a) Diameter (b) Flow at different steam/CO molar ratios .....	38
Figure 2-14. Effect of catalyst deactivation over time on CO conversion .....	39
Figure 2-15. COS conversion along the reactor after the catalyst lifetime of 5 years .....	40
Figure 2-16. Schematic of the SELEXOL unit .....	42
Figure 2-17. Schematic representation of the Sour Water Gas Shift Reactor system developed in MATLAB .....	44
Figure 2-18. Exchange of information between the sour WGS reactor model in MATLAB and the SELEXOL model in APD .....	46
Figure 2-19. Schematic of the combined cycle power plant .....	47
Figure 3-1. Steady state simulation result for all the 9 dependent variables .....	68
Figure 3-2. Steady state simulation result for all the dimensionless variables .....	68

Figure 3-3. Unsteady state simulation result for all the variables at the exit of the reactor .....	69
Figure 3-4. Unsteady state simulation result for all the dimensionless variables at the exit of the reactor .....	69
Figure 3-5. Unsteady behavior of species balance equation under isothermal and isobaric condition .....	73
Figure 3-6. Steady state values of WGS reactor model compared between detailed and simplified model: D – detailed, S-Simplified .....	78
Figure 3-7. Unsteady state values at exit of WGS reactor compared between detailed and simplified model: D – detailed, S-Simplified .....	79
Figure 4-1. Flowchart of FES algorithm in presence of numerical solution .....	87
Figure 4-2. Magnitude ratio for example in Table 4.1 .....	89
Figure 4-3. Flowchart of MR algorithm .....	90
Figure 4-4. Schematic of the CSTR system <sup>4</sup> .....	94
Figure 4-5. Schematic of the five-tank case-study <sup>4</sup> .....	99
Figure 4-6. TE process flowsheet <sup>5</sup> .....	104
Figure 4-7. Schematic of the SELEXOL process <sup>3</sup> .....	108
Figure 4-8. Number of irresolvable faults (left) and the corresponding sensor network cost (right) at different MR threshold values .....	115
Figure 5-1. Representation of adjacency matrix .....	120
Figure 5-2. Pseudo-fault representation for two sub-systems.....	123
Figure 6-1. Actual, measured and estimated values of differential variable $x_1$ .....	153
Figure 6-2. Actual, measured and estimated values of differential variable $x_2$ .....	153
Figure 6-3. Actual, measured and estimated values of algebraic variable $z$ .....	154
Figure 6-4. Schematic of the WGSR system .....	156
Figure 6-5. Actual (-), measured (*) and estimated (--) value at 9 <sup>th</sup> grid-point on the reactor for (a) <b><math>yCO</math></b> ( $\text{RMSE}_{\text{data}} = 5.005 \times 10^{-3}$ , $\text{RMSE}_{\text{est}} = 3.852 \times 10^{-3}$ ) (b) <b><math>yH2O</math></b> ( $\text{RMSE}_{\text{data}} = 5.003 \times 10^{-3}$ , $\text{RMSE}_{\text{est}} = 3.827 \times 10^{-3}$ ) (c) <b><math>Tg</math></b> ( $\text{RMSE}_{\text{data}} = 7.978 \times 10^{-3}$ , $\text{RMSE}_{\text{est}} = 4.945 \times 10^{-3}$ ) .....	159

Figure 6-6. Actual (-), measured (*) and estimated (--) value at 9 <sup>th</sup> grid-point on the reactor for (a) <b>P</b> ( $\text{RMSE}_{\text{data}} = 1.998 \times 10^{-3}$ , $\text{RMSE}_{\text{est}} = 0.894 \times 10^{-3}$ using Filter II) (b) <b>P</b> ( $\text{RMSE}_{\text{est}} = 5.312 \times 10^{-3}$ using Filter I) .....	159
Figure 6-7. Normalized fitness evolution for each model .....	166
Figure 7-1. HE configuration 1: leak simulated as mixing of inlet high pressure stream into outlet low pressure stream .....	177
Figure 7-2. HE configuration 2: leak simulated as mixing of outlet high pressure stream into inlet low pressure stream .....	177
Figure 7-3. CO mole fraction transient at reactor R <sub>1</sub> outlet for a ramp decrease in catalyst porosity .....	180
Figure 7-4. COS mole fraction transient at reactor R <sub>1</sub> outlet for a ramp decrease in catalyst porosity .....	180
Figure 7-5. Temperature transient at reactor R <sub>1</sub> outlet for a ramp decrease in catalyst porosity .....	181
Figure 7-6. CO mole fraction transient at reactor R <sub>2</sub> outlet for a ramp decrease in catalyst porosity .....	182
Figure 7-7. COS mole fraction transient at reactor R <sub>2</sub> outlet for a ramp decrease in catalyst porosity .....	182
Figure 7-8. Temperature response at the exit of R <sub>2</sub> as a result of ramp change in porosity. ....	183
Figure 7-9. CO response at the exit of the SELEXOL unit as a result of ramp change in porosity. ....	184
Figure 7-10. GA progress for different faults .....	187
Figure 7-11. Fault severity estimation in reactor R <sub>1</sub> using optimal solution for fault (a) F <sub>25</sub> (b) F <sub>26</sub> (c) F <sub>27</sub> (d) F <sub>31</sub> (e) F <sub>32</sub> .....	189
Figure 7-12. Fault severity estimation in reactor R <sub>1</sub> using final sensor network for fault (a) F <sub>25</sub> (b) F <sub>26</sub> (c) F <sub>27</sub> (d) F <sub>31</sub> (e) F <sub>32</sub> .....	192
Figure 7-13. Actual (-), measured (*) and estimated (--) value of different states at the outlet of the reactor R <sub>1</sub> for fault F <sub>25</sub> .....	193
Figure 7-14. Actual (-), measured (*) and estimated (--) value of different states at the outlet of the reactor R <sub>1</sub> for fault F <sub>26</sub> .....	194

Figure 7-15. Actual (-), measured (*) and estimated (--) value of different states at the outlet of the reactor R <sub>1</sub> for fault F <sub>27</sub> .....	195
Figure 7-16. Actual (-), measured (*) and estimated (--) value of different states at the outlet of the reactor R <sub>1</sub> for fault F <sub>31</sub> .....	196
Figure 7-17. Actual (-), measured (*) and estimated (--) value of different states at the outlet of the reactor R <sub>1</sub> for fault F <sub>32</sub> .....	197

## Chapter 1

### Introduction

It is well known that considerable coal resources exist in the United States. However, coal utilization is accompanied by the associated pollution related concerns. The major drawback to using coal is the growing concern of the impact of global greenhouse gas emissions and the effect of tighter emission regulations on the coal-based power plants. In addition to carbon and hydrogen, coal contains significant amounts of impurities, such as sulfur compounds and mercury, and as a result burning coal not only produces carbon dioxide ( $\text{CO}_2$ ), a major component of greenhouse gas, but also other pollutants that are hazardous to the environment. To overcome these problems, coal power plants should capture and sequester  $\text{CO}_2$ . However, the efficiency of traditional coal power plants, such as subcritical and supercritical power plants, are largely affected by addition of  $\text{CO}_2$  capture.<sup>1</sup> Therefore, advanced technologies such as integrated gasification combined cycle (IGCC) have been developed over the years that yield higher efficiencies in comparison to the traditional power plants and offer near-zero emission power generation by allowing capture and sequestration of  $\text{CO}_2$ .<sup>2,3</sup> Design and operation of energy producing, near “zero-emission” coal plants have become a national imperative. One of the major steps toward the success of IGCC is to ensure the plant operates safely while satisfying the carbon capture target (e.g. 90% carbon dioxide capture).

Faults or events that lead to loss in productivity occur over time. These faults, if not detected and mitigated at an early stage, can lead to severe loss in productivity, efficiency, and equipment damage, and can be a safety hazard. This thesis will provide a framework to identify the optimum placement, number, and type of sensors that will be sufficient for condition monitoring and fault diagnosis in an IGCC plant. The optimal sensor network identified through this framework helps in detection of any fault symptoms as the fault propagates in the system and identification of the origin of the detected fault. Moreover, using the identified network, the fault severity for certain faults and units can be estimated. This work could have a major impact on the design and operation of future fossil energy plants, particularly at the grassroots level where the sensor network is yet to be identified.

The theoretical and computational efforts that are developed through this thesis are delivered as a framework that can be used in combination with simulations of fossil energy systems. The framework developed in this thesis can be enhanced to include any other simulation system through appropriate use of first-principal modeling and state estimation techniques.

## **1.1 Approach**

### **1.1.1 Scientific Review**

While there is considerable amount of literature on sensor placement, computationally efficient sensor placement algorithms that provide a comprehensive solution as envisaged in this thesis are minimal. The sensor placement problem in its broadest sense has to use information regarding available sensors and their failure rates, available failure information and their occurrence rates, component and system models, criticality of the individual components to the process, nature of the component models available (lumped or distributed) to provide recommendations regarding the location, type, and number of sensors for an efficient component monitoring and fault diagnosis network. This is a challenging problem because while component-level approaches will fail to utilize the synergistic system-level interactions, a system-level view will result in computational intractability. This has been a major challenge in developing efficient solutions to this problem. The 2-tier solution approach proposed in this thesis follows a “divide-and-conquer” philosophy. The key to the success of this philosophy is in using appropriate models and information at the correct level of the problem. This is depicted in Figure 1-1.

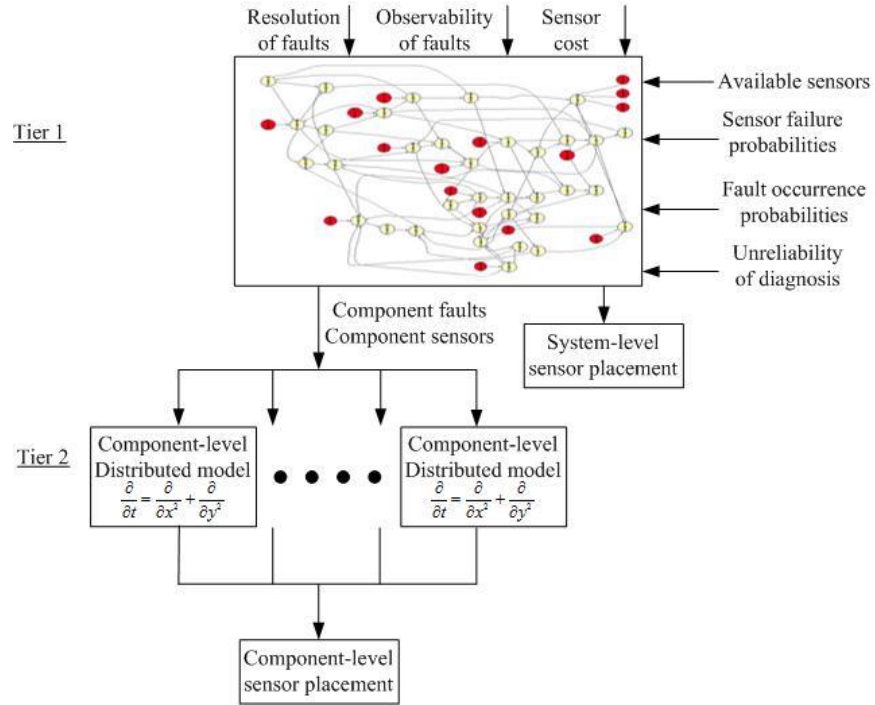


**Figure 1-1. Schematic of the 2-tier sensor placement approach**

### 1.1.2 2-Tier Sensor Placement

As shown in Figure 1-1, the sensor placement problem is decoupled into two tiers. Tier I deals with system-level sensor placement. A model that is appropriate at this level, that is, a qualitative math model is used. It should be noted that a plant-scale coupled partial differential equations (PDEs) can run into thousands of equations and solving them within an optimization loop for sensor placement will likely be computationally intractable. The previous works have demonstrated the use of graph models such as the signed directed graph (SDG) algorithm for plant-level diagnosis.<sup>4-10</sup> The objective function for sensor placement is a critical component in the resulting sensor placement algorithms. One objective can be resolving all the faults and hypothesized faults, where each hypothesized faults represents the set difference of two or more faults being resolved.<sup>9</sup> It should be noted that fault resolution in this thesis refers to the ability of a sensor network to distinguish between faults and identify the origin of the faults. An alternate objective is to maximize reliability of the fault diagnosis network with maximum possible resolution of failure origins as constraints imposed on the solution. The original cost minimization formulation

with maximum resolution satisfies the objective efficiently and will be used in tier I sensor placement.

The maximum resolution that is possible is a complex function of both the system characteristics and the model that is used in the sensor placement approach. Approaches in the literature ensure that all the faults that are resolvable are indeed resolved by the sensor placement algorithm and at the same time the fault diagnosis network is highly cost effective. Bhushan and Rengaswamy<sup>5</sup> showed how this sensor placement problem could be converted into an integer linear programming (ILP) problem using appropriate transformations through SDG algorithm. In this thesis, the SDG algorithm is enhanced by introducing the concept of magnitude ratio (MR). Magnitude ratio algorithm incorporates the information from numerical simulations and pairwise interaction between the variables into the SDG framework. This is the solution approach that will be used in this thesis. Tier I solution will identify the optimal cost sensor placements that achieve the maximum resolution possible given the system description and the qualitative cause-effect mathematical model of the system (obviously this system model will also include the faults and sensors of the individual components that are considered in tier II).

The contention is that it is more natural to handle the sensor placement problem at a component-level with high fidelity math models. This integrates system-level fault diagnosis with component-level condition monitoring. As a result, tier II sensor placement goal is estimation of failure severity at the component-level. The sensors identified at this level help not only in estimation of failure severity at the component-level but also in failure resolution when needed. This goal is achieved by coupling the idea of Extended Kalman Filter (EKF) with a Genetic Algorithm (GA) optimization approach as shown in Figure 1-2. A filter needs to be used because of the need to estimate severity levels. By augmenting fault magnitudes as parameters in the EKF, failure severity can be estimated. The main objective of tier II sensor placement is the identification of the optimal sensor locations with, for example, a fixed budget/number of sensors that result in the highest state estimates accuracy, thus, resulting in highly accurate estimate of the failure severity. For this, the PDEs in distributed model are converted to ordinary differential equations (ODEs) using method of lines. This is achieved by discretizing the spatial derivatives in PDEs, thus, resulting in discretized spatial variables that represent candidate locations for placing

sensors. The EKF uses the ODE system and measurements from sensors at the candidate locations to estimate the states in the system.

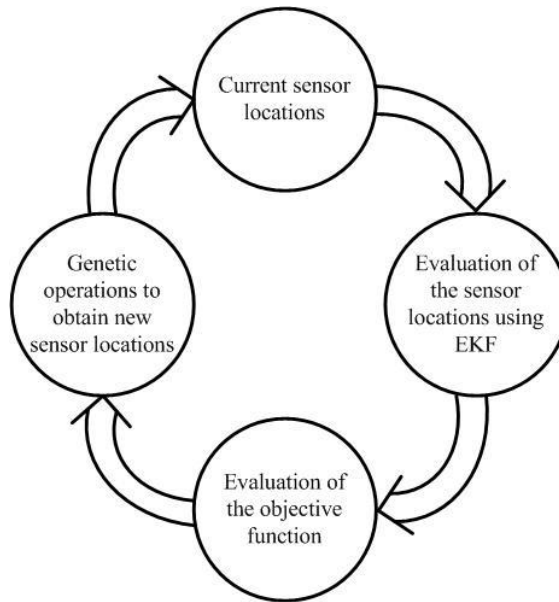


**Figure 1-2. Genetic algorithm approach**

Optimized sensor locations are identified using a genetic algorithm (GA) approach as shown in Figure 1-2. The decision variables are discrete (1 if a sensor is placed at a particular distributed location and 0 if not). The objective function is usually a squared error between the true and estimated values of all states of the system, including fault severity. Further, the objective function - which reflects how well the states and the severity of the fault are captured for a particular sensor network - is nonlinear and does not have a closed form analytical expression. This makes it difficult to optimize the sensor locations using standard math programming-based approaches. Evolutionary algorithm approaches have been demonstrated to successfully solve such problems in several application areas.<sup>11-15</sup> Once these sensor locations are identified, the actual fault diagnosis and condition monitoring in real-time can also be achieved using the models and methods used in the sensor placement algorithm as shown in Figure 1-3. Given a list of possible failures, plant-level data with the qualitative model is used to obtain the optimal sensor network. Based on the faults, the corresponding EKF is run to estimate failure severity. Hence, the sensor

placement algorithms seamlessly develop a fault detection and condition monitoring approach for eventual verification of the suggested sensor locations.

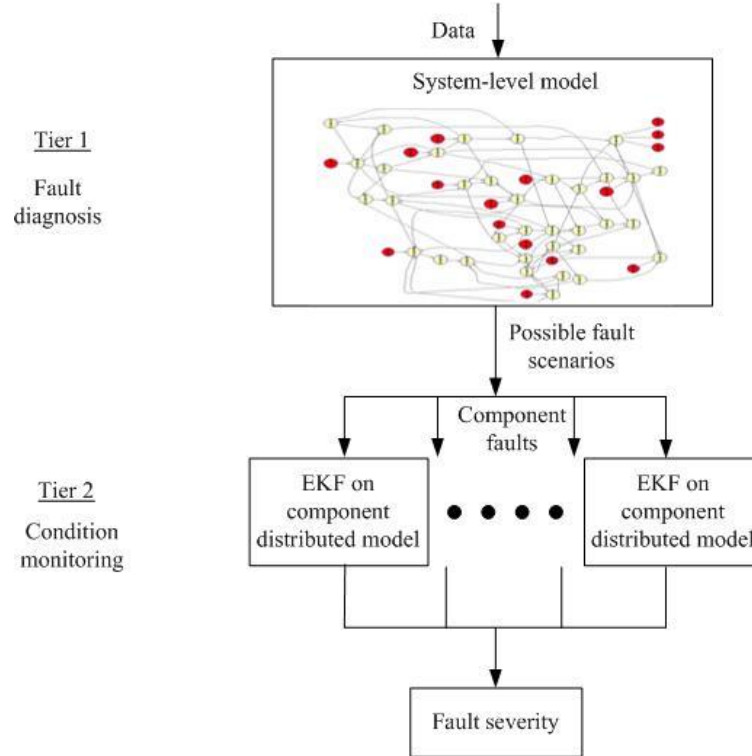


**Figure 1-3. Diagnostic approach for fault detection and condition monitoring**

### 1.1.3 Problem Tractability

#### 1.1.3.1 Model Simplification

Even if the first-principles model is tractable, embedding a first-principles model in an optimization loop may be intractable. The component level sensor placement algorithm consists of three primary computational modules that form an optimization loop: (i) solution to the first principles model, (ii) solution to the filter problem, and (iii) GA-related computations. States in the process model are estimated by solving the filter equations. If the process model is nonlinear, the model must be integrated and linearized at every time step of state estimation, which adds to the complexity of the problem. The GA optimizes a user defined objective function and searches in the vast solution space for the optimal solutions, where each attempt of the GA requires performing a state estimation

of the process model, thus, making the component-level sensor placement significantly computationally intensive and time consuming. In order to reduce the computational complexity, an efficient approach is to reduce the complexity of the process model, thus, the computations will be reduced for the entire optimization loop. A simple way to reduce the complexity of a process model is to linearize the model around the operating point. However, in presence of faults this approach may lead to unacceptable inaccuracies. The approach taken in this thesis is model simplification based on scaling analysis. The model simplification is attempted and implemented in component-level sensor placement. The implementation of scaling analysis at the component-level sensor placement is found to be sufficient for the work envisaged in this thesis and studying the use of reduced order models recommended for future efforts in component-level sensor placement.

### 1.1.3.2 Network Decomposition

The use of graph models for system-level sensor placement promises significant reduction in computations compared to the use of plant-scale coupled PDEs. Although the system-level sensor placement is performed by solving an ILP, there are limitations on how large the graph networks can be when considering fault resolution. Moreover, as more information is added to the system-level sensor placement algorithm, the plant-wide sensor placement will likely be computationally intractable. A general approach in graph theory for reducing the computational complexity is the use of graph partitioning techniques. In graph partitioning techniques, the graph is divided into smaller components with components holding specific properties. Due to the nature of graph partitioning problem, these problems are generally solved by developing heuristic and approximation algorithms. Typically, the graph partitioning algorithms attempt to group the most interacting components together and minimize the interaction between the groups. In this thesis, we have attempted to address the problem by studying the effect of graph partitioning on different parameters including computation time, fault resolution and sensor network cost. The result of this study opens the door for further progress and can help researchers when developing partitioning algorithms for fault detection and diagnosis.

## 1.2 IGCC Power plant

Although several configurations of IGCC plants are possible, the configuration considered in this work is similar to Case #2 in the baseline DOE studies that includes a GEE-type gasifier with CO<sub>2</sub> capture and removal.<sup>16</sup> Figure 1-4 shows a block diagram of an IGCC power plant. The key technologies in the IGCC process with CO<sub>2</sub> capture are coal gasification, acid gas removal (AGR), sour water gas shift (WGS) unit and combined cycle power generation technologies.

Coal is first processed to obtain the required particle size distribution and mixed with water before being fed to the gasifier as slurry. Oxygen-rich air from the air separation unit (ASU) enters the gasifier. Gasifier outlet is cooled in a radiant syngas cooler (RSC). Syngas gets separated from slag and goes to a scrubber where it is scrubbed with water. Steam is then added to the syngas and it is sent to a two-stage sour WGS reactor to produce hydrogen (H<sub>2</sub>) and carbon dioxide (CO<sub>2</sub>). The catalyst of the sour WGS reactor is also able to convert the Carbonyl sulfide (COS) present in the syngas into hydrogen sulfide (H<sub>2</sub>S).

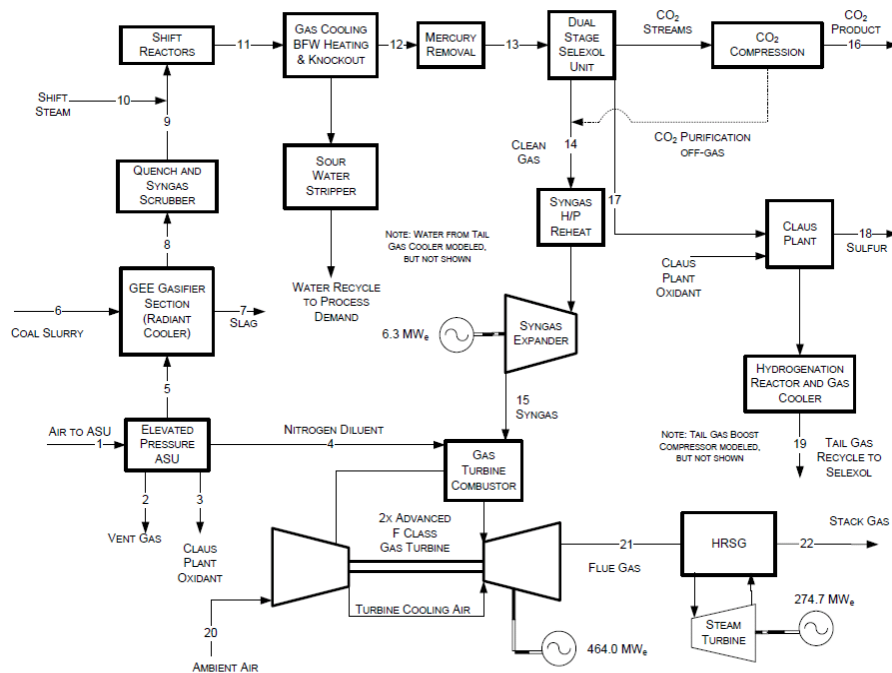


Figure 1-4. Schematic of the IGCC plant<sup>3</sup>

The shifted syngas from the sour WGS reactor is cooled in a series of heat exchangers and sent to the AGR unit. The AGR unit uses SELEXOL solvent to absorb CO<sub>2</sub>

and H<sub>2</sub>S. Captured CO<sub>2</sub> is compressed, processed, and sent for sequestration. Captured H<sub>2</sub>S is sent to the Claus-technology based sulfur recovery unit to produce elemental sulfur. The H<sub>2</sub>-rich syngas is reheated and sent to the gas turbine (GT). Nitrogen is used as a diluent in the GT. Heat is recovered from the hot flue gas that leaves the GT by generating steam in a heat recovery steam generator (HRSG) that operates at three pressure levels. The steam is sent to a steam turbine (ST) producing more electricity. The flue gas from the HRSG is vented from the stack. Finally, syngas is used in combined cycle to produce power.

Typical faults in this plant include the blocking of the RSC, leakage in pipes in the black water service, leakage in the sour syngas pipe before and after sour WGS reactors, failure of the ASU main air compressor (MAC), leakage in the Claus Catalytic Reactor, poisoning of the sour WGS reactor catalyst, poisoning of the Claus plant catalyst, fouling of the heat exchangers particularly those in the black-water, sour-water service, the exchangers in the Claus plant, and etc. It is guaranteed that all the possible faults are identified and considered, but the faults critical for improving the availability of the IGCC plant are considered although some may remain unresolved. The various types of sensors that will be considered in this thesis include temperature, pressure, flow, level, and composition sensors. Base case sensor placements will be generated using such sensors.

The reports from the TECO IGCC plant at Polk county, Florida provide immense insight into many of the typical problems.<sup>17</sup> Let's consider examples from one such report and how that will be modeled in Aspen Plus Dynamics. In an assessment of the plant availability during October, 2000-September, 2001 run of the TECO plant, the following faults were mentioned that led to shutdown during its fifth year of operation: 5 forced outages due to syngas and blackwater line leaks, plugged RSC outlet line, syngas scrubber outage, icing in the main exchanger in the ASU due to missed steps in the regeneration cycle of the air dryer, deposition of the heat stable salt in the MDEA absorber and etc.<sup>17</sup> It was mentioned that, "We could have eliminated or mitigated the losses in most cases".<sup>17</sup>

Faults can be simulated in the Aspen Plus Dynamics (APD) and the transient results can be used in the fault diagnosis algorithm. For example, the leak in the syngas line can be simulated by adding a pipe with a valve to the syngas line and opening the valve slowly through a "Flowsheet Task" in APD. The deposition of a solid in the tray of a distillation

column can be simulated by slowly blocking the open area of the tray implemented through script in APD. These changes can be done manually or by some predefined function written in script of APD. The commissioning, operational, and project execution experiences of the TECO IGCC power plant at Polk Country, Florida are extensively used in this project for identification of the faults at the plant level as well as at the unit level. A number of reports detailing the various phases of this plant are available in the public domain.<sup>17-22</sup> The reports of the pilot plant studies and the issues faced in the commercialization of the Texaco process are also available.<sup>23-26</sup> Operational experiences of these projects will also be utilized whenever applicable. A thorough review of the existing literature has led us to come up with a list of frequent and important faults encountered in an IGCC plant especially in sour WGS reactor, SELEXOL unit and combined cycle.

The system-level sensor placement is performed on SELEXOL unit and combined cycle as case studies for validating the system-level sensor placement algorithms. However, the 2-tier sensor placement is performed on gasification island. Gasification island is the term used for integrated system of 2-stage sour WGS reactor with inter-stage cooling and SELEXOL unit.

The main problem in the sour WGS reactor is the catalyst poisoning that includes catalyst activity, porosity and surface area reduction. These faults can be simulated by changing the activity, porosity or surface area of the catalyst in the sour WGS reactor model, respectively. In this thesis, a 1-D first-principles sour WGS reactor model is developed and used. This model considers mass, momentum, and energy balances as well as detailed kinetic models of the water gas shift and carbonyl sulfide hydrolysis reactions. The SELEXOL unit model is derived from the work of Bhattacharyya et al.<sup>3</sup> The sour WGS reactor is modeled in MATLAB while SELEXOL unit model is in APD platform. These models are integrated using SIMULINK.

### 1.3 Computation Tools

MATLAB®, a computing environment developed by MathWorks®, is one of the main engineering software used in this thesis for modeling and optimization. Except for the integrated models available in Aspen Plus®, all of the system- and component-level sensor placement algorithms and the corresponding simulations are performed in

MATLAB environment. Aspen Plus is a chemical process simulation software developed by AspenTech that is used in this thesis for simulation of gasification and combined cycle islands. The Simulink interface developed by MathWorks links the Aspen Plus to MATLAB for simulation of integrated systems including gasification island and combined cycle integrated with sour WGS reactor. IBM ILOG CPLEX® optimization toolbox for MATLAB is used within MATLAB environment for solving integer linear programming problems in system-level sensor placement while other optimization problems are solved using MATLAB's default optimization toolbox. The final optimization of component-level sensor placement which involves genetic search can be efficiently performed in parallel. The parallel computation is provided by Texas Tech University's High Performance Computing Center (HPCC). HPCC's computing resource, Hrothgar, has 86 teraflops in 7680 2.8 GHz cores and 12.3 teraflops in 1024 3.0 GHz cores. However, the regular MATLAB parallel computation license on HPCC is limited to use of 12 cores (increased to 20 cores in 2015) per each computing job.

## 1.4 Thesis Organization

*Chapter 1 – Introduction:* Discusses the purpose, relevance and impacts of the thesis. The fundamental information and overall approach of the thesis is briefly described.

*Chapter 2 – Process and Model Descriptions:* Describes the development of process models for sour water gas shift reactor, SELEXOL unit, gasification island process and combined cycle unit in complete detail. Simulation studies for model validation and sensitivity studies are also provided.

*Chapter 3 – Scaling Analysis and Model Simplification:* This chapter provides a mathematical approach for model simplification using scaling analysis which avoids the trial and error calculations of scales and dimensionless groups. The simplified model of the sour water gas shift reactor is developed in this chapter.

*Chapter 4 – System-Level Sensor Placement:* Describes qualitative-analysis of causal models for fault detection and introduces an enhancement to previously developed algorithms. Implementation of algorithms in presence of numerical simulations is

discussed as well. The developed algorithm is validated by considering different case studies.

*Chapter 5 – Network Decomposition:* Describes the necessity of graph partitioning for fault detection, as well as a method for sensitivity analysis of network systems for fault detection.

*Chapter 6 – Component-Level Sensor Placement:* Explains the constrained state estimation and the genetic algorithm involved in distributed sensor placement. For state estimation, the development and formulation of constrained extended Kalman filter for differential and algebraic systems are described, as well as the implementation on the sour water gas shift model and its simplified model. The optimization problem for sensor placement and the genetic algorithm properties used for finding its solution are also discussed.

*Chapter 7 – Implementation of 2-Tier Sensor Placement on Gasification Island Unit:* The algorithms developed in previous chapters are implemented on the gasification island to identify a 2-tier sensor placement approach for fault detection and fault severity estimation. The faults that are considered in the gasification island are also explained in this section.

*Chapter 8 – Summary and Recommendations:* Discusses the overall study results and conclusions. Moreover, this chapter discusses the direction for future research and provides explanation of the use of 2-tier sensor placement framework for other systems.

## Chapter 2

### Process and Model Descriptions

In this chapter, different units in an IGCC plant, including sour water gas shift (WGS) reactor, SELEXOL unit, gasification island, and combined cycle, are described. Since a high fidelity model of sour WGS is needed for component-level sensor placement, a first-principles model is developed and explained in detail. However, for other units, process roles and current state of the art models developed in the literature are discussed. The already developed models are then used for the purpose of sensor placement.

#### 2.1 Sour Water Gas Shift Reactor

Fossil fuels are the main sources of non-renewable energy used by humans. Among these fuels, coal is found in abundance in U.S., while costing less (on a specific energy basis) than other fossil fuels. In an IGCC plant, the coal is converted via a gasification process into syngas that is rich in hydrogen ( $H_2$ ) and carbon monoxide (CO). The syngas, treated in a sour water gas shift (WGS) process, produces valuable  $H_2$ , removable  $CO_2$  by hydrolysis of unwanted CO, and removable hydrogen sulfide ( $H_2S$ ) by hydrolysis of the harmful sulfur compounds such as carbonyl sulfide (COS). The syngas is then passed through an acid gas removal (AGR) process to remove  $H_2S$  and  $CO_2$  and purified hydrogen is eventually burned in a combustion turbine as part of the combined cycle to produce power. The combined cycle constitutes a combustion turbine that produces energy by combusting the hydrogen and a steam cycle that first generates steam by recovering the heat of combustion from the gas turbine effluent stream and then produces energy by expanding the resulting steam in steam turbines. This combined cycle operation is more efficient than its rival, traditional pulverized coal plants, which benefit only from power generation from steam turbines. However, the cost, availability, and complexity are disadvantages of IGCC technology that must be addressed before IGCC can be the prime technology for coal-based power generation. These disadvantages can be addressed by utilizing a combination of developments including design and optimization of each component of the IGCC plant.

To satisfy the overall CO<sub>2</sub> capture target in an IGCC plant with CO<sub>2</sub> capture, a certain extent of CO to CO<sub>2</sub> conversion must be achieved in the WGS reactors.<sup>3</sup> The water gas shift process can be sweet or sour.<sup>27</sup> The activity of conventional sweet shift catalysts such as iron- or copper-based catalysts reduce in presence of sulfur due to sulfur poisoning.<sup>28,29</sup> Therefore, in a sweet shift process, the COS present in the syngas is first hydrolyzed to H<sub>2</sub>S and then H<sub>2</sub>S is captured in an AGR unit before sending the syngas to the WGS reactors. Therefore, the plants with sweet shift processes require two reactor systems- a COS hydrolysis reactor system and a WGS reactor system. These are called reactor systems as one or more reactors with inter-stage coolers may be needed depending on the desired extent of conversion and process operating conditions. As the water contained in the syngas is cooled and condensed before sending it to the AGR unit, the syngas must be reheated and before sending it to the sweet shift reactors, substantial amount of steam must be injected to the syngas in order to drive the reaction equilibrium towards the products. In an IGCC process, the syngas from the gasifier passes through a water scrubber.<sup>3</sup> The syngas at the outlet of the scrubber is saturated with water and can be made available at a temperature that is suitable for the WGS reactor inlet. Therefore, if the sour syngas from the outlet of the scrubber is shifted, a higher overall efficiency can be achieved in comparison to the sweet shift process because of the higher temperature of the syngas and lower requirement of additional steam.<sup>30-33</sup> However, a sulfur-tolerant catalyst is required because of the presence of COS and H<sub>2</sub>S in the syngas. The sulfide-treated Cobalt/Molybdenum (Co/Mo) and Nickel/Molybdenum (Ni/Mo) impregnated alumina catalysts are sulfur-tolerant and can catalyze the shift reaction.<sup>34-36</sup> In addition, typical sour shift catalysts can convert COS and other organic sulfur compounds into H<sub>2</sub>S, which also helps in capturing H<sub>2</sub>S since it is removed easier than COS from the syngas in the AGR unit.<sup>37</sup> Actually, sulfur-tolerant catalysts require sulfur in the syngas to remain active and can operate in a wide temperature range.<sup>38</sup> Moreover, the startup procedure for the sour water gas shift catalysts is less complex.<sup>39</sup> In addition, the sour shift catalysts are less sensitive to operational conditions.<sup>39</sup> Because of these advantages, a sour shift process is preferred in an IGCC plant with CO<sub>2</sub> capture and a separate COS hydrolysis reactor is not needed.

The water gas shift reaction is a well-studied equilibrium reaction where several models of the sweet shift reactor have been developed.<sup>38,40-44</sup> Giunta et al.<sup>44</sup> have performed an extensive study on a 2-D heterogeneous dynamic model, validated with experimental data. In their work, consideration of the intraparticle mass transfer limitations by the definition of effectiveness factor, although negligible at catalyst diameters below 0.8 mm, returns good results for industrial-sized reactors, which have larger catalysts.<sup>42</sup> Adams and Barton<sup>42</sup> have developed a 1-D heterogeneous dynamic model and validated with the work of Choi and Stenger<sup>45</sup>. Steady-state models of WGS reactor and their validation with the experimental data have been reported in the work of Ding and Chan<sup>41</sup> and Chen et al.<sup>46</sup>. Francesconi et al.<sup>43</sup> have discussed optimization of the reactor at steady-state condition.

Most of the efforts in modeling the WGS reactors have focused on the sweet shift process where several catalysts at different conditions have been studied.<sup>47-51</sup> In comparison to the vast amount of work on the sweet shift catalysts, the amount of work on the sour shift catalysts is very little. A few experimental works can be found that have investigated the performance of the sour shift catalysts and have performed kinetic studies in the presence of a sulfiding agent such as COS or H<sub>2</sub>S, which are typically present at reasonable concentrations in the syngas obtained from a coal-fired gasifier.<sup>28,35,52-55</sup> Additionally, computational models developed for sour shift reactors are rare. Bell and Edgar<sup>38,40</sup> have developed 1-D pseudo-homogeneous model of a reactor that is filled with the Co/Mo based catalyst, which is similar to the catalyst used in this work with the exception that the catalyst used in this work is promoted with cesium.<sup>56</sup> Although they verified their steady-state and dynamic model with experimental results, their lab-scale reactor model cannot be scaled up to an industrial reactor due to their assumptions that are exclusive to lab-scale models and under-predict the results for industrial-scale reactors. In their work, they have ignored the momentum balance while modeling their reactor; therefore, information on the pressure drop across the reactor is not included. Pseudo-homogeneous models are sufficient only when intra-particle heat and mass transfer limitations are negligible, which is not the case for an industrial-scale reactor.<sup>57</sup> Since a typical industrial-scale sour shift reactor is filled with larger catalyst particles and operates at higher pressures compared to catalyst particle size and operating pressure in experimental studies, their model cannot be used for studying the performance of the

reactor under industrial conditions. Here, all these issues are addressed and a model that is applicable to both lab- and industrial-scale reactors is developed.

In almost all the papers, both experimental and computational, COS hydrolysis reaction concurrent with the WGS reaction have not been studied. It must be noted that a significant conversion of COS in the shift reactor(s) is desired so that the resulting H<sub>2</sub>S can be captured in the acid gas removal unit for satisfying the overall specifications on sulfur emission.<sup>3</sup> COS hydrolysis reaction would be expected to occur on the sour shift catalysts since the typical sour shift catalysts use Co/Mo supported on alumina and alumina has been reported to catalyze the COS hydrolysis reaction.<sup>58-60</sup> With this motivation, we have developed a dynamic model of a sour shift reactor by considering both WGS and COS hydrolysis reactions and have used this model for the typical feed conditions of an IGCC plant. For validating the model, experimental data are required for reactors where the feed contains COS in addition to the typical species present in the syngas. Unfortunately, the only experimental data that we could find in the existing literature for such feed conditions contain high measurement errors that necessitate reconciliation of the reported data.<sup>56,61</sup> Therefore, an algorithm is developed for data reconciliation and estimation of the kinetic parameters. The developed model is then used to study the effect of the length and diameter of the reactor, the steam-to-CO ratio, and the inlet temperature of the syngas on the key operating variables. In addition, dynamic responses are studied by simulating the change in the inlet temperature and catalyst activity that might occur due to poisoning of the catalyst or due to change in the catalyst microstructure during the course of reactor operation.

### 2.1.1 Process Description

The two key reactions that take place in the catalytic sour WGS reactor are the water gas shift reaction,



and COS hydrolysis reaction,



Both reactions are exothermic and feasible over wide range of temperatures. The standard heat of reactions are 41.1 kJ/mol and 30.2 kJ/mol for WGS reaction and COS hydrolysis, respectively.<sup>62</sup> For both reactions, low temperatures are preferred thermodynamically as the equilibrium will be pushed toward the products whereas high temperatures are preferred due to the reaction kinetics. Thus, there is a trade-off between thermodynamics and reaction kinetics for these reactions. Hence conventionally, this process is carried out in 2-stages and involves high- and low-temperature reactors with inter-stage cooling.

The catalyst modeled is a Cs promoted Co/Mo impregnated alumina that is commercially available as "Aldridge".<sup>63</sup> Overstreet<sup>61</sup> and Berispeks<sup>56</sup> have studied this catalyst extensively for different weight percents of cobalt and molybdenum oxides and tabulated the results for each catalyst. In this report, published experimental data for catalyst "Q" in the work of Berispeks<sup>56</sup> are reconciled by solving an optimization problem and the intrinsic kinetic parameters of the WGS reaction are estimated by performing regression analysis using the reconciled data.

In the next section, modeling of the 1-D heterogeneous sour WGS reactor is explained in detail. The modeling is followed by a section that describes the data reconciliation procedure proposed for extracting the kinetic parameters essential to the model. In the last section, a commercial size reactor that operates within typical sour WGS process conditions is simulated and the effects of different parameters on the performance of the reactor are presented.

### 2.1.2 Model Description

The mathematical model of the plug-flow reactor is developed by deriving the conservation laws for mass, energy and momentum. For this, radial variations of transport variables are neglected and the gradients are only considered in axial direction. In this section H<sub>2</sub>, CO, CO<sub>2</sub>, H<sub>2</sub>S, H<sub>2</sub>O and COS are considered to be present in the system. Although in industries other gasses such as N<sub>2</sub>, Ar and O<sub>2</sub> may be present, the model equations can be extended easily to include these components, as they are present in very small quantities and do not react. In general, the model can be applied to any sour gas shift reactor with any catalyst, but, since kinetic parameters for sour gas shift reactor catalyst are rarely available, the model is used to extract the kinetic parameters from available

experimental data for the “Aldridge” catalyst through a data reconciliation procedure.<sup>63</sup> A previous study of COS hydrolysis over alumina-based catalysts showed that the reaction follows an Eley-Rideal mechanism.<sup>64</sup> Hence, kinetic parameters for the COS hydrolysis are obtained from the work of Svoronos et al.<sup>64</sup>, whereas the rate parameters for the WGS reaction are obtained through data reconciliation considering a pseudo-first order reaction.<sup>56</sup>

### 2.1.2.1 Physical Properties

The syngas heat capacity is calculated assuming ideal mixture, as shown in Eqn. (2.3).<sup>62</sup>

$$C_p = \sum_{i=1}^N y_i C_{p,i} \quad (2.3)$$

The viscosity of the syngas,  $\mu$ , is estimated from Eqn. (2.4) as:<sup>42</sup>

$$\mu = \sum_{i=1}^N \frac{y_i \mu_i}{\sum_{j=1}^N \sqrt{M_j/M_i}} \quad (2.4)$$

where  $M$  is molecular weight of species denoted by indices  $i$  and  $j$ .

Assuming interactions between all pairs in the syngas, thermal conductivity of the mixture can be approximated by using the molar average thermal conductivity, Eqn. (2.5).

$$\lambda = \sum_{i=1}^N y_i \lambda_i \quad (2.5)$$

The effective diffusivity,  $D_e$ , is related to binary diffusivity,  $D_{ij}$ , through Eqn. (2.6):<sup>42</sup>

$$D_{eff,ij} = D_{ij} \left( \frac{\varepsilon}{\tau} \right) \quad (2.6)$$

It is difficult to find accurate tortuosity values for the catalyst; however, since the tortuosity of water gas shift catalysts are in the range of 2-9, a tortuosity value of 5 is chosen.<sup>42</sup> The porosity of the catalyst,  $\varepsilon$ , is assumed to be 0.38.<sup>43</sup> The binary diffusivity,  $D_{ij}$ , is the binary

diffusivity of species  $i$  into species  $j$ . An approximate equation for diffusion of species  $i$  into a mixture is given as:<sup>42</sup>

$$D_{i,m} = \frac{1 - y_i}{\sum_{j \neq i} \left( \frac{y_j}{D_{eff,ij}} \right)}$$

An analysis of the diffusivity of reactants, CO and H<sub>2</sub>O, into the mixture in an industrial scale reactor showed that the diffusivity of H<sub>2</sub>O into the mixture is the lowest and thus considered as the rate limiting for the WGS reaction. The binary diffusivities are calculated using Eqn. (2.7a)-(2.7b).<sup>42,65</sup>

$$D_{ij} = (AT^B/P)[\ln(C/T)]^{-2D} \exp(-E/T - F/T^2) \quad (2.7a)$$

$$D_{ij} = B/P \quad (2.7b)$$

Note that useful information for calculating the heat capacity, viscosity, thermal conductivity and binary diffusivity can be found in the work of Adams and Barton<sup>62</sup>.

### 2.1.2.2 Model Equations for Catalyst Pellets

The 1-D heterogeneous model has been developed using the effectiveness factor to account for intraparticle mass transfer limitations. For a first-order reaction, the overall effectiveness factor relates the actual reaction rate,  $r$ , to the reaction rate evaluated at the bulk concentration using various system parameters, such as reaction rate constant,  $k$ , and mass transfer coefficient,  $k_c$ .<sup>55</sup>

$$-r_A = \Omega k C_{A,bulk} \quad (2.8)$$

where the overall effectiveness factor is defined as:

$$\Omega = \frac{\eta}{1 + \eta k / k_c a_c} \quad (2.9)$$

The effectiveness factor is a function of Thiele modulus,  $\phi$ , and for a spherical catalyst it is calculated as:

$$\eta = \frac{3}{\phi^2} (\phi \coth \phi - 1) \quad (2.10)$$

and Thiele modulus is given as:

$$\phi = \frac{d_{cat}}{2} \sqrt{\frac{k}{D_e}} \quad (2.11)$$

The mass transfer coefficient can be calculated from Thoenes-Kramers correlation:<sup>66-67</sup>

$$k_c = \frac{1 - \varepsilon}{\varepsilon} \frac{D_{i,m}}{d_{cat}} Re^{1/2} Sc^{1/3} \quad (2.12)$$

where the diffusion of H<sub>2</sub>O into the mixture is considered for  $D_{i,m}$  since it is rate limiting. Schmidt number,  $Sc$ , and Reynolds number,  $Re$ , are calculated from:

$$Sc = \frac{\mu}{\rho D_e} \quad (2.13)$$

$$Re = \frac{\rho u d_{cat}}{\mu(1 - \varepsilon)} \quad (2.14)$$

The surface area per unit volume of the pellet,  $a_c$ , is estimated by Eqn. (2.15) and assuming ideal gas behavior, the linear gas velocity,  $u$ , is given by Eqn. (2.16):<sup>42-43</sup>

$$a_c = 6(1 - \varepsilon)/d_{cat} \quad (2.15)$$

$$u = \frac{GRT}{P} \quad (2.16)$$

### 2.1.2.3 Species Balance

Conservation equations are derived for all gas phase species:

$$\frac{\partial C_i}{\partial t} = -\frac{1}{A_c \varepsilon} \frac{\partial F_i}{\partial z} + \left( \sum r_i \right) \frac{1 - \varepsilon}{\varepsilon} \quad (2.17)$$

The above equation is rewritten assuming ideal gas behavior for the syngas mixture:<sup>42</sup>

$$\frac{\partial C_i}{\partial t} = -GR \frac{T_{gas}}{P} \frac{\partial C_i}{\partial z} - C_i GR \left[ \frac{1}{P} \frac{\partial T_{gas}}{\partial z} - \frac{T_{gas}}{P^2} \frac{\partial P}{\partial z} \right] + (r_{WGS,i} + r_{Hyd,i}) \frac{1 - \varepsilon}{\varepsilon} \quad (2.18)$$

where  $C_i$  is the molar concentration of species  $i$ ,  $z$  is the axial position,  $T$  is the gas phase temperature,  $P$  is pressure,  $R$  is the universal gas constant, and  $G$  is the molar flux, calculated using Eqn. (2.19) and the total inlet molar flow rate,  $F_0$ , entering the reactor with diameter  $d_{rct}$  as below:<sup>42</sup>

$$G = \frac{4F_0}{\pi d_{rct}^2 \varepsilon} \quad (2.19)$$

The boundary condition at the inlet to the reactor (*at z = 0*) can be expressed as  $C_i = C_{i,in}$ ,  $T_{gas} = T_{in}$ , and  $P = P_{in}$ , where  $C_{i,in}$ ,  $T_{in}$  and  $P_{in}$  are the concentration, temperature and pressure of the gas at the inlet to the reactor.

#### 2.1.2.4 Momentum Balance

A simplified momentum conservation equation is considered assuming pseudo-steady state. This approach only requires a model for calculating the pressure drop along the reactor. The Ergun equation is used for calculating the axial pressure profile in a packed bed, rewritten as:<sup>68</sup>

$$\frac{dP}{dz} = \frac{\rho u^2}{d_{cat}} \left( \frac{1 - \varepsilon}{\varepsilon^3} \right) \left( 1.75 + \frac{150}{Re} \right) \quad (2.20)$$

where  $\rho$  is the density of the fluid.

#### 2.1.2.5 Gas phase energy balance

The temperature variation across the reactor can be obtained by deriving the gas phase energy balance:

$$\frac{\partial T_{gas}}{\partial t} = \frac{1}{\rho_{gas} C_p} \left[ -C_p G \frac{\partial T_g}{\partial z} + \frac{h_f a_c}{\varepsilon} (T_{cat} - T_{gas}) \right] \quad (2.21)$$

where the heat transfer coefficient,  $h_f$ , can be estimated using:<sup>66</sup>

$$h_f = 1.37 \left( \frac{0.357}{\varepsilon} \right) (C_p GM) \left( \frac{\mu}{d_{cat} GM} \right)^{0.359} \left( \frac{\lambda M}{C_p \mu} \right)^{2/3} \quad (2.22)$$

The boundary condition can be expressed as  $T_{gas}$  (*at z = 0*) =  $T_{in}$ , where  $T_{in}$  is the temperature of the gas at the inlet to the reactor.

#### 2.1.2.6 Catalyst phase energy balance

Assuming that the temperature only varies in the  $z$  direction and neglecting radial temperature profile, the adiabatic energy balance for the catalyst phase is:

$$\frac{\partial T_{cat}}{\partial t} = \frac{1}{\rho_{cat} C_{p,cat}} \left[ K_{cat} \frac{\partial^2 T_{cat}}{\partial z^2} - \frac{h_f a_c}{1 - \varepsilon} (T_{cat} - T_{gas}) + r_{WGS} \Delta H_{R,WGS} + r_{Hyd} \Delta H_{R,hyd} \right] \quad (2.23)$$

For the catalyst phase temperature, following boundary conditions are considered:  $\partial T_{cat}/\partial z$  ( $z = L$ ) = 0 and  $T_{cat}(z = 0) = T_{gas}$ . Thermal conductivity of the catalyst is assumed to be the same as pure alumina, 35 W/m-K. Additionally, this equation requires the calculation of the heats of reaction using the enthalpy defined as:

$$H_i = \Delta H_{298}^f + \int_{298}^T C_{p,i}(T) dT \quad (2.24)$$

The standard heat of formation of CO, CO<sub>2</sub>, COS, H<sub>2</sub>O and H<sub>2</sub>S are -110.5, -393.5, -142, -241.9, and -20.63 kJ/mol, respectively.<sup>62</sup>

### 2.1.2.7 Reaction kinetics

Although the WGS reaction has been studied over sulfur-tolerant catalysts, such as Co/Mo catalyst, kinetics of the COS hydrolysis on the sour shift catalyst are rarely reported. Thus, the parameters of COS hydrolysis are derived from the open literature for alumina-based catalyst.<sup>64</sup> However, the parameters for the WGS reaction are obtained by analyzing the available experimental data. However, since the presence of measurement error is common in the data collected in experimental studies, a data reconciliation procedure is developed to obtain consistent data.

The rate equation for COS hydrolysis considering Eley-Rideal mechanism is expressed as:<sup>64</sup>

$$-r_{hyd} = k_{Hyd} \frac{P_{COS}}{1 + K_{eq,hyd} P_{H_2O}} \quad (2.25)$$

where the partial pressures are in kPa and the rate and equilibrium constants are given as:<sup>64</sup>

$$k_{hyd} = 4223.32 \exp \left( \frac{-25270 \left[ \frac{J}{mol} \right]}{RT_{cat}} \right) \quad (2.26)$$

$$K_{eq,hyd} = \exp\left(\frac{10010[K]}{T_{cat}} - 15.89\right) \quad (2.27)$$

Considering a pseudo-first order equilibrium reaction, the rate equation for the WGS reaction can be expressed as:

$$-r_{WGS} = \Omega k_{WGS} P \left( x_{CO} - \frac{x_{CO_2} x_{H_2}}{K_{eq,WGS} x_{H_2O}} \right) \quad (2.28)$$

where  $P$  is the pressure in *atm* and the rate constant,  $k_{WGS}$ , follows the Arrhenius equation and the equilibrium constant,  $K_{eq,WGS}$ , is given by Moe<sup>69</sup>:

$$k_{WGS} = k_0 \exp\left(\frac{-E_a}{RT}\right) \quad (2.29)$$

$$K_{eq,WGS} = \exp\left(\frac{4577.8[K]}{T_{cat}} - 4.33\right) \quad (2.30)$$

### 2.1.2.8 Pressure scale-up

The reaction kinetics derived from experimental data obtained at lower pressure are not applicable to industrial-sized reactors since they result in over-prediction of the reaction rates by orders of magnitude. Therefore, a pressure scale-up factor is used to address such over-predictions at high pressures. The reaction rate at higher pressures is related to the rate at atmospheric pressure as:<sup>70</sup>

$$r'_{WGS} = P_{scale} r_{WGS} \quad (2.31)$$

where  $P_{scale}$  is the pressure scale factor which is expressed as:<sup>42</sup>

$$P_{scale} = P^{(0.5 - \frac{P}{500})} \quad (2.32)$$

where  $P$  is the pressure in *atm*. Basically, Eqn. (2.31) implies that the reaction rate above atmospheric pressure is in the range of 1-5 times the reaction at atmospheric pressure and the equation is reported to be valid up to 55 *atm*.<sup>42</sup> So, the rate equation for the WGS reaction in Eqn. (2.28) is rewritten for high pressures as:

$$-r'_{WGS} = \Omega k_{WGS} P_{scale} \left( x_{CO} - \frac{x_{CO_2} x_{H_2}}{K_{eq,WGS} x_{H_2O}} \right) \quad (2.33)$$

### 2.1.2.9 Catalyst deactivation

The catalyst loses its activity over time mainly due to poisoning, fouling, and thermal and mechanical degradation. However, here, the catalyst is assumed to deactivate only due to thermal degradation (sintering). The catalyst activity is defined in terms of reaction rates for both WGS reaction and COS hydrolysis as:<sup>44</sup>

$$a_{(t)} = \frac{r_{(t)}}{r_{(0)}} \quad (2.34)$$

The catalyst deactivation equation is given by:<sup>44</sup>

$$\frac{da}{dt} = k_d(a - a_{\infty})^m \quad (2.35)$$

where  $m$ , the order of sintering, is reported to be either 1 or 2;  $a_{\infty}$  is limiting activity at infinite time; and  $k_d$  is the sintering rate constant. In the work of Giunta et al.<sup>44</sup>, the catalyst activity is given at some point in time which gives a good estimate for the  $a_{\infty}$  in this work.<sup>44,71</sup> Also here,  $m$  is assumed to be 2 and  $k_d$  is found by integrating Eqn. (2.35) for expected life time of Co/Mo catalyst, 5 years, until the catalyst reaches 99% of its limiting activity.<sup>44,71-72</sup>

### 2.1.3 Solution Approach

The system consists of a set of partial differential equations (PDEs) representing the state of the system. The PDEs in the modeling equations are converted to ODEs using the method of lines, where the spatial derivatives are discretized using a backward difference method. However, for solving the equations, the rate parameters for the water gas shift reaction need to be obtained from the available experimental data.<sup>56</sup> The experimental data were generated from an isothermal reactor under steady-state conditions.<sup>56</sup> Therefore, the energy balance equations are eliminated to achieve an isothermal reactor and the time derivatives are set to zero. The resulting set of nonlinear equations is solved using a trust-region-dogleg algorithm by 'fsolve' function in MATLAB. Later, a dynamic adiabatic reactor is simulated by scaling up the reactor and using the obtained parameters. In the data reconciliation simulations, 100 grid points are assumed for discretization of a 10 centimeter reactor. Increasing the number of grid points to 200,

resulted in less than 0.01% deviation in estimating the rate constant but increased the simulation time. Since the reactor model is used multiple times in data reconciliation and gross error detection, to reduce the simulation burden, 100 grid points are considered for the simulations. Equations are solved for the 26 meter long industrial reactor considering 300 grid points since increasing the grid points to 900 resulted only in less than 0.1% improvement in error and substantially longer processor time to solve the equations.

#### 2.1.4 Data Reconciliation

The experimental data from Berispek<sup>56</sup> are used to obtain the kinetic parameters of the WGS reaction. The experimental work has a dry-feed with a given composition passing through a water saturator, which is maintained at 60°C. Before entering the reactor, flowrate of the wet-feed is measured. The effluent of the catalytic reactor passes through a gas sampling valve where the gas sample is collected and is analyzed by a gas chromatograph. The outlet compositions from the sour shift reactor are reported for various reactor temperatures and wet-feed flowrates. The reactor operates at close to atmospheric pressure (715 mm Hg at the inlet) and the temperature is varied from 200 to 400°C in increments of 25°C. In this laboratory reactor (with a length of 10 cm and a diameter of 3/16 inches), the temperature is maintained constant along the reactor resulting in an isothermal condition and the reactor is filled with the “Aldridge”<sup>63</sup> catalyst. Even though several catalysts are investigated in the work of Berispek<sup>56</sup>, Catalyst Q has been considered here. Various properties of Catalyst Q, shown in Table 2.1, are used for obtaining the kinetic parameters.

**Table 2.1. Properties of Catalyst Q<sup>56</sup>**

Property	Value
Mesh range	20/60
Surface area	279 m <sup>2</sup> /g
Density	0.65 g/cm <sup>3</sup>
Porosity	0.38
Tortuosity†	5
Weight of the catalyst	5.24 g
Weight of the inert solids	1.2 g

†Tortuosity is assumed for the catalyst

In general, experimental data obtained from instruments such as temperature sensors, flow meters, and gas chromatographs are prone to measurement errors; however, mathematical techniques can be helpful in correcting the errors in order to get estimates close to the actual values. In the Berispek's<sup>56</sup> experimental work, COS and H<sub>2</sub>S are found in very small quantities, less than two percent, and high measurement errors can be observed in the reported compositions. For instance, even though the feed to the reactor contains COS, the results of gas chromatography show no sulfur compounds at the outlet of the reactor for a particular catalyst while the results are considerably different for another catalyst.<sup>56</sup> The discrepancy in the outlet mole fractions of COS and H<sub>2</sub>S reported for different catalysts justifies our expectation that these measurements are associated with high errors and require careful consideration as the sulfur balances are violated. Therefore in our work, a data reconciliation technique is used to minimize the measurement errors.

In the experimental data, the dry feed composition before the saturator, wet stream flowrate at the inlet of reactor, and the gas composition at the outlet of the reactor have been reported.<sup>56</sup> These data are inadequate for calculating the mole fraction of the gas at the inlet of the reactor as the extent of saturation in the saturator before entering the reactor is unknown. It should be noted that as the flowrate of the dry gas feed is changed, it is expected that the extent of saturation can also vary. In addition, discrepancy in the experimental data has been observed as reported before. Hence, the data on outlet mole fractions are reconciled by a sequential process as described below. To perform the data reconciliation, the water saturator used in the experiments is assumed as a stream of steam with unknown flowrate, which is well mixed with the dry feed of known composition and unknown flowrate before entering the reactor.

Figure 2-1 shows the method used to obtain the reconciled data and the corresponding parameters. In this approach, data corresponding to different operating conditions are individually reconciled, resulting in reconciled data and consolidated reaction rate constants at specific flow rates and temperatures. Then, the estimated reaction rate constants are used to calculate the activation energy and frequency factor of the WGS reaction. An alternative approach is to include all the data in a single formulation and directly estimate the activation energy and frequency factor. However, due to the presence of gross errors, this approach results in undesired estimation errors.<sup>73-75</sup> A gross error

detection approach based on the work of Narasimhan et al.<sup>74-75</sup> is performed and gross errors are detected in the reported mole fractions of COS and H<sub>2</sub>S. To do this, a null hypothesis is assumed and the objective functions for all individual experiments are calculated based on the sequential data reconciliation shown in Figure 2-1 and the objective functions are summed up. Then, separate data reconciliations are performed assuming a single gross error hypothesized. The test statistic is obtained as the maximum difference in objective function values between the null hypothesis and the gross error model of each variable. This approach is done in series until the test statistic is less than the test criteria, which is equal to chi-square value with the correct degrees of freedom at 5% level of significance.<sup>74-75</sup> This approach resulted in the identification of COS and H<sub>2</sub>S sensors as having gross errors.

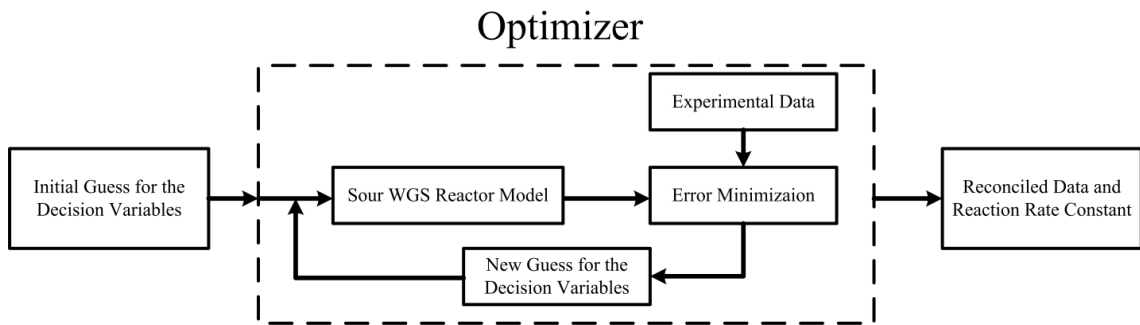


**Figure 2-1. Diagram of the data reconciliation procedure**

The decision variables for the objective function for this problem are: dry gas flow rate;  $F_{dry}$ ; steam flow rate;  $F_{stm}$ ; and the rate constant for the water gas shift reaction,  $k_{WGS}$ . The WGS reactor model is simulated to generate the outlet mole fractions by using the guesses for the decision variables. The optimizer minimizes the sum of the squared error between the model output and the experimental data as shown in Eqn. (2.36) until it finds the optimal values of the decision variables. The objective function involves two terms: the first term reduces the error between the outlet mole fractions from the model ( $y_{model}$ ) (reconciled values) and the experiments ( $y_{exp}$ ), while the second term reduces the error in the overall inlet flow rate. Since no information on the standard deviations for the gas chromatography measurements is provided in the work of Berispek<sup>56</sup>, standard deviation values used in the objective function are taken from the literature and are listed

in Table 2.2. Note that COS and H<sub>2</sub>S are omitted from the objective function due to the gross errors that exist in these measured values. The outlet mole fractions and a consolidated rate constant are estimated by using the proposed optimization formulation. It is worth mentioning again that, as can be seen in Figure 2-1, the data reconciliation is performed using a sequential approach. As a result, the model equations are embedded in the objective function and do not participate as constraints in the formulation. Therefore, an unconstrained optimization problem is solved individually for all flows at each temperature, which results in separate rate constants at each temperature. However, since the problem is non-convex, multiple simulations with different initial conditions are performed and the best solutions are retained. The optimization problem is solved in MATLAB using the 'fmin' function.

**Table 2.2. Standard deviation of different variables<sup>76-77</sup>**

Species	Standard deviation
H <sub>2</sub>	1%
CO	1%
CO <sub>2</sub>	1.4%
H <sub>2</sub> S	0.07%
H <sub>2</sub> O†	1%
COS†	0.07%
Flowrate	3%

†Standard deviation for H<sub>2</sub>O and COS are assumed

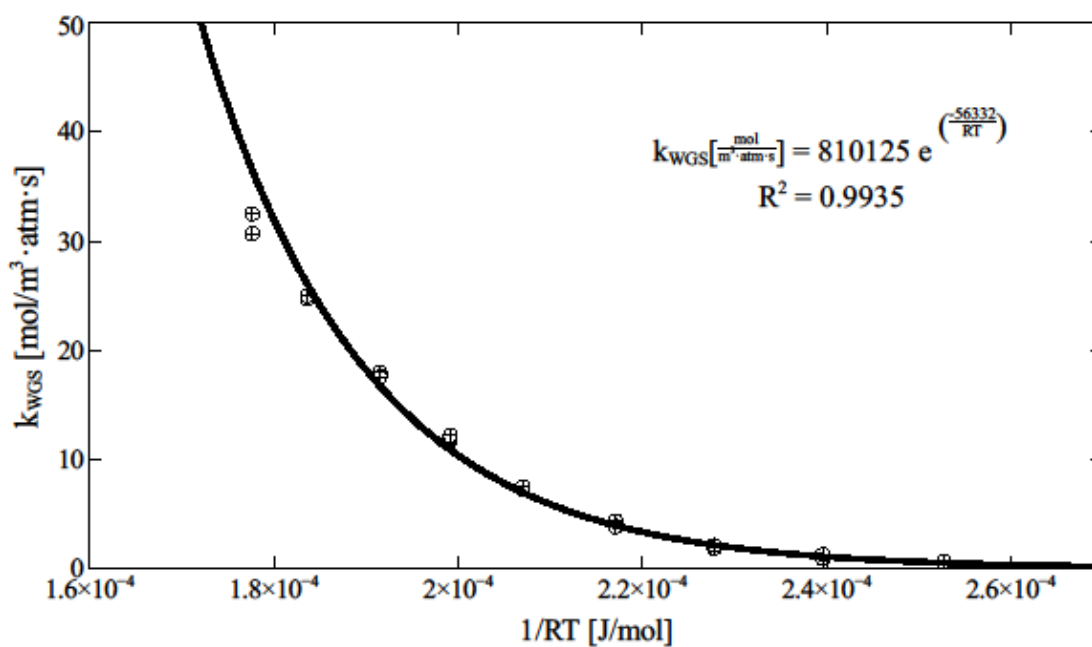
$$\min_{F_d, F_s, k_{WGS}} \sum_{\substack{j = H_2, CO, \\ CO_2, H_2O}} \left[ \frac{y_{model,j} - y_{exp,j}}{\sigma_j} \right]^2 + \left[ \frac{F_{dry} + F_{stm} - F_{exp}}{\sigma_F F_{exp}} \right]^2 \quad (2.36)$$

Table 2.3 shows the inlet and outlet mole fractions and the feed flow to the reactor ( $F_{dry} + F_{stm}$ ) for both the experimental and reconciled outputs at a particular temperature and flowrate. Reconciled mole fractions of H<sub>2</sub>, CO<sub>2</sub>, CO and H<sub>2</sub>O are in reasonable agreement with the experimental data.

**Table 2.3. Comparison of the reconciled and original mole fractions<sup>56</sup>**

Species	Original Data	Reconciled Data
H <sub>2</sub>	0.5467	0.5406
CO	0.2286	0.2289
CO <sub>2</sub>	0.1314	0.1371
H <sub>2</sub> S	0.0062	0.0113
H <sub>2</sub> O	0.0852	0.0818
COS	0.0019	0.0003
Flowrate[cm <sup>3</sup> /min]	92.6	92.5

Figure 2-2 is an Arrhenius plot for the obtained WGS reaction rate constant. Following values are obtained for the parameters,  $E_a$  is 56,332 J/mol and  $k_0$  is 810,125 mol/m<sup>3</sup>-atm-s. These rate parameters are used in Eqn. (2.28) for simulating the industrial scale reactor as described in the next section.

**Figure 2-2. Arrhenius plot for the water gas shift reaction**

### 2.1.5 Results and Discussions

A typical industrial sour gas shift process operates adiabatically and typically under high pressure. Considering an overall target of 90% carbon capture in an IGCC plant, a 2-stage WGS reactor system with high- and low-temperature reactors arranged in series with interstage coolers is required.<sup>3</sup> However, only the first stage is simulated here where the reactor is used to study the effect of different parameters on the reactor operation and the carbon capture goals are not considered explicitly as a 2-stage would then be required. The syngas in this simulation is composed of H<sub>2</sub>, CO, CO<sub>2</sub>, H<sub>2</sub>S, H<sub>2</sub>O and COS with mole fractions of 0.21929, 0.23021, 0.08880, 0.00465, 0.45696 and 9×10<sup>-5</sup>, respectively.<sup>16</sup> The reactor is filled with "Aldridge"<sup>63</sup> catalyst, catalyst Q, 2.2 mm in diameter and with porosity of 0.38; and the reactor is assumed to have no heat loss to the surrounding to satisfy the adiabatic condition.<sup>56</sup> With given composition and pressure for an IGCC case study, the reactor volume and the inlet temperature are adjusted to size a reactor with 10% overdesign and assuming length to diameter (*L/D*) of about 5.5.<sup>16</sup> Table 2.4 shows the sizing and operating conditions of the reactor.

**Table 2.4. Simulation condition<sup>16</sup>**

Condition	Value
Length	29 m
Diameter	5.2 m
Flow	4.9 kmol/s
Inlet Temperature	620 K
Inlet Pressure	54.437 atm

Figure 2-3 shows the CO mole fraction profile along the reactor with length increased to 40 meters. As the water gas shift reaction is equilibrium-limited, conversion will not change after reaching the equilibrium. This implies that for all operating conditions, a minimum length of the reactor is required to reach equilibrium. As in Figure 2-3, equilibrium is reached within almost the first 29 m of the reactor. Figure 2-4a and 2-4b show the COS mole fraction and gas temperature, respectively, as a function of the length of the reactor. In Figure 2-4a, it appears that only 9 m of the reactor is required for COS

hydrolysis to reach completion. Since COS hydrolysis is faster compared to WGS reaction, as in the sweet WGS reactor, the design would only require the first 29 meters of the reactor because no conversion is achieved after this point. When considering the design parameters for the sour WGS reactor, the required dimensions should be decided by considering the desired extent of WGS reaction. Although a longer reactor will have higher overall conversion, several other factors such as equipment cost and allowable pressure drop should be considered for deciding the final dimensions of the reactors. Note that in the subsequent studies the reactor length is fixed at 29 m.

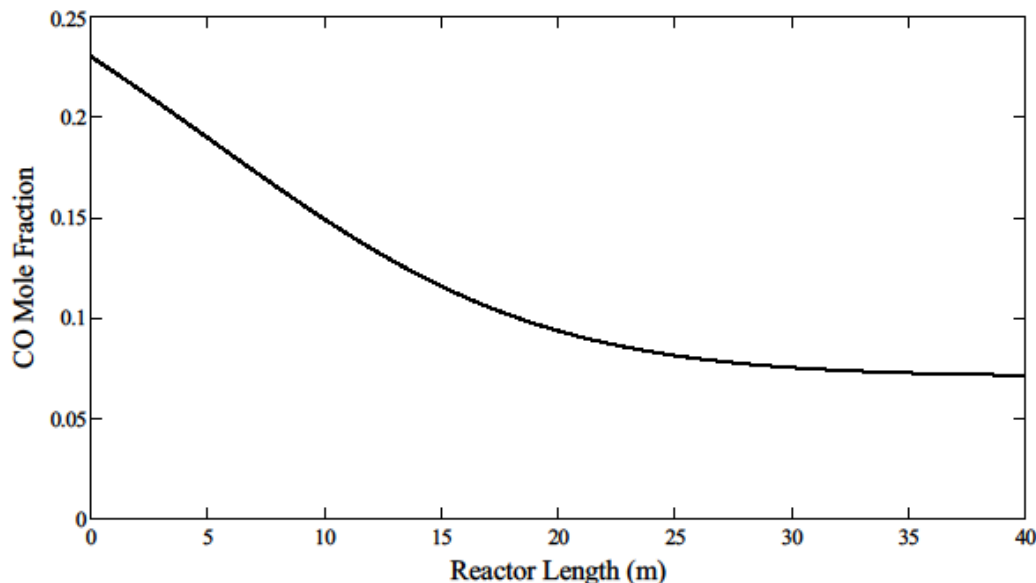
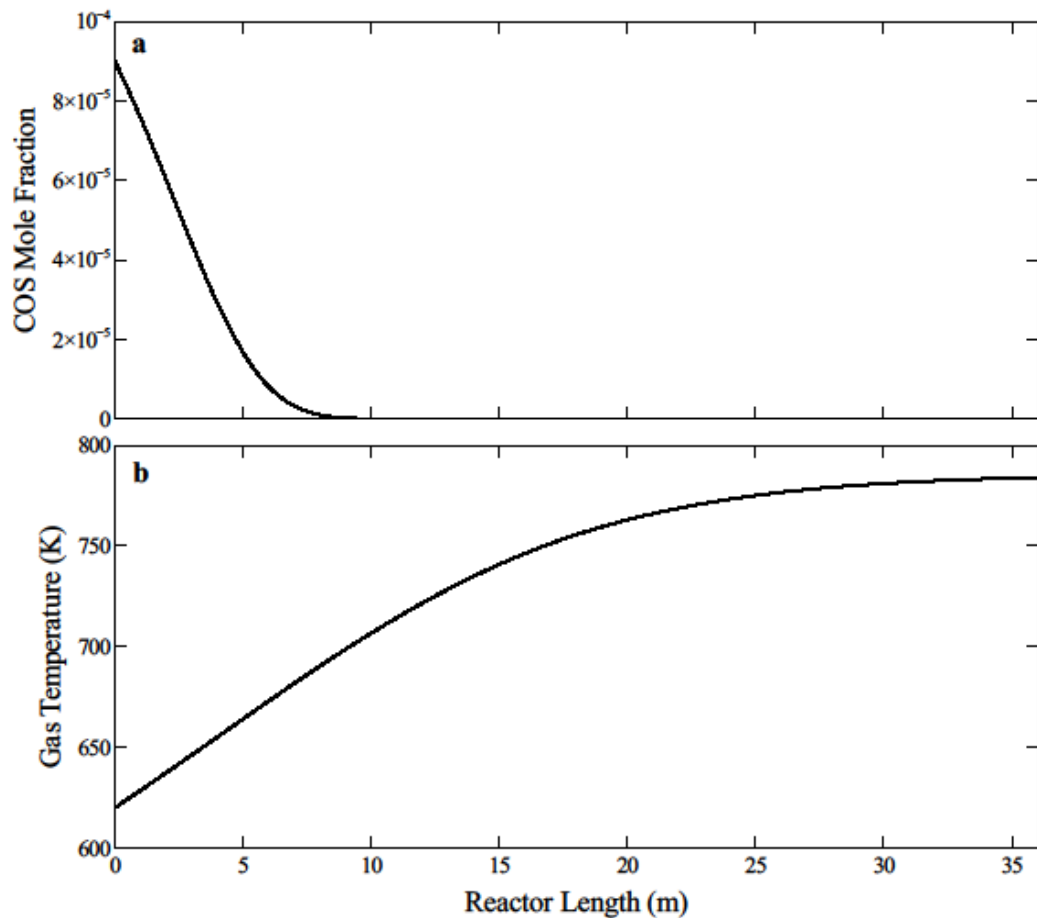


Figure 2-3. CO mole fraction profile along the reactor when length is increased to 40 m



**Figure 2-4. (a) COS mole fraction (b) Gas temperature profile along the reactor when length is increased to 40 m**

Figure 2-5 shows the axial profile of CO mole fraction as the reactor diameter is changed. For a given length, an increase in the diameter of the reactor increases the conversion of CO if equilibrium is not reached. It should be noted that an almost complete COS conversion is achieved for all diameters shown in Figure 2-5. Figure 2-6 shows the corresponding pressure profile. It is observed that as the diameter is decreased beyond certain value, the pressure drop increases substantially.

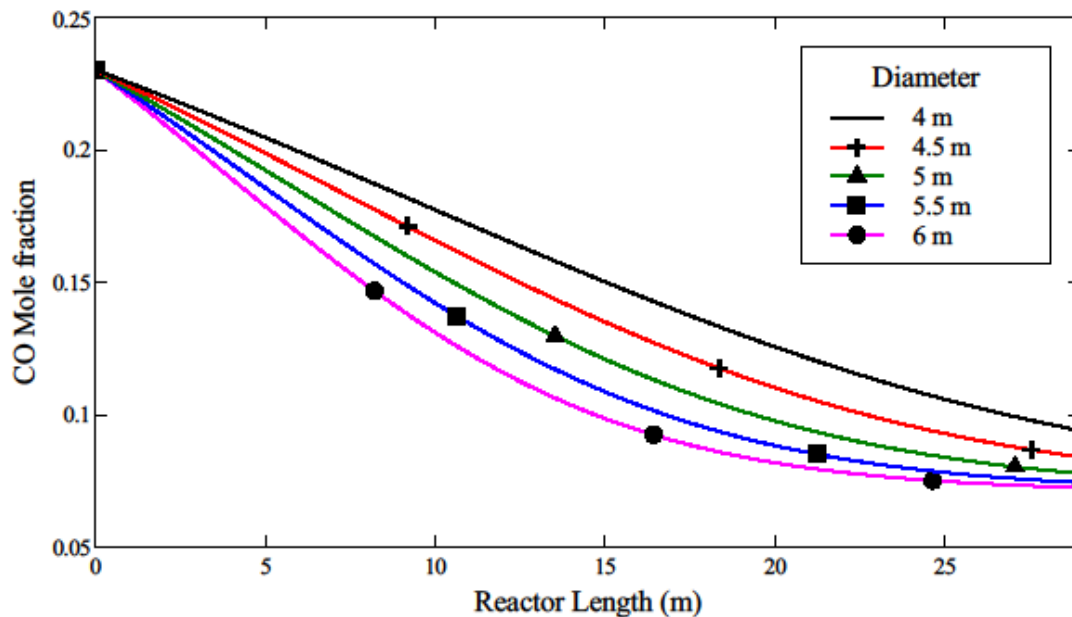


Figure 2-5. CO mole fraction profile for different reactor diameters

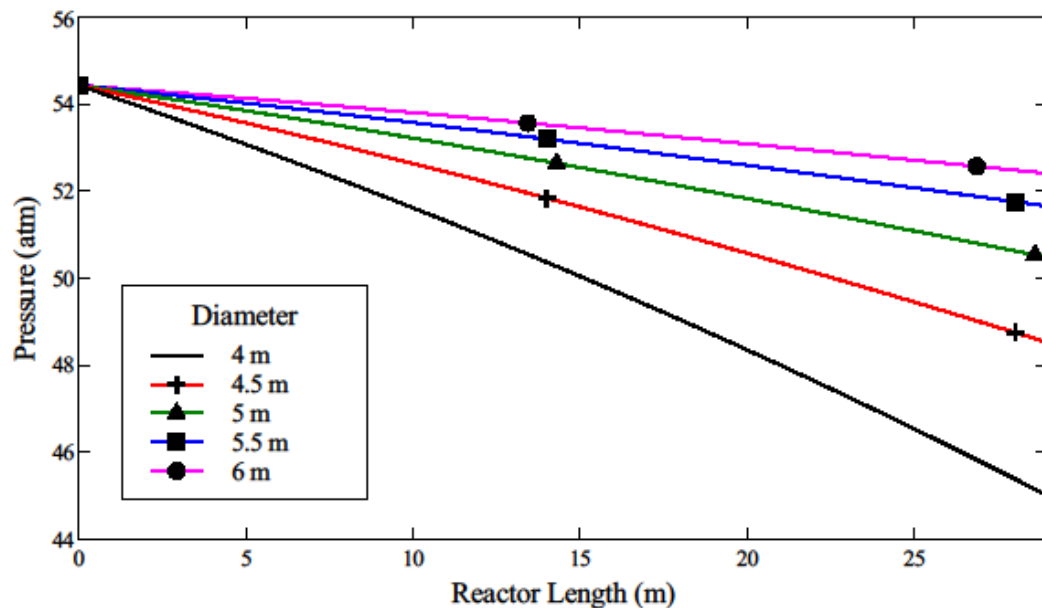


Figure 2-6. Pressure profile for different reactor diameters

Figure 2-7 shows the relation between the  $L/D$  ratio and pressure drop at constant reactor volume. This result indicates that as  $L/D$  increases, the pressure drop keeps increasing. It should be noted that a lower pressure drop is desired in the WGS reactor system so that higher partial pressure of  $\text{CO}_2$  can be achieved in the AGR unit. This is particularly important for achieving higher efficiency of the physical solvent-based  $\text{CO}_2$  capture process in the IGCC plant.<sup>3</sup>

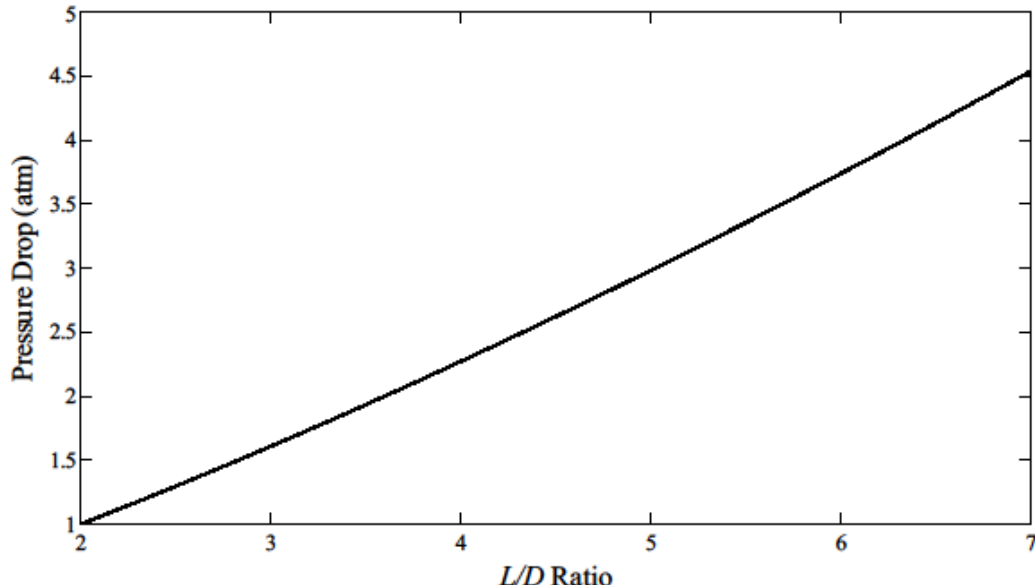
**Figure****2-7. Pressure drop vs. L/D ratio of the reactor**

Figure 2-8 and 2-9 show the conversion of CO and COS along the reactor for different inlet gas temperatures. As seen in Figure 2-8, the conversion at the outlet remains fairly constant, however, the conversion along the reactor reduces as the inlet temperature decreases. Even though the conversion of CO is slightly affected by the change in the inlet temperature, the COS conversion is not affected at higher inlet temperatures as seen in Figure 2-9. Figure 2-8 shows that the CO conversion decreases as the inlet temperature changes from 620 K. This happens due to the interplay between the thermodynamics and reaction kinetics as mentioned before. However, one can argue that reducing the temperature will not significantly reduce the conversion; and recovered heat from reducing the inlet temperature would increase the efficiency of the steam cycle. This is later studied when considering the effect of catalyst deactivation on the performance of the reactor.

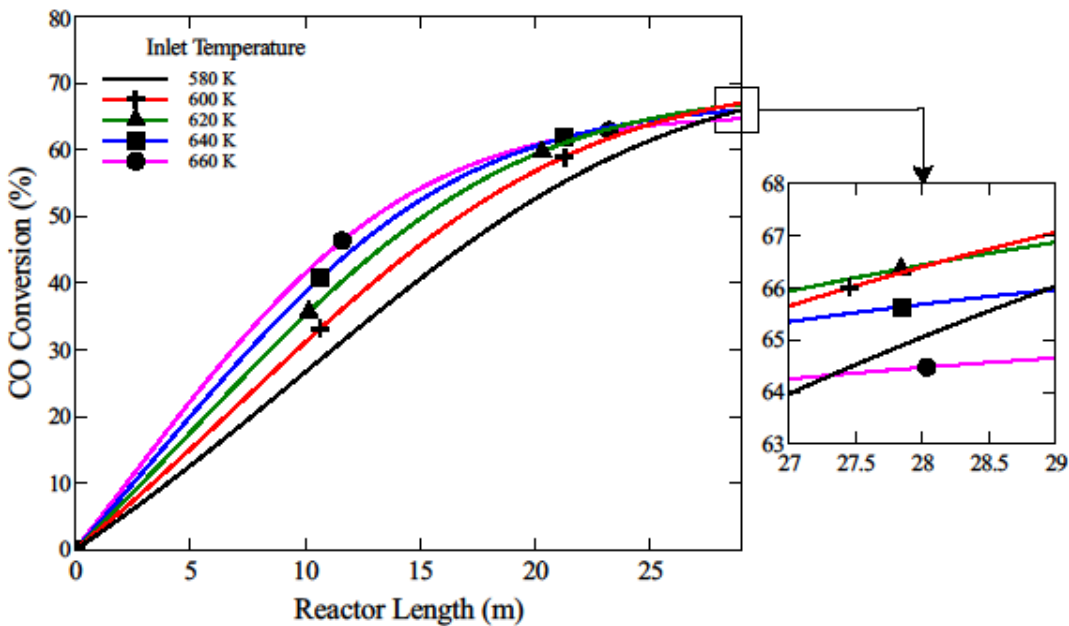


Figure 2-8. CO conversion profiles for different inlet gas temperatures

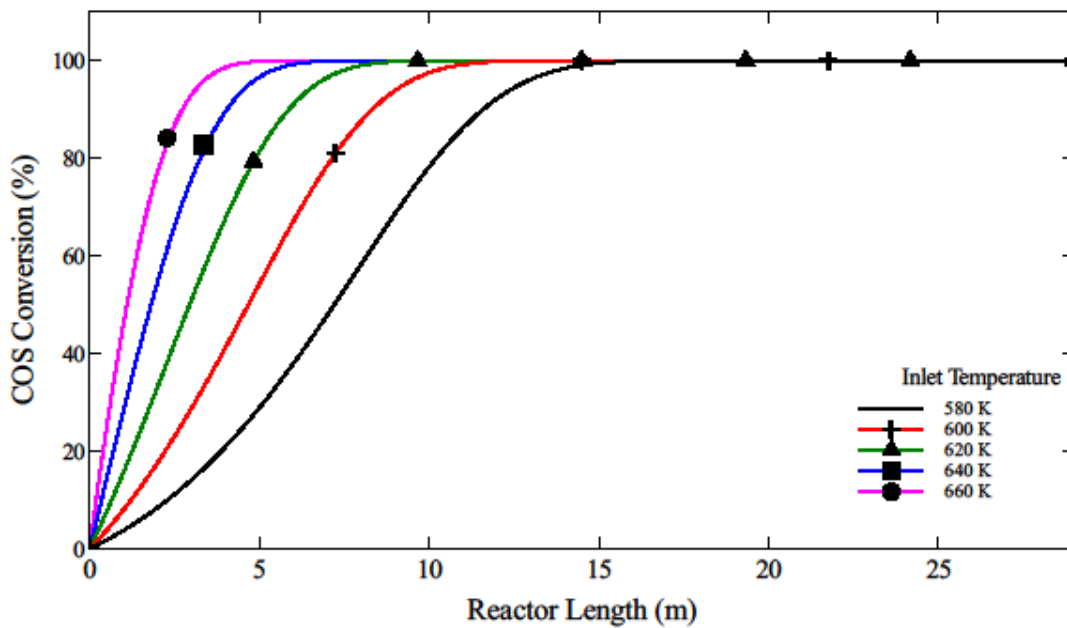
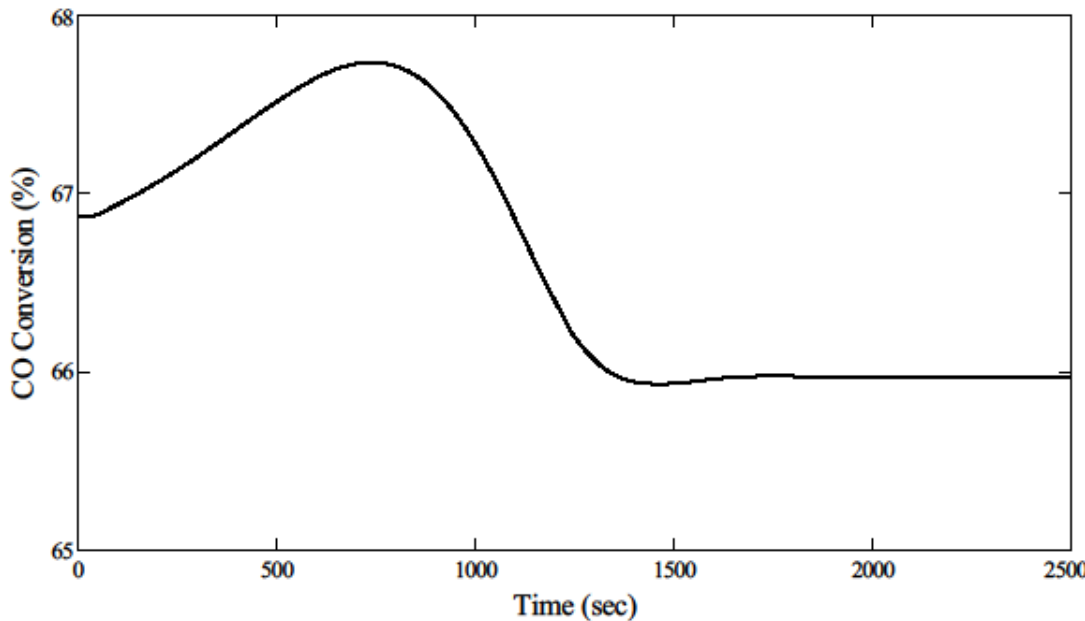


Figure 2-9. COS conversion profiles for different inlet gas temperatures

Figure 2-9 shows that high conversion is achieved at temperatures around the inlet operating temperature of 620 K and the COS conversion is not sensitive to the inlet temperature as the studied inlet temperatures are high enough to bring the COS hydrolysis reaction to completion. Although the magnified view in Figure 2-8 shows that an increase in the temperature results in a slightly lower conversion of CO, the reactor initially shows

inverse response to step increase in inlet temperature as shown in Figure 2-10. Figure 2-10 is generated by introducing a step increase in the inlet temperature from 620 to 640 K. When the inlet temperature rises, it takes some time for the temperature in the rest of the reactor to increase. So, initially the CO conversion increases due to higher reaction rate, but decreases later as the reaction temperature rises pushing the equilibrium to the left.



**Figure 2-10. CO conversion transient for a step change in inlet temperature from 620 to 640 K**

Figure 2-11 shows the dynamic response of gas temperature at the outlet of the reactor for the mentioned step increase in the inlet temperature. When the inlet temperature increases, more CO is consumed in the area near the inlet of the reactor, thus, the CO conversion increases initially as seen in Figure 2-10. This causes the CO concentration to reduce in the rest of the reactor, which at the same time reduces the reaction rate. Since reaction rate is decreased, less heat is generated by the exothermic reactions, thus, the temperature decreases initially. However, as the catalyst temperature slowly increases due to the higher heat input from the front end, the temperature increases. The COS conversion remains unchanged as the reactor temperature remains high enough to bring the reaction to completion in the early region of the reactor.

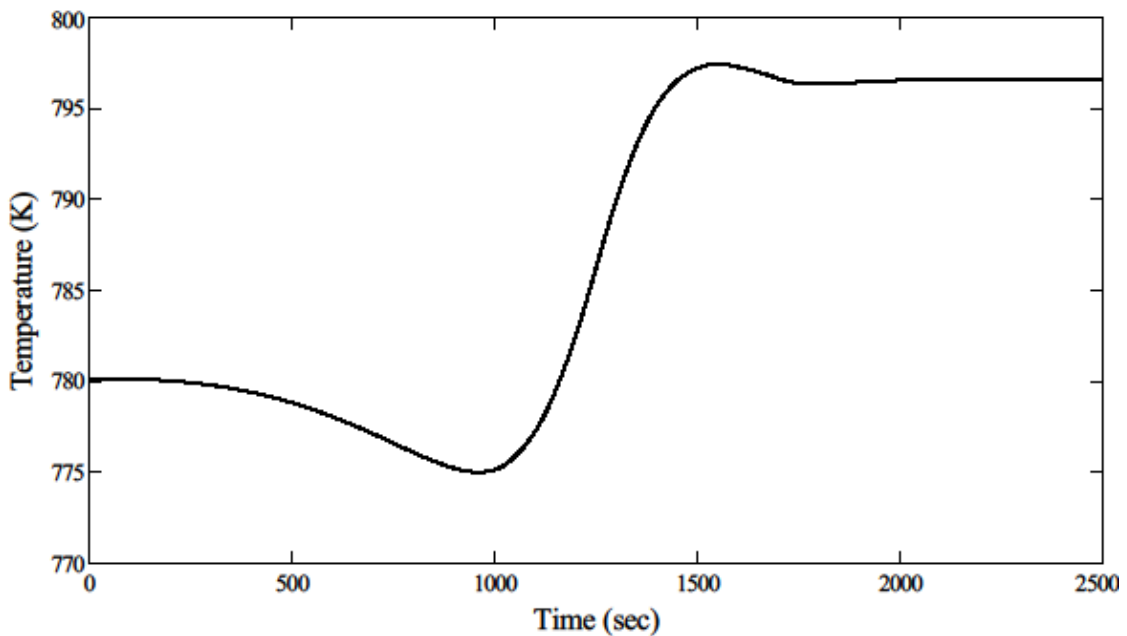


**Figure 2-11.** Temperature transient at the outlet of the reactor for a step change in inlet temperature from 620 to 640 K

In IGCC plants, additional steam is added to the syngas feed to achieve the desired conversion of CO. However, the required steam is extracted from the steam turbine.<sup>3</sup> Therefore, the production of electricity from the steam turbines gets reduced. It is therefore important to design the H<sub>2</sub>O/CO ratio at the inlet of the WGS reactors appropriately by considering an optimal CO conversion in the WGS reactor system. Figure 2-12 shows this relation between CO conversion and H<sub>2</sub>O/CO ratio. In Figure 2-12, increasing the molar ratio of steam to CO at constant dry flow rate (2,661 mol/s) increases the CO conversion until it reaches a maximum at a steam-to- CO ratio of about 4. However, increasing the ratio requires higher flow rate of steam, consequently, higher flow rate at the inlet to the reactor. Increasing the flow at the same residence time and superficial velocity requires higher reactor volume. This can be seen in Figure 2-13a and 2-13b where the reactor diameter and the flow are non-dimensionlized with respect to the values in Table 2.4. Thus, higher conversion must be weighed with respect to the capital cost of the reactor and the amount of steam taken from the steam cycle. Since the partial pressure of steam is in the denominator of Eqn. (2.25), it seems that increasing the steam content will reduce the COS hydrolysis rate. However, the COS conversion is not greatly affected by the amount of

steam present in the syngas. This is because the system's temperature is high enough to bring the COS hydrolysis to completion.

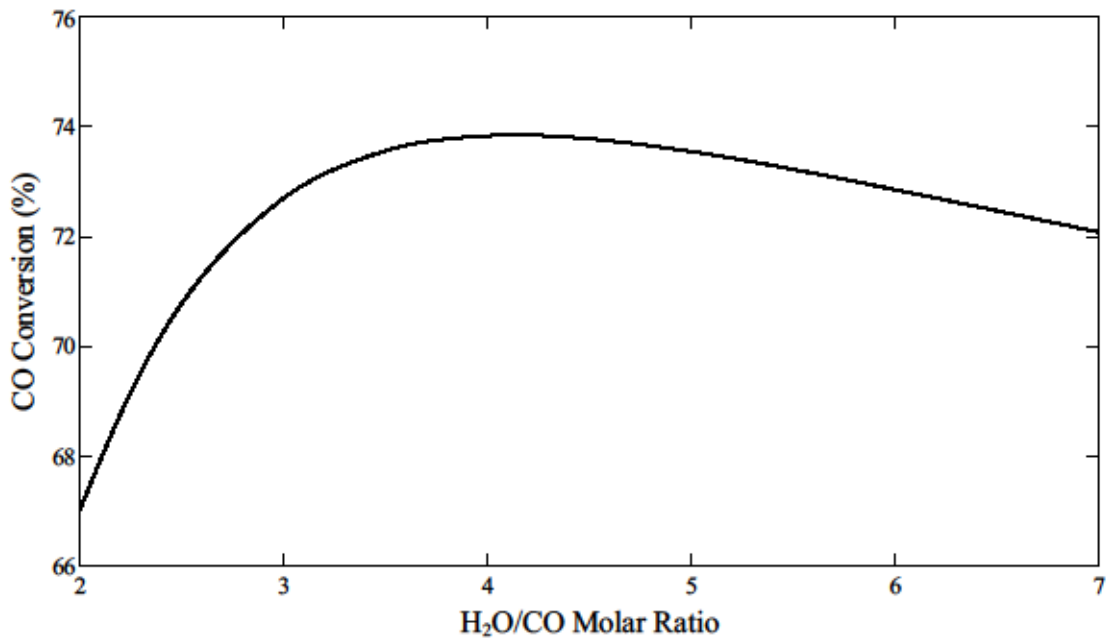


Figure 2-12. CO conversion profile for different steam/CO molar ratio

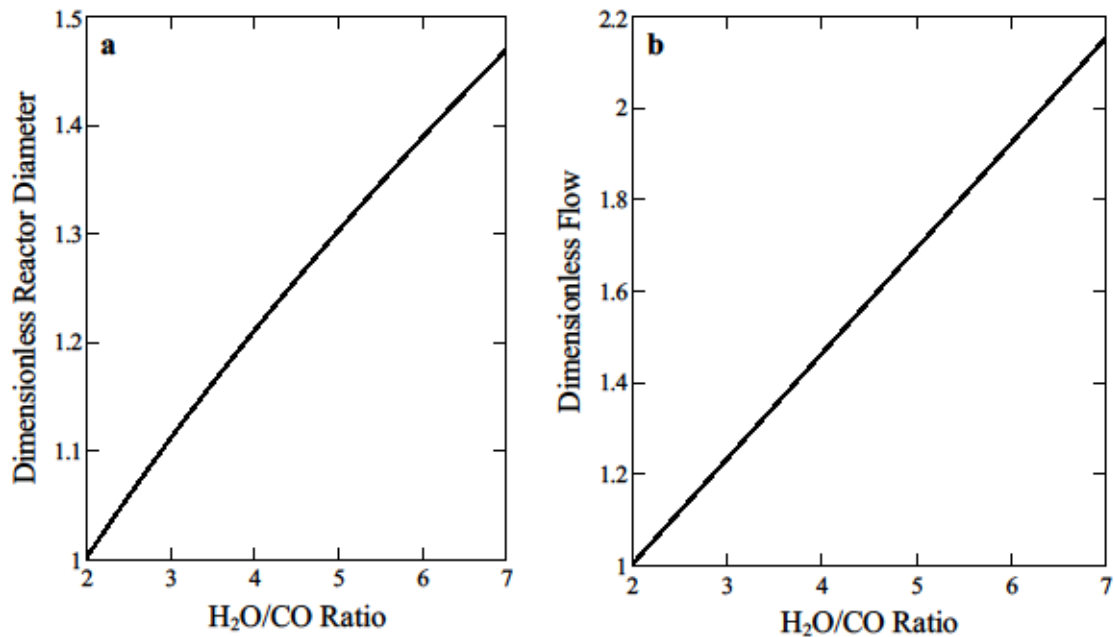
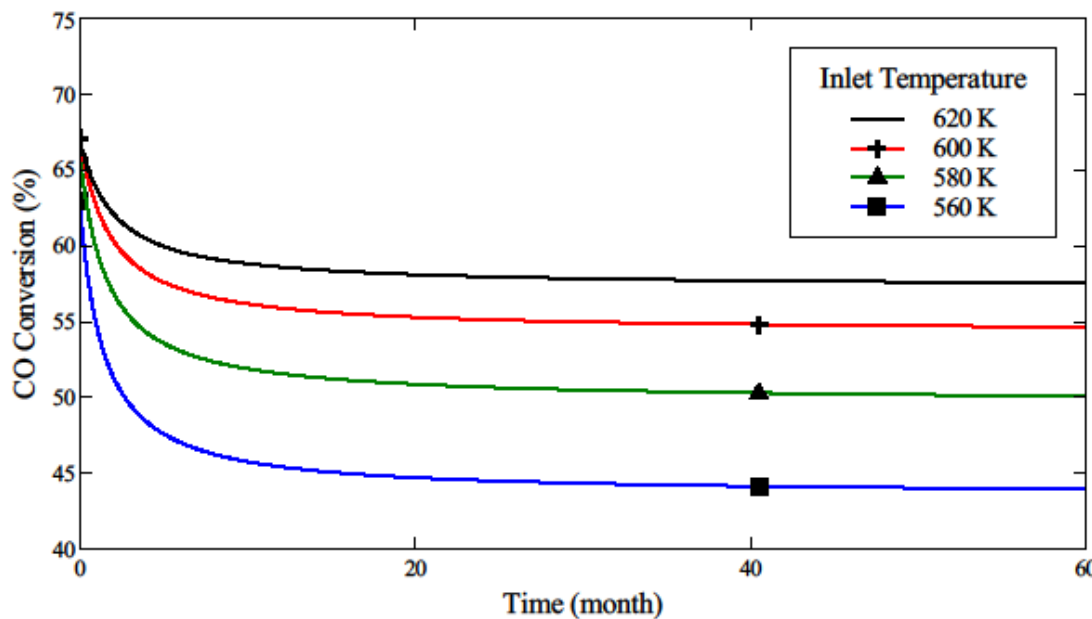


Figure 2-13. Required (a) Diameter (b) Flow at different steam/CO molar ratios

The catalyst deactivation due to sintering can lower the conversion in a sour WGS reactor. Figure 2-14 shows the effect of catalyst deactivation on CO conversion for

different inlet temperatures over the catalyst lifetime of 60 months (5 years).<sup>72</sup> From an optimization perspective, it can be argued that a lower inlet temperature would result in fairly acceptable conversion as can be seen in Figure 2-8 since lowering the temperature from 620 to 580 K will only decrease the conversion by approximately 1%. In return, the excess heat can be recovered to increase the efficiency of the steam cycle and the power generation. However, Figure 2-14 shows that at lower inlet temperatures, catalyst deactivation has substantial effect on the conversion of CO during the lifetime of the catalyst. Figure 2-14 shows that the CO conversion reduces drastically over time at lower temperatures. However, COS conversion remains at completion for the range of inlet temperature studied. Figure 2-15 shows the COS conversion along the reactor at different inlet temperatures after the period of 5 years. As seen in Figure 2-15, since the length and temperature are high enough for the range of temperature studied, the COS conversion remains at completion even in the presence of the catalyst deactivation. Although, as can be seen in Figure 2-15, the COS conversion along the reactor is drastically reduced at lower temperatures, this effect is compensated by the length of the reactor. Therefore, there is a trade-off between the efficiency of steam cycle and the extent of the reactions over catalyst lifetime. However, from the design perspective, the effect of catalyst deactivation can be compensated by overdesigning the reactor.



**Figure 2-14. Effect of catalyst deactivation over time on CO conversion**

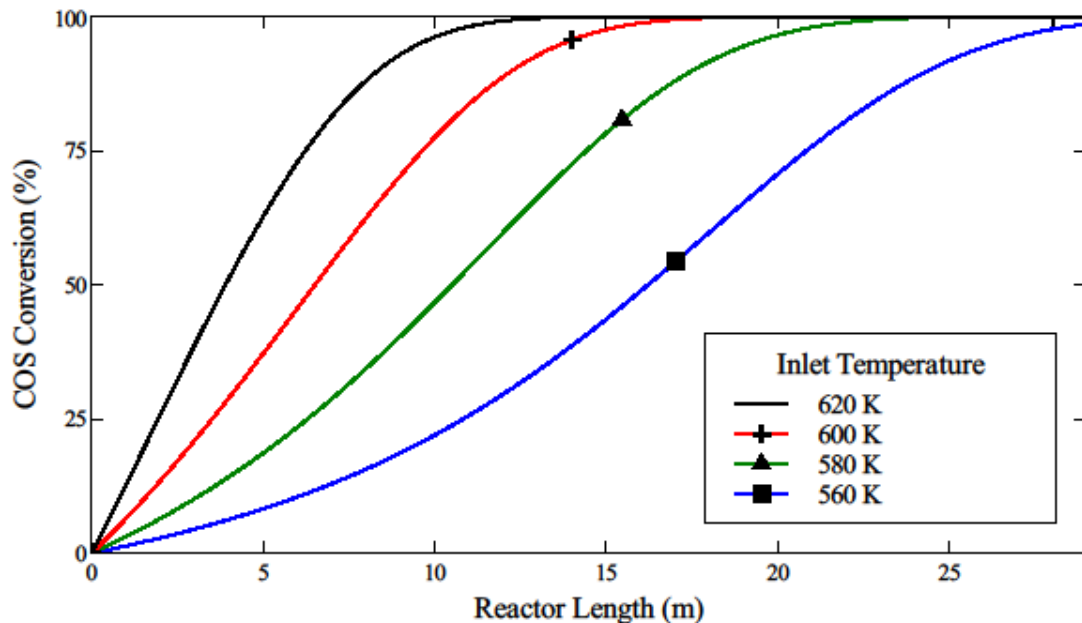


Figure 2-15. COS conversion along the reactor after the catalyst lifetime of 5 years

### 2.1.6 Conclusion

A 1-D dynamic model of a sour water gas shift reactor has been developed. The available experimental data for a sour WGS reactor have been reconciled to obtain consistent data. The proposed data reconciliation procedure uses the reactor model to reconcile the data while simultaneously extracting the rate constant. A minimization problem is solved for each run of the experimental work and the corresponding rate constant is obtained. The Arrhenius plot yields the pre-exponential factor and activation energy for the WGS reaction.

A simulation study under typical conditions of a sour WGS reactor as part of an IGCC plant is performed. The effects of different parameters on the performance of the reactor are investigated and results are presented. This study shows that the reactor should be designed with due consideration of the desired CO conversion as the WGS reaction is found to reach equilibrium further down the reactor. The study shows that the  $L/D$  ratio of the reactors should be appropriately designed by considering the pressure drop across the reactors as the efficiency of the AGR unit downstream of the WGS reactor is affected by the outlet pressure from the shift reactor system. For the range of inlet temperatures studied, i.e., 580-660 K, the COS conversion is found to be not affected by the feed temperature. In

addition, even though an increase in the temperature results in slightly lower CO conversion, the reactor shows inverse response to a step increase in the syngas inlet temperature. At constant flow, as the steam-to-CO ratio increases, the CO conversion reaches a maximum at steam-to-CO ratio of about 4 while the COS conversion remains at its highest value for the range of steam-to-CO studied. It is observed that the CO and COS conversions are not significantly affected by the catalyst deactivation if the inlet temperature is sufficiently high.<sup>78</sup>

## 2.2 Acid Gas Removal Plant – SELEXOL Unit

### 2.2.1 Process Description

The SELEXOL technology used in the AGR unit, as shown in Figure 1-4 uses chilled SELEXOL solvent to remove H<sub>2</sub>S and CO<sub>2</sub> present in the syngas. SELEXOL is a physical solvent, which is a mixture of dimethyl ethers of polyethylene glycol (DEPG), i.e. CH<sub>3</sub>(CH<sub>2</sub>CH<sub>2</sub>O)<sub>n</sub>CH<sub>3</sub>, where 3 ≤ n ≤ 9. The dual-stage SELEXOL unit in IGCC absorbs H<sub>2</sub>S in the first stage and CO<sub>2</sub> in the second stage. The captured CO<sub>2</sub> is recovered at three pressure levels and sent for compression. The H<sub>2</sub>S that is thermally stripped from the loaded solvent is sent to the Claus unit for sulfur recovery. A fault in this unit may result in reduction of plant efficiency, or loss of expensive solvent or other species, or can lead to hazardous conditions.

A schematic of the SELEXOL unit is shown in Figure 2-16. In this process, the syngas is fed to the bottom of the H<sub>2</sub>S absorber where the CO<sub>2</sub>-rich solvent from the bottom of the CO<sub>2</sub> absorber is fed to the top of the column. The H<sub>2</sub>S-lean syngas enters the CO<sub>2</sub> absorber where the lean solvent is fed at the top and partially regenerated semi-lean solvent is fed at the 5<sup>th</sup> stage from the top. A major portion of the solvent from the bottom of the CO<sub>2</sub> absorber goes through a series of four flash vessels. In the first flash vessel, significant amount of the dissolved H<sub>2</sub> is recovered from the solvent and sent back to the CO<sub>2</sub> absorber. The solvent then passes through the high pressure (HP), medium pressure (MP) and low pressure (LP) flash vessels for recovering CO<sub>2</sub>. The recovered CO<sub>2</sub> is sent to the compression unit for sequestration. The semi-lean solvent from the LP flash vessel is pumped back to the CO<sub>2</sub> absorber. Rich solvent from the H<sub>2</sub>S absorber is sent to the regenerator via a H<sub>2</sub>S concentrator. Before introducing the solvent to the H<sub>2</sub>S concentrator,

the solvent is heated up in a lean/rich heat exchanger. The CO<sub>2</sub>-rich stream from the top of the H<sub>2</sub>S concentrator is then recycled back to the H<sub>2</sub>S absorber. In the stripper, the reboiler in combination with steam stripping is used to thermally regenerate the solvent. The H<sub>2</sub>S-rich gas from the top of the stripper reflux vessel goes to the Claus unit for further treatment. The lean solvent exchanges heat in the lean/rich heat exchanger, which is chilled using liquid ammonia, and is pumped back to the CO<sub>2</sub> absorber. The make-up solvent is fed to the lean solvent to compensate for any loss of the solvent.

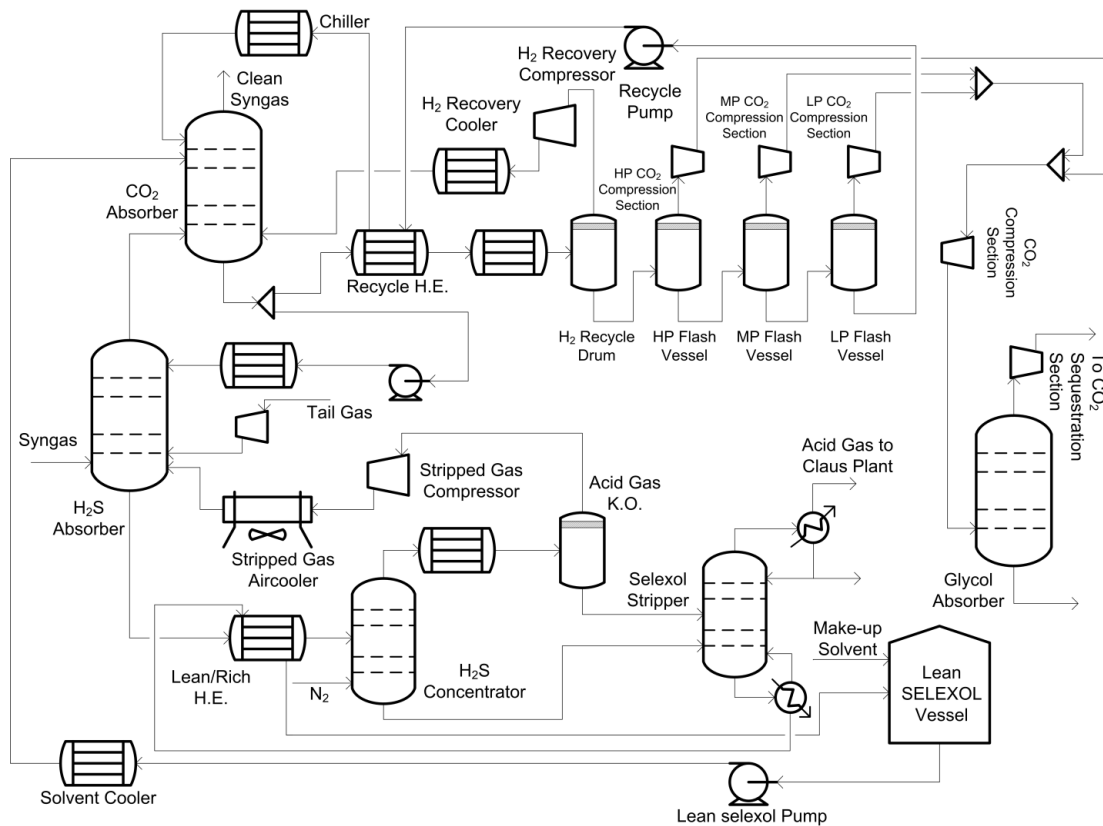


**Figure 2-16. Schematic of the SELEXOL unit**

### 2.2.2 Model Description

The design of the SELEXOL unit and development of the steady-state model in the Aspen Plus® and Aspen Plus Dynamics environment has been detailed by Bhattacharyya et al.<sup>3</sup> For the current fault simulation work, the SELEXOL model is first isolated and

solved for steady state. The control systems have been modified so as to ensure the process is stable in the range of operation of interest. Several structural modifications have been made, in order to simulate faults. The faults that can occur in SELEXOL are discussed in Chapter 4.

## 2.3 Gasification Island Process

### 2.3.1 Process Description

The gasification island model is considered for the implementation of two-tier sensor placement. The process consists of the sour WGS reactor combined with the SELEXOL unit. Typically, in the IGCC plant, the water gas shift process is performed by two reactors operating at different inlet temperatures. This allows for more residence time for the involving equilibrium reaction to reach the equilibrium, and to reduce the amount of COS in the reactor outlet. The outlet of the first reactor is fed to the second reactor, after which it is sent through a series of heat exchangers until finally being sent to the SELEXOL unit.

### 2.3.2 Model Description

In order to set-up the gasification island model, the sour WGS reactor model is enhanced to consider two trains consisting of two reactors in series with an intermediate cooler. The control system of the SELEXOL model was modified to ensure it was stable in the operating region of interest. Variables to be recorded were carefully selected so as to completely capture the fault progression through the simulation, while at the same time, reducing the memory load of the program to prevent the simulation to run slow.

The sour WGS reactor was modeled in MATLAB while the SELEXOL model was developed in Aspen Plus Dynamics (APD). The sour WGS reactor was not modeled using Aspen because, the in-house library reactor models in Aspen do not allow fault simulations, such as reduction in catalyst surface area, drop in catalyst porosity or catalyst activity. Plant level simulations on the other hand, are fairly easy to simulate using a process modeling software such as Aspen Plus or Aspen Dynamics. This brings forth the challenge of running two models in two different platforms, making them communicate and solve in a coupled manner.

Considering an overall target of 90% carbon capture in an IGCC plant, a 2-stage sour WGS reactor system with high- and low-temperature reactors arranged respectively in series with inter-stage coolers is required.<sup>3</sup> The single stage sour WGS reactor model developed previously can easily be extended to this configuration. A second sour WGS reactor model is developed similar to the first model that uses the outlet conditions of the first model as its inlet conditions. This reactor is sized in order to achieve equilibrium at about 90% of the length and the valve parameters are set so as to match the flowrates. Both stages are run independently until they reach steady-state. Once steady-state is reached in each of the stages, the code for the two stages is compiled into one m-file in MATLAB and the 2-stage sour WGS reactor system is solved as a single unit. Equations for an inter-stage heat exchanger (HE) are also added to the model. In order to make the current model compatible with the flowrates expected in an IGCC plant, an additional train of 2-stage sour WGS reactor system is assumed to run in parallel. A single train of the reactor system is shown in Figure 2-17.

In Figure 2-17, steam and syngas with known pressure and temperature are assumed to be well-mixed in the mixer and sent to the first stage reactor ( $R_1$ ). The product of the reactor  $R_1$  is then sent through a HE to reduce the stream temperature (e.g. reducing the temperature by 140 K) and the cooled stream is sent to the second stage reactor ( $R_2$ ). The system is pressure driven and the parameters of the valves  $V_1$ ,  $V_2$  and  $V_3$  determine the flow through the system. Standard PID type control equations are added to the model to ensure the process behaves as an industrial reactor system. It should be noted that in an industrial case, the valve  $V_3$  would not be located at the exit of the reactor system, or at the inlet of SELEXOL unit, but rather at the end of the AGR system. However, in order to close the system of equations and study the integrated model of 2-stage reactor system and SELEXOL unit, this valve is added to both models.

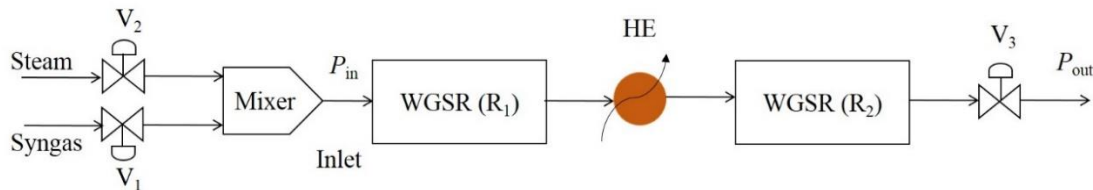


**Figure 2-17. Schematic representation of the Sour Water Gas Shift Reactor system developed in MATLAB.**

The inlet variables for the SELEXOL unit are initialized with the outlet variables of the sour WGS reactor system and the steady-state model is converged. This is done to make it easy to obtain initial convergence when the two models are integrated. The integration of the two models is done using SIMULINK. An Aspen Modeler Block is used to export the variables from the “workspace” in MATLAB and also to import the variables from APD.

The coupling of 2-stage sour WGS reactor and SELEXOL unit is done across the valve  $V_3$  in MATLAB and the first valve in the SELEXOL plant. The valve coefficients and the valve opening of the inlet valve to the SELEXOL unit are kept exactly the same as the valve  $V_3$  in MATLAB. The two valves are treated as though they are the same valve in an integrated flowsheet. Due to the coupled pressure-flow dynamics of the entire plant, the boundary conditions for the pressure at the output of the MATLAB model and the pressure at the input of the APD models are not static, but dynamic and are thus synchronized.

The MATLAB model is first solved for a fixed time-step using fixed inlet and outlet conditions. This time-step, along with the temperature, pressure and composition variables before the valve  $V_3$ , are sent to the APD model via SIMULINK. These variables are treated as input to the SELEXOL model. The APD model is then solved for the same time-step, and an updated value of the pressure variable after the inlet valve is sent back to MATLAB via SIMULINK. Finally, the exit pressure in the MATLAB simulation is updated. This process goes on for each time step until the end of the simulation. The schematic of the exchange of information across the platforms is shown in Figure 2-18. For the purpose of fault simulation, a fault is introduced to the system and the gasification island process is run for specified simulation time. The effect of faults on the process variables are captured by storing the values of variables on both MATLAB and APD models. The faults considered in the gasification island are listed in Chapter 7.

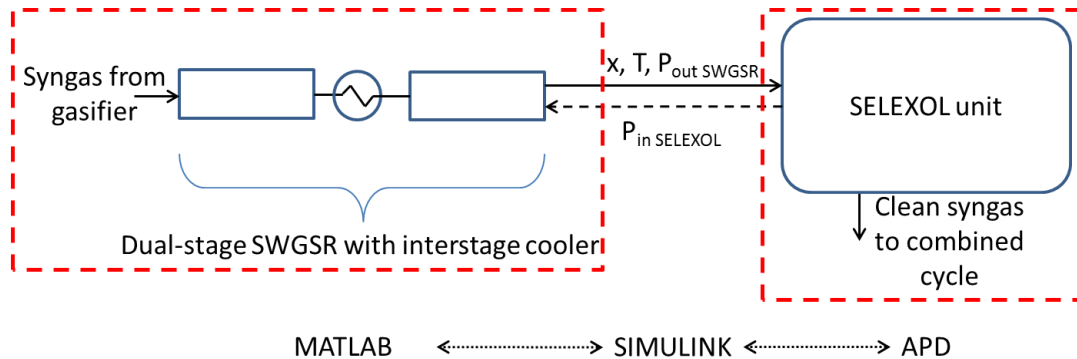


**Figure 2-18. Exchange of information between the sour WGS reactor model in MATLAB and the SELEXOL model in APD.**

## 2.4 Combined Cycle Unit

### 2.4.1 Process Description

A schematic of the combined cycle power plant is shown in Figure 2-19. Clean syngas exiting the SELEXOL unit is heated and mixed with N<sub>2</sub>, which is used as a diluent. After going through an expander, it is sent to the combustor of the GT. Hot exhaust gas from the GT is routed through the HRSG to generate 1,800 psig, 565°C super-heated HP steam, as well as reheat intermediate pressure (IP) steam to 565°C without supplemental firing. The HRSG also generates saturated HP steam (and possibly superheated steam as well) from gasification syngas cooling. The HP and IP superheated steam are routed to the ST to generate additional electric power. Finally, the flue gas leaves the system. The combined cycle model from the work of Bhattacharyya et al.<sup>3</sup> is used for this study and has been modified in order for us to be able to simulate the faults in the system.

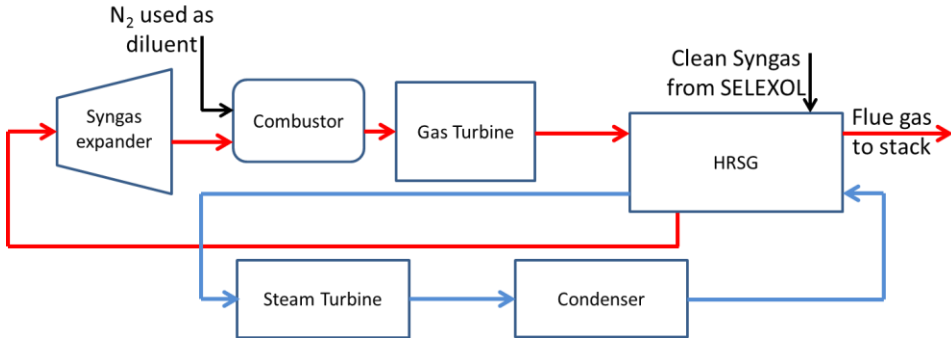


**Figure 2-19. Schematic of the combined cycle power plant**

#### 2.4.2 Model Description

The GT is simulated using turbine models available in the Aspen Plus library on the basis of the specifications of a GEE 7FB turbine. N<sub>2</sub> is used as a diluent and is adjusted by a design specification so that the lower heating value (LHV) of the syngas fuel is reduced to 4.55 MJ/ Nm<sup>3</sup> to keep the NOx concentrations in the ppmv (parts per million by volume) range in the exhaust. The combustion air is compressed in an axial flow compressor which raises the pressure to about 1.65 MPa. When the flow of combustion air is manipulated, the GT combustor temperature is maintained at 1377 °C with a specified heat loss equal to 1.5% of the lower heating value (LHV) of the syngas. The GT firing temperature is maintained at 1327 °C by adjusting the air flow rate to the combustor outlet gas before it reaches the first expansion stage for a design specification. The air flow rates to the second and third expansion stages are maintained at predetermined values. The isentropic efficiencies of the GT are adjusted such that the exhaust temperature is maintained at 566 °C. The isentropic efficiencies of all the three stages are assumed to be equal. The flue gas goes to the HRSG where steam is generated at three pressure levels. The flue gas is used to superheat the HP steam generated both in the HRSG evaporator and in the RSC before it finally exits the system at 132 °C, well above the cold end corrosion temperature.

The steam cycle generates steam from the flue gas and other process streams at three pressure levels. The minimum temperature approach is considered to be 10 °C in this study. HP steam, generated at 12.4 MPa and 538 °C, is mainly used for generating power

in the HP steam turbine (ST). IP steam is used in power generation, as well as in the reboilers. LP steam generated in the HRSG is mainly used for heating process streams and in the reboilers. Condensate at the outlet of the surface condenser and from the LP steam circuit and flash steam from the HP blow down drum are sent to the deaerator. The BFW at the outlet of the deaerator is pumped at various pressure levels for generating HP, IP, and LP steam. The HP stream is heated and sent to the RSC and HRSG. It is then superheated and sent to the HP turbine. IP BFW passes through the economizer and evaporator to generate IP steam which is sent to the IP turbine. The LP split of the BFW is used to generate LP and IP steam. The exit temperature of the flue gas above the cold end corrosion temperature is maintained by manipulating the flow of the BFW that goes to the LP steam evaporator. IP steam

## Chapter 3

### Scaling Analysis and Simplification of sour WGS Model

#### 3.1 Introduction

Scaling analysis is a systematic approach for identifying phenomena occurring at varying scales. This information can be used to simplify a given set of equation by discarding certain phenomena which occur at scales much lower than the scale of interest. In this approach, a given set of equations are made dimensionless, resulting in several dimensionless groups of varying magnitudes. The resulting dimensionless groups represent ratio of two phenomena described by the equations; and their magnitudes help in identifying the dominant phenomenon in the scale of interest. A number of authors have used scaling analysis for simplifying mathematical models and identifying the correlations for process performance using dimensionless groups. For example, Dahl et al.<sup>79</sup> have used scaling analysis to get insight into the behavior of fluid aerosol reactor without performing actual simulations. Kopaygorodsky et al.<sup>80</sup> used scaling analysis to identify key differences between the approximation of conventional pressure swing adsorption and ultra-rapid pressure swing adsorption. Kaisare et al.<sup>81</sup> used scaling analysis to identify phenomena occurring at varying scales in a reverse flow reactor. Balaji et al.<sup>82</sup> used scaling analysis for reverse flow reactor and have shown ways of simplifying the model equations. Rao et al.<sup>83</sup> studied pulsed pressure swing adsorber to identify useful correlations in terms of dimensionless numbers. Rezvanpour et al.<sup>84</sup> studied electro-hydrodynamic atomization process using scaling analysis to simplify the model and to find a correlation relating efficiency with a single dimensionless number involving the parameters of the process. Baldea and Daoutidis<sup>85</sup> studied autothermal reactors to identify a non-stiff model by separating fast and slow time scales. Krantz<sup>86</sup> described the method of scaling analysis in his book for various transport and reaction processes.

Unfortunately, there are two important gaps in all of the above works that use scaling analysis. In the scaling methodology described by Krantz<sup>86</sup>, all dependent and independent variables in the equations are made dimensionless by choosing appropriate

scale and reference factors. This results in a minimum parametric representation of the model equations. Hence, the solution of these equations can be expressed in terms of dimensionless groups. Typically, forming the dimensionless groups and obtaining the scales are done by trial-and-error. Moreover, in all of the works on scaling analysis, scaling of nonlinear terms in the equations are performed in an empirical manner. We address these gaps in the literature by: (i) proposing an approach that avoids the trial-and-error method for deriving scales, and (ii) we focus on nonlinear terms and suggest appropriate way to obtain scales for these terms. The proposed method of scaling analysis is general and straight-forward to apply to any given equations. This method relies on solving a nonlinear algebraic equation in the calculation of scales.

The proposed method is described in several steps and explained through examples of varying complexity. The techniques developed in this chapter are applied to sour water gas shift (WGS) reactor to calculate scales and reference values. Analysis of obtained scales and reference values through relevant dimensionless groups results in a simplified model of the sour WGS reactor. The performance of the simplified model using the obtained scales is studied by comparing the performance and computational load of the detailed and simplified models.

### **3.1.1 Model Simplification Using Current Scaling Analysis**

Systematic scaling analysis of model equations can help in identifying phenomena with varying importance thereby providing a rational approach for model simplification by eliminating terms with minimal impact on the solution of the model equations. Scaling analysis involves identifying appropriate scales and reference values to make the entire dependent and independent variables in a model to be dimensionless and vary in the order of 1, i.e. dimensionless variables will vary from zero to near one. This type of representation of a model is termed as “minimum parametric representation”. In this representation, it is easy to identify terms (which corresponds to some physical phenomena) of least importance and discard them to obtain simplified model.

In this section we first provide a general description of the scaling analysis and point out the deficiencies in the existing procedure at appropriate places. A systematic

method of scaling analysis is described below through several steps using a simple example.

**Step 1:** Consider the following system of equations

$$\frac{dy_1}{dx} = f_{11}(y_1, y_2, x) + f_{12}(y_1, y_2, x) \quad (3.1)$$

$$\frac{dy_2}{dx} = f_{21}(y_1, y_2, x) + f_{22}(y_1, y_2, x) \quad (3.2)$$

where  $f_{11}$ ,  $f_{12}$ ,  $f_{21}$ , and  $f_{22}$  represent any linear or nonlinear functions of dependent and independent variables. The initial conditions for the above equations are given by

$$y_1(x=0) = y_{10}; \quad y_2(x=0) = y_{20} \quad (3.3)$$

**Step 2:** Define appropriate scales and reference factors for the dependent and independent variables appearing in the equations and introduce them into the equations

$$y_1^* \equiv \frac{y_1 - y_{1,r}}{y_{1,s}}; \quad y_2^* \equiv \frac{y_2 - y_{2,r}}{y_{2,s}}; \quad x^* \equiv \frac{x}{x_s} \quad (3.4)$$

In the above definition, subscripts “ $s$ ” and “ $r$ ” represent scale and reference, respectively. Introducing the above definitions into Eqn. (3.1)-(3.3), we get

$$\frac{y_{1,s}}{x_s} \frac{dy_1^*}{dx^*} = f_{11}(y_1^* y_{1,s} + y_{1,r}, y_2^* y_{2,s} + y_{2,r}, x^* x_s) + f_{12}(y_1^* y_{1,s} + y_{1,r}, y_2^* y_{2,s} + y_{2,r}, x^* x_s) \quad (3.5)$$

$$\frac{y_{2,s}}{x_s} \frac{dy_2^*}{dx^*} = f_{21}(y_1^* y_{1,s} + y_{1,r}, y_2^* y_{2,s} + y_{2,r}, x^* x_s) + f_{22}(y_1^* y_{1,s} + y_{1,r}, y_2^* y_{2,s} + y_{2,r}, x^* x_s) \quad (3.6)$$

$$y_1^*(x^* x_s = 0) = \frac{y_{10} - y_{1,r}}{y_{1,s}}; \quad y_2^*(x^* x_s = 0) = \frac{y_{20} - y_{2,r}}{y_{2,s}} \quad (3.7)$$

For the terms on right hand side of Eqn. (3.5)-(3.6), once appropriate scaling definitions are introduced, we should be able to split them into a term involving only scales and reference values and another term involving only dimensionless variables. For example, after scaling the term  $f_{11}$ , it can be rewritten as a product of two terms  $f_{11,s} = f_{11}(y_{1,s}, y_{1,r}, y_{2,s}, y_{2,r}, x_s, x_r)$  and  $f_{11}^* = f_{11}(y_1^*, y_2^*, x^*)$ . This separation becomes

difficult for most of the nonlinear terms and handling of such nonlinear terms has not been addressed clearly in literature. For example, consider the nonlinear first order kinetic term

$$r_A = k_0 e^{-\frac{E_a}{RT}} C_A \quad (3.8)$$

The nonlinear term in Eqn. (3.8), after introducing the scaling definitions for the variables  $C_A$  and  $T$ , it becomes

$$r_A = k_0 e^{-\frac{E_a}{R(T^o T_s + T_r)}} (C_A^* C_{As} + C_{Ar}) \quad (3.9)$$

In Eqn. (3.9), it is difficult to separate the scale ( $r_{A,s}$ ) and dimensionless term ( $r_A^*$ ) corresponding to  $r_A$ . In the literature, it is suggested to use some characteristic maximum as the scale, however, obtaining such characteristic maximum is not obvious and clear.<sup>82,86</sup> Here, we will address the issue of defining scales for such nonlinear terms later in this chapter.

**Step 3:** Once scaling definitions are introduced into the corresponding equations, then the dimensionless equations can be formed by dividing each equation by a dimensional coefficient of any particular term in the equation. For each of Eqn. (3.5) and (3.6), we have three possibilities to form dimensionless equations. For example, for Eqn. (3.5):

$$\frac{dy_1^*}{dx^*} = \frac{x_s f_{11,s}}{y_{1,s}} f_{11}^* + \frac{x_s f_{12,s}}{y_{1,s}} f_{12}^* \quad (3.10)$$

$$\frac{y_{1,s}}{x_s f_{11,s}} \frac{dy_1^*}{dx^*} = f_{11}^* + \frac{f_{12,s}}{f_{11,s}} f_{12}^* \quad (3.11)$$

$$\frac{y_{1,s}}{x_s f_{12,s}} \frac{dy_1^*}{dx^*} = \frac{f_{11,s}}{f_{12,s}} f_{11}^* + f_{12}^* \quad (3.12)$$

In Eqns. (3.10)-(3.12), we have divided the equation by the dimensional coefficient of first, second and third terms, respectively. The dimensional coefficient has to be selected such that the resulting dimensionless equation is of order 1. This usually involves a trial and error method where each of these possibilities may need to be evaluated.

**Step 4:** Once a particular form of dimensionless equation is identified, then the next step is to calculate the scales and reference factors involved in these equations. This is again done by a trial and error method by assuming that a particular dimensionless group is dominant in the equation and making it equal to 1. For example, by considering Eqn. (3.10) and similar dimensionless equation for Eqn. (3.6), the scales can be found by considering the dimensionless groups in the first term in these equations to be dominant as:

$$\frac{x_s f_{11,s}}{y_{1,s}} = 1 \quad ; \quad \frac{x_s f_{21,s}}{y_{2,s}} = 1 \quad (3.13)$$

The scales  $y_{1,s}$  and  $y_{2,s}$  can be found by solving Eqn. (3.13) in the limit  $x_s$  approaches  $L$ . Once the scales are found, they can be substituted in the other dimensionless groups. If the resulting values of dimensionless groups are in the order of 1 or much less than 1, then the calculated scales are retained. If the values are much greater than 1, then either the chosen dominant dimensionless group or chosen form of dimensionless equation is incorrect and needs to be changed. As one can see, steps 3 and 4 involve trial-and-error method. In this chapter, we will develop a method which avoids this trial-and-error procedure and directly calculates the scales.

The reference factor for a variable is found from the dimensionless initial and boundary conditions of the corresponding equation by equating it to zero. Thus, from Eqn. (3.7), we can calculate  $y_{1,r}$  and  $y_{2,r}$  as

$$y_1^*(x^* x_s = 0) = \frac{y_{10} - y_{1,r}}{y_{1,s}} = 0 \quad \text{implies} \quad y_{1,r} = y_{10} \quad (3.14)$$

$$y_2^*(x^* x_s = 0) = \frac{y_{20} - y_{2,r}}{y_{2,s}} = 0 \quad \text{implies} \quad y_{2,r} = y_{20} \quad (3.15)$$

Once the scales are calculated from the correct form of dimensionless equation, simplification of corresponding equations can be undertaken by examining the values of dimensionless groups.

### 3.1.2 Improvements to the Method of Scaling Analysis

Here, we describe the development of a general and intuitive approach for scaling that can be applied to any given model equations. This approach avoids the trial-and-error method in the calculation of scales and is explained using the following steps:

1. Given a set of model equations with corresponding initial and boundary conditions, introduce definition of dimensionless variables involving scaling and reference values for all the dependent and independent variables, irrespective of whether any variable starts from zero or any fixed initial value. Also, introduce the definition of dimensionless term involving only the scale value for any term which is formed by the combination of dependent and independent variables.
2. Introduce the above definitions into the model equations. All the variables in the model are represented in terms of these definitions, i.e., variables are expressed in terms of defined scales, reference values and dimensionless variables.
3. Introduce the definitions in step 1 in the specified initial and boundary conditions.
4. Scaling strategy is to make the dimensionless variables to vary in the order of 1, i.e., when simulating the model equations using appropriate scale and reference values, the dimensionless variables in the equations should vary from 0 to near 1. Now the problem is to find those scaling and reference values for each of the variables involved.
5. In order to find scales and reference values, following assumptions are made
  - a) As the value of dimensionless variables need to be from zero to near one, we can safely assume the dimensionless variables in the model equations can take the value of 1.
  - b) The dimensionless variables in the boundary conditions corresponding to initial value of independent variables can be assumed to take the value of zero.
  - c) The dimensionless variables in the boundary conditions corresponding to final value of independent variables can be assumed to take the value of 1.
  - d) For certain cases where the dimensional variables take the value of zero at the final value of the independent variable, the corresponding dimensionless variable also can be assumed to take a value of zero

6. Based on the assumptions in the previous steps, the model equations will become algebraic equations containing scales and reference values. Using these algebraic equations along with the assumptions in the boundary conditions, calculate the scales and reference values.
7. Once the scales and reference values are found, then it is easy to form appropriate dimensionless groups involving these values and assess their relative importance in the equations.

Considering a system given by Eqn. (3.1)-(3.3), one needs to introduce dimensionless variables definition for dependent variables ( $y_1$  and  $y_2$ ), independent variable  $x$  and dimensionless term definition for nonlinear (or linear) functions ( $f_{11}, f_{12}, f_{21}$  and  $f_{22}$ ). This results in the following set of equations:

$$\frac{dy_1^*}{dx^*} = \frac{x_s f_{11,s}}{y_{1,s}} f_{11}^* + \frac{x_s f_{12,s}}{y_{1,s}} f_{12}^* \quad (3.16)$$

$$\frac{dy_2^*}{dx^*} = \frac{x_s f_{21,s}}{y_{2,s}} f_{21}^* + \frac{x_s f_{22,s}}{y_{2,s}} f_{22}^* \quad (3.17)$$

$$f_{11}^* f_{11,s} = f_{11}(y_1^* y_{1,s} + y_{1,r}, y_2^* y_{2,s} + y_{2,r}, x^* x_s + x_r) \quad (3.18)$$

$$f_{12}^* f_{12,s} = f_{12}(y_1^* y_{1,s} + y_{1,r}, y_2^* y_{2,s} + y_{2,r}, x^* x_s + x_r) \quad (3.19)$$

$$f_{21}^* f_{21,s} = f_{21}(y_1^* y_{1,s} + y_{1,r}, y_2^* y_{2,s} + y_{2,r}, x^* x_s + x_r) \quad (3.20)$$

$$f_{22}^* f_{22,s} = f_{22}(y_1^* y_{1,s} + y_{1,r}, y_2^* y_{2,s} + y_{2,r}, x^* x_s + x_r) \quad (3.21)$$

Also, introduce the dimensionless variables definition into the boundary conditions as

$$y_1^* y_{1,s} + y_{1,r} = y_{10}; \quad y_2^* y_{2,s} + y_{2,r} = y_{20} \quad (3.22)$$

$$x^* x_s + x_r = 0 \quad (3.23)$$

Eqn. (3.1) and (3.2) are simulated to a predefined final value of independent variable, which is given by  $x = L$ . Introducing dimensionless variable definitions to this equation becomes

$$x^* x_s + x_r = L \quad (3.24)$$

Now, assume the dimensionless variables and dimensionless terms in the Eqn. (3.16)-(3.21) take the value of 1. Similarly, assume the dimensionless variable in the Eqn. (3.23) and (3.24) take the value of zero; and the dimensionless variable in Eqn. (3.24) to take the value of 1. This results in the following algebraic equations for the calculation of scales and reference values

$$1 = \frac{x_s f_{11,s}}{y_{1,s}} + \frac{x_s f_{12,s}}{y_{1,s}} \quad (3.25)$$

$$1 = \frac{x_s f_{21,s}}{y_{2,s}} + \frac{x_s f_{22,s}}{y_{2,s}} \quad (3.26)$$

$$f_{11,s} = f_{11}(y_{1,s} + y_{1,r}, y_{2,s} + y_{2,r}, x_s + x_r) \quad (3.27)$$

$$f_{12,s} = f_{12}(y_{1,s} + y_{1,r}, y_{2,s} + y_{2,r}, x_s + x_r) \quad (3.28)$$

$$f_{21,s} = f_{21}(y_{1,s} + y_{1,r}, y_{2,s} + y_{2,r}, x_s + x_r) \quad (3.29)$$

$$f_{22,s} = f_{22}(y_{1,s} + y_{1,r}, y_{2,s} + y_{2,r}, x_s + x_r) \quad (3.30)$$

$$y_{1,r} = y_{10}; y_{2,r} = y_{20} \quad (3.31)$$

$$x_r = 0 \quad (3.32)$$

$$x_s + x_r = L \quad (3.33)$$

Once scales and reference values are calculated by solving these algebraic equations, it is straight-forward to form dimensionless groups, which can give information of phenomena occurring at various scales. This information can be subsequently used in possible simplification of these equations.

### 3.1.3 Illustrative Examples

In this section, we illustrate the proposed idea using various examples with different complexities.

### 3.1.3.1 Example 1. Steady Plug Flow Reactor

**Step 1:** The mathematical model of steady plug flow reactor is given by

$$\frac{dC_A}{dz} = -r_A; \quad \frac{dT}{dz} = B_1 r_A; \quad r_A = k_0 e^{-\frac{E_a}{RT}} C_A \quad (3.34)$$

The boundary conditions corresponding to the inlet are given by

$$C_A(z=0) = C_{A0}; T(z=0) = T_0 \quad (3.35)$$

The boundary condition corresponding to the outlet is given by  $z = L$ . The scaling and reference values are defined for the variables and the term involved in the equations

$$z^* = \frac{z - z_r}{z_s}; \quad C_A^* = \frac{C_A - C_{Ar}}{C_{As}}; \quad T^* = \frac{T - T_r}{T_s}; \quad r_A^* = \frac{r_A}{r_{As}} \quad (3.36)$$

**Step 2:** Introducing the definitions into the model equations

$$\frac{C_{As}}{z_s} \left( \frac{dC_A}{dz} \right)^* = -r_{As} r_A^* \quad (3.37)$$

$$\frac{T_s}{z_s} \left( \frac{dT}{dz} \right)^* = B_1 r_{As} r_A^* \quad (3.38)$$

$$r_{As} r_A^* = k_0 e^{-\frac{E_a}{R(T^* T_s + T_r)}} (C_A^* C_{As} + C_{Ar}) \quad (3.39)$$

**Step 3:** Introducing the definitions into the boundary conditions

$$C_A^* C_{As} (z^* z_s + z_r = 0) + C_{Ar} = C_{A0} \quad \text{at inlet} \quad (3.40)$$

$$T^* T_s (z^* z_s + z_r = 0) + T_r = T_0 \quad \text{at inlet} \quad (3.41)$$

$$z^* z_s + z_r = L \quad \text{at outlet} \quad (3.42)$$

**Step 4, 5 & 6:** Assuming dimensionless variables taking the value of 1 in the model equations, we have following algebraic equations

$$\frac{C_{As}}{z_s} = -r_{As}; \quad \frac{T_s}{z_s} = B_1 r_{As}; \quad r_{As} = k_0 e^{-\frac{E_a}{R(T_s + T_r)}} (C_{As} + C_{Ar}) \quad (3.43)$$

From the inlet conditions (assuming  $C_A^* = T^* = z^* = 0$ ) we have

$$C_{Ar} = C_{A0}; \quad T_r = T_0; \quad z_r = 0 \quad (3.44)$$

From the outlet condition (assuming  $z^* = 1$ ) we have  $z_r = L$ . The solution of the above algebraic equations will provide appropriate scales and reference values which will make the corresponding dimensionless variable to vary in the order of 1.

### 3.1.3.2 Example 2. Unsteady Plug Flow Reactor

The unsteady model of the plug flow reactor is represented by partial differential equations (PDE), which can be converted into ordinary differential equations (ODE) using method of lines procedure; and the scales can be found as in the previous example. In this case, we will have several scales and reference values for a variable, which is equal to the number of discretization points used in the method of lines procedure. Alternatively, we can restrict the number of scales and reference values to one for each variable, and calculate the corresponding values. In this example, we consider single scale and reference values for each variable.

**Step 1:** The mathematical model of unsteady plug flow reactor is given by

$$\frac{\partial C_A}{\partial t} = -v_1 \frac{\partial C_A}{\partial z} - r_A \quad (3.45)$$

$$\frac{\partial T}{\partial t} = -v_2 \frac{\partial T}{\partial z} + B_2 r_A \quad (3.46)$$

$$r_A = k_0 e^{-\frac{E_a}{RT}} C_A \quad (3.47)$$

Boundary conditions corresponding to initial value of independent variables, i.e. inlet conditions and initial conditions are given by

$$C_A(z = 0) = C_{A0}; \quad T(z = 0) = T_0; \quad C_A(t = 0) = f_1; \quad T(t = 0) = f_2 \quad (3.48)$$

Boundary conditions corresponding to final value of independent variables are given by

$$z = L; \quad t = t_{end} \quad (3.49)$$

The scaling and reference values are defined for the variables and term involved in the equation by

$$z^* = \frac{z - z_r}{z_s}; \quad t^* = \frac{t - t_r}{t_s}; \quad C_A^* = \frac{C_A - C_{Ar}}{C_{As}}; \quad T^* = \frac{T - T_r}{T_s}; \quad r_A^* = \frac{r_A}{r_{As}} \quad (3.50)$$

**Step 2:** Introducing the definitions into the model equations

$$\frac{C_{AS}}{t_s} \left( \frac{\partial C_A}{\partial t} \right)^* = -\nu_1 \frac{C_{AS}}{L} \left( \frac{\partial C_A}{\partial z} \right)^* - r_{AS} r_A^* \quad (3.51)$$

$$\frac{T_s}{t_s} \left( \frac{\partial T}{\partial t} \right)^* = -\nu_2 \frac{T_s}{L} \left( \frac{\partial T}{\partial z} \right)^* + B_2 r_{AS} r_A^* \quad (3.52)$$

$$r_{AS} r_A^* = k_0 e^{-\frac{E_a}{R(T^*T_s+T_r)}} (C_A^* C_{AS} + C_{Ar}) \quad (3.53)$$

**Step 3:** Introducing the definitions into the boundary conditions

$$C_A^* C_{AS} (z^* z_s + z_r = 0) + C_{Ar} = C_{A0}; \quad T^* T_s (z^* z_s + z_r = 0) + T_r = T_0 \quad (3.54)$$

$$C_A^* C_{AS} (t^* t_s + t_r = 0) + C_{Ar} = f_1; \quad T^* T_s (t^* t_s + t_r = 0) + T_r = f_2 \quad (3.55)$$

$$z^* z_s + z_r = L; \quad t^* t_s + t_r = t_{end} \quad (3.56)$$

**Step 4, 5 & 6:** Assuming dimensionless variables taking the value of 1 in the model equations, we will have following algebraic equations

$$\frac{C_{AS}}{t_s} = -\nu_1 \frac{C_{AS}}{z_s} - r_{AS} \quad (3.57)$$

$$\frac{T_s}{t_s} = -\nu_2 \frac{T_s}{z_s} + B_2 r_{AS} \quad (3.58)$$

$$r_{AS} = k_0 e^{-\frac{E_a}{R(T_s+T_r)}} (C_{AS} + C_{Ar}) \quad (3.59)$$

From the initial and boundary conditions assuming  $C_A^* = T^* = z^* = t^* = 0$  we have

$$C_{Ar} = C_{A0}; \quad T_r = T_0; \quad z_r = 0; \quad t_r = 0 \quad (3.60)$$

We can either take the above values as the reference variables for  $C_{Ar}$  and  $T_r$ , or, take some average single value from the initial conditions as given below

$$C_{Ar} = F_1; \quad T_r = F_2 \quad (3.61)$$

$F_1$  and  $F_2$  represent the average scalar values obtained from the initial distribution of the dependent variables over the domain  $(0, L)$ . From the other boundary condition, by assuming  $z^* = t^* = 1$ , we have

$$z_s = L; \quad t_s = t_{end} \quad (3.62)$$

### 3.1.3.3 Example 3. Boundary Value Problem with Neumann Boundary Condition

In the previous examples, reference variables are found by solving boundary condition while the scales for dependent variables are found by solving algebraic equations. In this example, we consider Neumann boundary condition and solve algebraic equations to find the reference variables. The equation and the corresponding boundary conditions are given as

$$\frac{d^2T}{dx^2} = f(T); \quad \frac{dT}{dx}(x = 0) = y_1; \quad \frac{dT}{dx}(x = L) = y_2 \quad (3.63)$$

Above model and boundary conditions can be rewritten as following two point boundary value problem

$$\frac{dT}{dx} = a; \quad \frac{da}{dx} = f(T); \quad a(x = 0) = y_1; \quad a(x = L) = y_2 \quad (3.64)$$

Introducing the scaling and reference values definition corresponding to  $T$  and  $a$ , the equations become

$$\frac{T_s}{L} \left( \frac{dT}{dx} \right)^* = a^* a_s + a_r; \quad \frac{a_s}{L} \left( \frac{da}{dx} \right)^* = f(T^* T_s + T_r) \quad (3.65)$$

Boundary conditions become

$$a^* a_s (x^* x_s + x_r = 0) + a_r = y_1; \quad a^* a_s (x^* x_s + x_r = L) + a_r = y_2 \quad (3.66)$$

Algebraic equations can be formed as before using the assumption of dimensionless variable taking the value of 1 or 0

$$\frac{T_s}{L} = a_s + a_r; \quad \frac{a_s}{L} = f(T_s + T_r) \quad (3.67)$$

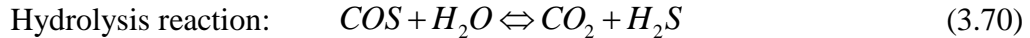
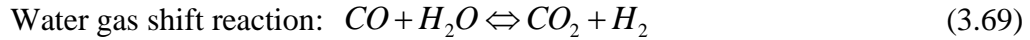
From the boundary conditions

$$a_r = y_1; \quad a_s + a_r = y_2; \quad x_r = 0; \quad x_s = L; \quad (3.68)$$

Solution to the above equations results in the scale and reference values for the variables  $T$  and  $a$ .

### 3.1.3.4 Example 4. Sour Water Gas Shift Reactor

Now, we consider our system of interest, the unsteady model of the sour water gas shift (WGS) reactor which involves differential and algebraic equations (DAE) with 9 dependent variables, Neumann type boundary condition and two equilibrium reactions with nonlinear kinetics. The scaling procedure is applied to this model as before and the algebraic equations for the calculation of scales and reference values are found. This example will be extended later to study the possible model simplification that can be attained from the assessment of resulting dimensionless groups. The unsteady model of sour WGS reactor and corresponding reaction kinetic equations are described in Chapter 2. In this model, the pressure drop equation is assumed to be quasi-steady. This model contains hyperbolic type PDE for species balance and parabolic type PDE for energy balance. As explained in Chapter 2, the following two reactions take place in the sour WGS reactor with the following equations describing the system:



Species balance:

$$\frac{\partial C_i}{\partial t} = -\frac{GRT_g}{P} \frac{\partial C_i}{\partial z} - C_i \frac{GRT_g}{P} \left( \frac{1}{T_g} \frac{dT_g}{dz} - \frac{1}{P} \frac{dP}{dz} \right) + (r_{wgs} \gamma_{wgs,i} + r_{hyd} \gamma_{hyd,i}) \frac{1-\varepsilon}{\varepsilon} \quad (3.71)$$

where  $i = 1$  to 6 represent, CO, H<sub>2</sub>O, CO<sub>2</sub>, H<sub>2</sub>, COS and H<sub>2</sub>S, respectively

Pressure drop equation:

$$\frac{dP}{dz} = -\frac{\rho_g}{d_{cat}} \left( \frac{GRT_g \varepsilon}{P} \right)^2 \left( \frac{1-\varepsilon}{\varepsilon^3} \right) \left( 1.75 + \frac{150 \mu P (1-\varepsilon)}{d_{cat} \varepsilon GRT_g \rho_g} \right) \quad (3.72)$$

Gas phase energy balance:

$$\frac{\partial T_g}{\partial t} = \frac{1}{\rho_g C_p} \left[ -C_p G \frac{\partial T_g}{\partial z} + \frac{h_f a_c}{\varepsilon} (T_{cat} - T_g) \right] \quad (3.73)$$

Catalyst phase energy balance:

$$\frac{\partial T_{cat}}{\partial t} = \frac{1}{\rho_{cat} C p_{cat}} \left[ K_{cat} \frac{\partial^2 T_{cat}}{\partial z^2} - \frac{h_f a_c}{1-\varepsilon} (T_{cat} - T_g) + r_{wgs} \Delta H_{R,wgs} + r_{hyd} \Delta H_{R,hyd} \right] \quad (3.74)$$

Reaction kinetic equations:

For water gas shift reaction we have

$$r_{wgs} = -\Omega k_{wgs} \left( \frac{P}{101325} \right)^{0.5 - \frac{P}{50662500}} \frac{RT_{cat}}{P} \left( C_{CO} - \frac{C_{CO_2} C_{H_2}}{K_{eq,wgs} C_{H_2O}} \right) \quad (3.75)$$

$$k_{wgs} = k_{01} e^{\frac{-E_{a1}}{RT_{cat}}} ; \quad K_{eq,wgs} = e^{\left( \frac{45778}{T_{cat}} - 4.33 \right)} \quad (3.76)$$

and for hydrolysis reaction we have

$$r_{hyd} = -k_{hyd} \left( \frac{10^{-3} (RT_{cat} C_{CO})}{1 + 10^{-3} (K_{eq,hyd} RT_{cat} C_{H_2O})} \right) \quad (3.77)$$

$$k_{hyd} = k_{02} e^{\frac{-E_{a2}}{RT_{cat}}} ; \quad K_{eq,hyd} = e^{\left( \frac{10010}{T_{cat}} - 15.89 \right)} \quad (3.78)$$

Initial and boundary conditions:

$$z = 0 ; \quad C_i = C_{i,in} ; \quad T_g = T_{g,in} ; \quad T_{cat} = T_{g,in} ; \quad P = P_{in} \quad (3.79)$$

$$z = L ; \quad \frac{dT_{cat}}{dz} = 0 \quad (3.80)$$

Eqn. (3.74), representing the catalyst phase energy balance, can be rewritten as following two equations

$$\frac{dT_{cat}}{dz} = T_{cat,z} \quad (3.81)$$

$$\frac{\partial T_{cat}}{\partial t} = \frac{1}{\rho_{cat} C p_{cat}} \left[ K_{cat} \frac{\partial T_{cat,z}}{\partial z} - \frac{h_f a_c}{1-\varepsilon} (T_{cat} - T_g) + r_{wgs} \Delta H_{R,wgs} + r_{hyd} \Delta H_{R,hyd} \right] \quad (3.82)$$

where the boundary condition corresponding to the new variable  $T_{cat,z}$  is given as

$$z = L ; \quad T_{cat,z} = 0 \quad (3.83)$$

Unsteady simulation of sour WGS reactor starts from initial time of  $t = 0$  with the given initial conditions for a given input disturbance and is simulated until a predefined time  $t_{end}$ , or, until the system reaches new steady-state corresponding to the input disturbance. From the initial and final time of simulation, scale and reference values for the time variable can be calculated. Similarly, for the other independent variable,  $z$ , scale and reference values can be calculated by its value at the inlet and outlet of the reactor.

In the above model, there are various terms involving combination of dependent variables. Therefore, we need to introduce scaling definitions for such terms in addition to the dependent and independent variables involved in the model equation. These terms include

$$N_1 = \frac{GRT_g}{P}; \quad N_2 = \frac{C_i GR}{P}; \quad N_3 = \frac{C_i GRT_g}{P^2}; \quad N_4 = (T_{cat} - T_g) \quad (3.84)$$

In addition to the above terms, we have to consider the reaction kinetic terms. Hence, we define the scaling and reference values for the dependent and independent variables and for the terms involving these variables as

$$\begin{aligned} z^* &\equiv \frac{z - z_r}{z_s}; \quad t^* \equiv \frac{t - t_r}{t_s} \\ C_i^* &\equiv \frac{C_i - C_{i,r}}{C_{i,s}}; \quad T_g^* \equiv \frac{T_g - T_{g,r}}{T_{g,s}}; \quad T_{cat}^* \equiv \frac{T_{cat} - T_{cat,r}}{T_{cat,s}} \\ P^* &\equiv \frac{P - P_r}{P_s}; \quad T_{cat,z}^* \equiv \frac{T_{cat,z} - T_{cat,z,r}}{T_{cat,z,s}} \\ r_{wgs}^* &\equiv \frac{r_{wgs}}{r_{wgs,s}}; \quad r_{hyd}^* \equiv \frac{r_{hyd}}{r_{hyd,s}}; \quad N_1 \equiv \frac{N_1}{N_{1,s}} \\ N_2 &\equiv \frac{N_2}{N_{2,s}}; \quad N_3 \equiv \frac{N_3}{N_{3,s}}; \quad N_4 \equiv \frac{N_4}{N_{4,s}} \end{aligned} \quad (3.85)$$

Introducing the scaling definitions and assuming appropriate dimensionless variable to take the value of 1 or 0, following algebraic equations are formed:

Algebraic equation for species concentration scale:

$$\frac{C_{i,s}}{t_s} = -N_{1,s} \frac{C_{i,s}}{z_s} - N_{2,s} \frac{T_{g,s}}{z_s} + N_{3,s} \frac{P_s}{z_s} + (r_{wgs,s} \gamma_{wgs,i} + r_{hyd,s} \gamma_{hyd,i}) \frac{1-\varepsilon}{\varepsilon} \quad (3.86)$$

Algebraic equation for pressure scale:

$$\frac{P_s}{z_s} = -\frac{1.75\rho_g(1-\varepsilon)N_{1,s}^2}{d_{cat}\varepsilon} - \frac{(1-\varepsilon)^2}{\varepsilon^2} \frac{150\mu N_{1,s}}{d_{cat}^2} \quad (3.87)$$

Algebraic equation for gas phase temperature scale:

$$\frac{T_{g,s}}{t_s} = -\frac{G}{\rho_g} \frac{T_{g,s}}{z_s} + \frac{h_f a_c}{\varepsilon \rho_g C_p} N_{4,s} \quad (3.88)$$

Algebraic equation for catalyst phase temperature scale:

$$\frac{T_{cat,s}}{t_s} = \frac{K_{cat}}{\rho_{cat} C_p} \frac{T_{cat,z,s}}{z_s} - \frac{h_f a_c}{\rho_{cat} C_p (1-\varepsilon)} N_{4,s} + \frac{\Delta H_{R,wgs}}{\rho_{cat} C_p} r_{wgs,s} + \frac{\Delta H_{R,hyd}}{\rho_{cat} C_p} r_{hyd,s} \quad (3.89)$$

Algebraic equation for catalyst phase temperature gradient scale:

$$\frac{T_{cat,s}}{z_s} = (T_{cat,z,s} + T_{cat,z,r}) \quad (3.90)$$

Introducing scaling definitions to the reaction kinetic terms and to terms involving combination of dependent variables, following additional algebraic equations are formed:

$$r_{wgs,s} = -\Omega k_{wgs,s} \left( \frac{P_s + P_r}{101325} \right)^{0.5 - \frac{P_s + P_r}{50662500}} \frac{R(T_{cat,s} + T_{cat,r})}{P_s + P_r} \left( (C_{CO,s} + C_{CO,r}) - \frac{(C_{CO_2,s} + C_{CO_2,r})(C_{H_2,s} + C_{H_2,r})}{K_{eq,wgs,s}(C_{H_2O,s} + C_{H_2O,r})} \right) \quad (3.91)$$

$$k_{wgs,s} = k_{01} e^{\frac{-E_a}{R(T_{cat,s} + T_{cat,r})}} \quad (3.92)$$

$$K_{eq,wgs,s} = e^{\left( \frac{45778}{T_{cat,s} + T_{cat,r}} - 4.33 \right)} \quad (3.93)$$

$$r_{hyd,s} = -k_{hyd,s} \left( \frac{10^{-3} R(T_{cat,s} + T_{cat,r})(C_{CO,s} + C_{CO,r})}{1 + 10^{-3} K_{eq,hyd,s} R(T_{cat,s} + T_{cat,r})(C_{H_2O,s} + C_{H_2O,r})} \right) \quad (3.94)$$

$$k_{hyd,s} = k_{02} e^{\frac{-E_a}{R(T_{cat,s} + T_{cat,r})}} \quad (3.95)$$

$$K_{eq,hyd,s} = e^{\left(\frac{10010}{T_{cat,s} + T_{cat,r}} - 15.89\right)} \quad (3.96)$$

$$N_{1,s} = \frac{GR(T_{g,s} + T_{g,r})}{(P_s + P_r)}; \quad N_{2,s} = \frac{(C_{i,s} + C_{i,r})GR}{(P_s + P_r)} \quad (3.97)$$

$$N_{3,s} = \frac{(C_{i,s} + C_{i,r})GR(T_{g,s} + T_{g,r})}{(P_s + P_r)^2}; \quad N_{4,s} = (T_{cat,s} + T_{cat,r} - T_{g,s} - T_{g,r}) \quad (3.98)$$

From the boundary conditions, we have

$$C_{i,r} = C_{i,in}; \quad T_{g,r} = T_{g,in}; \quad T_{cat,r} = T_{cat,in}; \quad P_r = P_{in}; \quad z_r = 0; \quad t_r = 0 \quad (3.99)$$

$$z_s = L; \quad t_s = t_{end} \quad (3.100)$$

As the catalyst phase temperature gradient variable takes the value of zero at outlet, we can assume the corresponding dimensionless variable takes the value of zero at the outlet. This results in a reference value for the catalyst temperature gradient to be zero,  $T_{cat,z,r} = 0$ .

### 3.1.4 Numerical Results for Sour WGS Example

#### 3.1.4.1 Scales Calculation and Model Simulation

In this section, the scales and reference values are calculated using the parameters and boundary conditions for the sour WGS reactor model. The parameters and the boundary condition values for sour WGS reactor model are given in Table 3.1. These parameters are introduced into the above algebraic equations to calculate the appropriate scales for the variables. Afterwards, the unsteady behavior of sour WGS reactor model is simulated by introducing a step change in the inlet variables of steady-state sour WGS reactor. Values of the inlet conditions before the step change (steady-state inlet values) and after the step change (values obtained by simulating unsteady model) are also given in Table 3.1. The dynamic simulation is carried out from an initial time value of 0 for a duration of 2800 seconds. Then, using the dynamic values for the variables and the

corresponding scales and reference values, the values of dimensionless variables are calculated using the corresponding scaling definitions.

**Table 3.1. Parameters and inlet conditions for the sour WGS reactor**

Parameter	Value
Reactor length ( $L$ )	29 m
Catalyst porosity ( $\varepsilon$ )	0.38
Heat transfer coefficient ( $h_f$ )	100 W/m <sup>2</sup> -K
Heat of WGS reaction ( $\Delta H_{wgs}$ )	$3.85 \times 10^4$ J/mol
Heat of hydrolysis reaction ( $\Delta H_{hyd}$ )	$3.1 \times 10^4$ J/mol
Average density of gas ( $\rho_g$ )	20.5 mol/m <sup>3</sup>
Viscosity of gas mixture ( $\mu_g$ )	$2.5 \times 10^{-5}$ N-s/m <sup>2</sup>
Specific heat of gas ( $Cp_g$ )	35 J/mol-K
Density of catalyst ( $\rho_{cat}$ )	650 kg/m <sup>3</sup>
Specific heat of catalyst ( $Cp_{cat}$ )	880 J/kg-K
Specific area per unit volume of catalyst ( $a_c$ )	$1.69 \times 10^3$ m <sup>2</sup> /m <sup>3</sup>
Thermal conductivity of catalyst ( $K$ )	35 W/m-K
Diameter of catalyst ( $d_{cat}$ )	$3.5 \times 10^{-3}$
<b>Inlet condition</b>	
	Values at steady initial state      Values during dynamic simulation and final steady state
$C_{CO,in}$ (mol/m <sup>3</sup> )	246.34      238.64
$C_{H_2O,in}$ (mol/m <sup>3</sup> )	488.97      473.69
$C_{CO_2,in}$ (mol/m <sup>3</sup> )	95.02      92.05
$C_{H_2,in}$ (mol/m <sup>3</sup> )	234.65      227.32
$C_{COS,in}$ (mol/m <sup>3</sup> )	0.0963      0.0933
$C_{H_2S,in}$ (mol/m <sup>3</sup> )	4.98      4.82
$T_{in}$ (K)	620      640
$P_{in}$ (Pa)	$5.52 \times 10^6$ $5.52 \times 10^6$

The calculated scale values for the variables involved in the sour WGS reactor model equations are shown in Table 3.2. The scales for the variables, decreasing along the length of the reactor (including reactants concentration, pressure and etc.) take negative values; therefore, corresponding dimensionless variables vary from 0 to near positive 1. The inlet values corresponding to the dynamic simulation form the reference values for the corresponding variables. The simulation results are plotted in Figure 3-1 to 3-4. In Figure 3-1 and 3-2, steady-state results for a step change in input, is plotted for the actual and corresponding dimensionless variables. In Figure 3-3 and 3-4, dynamic simulation results are plotted using the values of the variables at the exit of the reactor for the actual and corresponding dimensionless variables.

**Table 3.2. Scale values for the variables in sour WGS reactor**

Scales	Values	Scales	Values
$C_{CO,s}$	-87.487	$N_{2,CO,s}$	0.149
$C_{H_2O,s}$	-119.558	$N_{2,H_2O,s}$	0.350
$C_{CO_2,s}$	42.556	$N_{2,CO_2,s}$	0.133
$C_{H_2,s}$	24.066	$N_{2,H_2,s}$	0.249
$C_{COS,s}$	-0.0913	$N_{2,COS,s}$	$1.9744 \times 10^{-6}$
$C_{H_2S,s}$	-0.578	$N_{2,H_2S,s}$	0.0042
$T_{g,s}$	55.358	$N_{3,CO,s}$	$2.035 \times 10^{-5}$
$T_{cat,s}$	55.449	$N_{3,H_2O,s}$	$4.769 \times 10^{-5}$
$P_s$	$-4.1 \times 10^5$	$N_{3,CO_2,s}$	$1.813 \times 10^{-5}$
$z_s$	29	$N_{3,H_2,s}$	$3.385 \times 10^{-5}$
$t_s$	2800	$N_{3,COS,s}$	$2.689 \times 10^{-10}$
$r_{wg,s,s}$	-0.939	$N_{3,H_2S,s}$	$5.713 \times 10^{-7}$
$r_{hyd,s}$	-0.0013	$N_{1,s}$	0.688
		$N_{4,s}$	0.0912

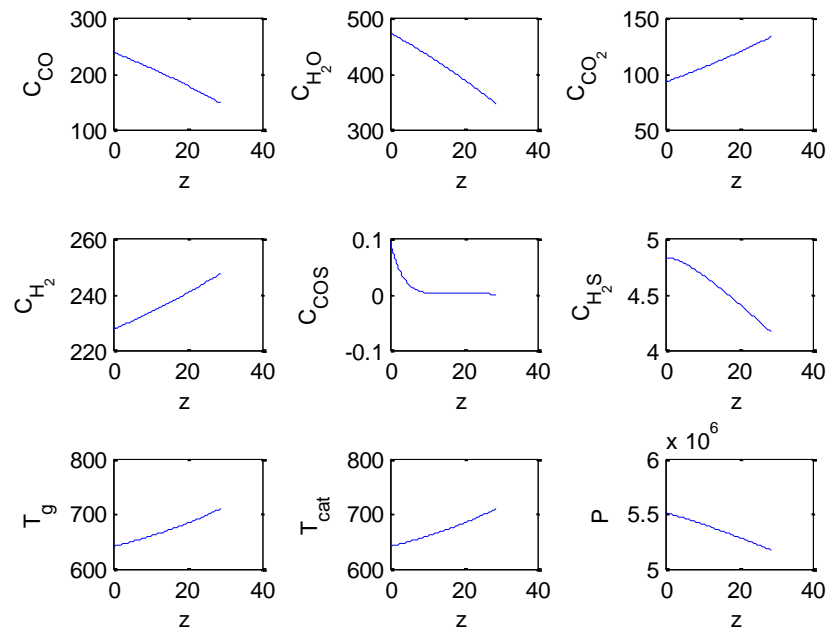


**Figure 3-1. Steady state simulation result for all the 9 dependent variables**

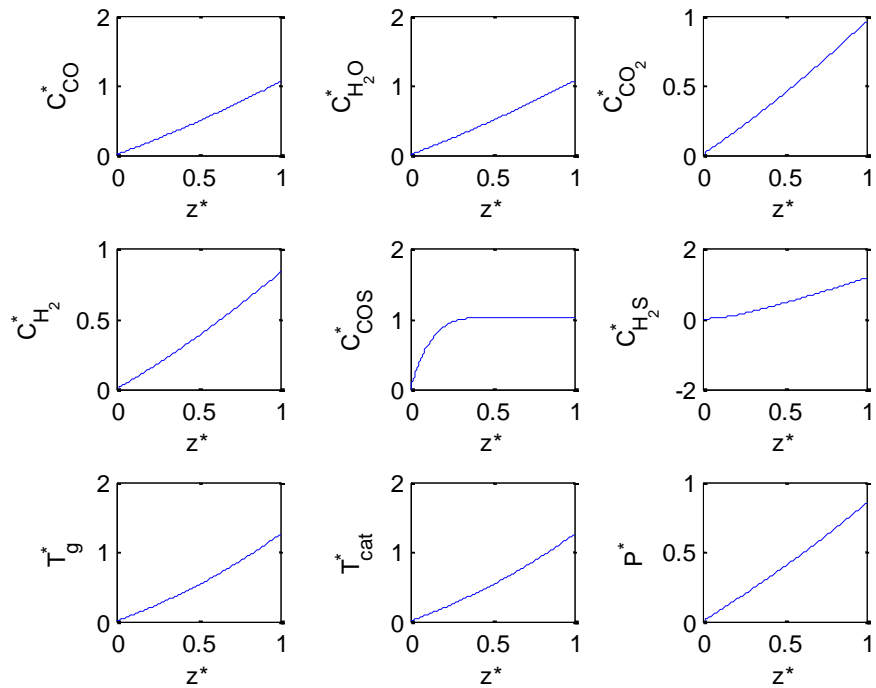


**Figure 3-2. Steady state simulation result for all the dimensionless variables**

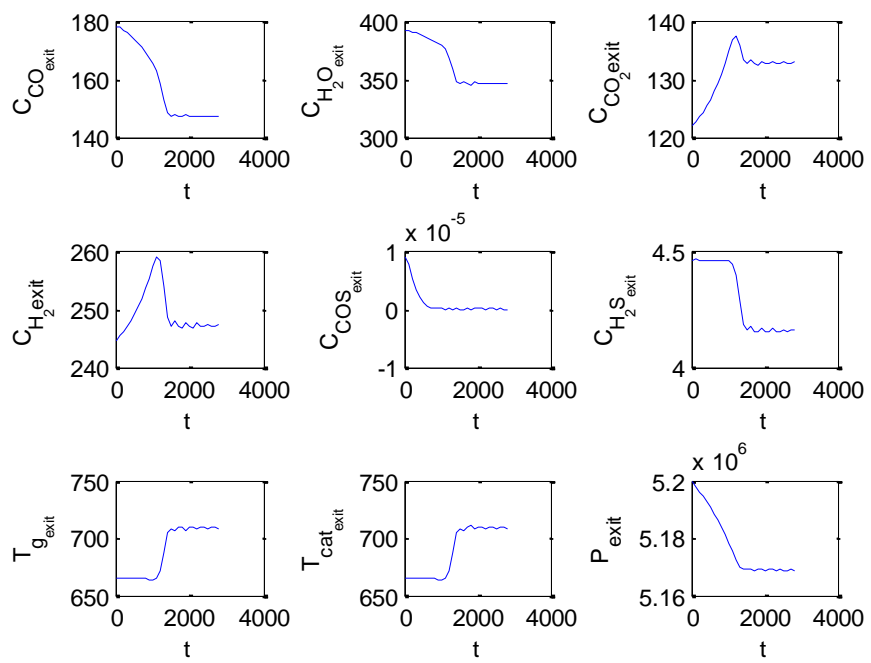


**Figure 3-3. Unsteady state simulation result for all the variables at the exit of the reactor**

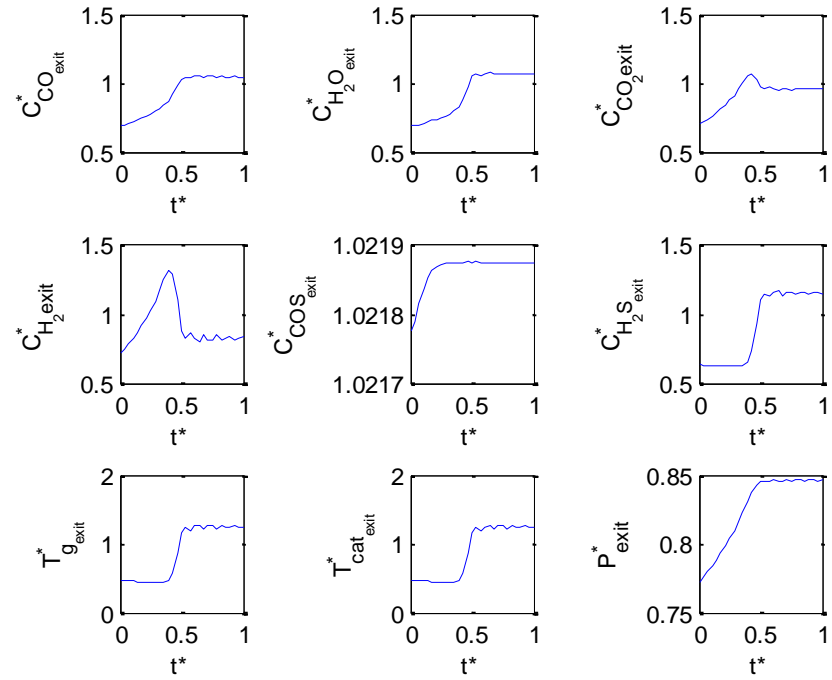


**Figure 3-4. Unsteady state simulation result for all the dimensionless variables at the exit of the reactor**

From the above results, we can see that the dimensional variables take values based on the given parameters and boundary conditions; and the corresponding dimensionless variables take the values between near 0 to near 1. Also, we can see that for the variables decreasing with respect to either the length or time, corresponding dimensionless variables increase from near zero 0 to near 1. For steady-state values, the dimensionless variables vary from exact zero to near 1, whereas for the unsteady values, dimensionless variables vary from near zero to near 1. This is because for steady-state case, inlet values are taken to be the reference values and this makes the steady-state dimensionless variables to take the value of exact zero at the inlet. In contrast, for dynamic case, we have two choices for the calculation of reference and scale values, one is to use the inlet and initial conditions and the other is to use only inlet condition. In the former case, there are many scales and reference values for each variable corresponding to the number of discretization points. In the latter case, we have single scale and reference values. As we have used only the inlet values as reference values, dimensionless variables at discretization points will not take the exact value of zero at the initial time. Nevertheless, we can see that the values of dimensionless variables are in the order of 1 and hence the calculated scale and reference values form a representative of the dynamic variations of sour WGS reactor model. Therefore, any simplifications of model equations using these values will be reasonable and will closely represent the behavior of corresponding detailed model.

### 3.1.4.2 Model Simplification based on the Dimensionless Groups

Here, we analyze the model equations using the calculated scales and reference values and simplify the sour WGS reactor model equations by discarding certain less important terms based on the values of dimensionless groups, which are formed from the values of parameters, scales and reference values of the variables. As mentioned earlier, a dimensionless group represents ratio of two phenomena described by the model equation with the value of the group indicating the dominant phenomenon. In the unsteady species balance for the sour WGS reactor model, following phenomena are considered:

- Rate of accumulation of species per unit volume, represented by the term  $\frac{C_{i,s}}{t_s}$

- Rate of convection of species per unit volume due to concentration variation, represented by the term  $N_{1,s} \frac{C_{i,s}}{z_s}$
- Rate of convection of species per unit volume due to temperature variation, represented by the term  $N_{2,s} \frac{T_{g,s}}{z_s}$
- Rate of convection of species per unit volume due to pressure variation, represented by the term  $N_{3,s} \frac{P_s}{z_s}$
- Rate of production/depletion of species per unit volume due to water gas shift reaction, represented by the term  $r_{wgs,s} \gamma_i \left( \frac{1-\varepsilon}{\varepsilon} \right)$
- Rate of production/depletion of species per unit volume due to hydrolysis reaction, represented by the term  $r_{hyd,s} \gamma_i \left( \frac{1-\varepsilon}{\varepsilon} \right)$

Dimensionless groups can be formed by considering any two phenomena. Table 3.3 shows the absolute values of dimensionless groups for the species balance equations. The value of the phenomenon corresponding to convection of species due to concentration gradient is higher compared to the other phenomena. Hence, this convection phenomenon is chosen to form dimensionless groups.

**Table 3.3. Values of dimensionless groups for species balance equation of WGS reactor model**

Species	Group-1	Group-2	Group-3	Group-4	Group-5	Group-6
	$\frac{z_s}{N_{1,s}t_s}$		$\frac{N_{2s}T_{gs}}{N_{1,s}C_{i,s}}$	$\frac{N_{3s}P_s}{N_{1,s}C_{i,s}}$	$\frac{r_{wgs,s}\gamma_i z_s(1-\varepsilon)}{\varepsilon N_{1,s}C_{i,s}}$	$\frac{r_{hyd,s}\gamma_i z_s(1-\varepsilon)}{\varepsilon N_{1,s}C_{i,s}}$
$C_{CO}$	0.0150	1	0.137	0.1387	0.453	0
$C_{H_2O}$	0.0153	1	0.24	0.243	0.55	$7.62 \times 10^{-4}$
$C_{CO_2}$	0.0150	1	0.252	0.253	1.52	$2.1 \times 10^{-3}$
$C_{H_2}$	0.0154	1	0.85	0.855	2.74	0
$C_{CO}$	0.0151	1	0.174	$1.76 \times 10^{-3}$	0	0.98
$C_{H_2S}$	0.0150	1	0.585	0.59	0	0.155

From the values of dimensionless groups in Table 3.3, we can make various conclusions. Considering the values of dimensionless Group-6, we can conclude that the contribution of  $C_{H_2O}$  and  $C_{CO_2}$  in hydrolysis reaction is low and hence the term involving this reaction for these species can be neglected. Similarly, considering the dimensionless Group-4, we can conclude that the convection of  $C_{CO}$  due to pressure gradient is low, thus, this term can also be neglected. Considering the values of dimensionless Group-1, we can conclude that for all the species, rate of accumulation is smaller than convection. This implies that dynamic behavior of the species balance is significant only for a short period of time. This time period can be found by equating this dimensionless group to 1 and calculating the resulting time as

$$\frac{z_s}{N_{1,s}\delta_{ct,s}} = 1 \Rightarrow \delta_{ct,s} \approx 42 \text{ Seconds} \quad (3.101)$$

The short time taken by the dynamic behavior of species balance can also be verified by simulating the WGS reactor under isothermal and isobaric condition. From Figure 3-5, we can observe that all the species concentration variables reach steady-state after approximately 50 seconds.

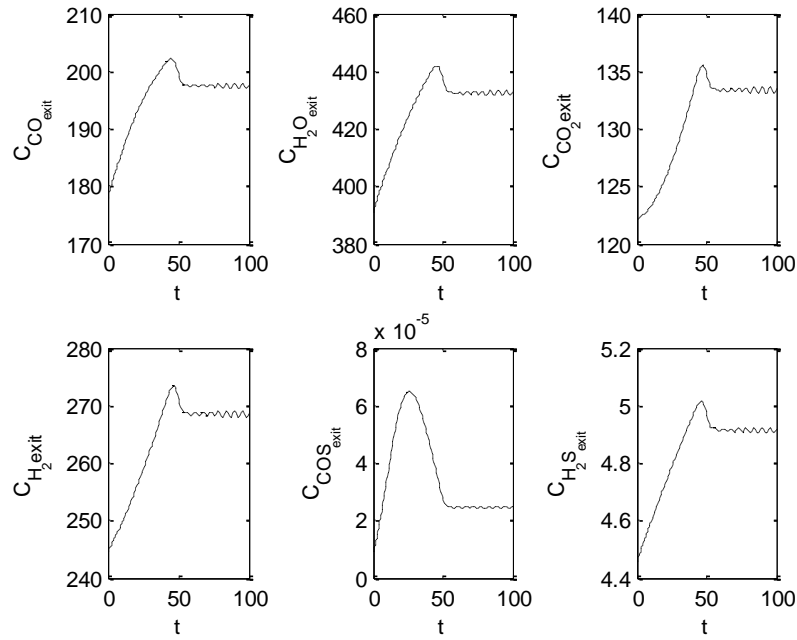


**Figure 3-5. Unsteady behavior of species balance equation under isothermal and isobaric condition**

In dynamic gas phase energy balance, following phenomena are considered:

- Rate of accumulation of gas phase energy per unit volume, represented by the term

$$\frac{\rho_g C_p g T_{g,s}}{t_s}$$

- Rate of convection of energy per unit volume in gas phase, represented by the term

$$\frac{G C_p g T_{g,s}}{z_s}$$

- Rate of transfer of energy per unit volume in gas phase, represented by the term

$$\frac{h_f a_c N_{4,s}}{\varepsilon}$$

Similarly, in dynamic catalyst phase energy balance, following phenomena are considered:

- Rate of accumulation of energy per unit volume in catalyst phase, represented by

the term  $\frac{\rho_{cat} C_p_{cat} T_{cat,s}}{t_s}$

- Rate of conduction of energy per unit volume in catalyst phase, represented by the term  $\frac{K_{cat}T_{cat,s}}{z_s^2}$
- Rate of transfer of energy per unit volume in catalyst phase, represented by the term  $\frac{h_f a_c N_{4,s}}{(1-\varepsilon)}$
- Rate of production of energy per unit volume in catalyst phase due to water gas shift reaction, represented by the term  $r_{wgs,s} \Delta H_{R,wgs}$
- Rate of production of energy per unit volume in catalyst phase due to hydrolysis reaction, represented by the term  $r_{hyd,s} \Delta H_{R,hyd}$

Table 3.4 shows the absolute values of dimensionless groups formed by dividing each of the phenomena with convection phenomena for gas phase energy balance; and with energy production phenomena from water gas shift reaction for catalyst phase energy balance.

**Table 3.4. Values of dimensionless groups for energy balance equations of sour WGS reactor model**

Energy balance (symbol)		Group-1	Group-2	Group-3	Group-4	Group-5
Gas phase	Term	$\frac{\rho_g z_s}{Gt_s}$		$\frac{h_f a_c z_s N_{4,s}}{G\varepsilon C_{pg} T_{g,s}}$	-	-
	Value	$3.5 \times 10^{-4}$	1	0.99	-	-
Catalyst phase	Term	$\frac{\rho_{cat} C_p_{cat} T_{cat,s}}{r_{wgs,s} \Delta H_{R,wgs} t_s}$	$\frac{K_{cat} T_{cat,s}}{r_{wgs,s} \Delta H_{R,wgs} z_s^2}$	$\frac{h_f a_c z_s N_{4,s}}{G\varepsilon C_{pg} T_{g,s}}$	$\frac{r_{hyd,s} \Delta H_{R,hyd}}{r_{wgs,s} \Delta H_{R,wgs}}$	
	Value	0.313	$6.39 \times 10^{-5}$	0.69	1	$1.11 \times 10^{-3}$

From the dimensionless group values in Table 3.4, it can be concluded that the rate of accumulation for gas phase energy balance is negligible compared to convection. This means dynamic behavior of gas phase energy balance is significant only for a short period of time. This time period can be calculated as

$$\frac{\rho_g z_s}{G \delta_{T_{t,s}}} = 1 \Rightarrow \delta_{T_{g,t,s}} \approx 1 \text{ Second} \quad (3.102)$$

Similarly, rate of energy conduction in catalyst phase is negligible compared to the rate of energy generation from WGS reaction. Also, rate of energy generation from hydrolysis reaction is negligible. By comparing the temperature scales and reference values of gas and catalyst phases, we can observe that the values are very close to each other. This means that both the gas and catalyst temperature variables vary in similar manner along the length of the reactor. Hence, both variables can be considered to be equal and representing a single state. Using all the simplifications described, new energy balance equation can be formed as

$$\frac{\partial T}{\partial t} = \frac{1}{\rho_{cat} C_{p,cat}} \left[ -\frac{G\varepsilon C_{pg}}{1-\varepsilon} \frac{\partial T}{\partial z} + r_{wgs} \Delta H_{R,wgs} \right] \quad (3.103)$$

Based on the new energy balance, new dimensionless groups can be formed as shown in Table 3.5.

**Table 3.5. Values of dimensionless groups for new energy balance equation and pressure drop equation**

Symbol		Group-1	Group-2	Group-3
$T$	Term	$\frac{\rho_{cat} C_{p,cat} (1-\varepsilon) z_s}{G\varepsilon C_{pg} t_s}$		$\frac{(1-\varepsilon) r_{wgs,s} \Delta H_{R,wgs} z_s}{G\varepsilon C_{pg} T_{g,s}}$
	Value	0.455	1	1.45
$P$	Term		$\frac{1.75 \rho_g (1-\varepsilon) N_{1,s}^2 z_s}{P_s d_{cat} \varepsilon}$	$\frac{z_s (1-\varepsilon)^2 150 \mu N_{1,s}}{P_s \varepsilon^2 d_{cat}^2}$
	Value	1	0.55	0.03

From the dimensionless Group-1, the time period of dynamic behavior of new energy balance can be calculated as

$$\frac{\rho_{cat} C_{p,cat}(1-\varepsilon)z_s}{G\varepsilon C_{pg}\delta_{Tr,s}} = 1 \Rightarrow \delta_{Tr,s} \approx 1274 \text{ Seconds} \quad (3.104)$$

From Figure 3-3, we can see that dynamic behavior of combined species and energy balance takes approximately 1274 seconds. Comparing the dynamic time period for species (42 seconds) and energy balance (1274 seconds), it can be concluded that dynamic behavior of species is only a small fraction of dynamic behavior of temperature. This means that we can safely assume the species balance to be quasi-steady during the simulation of sour WGS reactor model.

Similar analysis can be done for pressure drop equation and following dimensionless numbers can be formed as shown in Table 3.5. The values of dimensionless groups indicate that all the terms in the equation are important and no further simplification is possible.

Considering all the simplifications described, following simplified model can be derived:

Simplified Species balance:

$$\frac{dC_i}{dz} = -C_i \left( \frac{1}{T_g} \frac{dT_g}{dz} - \frac{1}{P} \frac{dP}{dz} \right) + (r_{wgs} \gamma_{wgs,i}) \frac{(1-\varepsilon)P}{GRT_g \varepsilon} \quad (3.105)$$

$i = \text{CO, H}_2\text{O, CO}_2 \text{ and H}_2$

$$\frac{dC_{cos}}{dz} = -C_{cos} \left( \frac{1}{T_g} \frac{dT_g}{dz} \right) + (r_{hyd} \gamma_{hyd,COS}) \frac{(1-\varepsilon)P}{GRT_g \varepsilon} \quad (3.106)$$

$$\frac{dC_{H_2S}}{dz} = -C_{H_2S} \left( \frac{1}{T_g} \frac{dT_g}{dz} - \frac{1}{P} \frac{dP}{dz} \right) + (r_{hyd} \gamma_{hyd,H_2S}) \frac{(1-\varepsilon)P}{GRT_g \varepsilon} \quad (3.107)$$

Pressure drop equation:

$$\frac{dP}{dz} = -\frac{\rho_g}{d_{cat}} \left( \frac{GRT_g \varepsilon}{P} \right)^2 \left( \frac{1-\varepsilon}{\varepsilon^3} \right) \left( 1.75 + \frac{150 \mu P (1-\varepsilon)}{d_{cat} \varepsilon GRT_g \rho_g} \right) \quad (3.108)$$

Simplified energy balance:

$$\frac{\partial T}{\partial t} = \frac{1}{\rho_{cat} C_{p,cat}} \left[ -\frac{G\varepsilon C_{pg}}{1-\varepsilon} \frac{\partial T}{\partial z} + r_{wgs} \Delta H_{R,wgs} \right] \quad (3.109)$$

The inlet conditions and reaction kinetic equations remain the same as in detailed model. The simplifications from scaling analysis resulted in conversion of parabolic type model to hyperbolic type PDE model. Further, energy balance equations for gas phase and catalyst phase are simplified to a single energy balance and resulted in removing one boundary condition.

### 3.1.4.3 Comparison of Detailed and Simplified Models

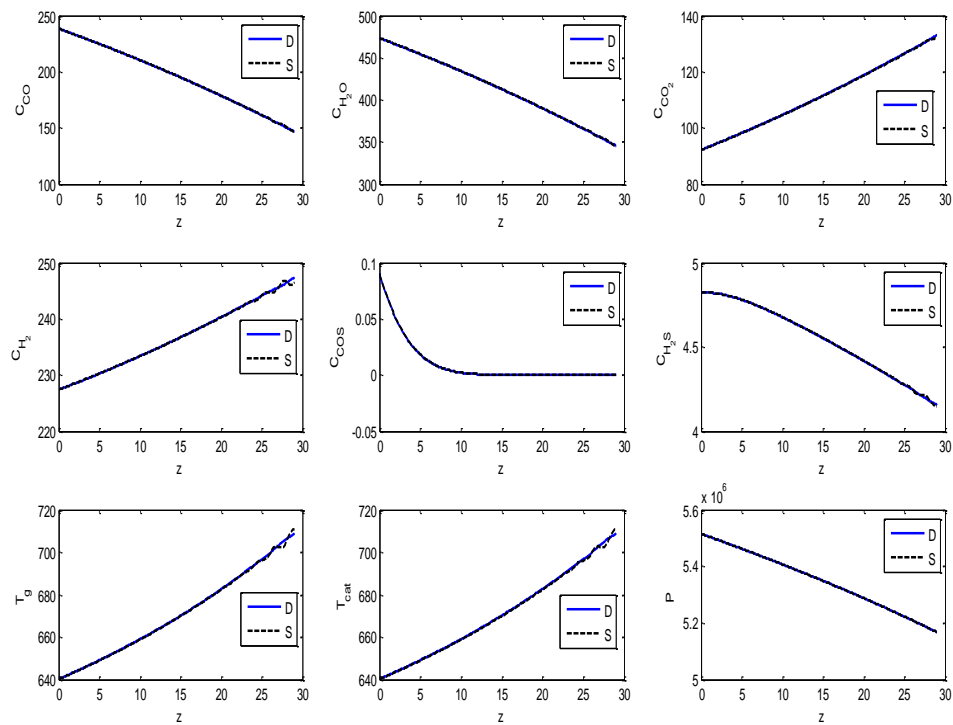
The simplified model obtained through scaling analysis is studied by comparing the simulation results with that generated from the detailed model. The percentage change in the average values of the variables between detailed and simplified models along with computational load of each model are considered as metrics for comparison. These metrics represent the accuracy of the simplified model and its computational efficiency compared to the detailed model. For accuracy, the average error percentage of a variable during dynamic simulations between both models is given by

$$V_{avg,error} = \frac{\left| \frac{1}{t_{end}L} \int_0^{t_{end}} \int_0^L V_{detailed} dz dt - \frac{1}{t_{end}L} \int_0^{t_{end}} \int_0^L V_{simplified} dz dt \right| \times 100}{\frac{1}{t_{end}L} \int_0^{t_{end}} \int_0^L V_{detailed} dz dt} \quad (3.110)$$

where  $V$  represents the variable under consideration (e.g. temperature). In Eqn. (3.110), integrals are calculated numerically based on the values of the corresponding variables. Computational load is measured based on processor time required for dynamic simulation of each model for the entire simulation time. Table 3.6 shows the values of the metrics. From the values in Table 3.6, we can see that error percentages, calculated by Eqn. (3.110) are quite small, thus, we can consider the simplified model as a good approximation of the detailed model for the given parameters and inlet conditions. Moreover, the computational load of the simplified model is found to be reduced by approximately 32% compared to the detailed model. Figure 3-6 and Figure 3-7 show the comparison of steady-state and dynamic values of detailed and simplified models for different variables.

**Table 3.6. Comparison of the reduced model vs the detailed model**

Variable/Model	Measure	Value (%)
$C_{CO}$	$C_{CO,avg,error}$	0.0057
$C_{H_2O}$	$C_{H_2O,avg,error}$	0.0089
$C_{CO_2}$	$C_{CO_2,avg,error}$	0.0953
$C_{H_2}$	$C_{H_2,avg,error}$	0.0189
$C_{COS}$	$C_{COS,avg,error}$	0.7031
$C_{H_2S}$	$C_{H_2S,avg,error}$	0.004
$T_g$	$T_{g,avg,error}$	0.0154
$T_{cat}$	$T_{cat,avg,error}$	0.0276
$P$	$P_{avg,error}$	$7.52 \times 10^{-4}$
Detailed model	Computational load, s	144.2
Simplified model	Computational load, s	98.9


**Figure 3-6. Steady state values of WGS reactor model compared between detailed and simplified model: D – detailed, S-Simplified**

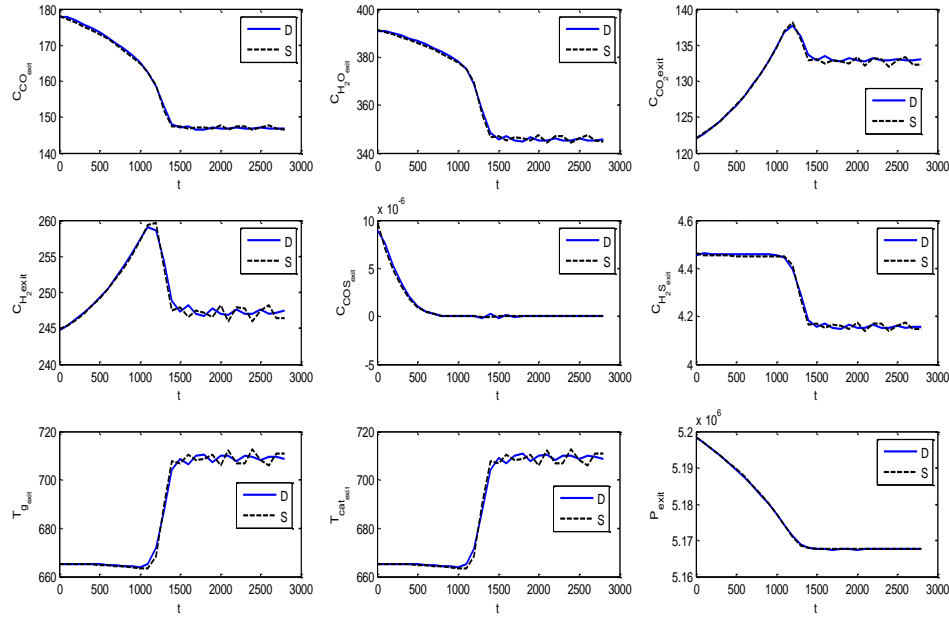


**Figure 3-7. Unsteady state values at exit of WGS reactor compared between detailed and simplified model: D – detailed, S-Simplified**

### 3.2 Conclusion

Scaling analysis has been systematically applied to model equations for simplifying the equations and obtaining a simplified model. In this analysis, two important difficulties, one in handling nonlinear terms and another in performing trial-and-error procedure, are addressed. The improvements proposed in the method of scaling analysis allow straightforward handling of nonlinear terms and avoid the trial-and-error procedure currently used in the literature by reducing the problem of obtaining scales and reference values to simply solving algebraic equations. The resulting scales and reference values are shown to be appropriate in making the corresponding dimensionless variable to vary in the order of 1 through numerical examples. The proposed approach is applied on our 1-D sour WGS reactor model and subsequently the method is used for obtaining a simplified model of the reactor. The simplified model is obtained by eliminating the phenomena that occur at much lower scales. The simulation results show that the obtained simplified model is in good agreement with the detailed model while also reducing the computational load.

## Chapter 4

### System-Level Sensor Placement

#### 4.1 Introduction

Highly integrated and complex processes and advancements in control technologies for controlling these processes have increased the necessity of cost-effective automated diagnostic systems that can efficiently detect, identify and diagnose abnormalities and their origins as they propagate in the process. The diagnostic systems traditionally use underlying mathematical models and the on-line measurement from sensors specific to the process. As a fault enters a system, it affects the process variables, which deviate from normal operating conditions. Diagnostic systems compare the response of the process variables with respect to a reference model in the presence of faults in order to detect fault symptoms and monitor the performance of the process which depends crucially on the location of the sensors that capture the behavior of process variables. However, it is not economically viable and practically possible to measure all the process variables. Therefore, designing a cost-effective sensor network based on various criteria, e.g. observability, reliability, diagnosability, estimability etc., poses a unique problem for process engineers. Several techniques have been reported in the literature, such as fault trees, cause-effect diagraphs, fuzzy logic-based methods, neural network, principal component analysis, qualitative trend analysis, support vector machines, hidden Markov model-based methods, and multivariate analysis techniques for sensor placement for fault diagnosis. For a broader discussion on available techniques, interested readers are referred to the review articles by Kramer and Mah<sup>87</sup>, Bagajewicz<sup>88</sup>, Frank et al.<sup>89</sup>, Venkatasubramanian et al.<sup>90</sup>

Generally, the diagnostic systems are categorized into quantitative model-based, qualitative model-based and process history based techniques.<sup>90</sup> The model-based techniques are centered around fundamental first-principal mathematical equations of the process, whereas the process history techniques rely on the analysis of long-time acquired process data.<sup>90</sup> Cause and effect models such as the directed graph (DG) and signed

directed graphs (SDG) are popular qualitative model-based techniques that have been studied in the context of sensor placement for fault diagnosis (FD) by many researchers. The DG representation is one where the nodes (representing process variables and root causes) are connected by arcs. The SDG is a DG where a positive or negative sign is associated with each arc. In both the representations, the direction of the arcs are from 'cause' nodes to the 'effect' nodes.<sup>90</sup> Iri et al.<sup>91</sup> were first to use SDG representation for FD where they used SDG representation to identify the origin of failure for the available set of measurements. While the various fault observability and resolvability criteria for graph models used by the researchers are fundamentally analogous, e.g. diagnostic observability means at least one variable corresponding to the actual fault is estimated correctly<sup>92-93</sup>, this study follows the definition by Raghuraj et al.<sup>9</sup> Fault observability means that at least one of the sensors in the network can observe the fault, and fault resolution means that the fault can be uniquely identified from other faults by the sensor network.

The problem of sensor placement (SP) was first tackled by Lambert<sup>94</sup> using a fault tree representation based on failure probabilities. Madron and Veverka<sup>95</sup> solved the problem constrained to observability and redundancy. Chang et al.<sup>96</sup> adopted the concept of observability and resolution and proposed a sensor placement method to minimize the number of sensors while ensuring the observability and highest resolution. Raghuraj et al.<sup>9</sup> incorporated the concept of fault observability and resolution into DG representation of the process and proposed an approach to identify the optimal location of the sensors. Bhushan and Rengaswamy<sup>4</sup> extended the work of Raghuraj et al.<sup>9</sup> to SDG analysis for FD and continued the work by taking into account additional quantitative information such as fault occurrence probabilities, sensor failure probabilities, sensor costs and order of magnitude.<sup>97</sup> Bhushan and Rengaswamy<sup>5</sup> presented their framework by formulating the problem as a mixed integer linear programming (MILP) formulation by using the bipartite matrix for various fault diagnostics and reliability criteria. Bagajewicz<sup>98</sup> proposed a procedure where the problem is formulated as an optimization problem for cost minimization with respect to precision, error-detectability, resilience and availability. Recent efforts in cause-effect modellings are centered around incorporating useful concepts or adding more information that improve the FD by DG and SDG models. Bhushan et al.<sup>7</sup> and Yang et al.<sup>99</sup> incorporated robustness and false alarm rates into SDG,

respectively. Recently, Chen and Chang<sup>100</sup> enhanced the SDG algorithm by considering the sequence in which the faults propagates throughout the process. In their work, the problem is posed as a binary integer linear programming (BILP) formulation with sensor pairs as additional decision variables. In this work, the SDG algorithm is enhanced by taking advantage of available numerical data and the relationship among the variables. An algorithm is proposed based on magnitude of pairs of variables to enhance the diagnostic capability of SDG. The sensor placement problem is posed as a BILP formulation by using the bipartite matrix while ensuring observability and maximum possible resolution.

In almost all of the works using cause-effect models, the sensor network design is obtained by considering the qualitative simulation of the process; numerical solutions are used to verify the sensor network. However, the problem of spurious solutions, which refers to the solutions that are not realizable physically, inherent in qualitative models might reduce the efficacy of the sensor placements, particularly for complex processes. On the other hand, optimization solutions involving large-scale first-principles models for sensor placement might still be intractable. As a result, a compromise might be to directly utilize the numerical solution of the process models in the traditional sensor placement algorithms. We believe that this approach while keeping the sensor placement algorithms still tractable will also enhance the specificity of these algorithms. In this work, the SDG algorithm is enhanced by taking advantage of available numerical data and the relationship among the variables. We adapt the DG and SDG philosophy under the assumption that a numerical solution is available and propose magnitude ratio (MR) – ratio of the changes in a pair of process variables in response to a fault – to improve sensor placements for FD. The sensor placement problem is posed as a BILP formulation by using the bipartite matrix while ensuring observability and maximum possible resolution. Moreover, we generalize this idea of magnitude ratio to the realistic case of multiple process variables and multiple faults. We also study the fault evolution sequence (FES) – sequence in which a pair of sensor variables deviate from their nominal values in response to a fault - for improvements in the sensor placements for FD.

## 4.2 Sensor Placement Approach

To facilitate the use of MR and FES information in a SP algorithm, a set of artificial sensors, which correspond to pair-wise sensors from the original list of sensors are defined. In MR algorithm, artificial sensors represent the magnitude ratio of the corresponding pairs; and in FES algorithm, artificial sensors represent the sequence in which the corresponding pairs respond to the faults as the faults propagate in the system. We believe these enhancements not only improve the capability of the SP algorithms, but they can be viewed as independent components of a more general and complex SP problem that is decomposed into simple, yet efficient components.

Theoretically, the SP problem can be thought of as an optimization problem that requires minimization of the cost of the sensor network while satisfying the underlying mathematical equations and constrained to some fault diagnosis performance metrics. However, the major drawbacks to this theoretical view are: (i) solving such minimization problems for large complex systems is computationally expensive, (ii) the underlying mathematical equations must be embedded within the optimizer and might require solution to a mixed-integer non-linear programming problem, (iii) it is in general non-obvious and difficult to define fault diagnosis performance metrics, and (iv) finally, simple engineering interpretation of the results might be difficult. We believe that one way to resolve these drawbacks is to decompose the underlying mathematical model into smaller and simpler interacting building blocks of information such as DG, SDG, FES and MR. By doing this, the resultant optimization problem can be solved easily as the underlying complex mathematical equations are removed from the optimizer. The complexity of optimization problem can be reduced to solving an integer linear programming problem. Further, the sensor placement results can be easily interpreted. Moreover, further improvements can be achieved by adding more information components to the model description. One such example could be qualitative trends or “signatures” that faults leave in the measured variables.

Another interpretation of this approach is that the sensor placement problem is simplified and efficiently solved through the use of appropriate features. The DG and SDG develop qualitative features, whereas FES is a purely temporal feature. Clearly, none of

these are quantitative features. The MR is probably the simplest quantitative feature that one could include in the sensor placement algorithm; this has not been attempted before. We will show that the inclusion of this feature can help in both better resolvability and also in deriving more cost-effective sensor placements with the same level of performance.

### 4.3 SDG and FES Algorithms in the Presence of Numerical Simulations

In a process system, a change in one variable can cause one or more variables to change significantly. These cause-effect (CE) relations among the variables are very useful for diagnosing faults in the system. The optimum number and locations of sensors for diagnosis of a process can be identified through an algorithmic approach when process simulation is available. Such an approach is detailed next. First, the total number of faults ( $M$ ) that one is interested in diagnosing is chosen. Then under the assumption of occurrence of one fault at a time, fault simulations are performed. Next, the candidate sensor locations ( $N$ ) are chosen. Fault sets - which are a set of all the sensors that respond to the occurrence of a fault - are generated. Due to large differences in the magnitude and direction of change of the process variables in response to the occurrence of a fault, it is important to use a threshold value for each process variable while developing the fault sets. A variable should be included in a fault set whenever that process variable deviates beyond the threshold limit. The extent of deviation in a particular process variable depends on its actual operating value, type, operating condition, noise and disturbances. For simplicity, we have considered the threshold limit on the process variables as  $\pm 2\sigma$  variation of the sensor that measures the variable where  $\sigma$  is the standard deviation, e.g. 2 °F for temperature sensors.<sup>101</sup> If the variable changes from its nominal value beyond the  $\pm 2\sigma$  of the sensor that measures the variable, the variable is assumed to be changed from its nominal value.

All the faults are introduced at the same operating condition. No disturbance is introduced into the system during fault simulations. In DG, if a variable changes beyond its operating limit, a "1" is assigned, otherwise "0" is assigned, i.e.  $R_{DG} \in \{0,1\}$ . This operation returns a row vector for each fault with the dimension of  $1 \times N$  and performing this operation for  $M$  faults will return matrix  $A^{DG}$  with the dimension of  $M \times N$ . In SDG, "1" is assigned if the variable changes beyond the upper limit and "-1" if it changes beyond the lower limit. If the variable stays within its limits, "0" is assigned. Note that the

deviations are based on the incipient response of the process, thus, if a variable response changes during the course of the fault evolution, e.g. "1" then after some time "-1", only the initial response is considered, i.e. "1". Therefore,  $R_{SDG} \in \{-1, 0, 1\}$ . Considering all the faults, the matrix  $A^{SDG}$  of dimension  $M \times N$  is obtained. The constraint matrix is constructed by augmenting the observability ( $A^{obs}$ ) and resolution matrices ( $A^{res}$ ),  $A = \begin{bmatrix} A^{obs} \\ A^{res} \end{bmatrix}$ . For observability, since only observing the fault is required and not the direction,  $A^{obs} = A^{DG}$ . For resolution, symmetric difference sets of the form  $A_{ij}^{res} = A_i^{SDG} \cup A_j^{SDG} - A_i^{SDG} \cap A_j^{SDG}$  for each pair of faults results in matrix  $A^{res}$  with the dimension  $M C_2 \times N$ .<sup>4-5,102</sup> However, it is possible that some of the faults may produce deviation in the same direction for the same set of variables. In that case, the corresponding rows in the observability matrix are the same. If  $q$  rows are same in the observability matrix, the resolution matrix will have  $q C_2$  number of rows with zero elements. Therefore, those faults cannot be resolved.

A binary integer programming problem for sensor placement is formulated for minimizing the sensor cost subjected to fault observability and resolution considering all the process variables as decision variables. A binary decision variable is assigned to each process variable; if the decision variable takes a value of "1" then a sensor is placed to measure that variable and a "0" value implies that the variable is not measured. The constraint matrix,  $\mathbf{A}$ , in the optimization problem represents the coefficient matrix obtained by DG and SDG. Since for observability and resolution at least one sensor must be picked by the optimizer, the  $b$  vector represents the constant vector of unity with  $(M + M C_2)$  rows.

$$\min \sum_j^N w_j x_j \quad (4.1)$$

Subject to:

$$Ax^T \geq b$$

and  $x_j$  binary

$w_j$  is weight for the sensor for  $j=1, \dots, N$

where

$$A = \begin{bmatrix} 1 & 0 & 0 & 1 & \cdots & 1 \\ 0 & 0 & 1 & 1 & \cdots & 1 \\ \vdots & \vdots & \vdots & \vdots & \ddots & \vdots \\ 0 & 1 & 0 & 1 & \cdots & 1 \end{bmatrix}_{(M + {}^M C_2 - {}^q C_2) \times N} \quad b = \begin{bmatrix} 1 \\ 1 \\ \vdots \\ 1 \end{bmatrix}_{(M + {}^M C_2 - {}^q C_2) \times 1}$$

The sign of the variables' response to a fault and the sequence in which the variables respond to a fault can be utilized to enhance the fault resolution. The FES algorithm, proposed by Chen and Chang<sup>100</sup>, takes into account the sequence in which fault propagates through the process. This is the first work where this approach was proposed. In their work, sensors are paired together and assumed as a pseudo-sensor to obtain the sequence information. Since the work of Chen and Chang<sup>100</sup> is based on qualitative analysis without numerical simulations and the current work assumes that numerical solutions are available, an algorithmic approach for FES had to be developed. This is described below.

After a set of  $M$  faults are modeled individually, the sequence in which sensors capture the changes in the process variables for each fault is determined by the time elapsed from a reference time, which is set before any variable goes beyond the threshold limit. As soon as a variable goes beyond the threshold limit, it is added to the sequence. To pair the sensors,  ${}^N C_2$  combinations are considered as the available pairs and a base sequence is assumed for each pair as  $\{S_i, S_j\}$  where  $j > i$  and  $S$  represents the corresponding sensor. The pairs used in this study are of the form of  $P_{ij}$ , where  $P_{ij}$  is the pseudo-sensor assigned to the sequence of sensors  $S_i$  and  $S_j$ . This will result in the generation of  $\frac{N(N-1)}{2}$  pseudo-sensors as pairs. If the sequence of any pair ( $P_{ij}$ ) is in the same sequence as the base pairs, "1" is assigned to that pair variable, if the pair is in the opposite sequence of the base pairs, "-1" is assigned and for all others "0" is assigned to the pair variables. However, it would not be possible in practice to determine the sequence of pairs of variables if the time elapsed between the responses is short. Thus, a threshold time is defined to determine if responses can be arranged in the sequence. If the difference in response time of the pair is greater than the time threshold then it will take the values as described, otherwise, "0" is assigned to distinguish them from pairs that can be practically assumed in sequence. Therefore,  $P \in \{-1, 0, 1\}$ . This operation will return a matrix with dimension  $M \times {}^N C_2$ . Figure 4-1 shows the

flowchart of FES algorithm in presence of numerical solution. In this flowchart,  $G$  is the measurement value,  $t$  is the time elapsed from a reference time until the sensor magnitude (measured value) goes beyond the threshold limit,  $T_i$  and  $T_j$  are the operational threshold limit, and  $T_t$  is the time threshold.

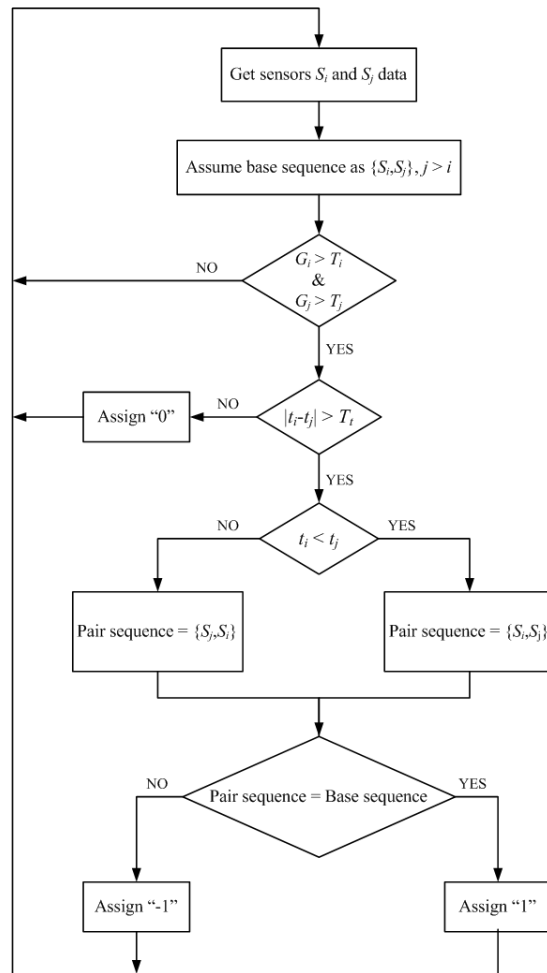


**Figure 4-1. Flowchart of FES algorithm in presence of numerical solution**

#### 4.4 Sensor Placement Using Magnitude Ratio

Qualitative reasoning, in general, predominantly focuses on the behavior of single process variables and neglects relationship among process variables.<sup>103</sup> Other than the information available from single variables, partial information such as absolute value

ranges, relative orders of magnitudes and approximate numerical values can be utilized.<sup>103</sup> Qualitative reasoning disregards such available information and practices reasoning at a very abstract level. Thus, the focus is on the signs exclusively and practical use of numerical values is excluded. Explicit use of numerical information in conjunction with qualitative reasoning makes such reasoning more applicable for engineering systems. Such reasoning has been reported in the work of Mavrovouniotis and Stephanopoulos<sup>103</sup>, and Raiman<sup>104</sup> for FD. In their work, the order of magnitude reasoning is discussed through the definition of three relations among quantities: A is negligible in relation to B, A has the same sign and is close to B, and A has the same sign and order of magnitude as B. Although this approach uses quantitative information of the variables, it cannot relate numbers to order of magnitude relations; and order of magnitude reasoning contains no extra information when full numerical solutions are available.<sup>103</sup> Therefore, a somehow similar reasoning is proposed that take advantage of the available numerical data. The magnitude ratio can be thought as reasoning by  $A \gg B$  or  $A \approx B \approx 1$ , where, A and B represent the ratio of normalized magnitude of the sensors. To better understand this idea, consider the example in Table 4.1. SDG algorithm cannot distinguish between  $F_1$  and  $F_2$ , but, we can examine the ratio of the sensors and see if we can distinguish between these faults. Figure 4-2 shows the ratio of  $S_1$  to  $S_2$  for each fault. Note that the magnitude of each sensor is normalized by its steady state value. The magnitude ratio for fault  $F_1$  is much higher than that of  $F_2$ 's. This indicates that the sensor  $S_1$  is much more affected than  $S_2$ , or vice versa, for  $F_1$  compared to  $F_2$ . Therefore, this way we can distinguish between faults  $F_1$  and  $F_2$ .

**Table 4.1. SDG example**

Fault	Sensor	
	$S_1$	$S_2$
$F_1$	1	-1
$F_2$	1	-1

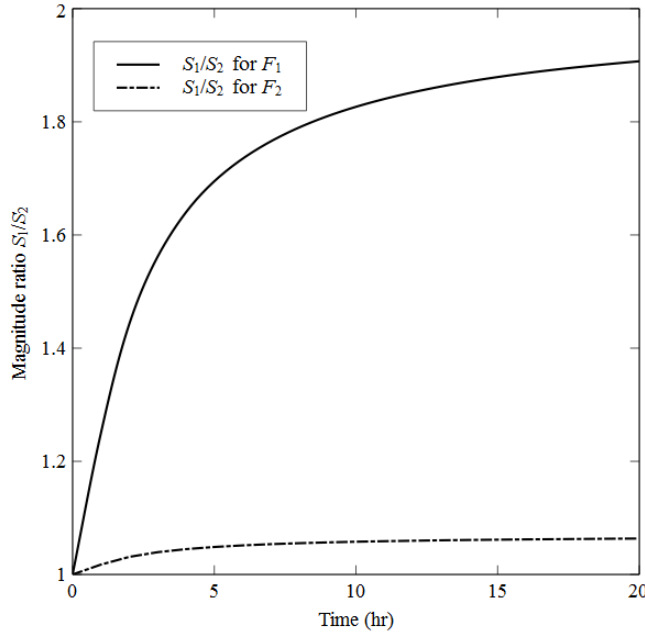


Figure 4-2. Magnitude ratio for example in Table 4.1

Generally, the extent that a variable is affected by a fault gives an insight into the propagation of the fault through the process. Although both quantitative and qualitative analysis shows that changes in variables can be utilized, as in DG and SDG, some variables are affected more by a fault while others are less affected. While this information is neglected in DG, SDG and FES, magnitude ratio can uncover such information from the relationship between pairs of variables. The magnitude ratio of a pair of sensors,  $S_i$  and  $S_j$ , is written as:

$$r_{ij} = \frac{G_i/G_{i,ss}}{G_j/G_{j,ss}} \quad (4.2)$$

where  $G_i$  and  $G_j$  are the magnitude of the sensors  $S_i$  and  $S_j$  and are normalized by their steady-state values  $S_{i,ss}$  and  $S_{j,ss}$ , respectively. Note that both  $S_i$  and  $S_j$  must at least go beyond their threshold limit to be considered for further analysis. The magnitude ratio,  $r_{ij}$ , is initially at "1". After a fault is introduced to the system,  $R_{ij}$  changes from its steady state ("1"), and can change in either direction. Recall that the pair  $P_{ij}$  is assigned to the sensors  $S_i$  and  $S_j$ , here, if  $r_{ij} \gg 1$ ,  $P_{ij}$  is assigned "1", if  $r_{ij} \ll 1$ ,  $P_{ij}$  is assigned "-1" and  $P_{ij}$  is

assigned "0" if otherwise. For this, a threshold is required to satisfy the inequalities. Therefore, the threshold value is tuned for maximum fault resolvability by a sensitivity analysis of the upper threshold value. Note that the lower threshold is calculated as the inverse of the upper threshold. If a variable is at "0" initially - like the error in a controller -  $P_{ij}$  is assigned "0". Eventually,  $P \in \{-1, 0, 1\}$  and after simulation of  $M$  faults, the operation will return a matrix with dimension  $M \times {}^N C_2$ , same as in the FES algorithm. Figure 4-3 shows the flowchart of MR algorithm. In this flowchart,  $T_{MR}$  is the MR threshold value.

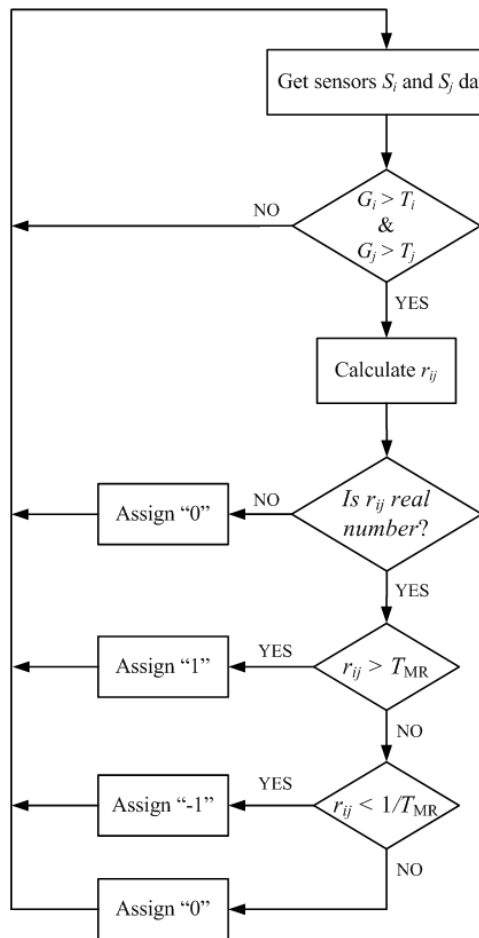


**Figure 4-3. Flowchart of MR algorithm**

## 4.5 Constraint Matrix for FES and MR

Similar to the resolvability problem of SDG,  ${}^M C_2$  pseudo-faults with corresponding symmetric differences of fault sets is constructed using the information provided by the  $P$  matrix. This results in an  ${}^M C_2 \times {}^N C_2$  matrix that contains the fault resolution by FES or MR. The constraint matrix for SDG, before removing any zero rows, have  $(M + {}^M C_2) \times N$  dimension with first  $M$  rows representing the observability and the following  ${}^M C_2$  rows representing the fault resolution. To add the resolution by FES or MR, the constraint matrix is augmented by  ${}^N C_2$  columns which consist of two blocks. An  $M \times {}^N C_2$  block of zeros is generated for observability, since FES and MR do not contribute to fault observability. In addition, an  ${}^M C_2 \times {}^N C_2$  block is generated by performing symmetric difference set on FES matrix (resulting in  $A^{FES}$  matrix) or MR matrix (resulting in  $A^{MR}$  matrix). The new augmented constraint matrix is treated as in SDG where rows that are the same and the rows that contain only zeros should be removed. Note that in order to solve the optimization problem, these rows must be removed from the constraint matrix  $A$  and the constant vector  $b$ .

After construction of the new augmented constraint matrix, the optimization problem has  $N + {}^N C_2$  decision variables, including the sensors and pseudo-sensors. However, to ensure consistency between the sensors and corresponding pseudo-sensors, the following constraint should be added to the optimization problem (augmented constraint matrix) for each pseudo sensor:<sup>100</sup>

$$\begin{aligned} (1 - x_i) + (1 - x_j) + x_{ij} &\geq 1 \\ (1 - x_{ij}) + x_i &\geq 1 \\ (1 - x_{ij}) + x_j &\geq 1 \end{aligned} \tag{4.3}$$

where  $x_{ij}$  is the pseudo-sensor corresponding to the sensors  $x_i$  and  $x_j$  in the decision variables. Eqn. (4.3) implies that per each pair of sensors, three linear inequality constraints must be added to the optimization problem constraints; therefore, the constraint matrix and the constant vector must augment with the consistency matrix,  $A^{cons}$ , with the dimension of  $(3 \times {}^N C_2) \times (N + {}^N C_2)$  and a vector of unity with the dimension of  $(3 \times {}^N C_2) \times 1$ , respectively.

## 4.6 Formulation Summary

### 4.6.1 Optimization Problem

The optimization problem in Eqn. (4.1) is summarized as:

$$\min \sum_j^N w_j x_j \quad (4.4)$$

Subject to:

$$Ax^T \geq b$$

$$x_j \text{ binary}$$

where

$$A = \begin{bmatrix} A^{obs} & 0_{M \times N_{C_2}} \\ A^{res} & 0_{M_{C_2} \times N_{C_2}} \\ 0_{M_{C_2} \times N} & A^* \\ A^{cons} & \end{bmatrix}_{(M + M_{C_2} + 3 \times N_{C_2} - q_{C_2}) \times (N + N_{C_2})} \quad b = \begin{bmatrix} 1 \\ 1 \\ \vdots \\ 1 \end{bmatrix}_{(M + M_{C_2} + 3 \times N_{C_2} - q_{C_2}) \times 1}$$

where  $A^* = A^{FES}$  for FES algorithm and  $A^* = A^{MR}$  for MR algorithm. Note that a joint FES and MR algorithm can be obtained by  $A^* = A^{FES \& MR} = A^{FES} \cup A^{MR}$ .

### 4.6.2 Solution Approach

The sensor network design is posed as a BILP and can be solved by a number of commercially available optimization software. In this work, the optimization problem is formulated in MATLAB and the solution is obtained by the CPLEX optimization toolbox integrated in MATLAB.

## 4.7 Results

In this section, five illustrative case studies are used to demonstrate the performance of FES and MR algorithms. A set of predefined faults are simulated in each case while assuming no disturbances exist in the system. Table 4.2 shows the sensors' cost assumed in all three cases which are normalized by the cost of flow sensor.<sup>101</sup> In all cases, MR algorithm is performed for three different levels of MR threshold value as low, medium

and high with values 1.1, 1.5 and 2, respectively. Results are compared for FES and MR algorithms individually and jointly. Detail tabulated results for the SDG, FES and MR algorithms are provided in the supporting document published in Mobed et al.<sup>105</sup> Also, sensitivity analysis of the MR threshold value is performed for each case study and the results are included in the same supporting document.

**Table 4.2. Type and cost of each sensor used in all case studies<sup>190</sup>**

Sensor type	Cost
Temperature sensor	0.1
Power	0.1
Pressure sensor	0.5
Flow sensor	1
Level sensor	1
Concentration sensor	10

#### 4.7.1 CSTR Case Study

The CSTR system used in the work of Bhushan and Rengaswamy<sup>4</sup> is considered in this work for application of FES and MR algorithms. For more details of the process, interested readers are referred to their work.<sup>4</sup> Figure 4-4 shows the schematic of the CSTR system. Table 4.3 and Table 4.4 show lists of measured variables and simulated faults in the CSTR system. Faults are simulated one by one and measured variables are stored for later implementation of FES and MR algorithms. As seen in Table 4.4, all faults except  $U$  and  $C_d$  can change in both directions with "+" representing increase and "-" decrease in the fault. The heat transfer coefficient,  $U$ , and the catalyst activity,  $C_d$  can only decrease due to nature of the fault. Therefore, these faults are unidirectional and can only change in "–" direction.

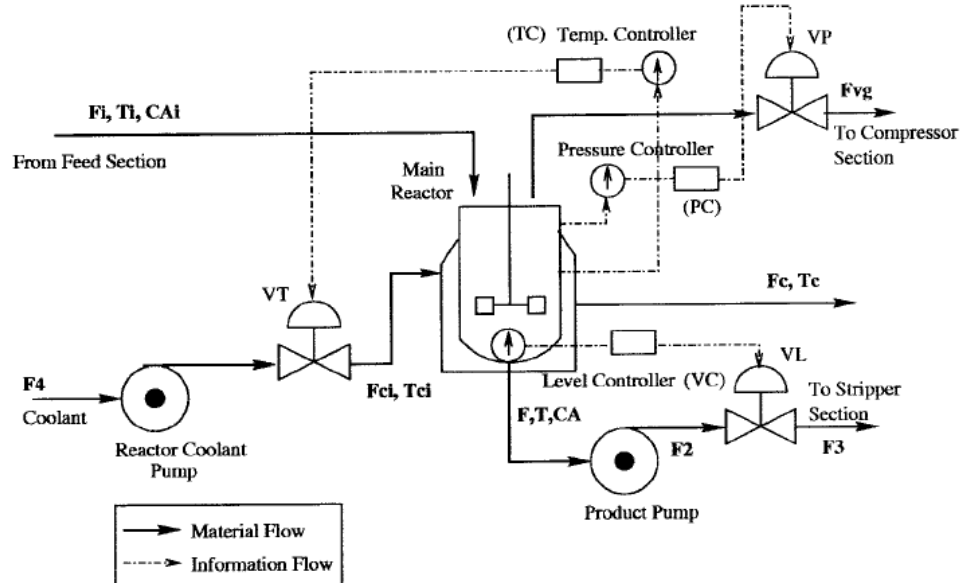

 Figure 4-4. Schematic of the CSTR system<sup>4</sup>

Table 4.3. List of measured variables in CSTR system

Sensor no.	Measured variable	Description	Sensor no.	Measured variable	Description
s1	C <sub>A</sub>	CSTR Outlet concentration	s5	VL	Level controller valve opening
s2	T <sub>c</sub>	Coolant outlet temperature	s6	VT	Temperature controller valve opening
s3	F	CSTR outlet flow rate	s7	VP	Pressure controller valve opening
s4	F <sub>c</sub>	Coolant flow rate			

Table 4.4. List of simulated faults and the corresponding affected sensors in CSTR system

Fault	Description	Affected sensors
1	C <sub>Ai</sub> <sup>+</sup> Inlet concentration	s1,s2,s4,s6,s7
2	C <sub>Ai</sub> <sup>-</sup>	s1,s2,s4,s6,s7
3	T <sub>i</sub> <sup>+</sup> Inlet temperature	s4,s6,s7

4	$T_i^-$		s4,s6,s7
5	$F_i^+$	Inlet flow rate	s1,s3,s4,s5,s6,s7
6	$F_i^-$		s1,s3,s4,s5,s6,s7
7	$T_{Ci}^+$	Coolant outlet temperature	s4,s6,s7
8	$T_{Ci}^-$		s2,s4,s6,s7
9	U	Heat transfer coefficient	s4,s6
10	$C_d$	Catalyst deactivation	s1,s2,s4,s6,s7

**Table 4.5. Results of applying different algorithms to CSTR system**

Algorithm(s)	MR threshold level	Selected sensors	Sensor network cost	Unresolvable fault sets
SDG		s1,s2,s6,s7	10.7	[3,7]
FES		s2,s6,s7	0.7	[3,7]
MR	Low	s1,s2,s6,s7	10.7	[3,7]
	Medium	s2,s6,s7	0.7	[ ]
	High	s2,s6,s7	0.7	[3,7]
	Low	s2,s6,s7	0.7	[3,7]
FES & MR	Medium	s2,s6,s7	0.7	[ ]
	High	s2,s6,s7	0.7	[3,7]

Both FES and MR algorithms are run individually and in combination. Although both algorithms are associated with SDG, for illustration, SDG is also performed individually and results are shown in Table 4.5. FES algorithm has less number of variables measured compared to SDG, thus, decreasing the capital cost of the network. However, there is still a fault set that cannot be resolved by FES. At low MR threshold level, MR

algorithm shows no improvement over the associated SDG algorithm and the results are the same as if the SDG is performed individually. The combination of both MR and FES algorithms take advantage of the FES as it has lower sensor network cost. At medium MR threshold level, MR algorithm chooses the same sensors as FES but it can resolve all the faults, thus, the algorithm shows improvement in terms of fault resolvability compared to FES algorithm. The combination of both algorithms takes advantage of the MR algorithm as it can resolve all the faults. At high MR threshold level, although MR algorithm again chooses the same sensors as FES, it cannot resolve all the faults. The combination of both algorithms uses the same sensors as if the MR or FES performed individually since the sensor network cost and number of irresolvable faults is the same for both algorithms. Table 4.4 and 23 show the affected variables and variables that can be used for fault resolution, respectively. The fault resolution of MR algorithm shown in Table 4.6 is shown only for medium MR threshold level (value of 1.5). In Table 4.6 and the upcoming tables for fault resolution, each single sensor (i.e. s1) represent the sensor that can individually resolve the corresponding pair of faults and each sensor pair (i.e. P<sub>1,2</sub> which represents pair s1 and s2) represent pairs of sensors that can resolve the corresponding pair of faults.

**Table 4.6. Fault resolution by SDG, FES and MR in CSTR system**

Fault	Resolution sensors		Fault	Resolution sensors	
	Single	Pair		Single	Pair
	FES	MR		FES	MR
[1,2]	s1,s2,s		[3,10]	s1,s2,	P <sub>1,4</sub> , P <sub>1,6</sub> ,
	4,s6,s			s4,s6,	P <sub>1,7</sub> ,
	7			s7	P <sub>2,4</sub> , P <sub>2,6</sub> , P <sub>2,7</sub>
[1,3]	P <sub>1,2</sub> , P <sub>1,6</sub> , P <sub>1,7</sub> ,		[4,5]		P <sub>1,4</sub> , P <sub>1,6</sub> ,
	P <sub>2,4</sub> , P <sub>2,6</sub> , P <sub>2,7</sub> ,			s1,s3,	P <sub>1,7</sub> , P <sub>2,4</sub> ,
	P <sub>4,6</sub> , P <sub>4,7</sub> , P <sub>6,7</sub>			s5,s7	P <sub>2,6</sub> , P <sub>2,7</sub>
[1,4]	s1,s2,s	P <sub>1,2</sub> , P <sub>1,6</sub> , P <sub>1,7</sub> ,	[4,6]		P <sub>1,3</sub> , P <sub>1,4</sub> ,
	4,s6,s	P <sub>2,4</sub> , P <sub>2,6</sub> , P <sub>2,7</sub> ,			P <sub>1,5</sub> , P <sub>1,6</sub> ,
	7	P <sub>4,6</sub> , P <sub>4,7</sub> , P <sub>6,7</sub>		4,	P <sub>1,7</sub>
				s5,s6	

		$P_{1,2}, P_{1,3}, P_{1,4},$ $P_{1,5}, P_{1,6}, P_{1,7},$ $P_{2,4}, P_{2,6}, P_{2,7},$ $P_{4,6}, P_{4,7}, P_{6,7}$			
[1,5]	s2,s3,s 4,s5,s 6		[4,7]	s4,s6,s 7	$P_{4,7}, P_{6,7}$
[1,6]	s1,s2,s 3,s5,s 7	$P_{1,2}, P_{1,3}, P_{1,4},$ $P_{1,5}, P_{1,6}, P_{1,7},$ $P_{2,4}, P_{2,6}, P_{2,7},$ $P_{4,6}, P_{4,7}, P_{6,7}$	[4,8]	s2	$P_{2,4}, P_{2,6},$ $P_{4,7}, P_{6,7}$
[1,7]	s1,s2	$P_{1,2}, P_{1,6}, P_{1,7},$ $P_{2,4}, P_{2,6}, P_{2,7},$ $P_{4,6}, P_{4,7}, P_{6,7}$	$P_{4,7}, P_{6,7}$	[4,9]	s4,s6,s 7
[1,8]	s1,s4,s 6,s7	$P_{1,2}, P_{1,6}, P_{1,7},$ $P_{2,4}, P_{2,6}, P_{2,7},$ $P_{4,6}, P_{4,7}, P_{6,7}$	$P_{2,4},$ $P_{2,6},$ $P_{4,7}, P_{6,7}$	[4,10]	$P_{1,4}, P_{1,6},$ $P_{1,7}, P_{2,4},$ $P_{2,6}, P_{2,7}$
[1,9]	s1,s2,s 7	$P_{1,2}, P_{1,6}, P_{1,7},$ $P_{2,4}, P_{2,6}, P_{2,7},$ $P_{4,6}, P_{4,7}, P_{6,7}$		[5,6]	s1,s3,s 4, s5,s6,s 7
[1,1] 0]	s2,s4, s6,s7	$P_{1,2}, P_{1,4}, P_{1,6},$ $P_{1,7}, P_{4,6}, P_{4,7},$ $P_{6,7}$	$P_{1,6},$ $P_{1,7},$ $P_{2,4},$	[5,7]	$s1,s3,s$ 4, $s5,s6$
[2,3]	s1,s2,s 4,s6,s 7	$P_{1,2}, P_{1,6}, P_{1,7},$ $P_{2,4}, P_{2,6}, P_{2,7},$ $P_{4,6}, P_{4,7}, P_{6,7}$		[5,8]	$P_{1,3}, P_{1,4},$ $P_{1,5}, P_{1,6},$ $P_{1,7}$
[2,4]	s1,s2	$P_{1,2}, P_{1,6}, P_{1,7},$ $P_{2,4}, P_{2,6}, P_{2,7},$ $P_{4,6}, P_{4,7}, P_{6,7}$		[5,9]	$P_{1,3}, P_{1,4},$ $P_{1,5}, P_{1,6},$ $P_{1,7}$
[2,5]	s1,s2,s 3,s5,s 7	$P_{1,2}, P_{1,3}, P_{1,4},$ $P_{1,5}, P_{1,6}, P_{1,7},$ $P_{2,4}, P_{2,6}, P_{2,7},$ $P_{4,6}, P_{4,7}, P_{6,7}$		[5,10]	$P_{1,3}, P_{1,5},$ $P_{2,4}, P_{2,6},$ $P_{2,7}$
[2,6]	s2,s3,s 4,s5,s 6	$P_{1,2}, P_{1,3}, P_{1,4},$ $P_{1,5}, P_{1,6}, P_{1,7},$	[6,7]	s1,s3, s5,s7	$P_{1,3}, P_{1,4},$ $P_{1,5}, P_{1,6},$ $P_{1,7}$

		$P_{2,4}, P_{2,6}, P_{2,7},$ $P_{4,6}, P_{4,7}, P_{6,7}$			
[2,7]	4,s6,s 7	$P_{1,2}, P_{1,6}, P_{1,7},$ $P_{2,4}, P_{2,6}, P_{2,7},$ $P_{4,6}, P_{4,7}, P_{6,7}$	$P_{4,7}, P_{6,7}$	[6,8]	$s1,s2,s$ 3, $s4,s5,s$ 6
[2,8]	s1,s2	$P_{1,2}, P_{1,6}, P_{1,7},$ $P_{2,4}, P_{2,6}, P_{2,7},$ $P_{4,6}, P_{4,7}, P_{6,7}$	$P_{2,4}, P_{2,6},$ $P_{4,7}, P_{6,7}$	[6,9]	$s1,s3,$ $s5,s7$
[2,9]	4,s6,s 7	$P_{1,2}, P_{1,6}, P_{1,7},$ $P_{2,4}, P_{2,6}, P_{2,7},$ $P_{4,6}, P_{4,7}, P_{6,7}$		[6,10]	$s1,s2,s$ 3, $s4,s5,s$ 6
[2,1 0]	s1	$P_{1,2}, P_{1,4}, P_{1,6},$ $P_{1,7}, P_{4,6},$ $P_{4,7}, P_{6,7}$	$P_{1,6},$ $P_{1,7},$ $P_{2,4},$	[7,8]	$P_{1,4},$ $P_{1,6},$ $P_{1,7},$ $P_{2,6}, P_{2,7}$
[3,4]	s4,s6,s 7			[7,9]	$s2,s4,$ $s6,s7$
[3,5]	s1,s3,s 4,s5,s 6	$P_{1,3}, P_{1,4}, P_{1,5},$ $P_{1,6}, P_{1,7}$		[7,10]	$s1,s2,s$ 4, $s6,s7$
[3,6]	s1,s3, s5,s7	$P_{1,3}, P_{1,4}, P_{1,5},$ $P_{1,6}, P_{1,7}$		[8,9]	$s2,s4,$ $s6,s7$
[3,7]			$P_{4,7}, P_{6,7}$	[8,10]	$P_{1,4}, P_{1,6},$ $P_{1,7}, P_{2,4},$ $P_{2,6}, P_{2,7}$
[3,8]	s2,s4, s6,s7		$P_{2,4},$ $P_{2,6},$ $P_{4,7}, P_{6,7}$	[9,10]	$s1,s2,s$ 4, $s6,s7$
[3,9]	s7				$P_{1,4}, P_{1,6},$ $P_{1,7}, P_{2,4},$ $P_{2,6}, P_{2,7},$

#### 4.7.2 Five-Tank Case Study

The five-tank system from Bhushan and Rengaswamy<sup>4</sup> is considered as the next case study in this work. Figure 4-5 shows the schematic of the process. Lists of measured variables and simulated faults are shown in Table 4.7 and Table 4.8, respectively.

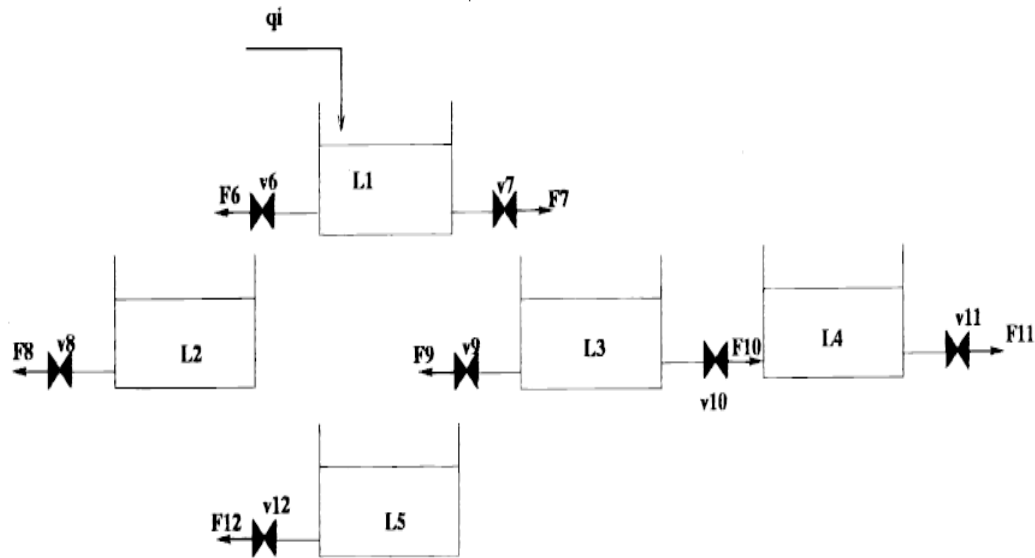


**Figure 4-5. Schematic of the five-tank case-study<sup>4</sup>**

**Table 4.7. List of measured variables in five-tank case-study**

Sensor no.	Measured variable	Description	Sensor no.	Measured variable	Description
s1	L1	Level in Tank 1	s7	F7	Stream 7
s2	L2	Level in Tank 2	s8	F8	Stream 8
s3	L3	Level in Tank 3	s9	F9	Stream 9
s4	L4	Level in Tank 4	s10	F10	Stream 10
s5	L5	Level in Tank 5	s11	F11	Stream 11
s6	F6	Stream 6	s12	F12	Stream 12

**Table 4.8. List of simulated faults and the corresponding affected sensors in five-tank case-study**

Fault	Description	Affected sensors
1	$q_i^+$	Inlet flow s1,s2,s3,s4,s5,s6,s7,s8,s9,s10,s11,s12

2	$q_i^-$		s1,s2,s3,s4,s5,s6,s7,s8,s9,s10,s11,s12
3	V6		s1,s2,s3,s4,s5,s6,s7,s8,s9,s10,s11,s12
4	V7		s1,s2,s3,s4,s5,s6,s7,s8,s9,s10,s11,s12
5	V8		s2,s8
6	V9	Valve closed	s2,s3,s4,s5,s8,s9,s10,s11,s12
7	V10		s2,s3,s4,s5,s8,s9,s10,s11,s12
8	V11		s2,s3,s4,s5,s8,s9,s10,s11,s12
9	V12		s2,s5,s8,s12
10	LT1		s1,s2,s3,s4,s5,s6,s7,s8,s9,s10,s11,s12
11	LT2		s2,s8
12	LT3	Leakage in tank	s3,s4,s5,s9,s10,s11,s12
13	LT4		s3,s4,s5,s9,s10,s11,s12
14	LT5		s5,s12

---

The solution to the optimization problem is shown in Table 4.9 that compares the different algorithms. Although faults  $q_i^-$  and  $LT1$  are not resolvable by SDG, both FES and MR can resolve these faults. At low and medium MR threshold level, the cost of the sensor network is the same as FES as well as SDG. Interestingly, at low MR threshold level, the combination of both algorithms picks a subset of the selected sensors by both algorithms and resolves all the faults at lower sensor network cost. At medium MR threshold level, the sensor network cost is similar to the sensor network cost of the FES algorithm, thus, the combination of the algorithms will have the same result as if the algorithms are performed individually. Interestingly, the selected sensors are not a combination of sensors selected through individual algorithms since there are multiple solutions to the optimization problem when algorithms are combined. At high MR threshold value, the sensor network cost is reduced compared to other algorithms, thus, the combination of the algorithms will have the same sensor network cost as the MR algorithm. Table 4.8 and Table 4.10 show

the affected variables for each fault and the fault resolution using all algorithms individually. The fault resolution of MR algorithm shown in Table 4.10 is shown only for low MR threshold level (value of 1.1). For compactness, only key rows of the fault resolution are shown and pairs that are combination of sensors in SDG results are not shown.

**Table 4.9. Results of applying different algorithms to five-tank case-study**

Algorithm(s)	MR threshold level	Selected sensors	Sensor network	Irresolvable fault
			cost	sets
SDG		s2,s4,s5,s10	4	[2,10]
FES		s2,s4,s9,s12	4	[]
	Low	s2,s10,s11,s12	4	[]
MR	Medium	s2,s10,s11,s12	4	[]
	High	s2,s5,s10	3	[]
	Low	s2,s11,s12	3	[]
FES & MR	Medium	s2,s8,s10,s12	4	[]
	High	s2,s5,s10	3	[]

**Table 4.10. Fault resolution by SDG, FES and MR in five-tank case-study**

Fault	Resolution sensors		Fault	Resolution sensors	
	Singles	Pairs		Singles	Pairs
	FES	MR		FES	MR
[1,4]	s2,s7,s8		P <sub>5,9</sub>	[4,10]	s1,s3,s4,s 5,s6,s9,s1 0,s11,s12
[1,6]	s1,s5,s6, s7,s8,s9, s12		P <sub>2,3</sub>	[4,11]	s1,s3,s4,s 5,s6,s7,s9 ,s10,s11,s
					12

[1,7]	s1,s4,s6, s7,s8,s10 ,s11	P <sub>2,9</sub>	P <sub>2,3</sub> ,P <sub>5,9</sub>	[6,8]	s5,s9,s10, s11,s12	P <sub>3,4</sub>	P <sub>3,4</sub>
[1,8]	s1,s6,s7, s8,s10,s1 1	P <sub>2,9</sub> ,P <sub>3,4</sub> , P <sub>4,9</sub>	P <sub>2,3</sub> , P <sub>3,4</sub>	[6,9]	s3,s4,s5,s 9,10,s11	P <sub>2,12</sub> , P <sub>8,12</sub>	P <sub>8,12</sub>
[2,4]	s1,s3,s4, s5,s6,s9, s10,s11,s 12	P <sub>2,8</sub>		[6,10]	4,s6,s7,s1 0,s11	P <sub>5,12</sub> , P <sub>8,9</sub>	P <sub>8,9</sub> , P <sub>8,12</sub> , P <sub>9,12</sub>
[2,6]	s1,s2,s3, s4,s6,s7, s10,s11	P <sub>5,12</sub> , P <sub>8,9</sub>	P <sub>8,9</sub>	[6,12]	s2,s3,s4,s 8,s10,s11	P <sub>5,12</sub>	P <sub>5,9</sub> , P <sub>9,12</sub>
[2,7]	s1,s2,s3, s5,s6,s7, s9,s12	P <sub>8,10</sub>	P <sub>4,8</sub>	[6,13]	s2,s3,s4,s 8,s11	P <sub>5,12</sub> , P <sub>9,10</sub>	P <sub>5,9</sub> , P <sub>5,12</sub> , P <sub>9,12</sub>
[2,8]	s1,s2,s3, s4,s5,s6, s7,s9,s12	P <sub>8,10</sub> ,P <sub>8,1</sub> , 1,P <sub>10,11</sub>	P <sub>8,10</sub> , P <sub>8,11</sub> , P <sub>10,11</sub>	[6,14]	s2,s3,s4,s 8,s9,s10,s 11		
[2,9]	s1,s2,s3, s4,s5,s6, s7,s9,s10 ,s11	P <sub>8,12</sub>	P <sub>8,12</sub>	[7,8]	s4	P <sub>2,11</sub> , P <sub>8,10</sub> , P <sub>8,11</sub> , P <sub>10,11</sub>	P <sub>5,9</sub> , P <sub>8,10</sub> , P <sub>8,11</sub> , P <sub>10,11</sub>
[2,12]	s1,s2,s6, s7,s8		P <sub>3,4</sub> , P <sub>3,10</sub> , P <sub>4,10</sub> , P <sub>5,9</sub> , P <sub>5,11</sub> , P <sub>9,10</sub> , P <sub>9,12</sub> , P <sub>11,12</sub>	[7,9]	s3,s4,s9,s 10,s11,s1 2		P <sub>2,5</sub>
[2,13]	s1,s2,s6, s7,s8,s10	P <sub>3,4</sub> , P <sub>3,11</sub> , P <sub>4,9</sub> , P <sub>9,11</sub>	P <sub>3,12</sub> , P <sub>3,5</sub> , P <sub>3,9</sub> , P <sub>3,11</sub> , P <sub>5,9</sub> , P <sub>5,11</sub> , P <sub>5,12</sub> , P <sub>9,12</sub>	[7,10]	s1,s2,s3,s 5,s6,s7,s9 ,s12	P <sub>8,10</sub>	P <sub>4,8</sub> , P <sub>4,10</sub> , P <sub>4,11</sub> , P <sub>8,10</sub> , P <sub>8,11</sub> , P <sub>10,11</sub>

[3,6]	s1,s3,s4, s6,s7,s8, s10,s11	$P_{5,12}$	[7,12]	s2,s3,s5,s 8,s9,s12	$P_{4,10}$
[3,7]	s1,s3,s5, s6,s7,s8, s9,s12	$P_{2,4},P_{2,11}$	[8,9]	s3,s4,s9,s 10,s11,s1 2	$P_{2,5}$
[3,8]	s1,s3,s4, s5,s6,s7, s8,s9,s12	$P_{10,11}$	$P_{10,11}$	[8,10] 4,s5,s6,s7 ,s9,s12	$P_{8,10},$ $P_{8,11},$ $P_{10,11}$
[3,9]	s1,s3,s4, s5,s6,s7, s8,s9,s10 ,s11	$P_{2,12}$	[8,12]	s2,s3,s4,s 5,s8,s9,s1 2	$P_{10,11}$ $P_{10,11}$
[3,14]	s1,s2,s3, s4,s6,s7, s8,s9,s10 ,s11	$P_{5,12}$	[9,10]	s1,s2,s3,s 4,s5,s6,s7 ,s9,s10,s1 1	$P_{8,12}$ $P_{8,12}$
[4,6]	s1,s2,s5, s6,s7,s9, s12		[10,12]	s1,s2,s6,s 7,s8	$P_{3,5}, P_{3,9},$ $P_{3,10},$ $P_{3,11},$ $P_{3,12}, P_{4,5},$ $P_{4,9}, P_{4,10},$ $P_{4,11},$ $P_{4,12},$ $P_{5,10},$ $P_{5,12},$ $P_{10,11},$ $P_{10,12}$
[4,7]	s1,s2,s4, s6,s7,s10 ,s11		[10,13]	s1,s2,s6,s 7,s8,s10	$P_{3,4},$ $P_{4,5}, P_{4,9},$ $P_{3,11},$ $P_{4,11},$ $P_{4,9}, P_{9,11}$ $P_{11,12}$

[4,8]	s1,s2,s6, s7,s10,s1	P <sub>3,4</sub> ,P <sub>4,9</sub>	P <sub>3,4</sub> , P <sub>5,9</sub>	[12,13]	s10	P <sub>3,4</sub> , P <sub>3,11</sub> , P <sub>4,9</sub> , P <sub>9,11</sub>	P <sub>3,4</sub> , P <sub>3,5</sub> , P <sub>3,9</sub> , P <sub>3,11</sub> , P <sub>5,12</sub> , P <sub>11,12</sub>
1				]			

### 4.7.3 Tennessee Eastman Case Study

Tennessee Eastman (TE) process, first introduced by Downs and Vogel<sup>106</sup>, has been widely used as a benchmark problem for process control, optimization, diagnosis and etc. Figure 4-6 shows the schematic of the TE process. An MPC controlled TE developed by Ricker and Lee<sup>107</sup> is considered in this work. A detailed description of the process with detailed qualitative SDG analysis of the process has been presented by Bhushan and Rengaswamy<sup>5</sup> and Maurya et al.<sup>102</sup> A total of 33 faults considered by Maurya et al.<sup>102</sup> are simulated in the process and the 40 variables are stored together for further analysis. Table 4.11 and Table 4.12 show lists of variables and faults considered in this work, respectively.

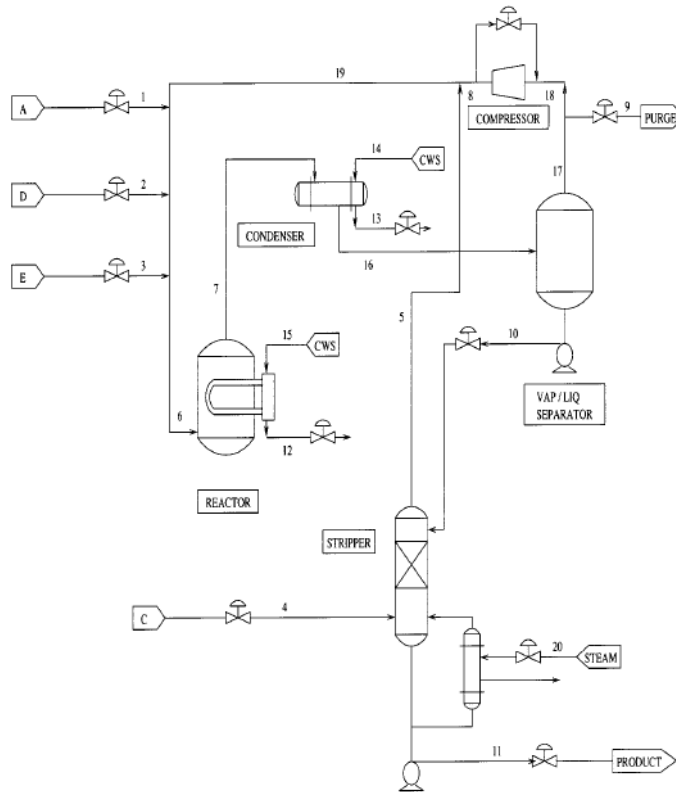


Figure 4-6. TE process flowsheet<sup>5</sup>

**Table 4.11. List of measured variables in TE process<sup>102</sup>**

Sensor no.	Measured variable	Description	Sensor no.	Measured variable	Description
s1	F7	Stream 7	s21	y <sub>D,6</sub>	D in stream 6
s2	F1	Stream 1	s22	y <sub>E,6</sub>	E in stream 6
s3	F2	Stream 2	s23	y <sub>F,6</sub>	F in stream 6
s4	F3	Stream 3	s24	y <sub>A,9</sub>	A in stream 9
s5	F4	Stream 4	s25	y <sub>B,9</sub>	B in stream 9
s6	F8	Stream 8	s26	y <sub>C,9</sub>	C in stream 9
s7	F9	Stream 9	s27	y <sub>D,9</sub>	D in stream 9
s8	F10	Stream 10	s28	y <sub>E,9</sub>	E in stream 9
s9	F11	Stream 11	s29	y <sub>F,9</sub>	F in stream 9
s10	T <sub>cr</sub>	Reactor temperature	s30	y <sub>G,9</sub>	G in stream 9
s11	T <sub>cs</sub>	Separator temperature	s31	y <sub>H,9</sub>	H in stream 9
s12	P <sub>r</sub>	Reactor pressure	s32	x <sub>G,11</sub>	G in stream 11
s13	VLR	Reactor liquid holdup	s33	x <sub>H,11</sub>	H in stream 11
s14	P <sub>s</sub>	Separator pressure	s34	P <sub>A,r</sub>	A in reactor
s15	VLS	Separator liquid holdup	s35	P <sub>C,r</sub>	C in reactor
s16	VLP	Product liquid holdup	s36	P <sub>D,r</sub>	D in reactor
s17	F6	Stream 6	s37	P <sub>E,r</sub>	E in reactor
s18	y <sub>A,6</sub>	A in stream 6	s38	VLR <sub>e</sub>	Error signal VLR <sub>r</sub>
s19	y <sub>B,6</sub>	B in stream 6	s39	VLS <sub>e</sub>	Error signal VLS <sub>s</sub>
s20	y <sub>C,6</sub>	C in stream 6	s40	VLP <sub>e</sub>	Error signal VLP <sub>p</sub>

**Table 4.12. List of simulated faults in TE process<sup>102</sup>**

Fault no.	Description	Fault no.	Description
1,9	F1 <sup>+</sup> , F1 <sup>-</sup>	17,26	VLR <sub>m</sub> <sup>set+</sup> , VLR <sub>m</sub> <sup>set-</sup>

2,10	F2 <sup>+</sup> , F2 <sup>-</sup>	18,27	VLR <sub>VP,bias</sub> <sup>+</sup> , VLR <sub>VP,bias</sub> <sup>-</sup>
3,11	F3 <sup>+</sup> , F3 <sup>-</sup>	19,28	VLS <sub>m,bias</sub> <sup>+</sup> , VLS <sub>m,bias</sub> <sup>-</sup>
4,12	F4 <sup>+</sup> , F4 <sup>-</sup>	20,29	VLS <sub>m</sub> <sup>set+</sup> , VLS <sub>m</sub> <sup>set-</sup>
5,13	F8 <sup>+</sup> , F8 <sup>-</sup>	21,30	VLS <sub>VP,bias</sub> <sup>+</sup> , VLS <sub>VP,bias</sub> <sup>-</sup>
6,14	F9 <sup>+</sup> , F9 <sup>-</sup>	22,31	VLp <sub>m,bias</sub> <sup>+</sup> , VLp <sub>m,bias</sub> <sup>-</sup>
7,15	T <sub>r</sub> <sup>+</sup> , T <sub>r</sub> <sup>-</sup>	23,32	VLp <sub>m</sub> <sup>set+</sup> , VLp <sub>m</sub> <sup>set-</sup>
8	C <sub>d</sub> <sup>-</sup>	24,33	VLp <sub>VP,bias</sub> <sup>+</sup> , VLp <sub>VP,bias</sub> <sup>-</sup>
16,25	VLR <sub>m,bias</sub> <sup>+</sup> , VLR <sub>m,bias</sub> <sup>-</sup>		

Table 4.13 shows the comparison of SDG, FES and MR for TE process. FES is preferred over SDG algorithm as it has lower sensor network cost and number of irresolvable fault sets. At low MR threshold level, MR resolves same number of faults with lower sensor network cost compared to FES. As can be seen in Table 4.13, FES and MR have the same sensors except that "s12" -pressure sensor- is not present in the network for MR algorithm. Therefore, the combination of both algorithms takes advantage of the MR algorithm. At medium MR threshold level, MR only shows slight improvement over SDG algorithm in terms of the sensor network cost, thus, the combination of both FES and MR takes advantage of the FES. At high MR threshold level, MR shows no improvement over SDG algorithm and the combination of both FES and MR takes advantage of the FES algorithm. For compactness, presenting large matrix of affected variables and faults resolution are avoided. Table 4.14 only presents fault resolution for the fault sets that are resolvable by FES and MR algorithms but not SDG.

**Table 4.13. Results of applying different algorithms to TE process**

<b>Algorithm(s)</b>	<b>MR</b>		<b>Sensor</b>	
	<b>value</b>	<b>Selected sensors</b>	<b>network</b>	<b>Irresolvable fault sets</b>
	<b>level</b>		<b>cost</b>	
SDG		s2,s3,s7,s8,s9,s10,s11,s15,s16	7.2	[16,26],[16,27],[17,18], [17,25],[18,25],[19,29], [20,28],[22,32],[23,31],

				[26,27]
FES		s2,s7,s8,s9,s11,s12,s15,s16	6.6	[16,26],[17,25],[19,29], [20,28],[22,32],[23,31]
	Low	s2,s7,s8,s9,s11,s15,s16	6.1	Same as FES
MR	Medium	s2,s3,s7,s8,s9,s11,s15,s16	7.1	Same as SDG
	High	s2,s3,s7,s8,s9,s10,s11,s15,s16	7.2	Same as SDG
	Low	s2,s7,s8,s9,s11,s15,s16	6.1	Same as FES
FES & MR	Medium	s2,s7,s8,s9,s11,s12,s15,s16	6.6	Same as FES
	High	s2,s7,s8,s9,s11,s12,s15,s16	6.6	Same as FES

**Table 4.14. Fault resolution by SDG, FES and MR in TE process**

Fault	Resolution sensors		Fault	Resolution sensors	
	Singles	Pairs		Single	Pairs
	FES	MR		FES	MR
[16,27]	P <sub>8,16</sub> ,P <sub>8,4</sub>	P <sub>8,13</sub> , P <sub>8,16</sub> ,	[18,25]	P <sub>8,16</sub> ,P <sub>8,4</sub>	P <sub>8,13</sub> , P <sub>8,16</sub> ,
		P <sub>9,13</sub> , P <sub>9,15</sub> ,			P <sub>9,13</sub> , P <sub>9,16</sub> ,
		P <sub>9,16</sub> , P <sub>11,13</sub> ,			P <sub>11,13</sub> ,P <sub>15,16</sub>
		0			0
[17,18]	P <sub>8,16</sub> ,P <sub>8,4</sub>	P <sub>11,16</sub> , P <sub>14,16</sub> ,	[26,27]	P <sub>8,16</sub> ,P <sub>8,4</sub>	P <sub>8,13</sub> , P <sub>8,16</sub> ,
		P <sub>15,17</sub> , P <sub>16,17</sub>			P <sub>9,13</sub> , P <sub>9,15</sub> ,
		0			P <sub>9,16</sub> , P <sub>11,13</sub> ,
		P <sub>11,13</sub> , P <sub>15,16</sub>			P <sub>11,16</sub> , P <sub>14,16</sub> ,
					P <sub>15,17</sub> , P <sub>16,17</sub>

#### 4.7.4 SELEXOL Process Case Study

As a unit in integrated gasification combined cycle (IGCC), the acid gas removal unit is used for removing H<sub>2</sub>S and CO<sub>2</sub> contents of the syngas using SELEXOL solvent. The pressure-driven dynamic model SELEXOL process that is used in our work is developed in the work of Bhattacharyya et al.<sup>3</sup>, where Figure 4-7 shows the configuration of the SELEXOL process used in their study. The entire model has 24597 variables.

However, considering all the variables makes the FES and MR algorithms intractable. Therefore, only variables that respond to DG (or SDG) algorithms are taken to account since the rest of the variables will not have any effect in FES and MR. After removing such variables, 542 variables are left for performing the algorithms. In order to save space, showing the lists of all measured variables and variables that respond to each fault are avoided and only the key variables are shown in Table 4.15. Table 4.16 shows the list of faults considered in the SELEXOL process.

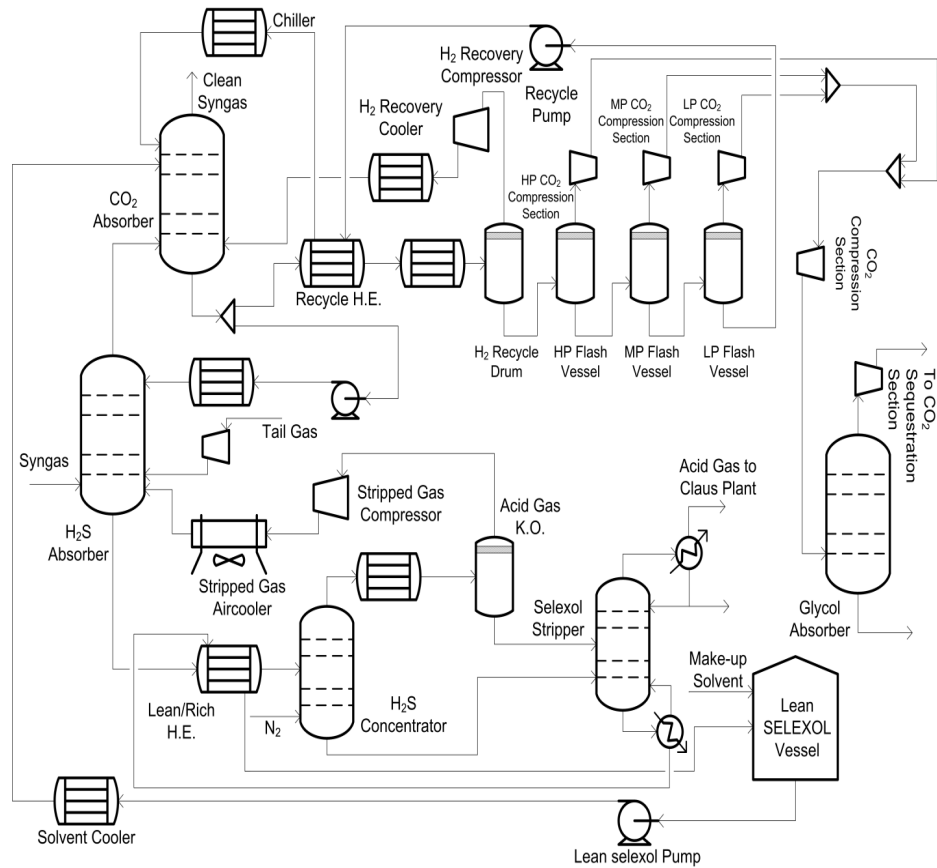


**Figure 4-7. Schematic of the SELEXOL process<sup>3</sup>**

Table 4.17 shows the comparison of different algorithms for SELEXOL process. Although all faults are resolvable by all algorithms, there is a slight improvement in sensor network cost by applying FES and MR compared to SDG. All algorithms suggest that for resolving all faults, flow and concentration sensors are mainly required. FES algorithm uses a temperature sensor less than SDG although only sensor s1 is the same in both algorithms. Therefore, the sensor network cost is reduced. At low and medium MR threshold level, less temperature sensors are selected and the sensor network cost is reduced

compared to FES and the combination of FES and MR takes advantage of the results of MR. At high MR threshold level there is no improvement from SDG and the combination of FES and MR takes advantage of results of FES.

**Table 4.15. List of measured variables in SELEXOL process**

<b>Sensor no.</b>	<b>Sensor type</b>	<b>Location</b>
s1	Composition (N <sub>2</sub> )	7 <sup>th</sup> tray of SELEXOL stripper
s2	Composition (NH <sub>3</sub> )	10 <sup>th</sup> tray of SELEXOL stripper
s3	Temperature	Pure SELEXOL stream from SELEXOL stripper
s4	Temperature	10 <sup>th</sup> tray of CO <sub>2</sub> absorber
s5	Temperature	1 <sup>st</sup> stage compression of LP CO <sub>2</sub>
s6	Flow rate	CO <sub>2</sub> stream top of flash vessel at MP
s7	Flow rate	Make-up SELEXOL stream
s8	Composition (H <sub>2</sub> S)	10 <sup>th</sup> tray of SELEXOL stripper
s9	Temperature	6 <sup>th</sup> tray of H <sub>2</sub> S concentrator
s10	Temperature	6 <sup>th</sup> tray of SELEXOL stripper
s11	Flow rate	CO <sub>2</sub> stream from LP flash vessel to 1 <sup>st</sup> stage compressor
s12	Composition (H <sub>2</sub> S)	5 <sup>th</sup> tray of CO <sub>2</sub> absorber
s13	Flow rate	CO <sub>2</sub> stream from HP flash vessel to mix with MP stream
s14	Composition (COS)	4 <sup>th</sup> tray of H <sub>2</sub> S concentrator
s15	Temperature	7 <sup>th</sup> tray of CO <sub>2</sub> absorber
s16	Flow rate	CO <sub>2</sub> stream from MP flash vessel to mix with LP stream
s17	Composition (SELEXOL)	8 <sup>th</sup> tray of SELEXOL stripper
s18	Composition (H <sub>2</sub> S)	4 <sup>th</sup> tray of CO <sub>2</sub> absorber

s19	Composition (NH <sub>3</sub> )	11 <sup>th</sup> tray of SELEXOL stripper
s20	Composition (H <sub>2</sub> S)	Bottom stream of H <sub>2</sub> S absorber fed to concentrator
s21	Temperature	Circulating SELEXOL stream from tank
s22	Composition (H <sub>2</sub> S)	8 <sup>th</sup> tray of SELEXOL stripper
s23	Composition (NH <sub>3</sub> )	9 <sup>th</sup> tray of SELEXOL stripper
s24	Temperature	SELEXOL mixing tank temperature
s25	Flow rate	CO <sub>2</sub> stream from HP flash vessel to mix with MP stream

---

**Table 4.16. List of simulated faults in SELEXOL process**

Fault no.	Fault symbol	Description
1	F1	Reduction in area of 13 <sup>th</sup> tray of CO <sub>2</sub> absorber by 15%
2	F2	Reduction in area of bottom (15 <sup>th</sup> ) tray of CO <sub>2</sub> absorber by 15%
3	F3	Reduction in area of 23 <sup>rd</sup> tray of H <sub>2</sub> S absorber by 15%
4	F4	Reduction in area of bottom (26 <sup>th</sup> ) tray of H <sub>2</sub> S absorber by 15%
5	F5	Reduction in area of 4 <sup>th</sup> tray of H <sub>2</sub> S concentrator by 15%
6	F6	Reduction in area of bottom (6 <sup>th</sup> ) tray of H <sub>2</sub> S concentrator by 15%
7	F7	Reduction in overall heat transfer coefficient of Lean/Rich H.E. by 15%
8	F8	1% leakage in the H <sub>2</sub> recovery compressor suction line
9	F9	1% vapor leakage in H <sub>2</sub> recovery flash drum
10	F10	1% vapor leakage in CO <sub>2</sub> high pressure flash drum
11	F11	1% vapor leakage in CO <sub>2</sub> low pressure flash drum
12	F12	1% vapor leakage in CO <sub>2</sub> medium pressure flash drum
13	F13	Reduction in area of 8 <sup>th</sup> tray of SELEXOL stripper by 15%
14	F14	Reduction in area of bottom (11 <sup>th</sup> ) tray of SELEXOL stripper by 15%

---

**Table 4.17. Results of applying different algorithms to SELEXOL process**

Algorithm(s)	MR value level	Selected sensors	Sensor	Irresolvable fault
			network cost	sets
SDG		s1,s2,s3,s4,s5,s6,s7	22.3	[ ]
FES		s1,s7,s8,s9,s10,s11	22.2	[ ]
MR	Low	s1,s7,s12,s13	22	[ ]
	Medium	s7,s8,s14,s15,s16	22.1	[ ]
	High	s1,s6,s7,s10,s15,s16,s1 7	22.3	[ ]
FES & MR	Low	s7,s11,s18,s19	22	[ ]
	Medium	s7,s8,s11,s20,s21	22.1	[ ]
	High	s7,s10,s22,s23,s24,s25	22.2	[ ]

#### 4.7.5 Combined Cycle Case Study

##### 4.7.5.1 Fault Simulation

The faults simulated in the combined cycle island include leakage at several locations, fouling within a few heat exchangers and an increased loss of heat through the combustor. Since the turbines itself are highly advanced and consist of several inbuilt sensors that detect and report any deviation from operation immediately, faults in these units have not been simulated. The leakage faults are mainly considered for the heat exchangers where high pressure differences exist between the shell and tube sides. Fouling is a concern within the heat exchangers as well. These faults are modeled similar to the methods mentioned earlier for the SELEXOL unit. The GT combustor has insulation to prevent heat loss to the environment. However, the insulation might get damaged in the course of operation and this can be modeled by increasing the heat loss in the GT combustor block.

The combined cycle section was segregated from the plant wide model developed in the works of Bhattacharyya et al.<sup>3</sup> The faults to be simulated in the combined cycle unit were identified. The faults that were selected and implemented are shown below. With the

exception of Fault E, all faults are simulated with a ramp function of 1 hour duration initiated after half an hour of simulation.

A. Leakage from the high pressure steam flash vessel

Steam at very high temperature and pressure is produced in a steam generator unit using the heat from hot flue gas. The steam produced is then sent to the high pressure steam turbine. A leakage in the high pressure steam generator can cause mixing of the steam with the flue gas which could build up in the steam cycle.

B. Leakage within a HE between syngas and steam streams

A leakage fault can occur in the heat exchanger that is used to heat in the hydrogen rich syngas from the SELEXOL plant before being sent to the combustor. The steam is at higher pressure and a rupture in the tube can result in steam entering the gas cycle. This can negatively impact the combustion process and the power generated in the gas turbines.

C. Leakage within a condenser between steam and water streams

Usually a composition sensor placed at the one of the streams exiting the HE would be able to detect any leakage taking place within the HE. However, if the heat transfer involves two streams of the same material, a leak may become difficult to detect. A leak fault is simulated in the heat exchanger that uses cooling water to cool steam.

D. Fouling simulated as loss of area within HE

A fouling fault is simulated in the heat exchanger used to cool the flue gas from the combustor using steam. The combustor flue gas can have particulate matter entrained from the N<sub>2</sub> stream that can deposit on the walls of the HE. This fault is simulated by decreasing the surface area of the HE.

E. Increase in heat loss from the combustor

The combustor operates at high temperature and has insulation to limit the heat loss to the environment. However, the insulation may get damaged in course of operation. This fault is modeled by introducing a step change in the heat loss from the GT combustor block after half an hour of simulation time.

F. Leakage within a HE between combusted syngas and steam stream.

A leakage in an IP steam generator HE is simulated where heat from the flue gas at almost atmospheric pressure is used to generate steam. It is desired to observe if a sensor can be found to differentiate faults in heat exchangers operating at different pressures.

#### G. Fouling simulated as loss of area within HE

This fault is simulated in the same HE as Fault B. In the SELEXOL process, there can be some foaming or formation of undesirable chemicals on the trays of the absorbers. These materials can be carried by the syngas and can be deposited on the heat exchanger surfaces thereby reducing the surface area for heat exchange.

#### 4.7.5.2 Sensor Placement Results

The faults considered in the combined cycle power plant are simulated at three severity levels as shown in Table 4.18.

**Table 4.18. Faults at different severity level simulated in the combined cycle model**

Fault type	Fault #	Fault sim.	Duration	Severity
A	1-3	Ramp	1 hour	0.5%, 1%, 2% leak valve opening
B	4-6	Ramp	1 hour	0.1%, 0.2%, 0.4% leak valve opening
C	7-9	Ramp	1 hour	5%, 10%, 20% leak valve opening
D	10-12	Ramp	1 hour	80%, 90%, 95% area available
E	13-15	Step	-	90%, 95%, 98% of original heat loss
F	16-18	Ramp	1 hour	0.05%, 0.2%, 0.5% of leak valve opening
G	19-21	Ramp	1 hour	85%, 90%, 95% of area available

Faults at three severity levels, namely high, medium and low level, are considered. It is expected that the effect of the high severity level should be captured by the algorithm easily. The low level faults might be the most difficult to be resolved by the algorithm. It was desired to observe what level of fault severity can be detected by the sensor network and the minimum number of sensors required to detect them. 736 variables pre-selected as

candidate sensor placement variables and their historical data are recorded for the sensor placement algorithm. These variables include temperature, pressure, flow, concentration, power and level. Table 4.2 shows the weight and threshold value for each type of variables used in the algorithm.

Table 4.19 and Table 4.20 show the results of the different algorithms for fault resolution of combined cycle. The location and number of sensors selected by the FES differ from that of the SDG algorithm in Table 4.19. The cost of the final sensor network in the FES is lower, although it can be seen that both algorithms are not able to differentiate between two set of the faults.

Fault 8 and 9 are two severities of a leak in a heat exchanger resulting in the mixing of steam and water. Although this fault is expected to be difficult to detect and resolve, the two algorithms are able to resolve this fault at a lower fault severity (fault 7). Faults 14 and 15 may be difficult to resolve between because the difference in severity of these faults is relatively small.

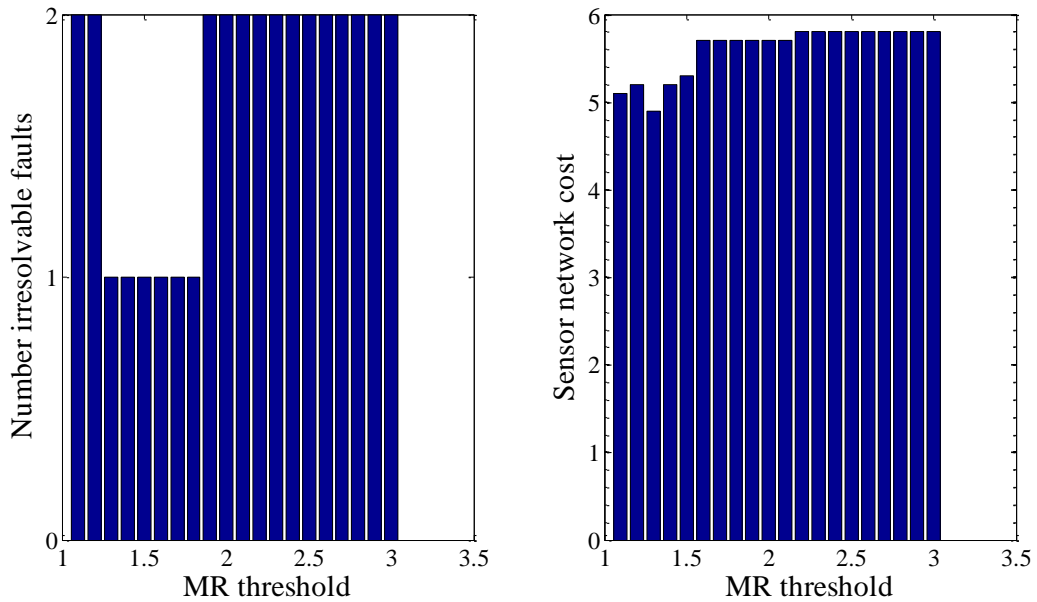
**Table 4.19. SDG and FES algorithms results**

Algorithm	# Sensors	Sensor network cost	Unresolvable fault sets
SDG	13	5.8	[8,9] [14,15]
FES	12	4.8	[8,9] [14,15]

Table 4.20 shows that in the range of 1.3 - 1.8 of MR threshold value, the MR algorithm can resolve between faults [8,9]. However, the sensor network cost is sensitive to the MR threshold value in this range as can be seen in Figure 4-8. Figure 4-8 shows the number of unresolvable faults and the corresponding sensor network cost for different MR threshold values. It can be seen that for low and medium MR range, the cost of the sensor network selected is lower than that of the high MR range.

**Table 4.20. MR algorithm results**

Algorithm	MR threshold value	Unresolvable fault sets
MR	1.1 - 1.2	[8,9] [14,15]
	1.3 - 1.8	[14,15]
	1.9 - 3	[8,9] [14,15]

**Figure 4-8. Number of irresolvable faults (left) and the corresponding sensor network cost (right) at different MR threshold values**

## 4.8 Conclusion

The case studies clearly bring out the value of every piece of information that is used in sensor placement. Further, because of this, it is also easy to interpret and explain the results to the operator. If a pseudo-sensor corresponding to a MR pair helps in resolution then a corresponding explanation such as, for example, “Temp T-101 has increased by a large amount, whereas concentration C-502 shows only moderate increase indicative of F15” fault can be provided. Further, it is possible to use these results directly in the development of a diagnostic approach for each of these case studies. Finally, the

optimization algorithms are solved, even at a flow-sheet level, in a very short time. It will be extremely difficult to solve problems at this scale if one were to take recourse to a full-scale optimization problem that incorporates the nonlinear dynamic first-principles model within the optimizer. A more computationally efficient approach might be to add the detailed first principles model as the next level of information to address only the faults that are left unresolvable after MR and FES information have been used in identifying the sensor placements. Elegant computational approaches to realize this will be one avenue for future work.

## Chapter 5

### Network Decomposition

#### 5.1 Introduction

As mentioned in previous chapter, using the qualitative approach in presence of numerical solution reduces the complexity of optimization problem into solving an integer linear programming problem. However, complexity is not limited to just solving non-linear problems and can be found in linear problems as well (particularly in combinatorial problems), especially as the size of the system increases. One of the main issues is the memory limitations of computers for storage and computations. A computing machine is not only limited by the amount of information it can store for a particular problem, for a simple example, the augmented FES-MR matrix or constraint matrix, it is also limited by the amount of memory available for computations, resulting in slower computations due to low availability of memory. Therefore, diagraph-based causal models are vulnerable to such complexities though the problem is defined as a linear optimization problem. It is of interest to see how the computational complexities of diagraph-based fault detection can be reduced even at an abstract level.

Generally, in graph theory, a system can be depicted by a set of vertices and edges that connect the vertices. Vertices can represent the system variables or any aspect of a system, for example sources and clients in a wireless network or variables in diagraph-based fault detection, while the edges represent the relationship between the vertices. Mathematical efforts in graph theory have been made to reduce the computational complexities by reducing the problem into smaller components, namely “graph partitioning” technique. In graph partitioning, one tries to decompose the graph into smaller sub-systems with specific properties. However, none of the existing works in graph partitioning consider fault detection as an objective of partitioning. Almost all of the works in the area of graph partitioning focus solely on minimizing the number of edges running between the sub-systems. However, it is not intuitive for one to think that the same reasoning holds while considering fault detection and diagnosis. Although, it is intuitive

that the solution to the decomposed graph can be sub-optimal compared to the solution to the original graph, in some cases this compromise might be acceptable due to the complexity reduction achieved by the decomposition. In the best case, at least a solution can be obtained for a large graph through graph decomposition. Therefore, progress is needed in considering the fault detection within the graph partitioning framework.

The graph partitioning problem is generally an NP-hard (non-deterministic polynomial-time hard) problem. In computational complexity theory, NP-hard problems, although not proven, are a class of problems whose solution cannot be found in polynomial time and are obtained by heuristic algorithms. Developing a graph partitioning algorithm requires an enormous amount of effort in order to come up with a suitable algorithm that fits the fault detection context. A breakthrough for such pure heuristic analysis is to initially gain some knowledge regarding the impact of graph partitioning on different aspects of fault detection. Therefore, in this work, we perform a sensitivity analysis of different parameters of a system and study the trade-off between the fault detection optimality and computation speed.

Different systems have different properties with different possible decompositions, thus, the study includes a Monte Carlo simulation of pool of random systems with similar properties and different decomposition. The random systems are constructed by a bottom-up design. In this approach, initially random sub-systems are generated; and the overall system is obtained by cross-connecting the sub-systems. Certain constraints on the overall system, such as total connectivity, are handled at the sub-system level, which ensures the constraint satisfaction at overall level.

For simplicity, each random system represents a directed graph (DG). More complex systems can be achieved if the edges not only represent the direction but are also associated with real or integer quantities. Directed graph is the most widely used causal model, a popular technique in model-based analysis for fault detection. For simplicity, in this work, fault detection is performed by only considering the directed graph (DG) algorithm. In a DG formulation for a process where vertices represent the variables and edges represent the relation between the variables, one tries to find a network of sensors with minimum cost that satisfies fault detection constraints. Constraint in the minimization problem are

related to detecting all the faults and identifying the exact fault from other faults (isolation). This approach is named “sensor placement”. Sensor placement is formulated as a binary integer linear programming problem constrained to fault detection and resolution. A thorough study of DG algorithm can be found in previous sections. It is worth mentioning that a major part of the DG analysis is to find the initial response table (IRT). The initial response table is a matrix of binary values (for DG analysis, while this can be different for other algorithms) that represents from each vertex what other vertices can be reached directly or indirectly through other vertices. Using the IRT, optimization constraints related to fault detection and resolution can be obtained. Therefore, IRT is critical to fault detection and must be consistent with the system of interest. While generating a random system, IRT is obtained using the DG matrix that represents the system.

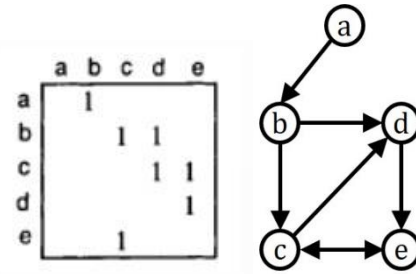
### 5.1.1 Method

#### 5.1.1.1 Assumptions

As mentioned before, the random system generation is performed in a bottom-up process where first sub-systems are generated and the overall system is obtained by cross-connecting the sub-systems. Generating random systems for fault detection requires some basic assumptions that must be met by the random systems.

- Faults in the system are presented by independent nodes. Fault nodes are the only nodes that have no inward edges.
- All the nodes must be connected to at least one other node.
- There is no self-connection in the system.

A mathematical representation of a directed graph is by use of node adjacency matrix. Rows and columns of node adjacency matrix represent the vertices and each  $(i,j)^{\text{th}}$  entry is assigned “1” if there is a directed edge; and “0” otherwise. Figure 5-1 shows an example of the node adjacency matrix for the corresponding DG.

**Figure 5-1. Representation of adjacency matrix**

Generating random systems requires some parameters to be provided in advance. These parameters include:

- a. Number of sub-systems ( $N_s$ ): A scalar that represent the total number of sub-systems that are present in the system.
- b. Number of nodes ( $N_n$ ): A  $1 \times N_s$  vector where each array in the vector represents the number of nodes in each sub-system.
- c. Number of edges ( $N_e$ ): A  $1 \times N_s$  vector where each array in the vector represents the number of edges in each sub-system.
- d. Number of cross-connection edges ( $N_{ce}$ ): A  $1 \times N_s(N_s-1)/2$  vector of values where each array represents the number of edges between each pair of sub-systems.
- e. Number of faults ( $N_f$ ): A  $1 \times N_s$  vector where each array in the vector represents the number of faults in each sub-system.
- f. Number of fault edges ( $N_{fe}$ ): A  $1 \times N_f$  vector where each array in the vector represents the total number of output edges of the faults in each sub-system.

It should be mentioned that all the parameters must be positive integers and must follow the mentioned assumptions, for example,  $N_{fe} \geq N_f$ , otherwise, there will be at least a fault node without any edges.

### 5.1.1.2 Algorithm

In order to explain the algorithm, first, the logical reachability matrix must be defined. Each  $(i,j)^{\text{th}}$  entry in the adjacency matrix shows the number of possible ways to go from  $i^{\text{th}}$  node to the  $j^{\text{th}}$  node with distance of one. Considering the squared matrix of adjacency matrix, each  $(i,j)^{\text{th}}$  entry in the squared adjacency matrix shows the number of possible ways to go from  $i^{\text{th}}$  node to the  $j^{\text{th}}$  node with distance of two; and so on for higher

powers of the adjacency matrix. The reachability matrix is defined as the sum of all powers of the adjacency matrix up to  $N_n^{th}$  power. Each array in this special matrix shows the total number of ways to go from  $i^{th}$  to  $j^{th}$  node with any distance. Since we are only interested if there is any connection between two nodes by any distance, thus, the reachability matrix is transformed into a logical form where the non-zero arrays in the reachability matrix is assigned “1”. It should be noted that self-connections, if any, must be turned to zero for further analysis.

The algorithm consists of these steps for each sub-system:

1. Initialize the adjacency matrix
2. Randomly pick  $N_e$  arrays in adjacency matrix and assign “1” (Self-connections excluded)
3. Check if constraints are satisfied
  - a. All nodes are connected: Sum of each row of logical reachability matrix is equal to  $N_n-1$
  - b. All nodes have at least one input edge: Sum of each column of adjacency matrix is greater or equal to one
4. Randomly connect the faults
  - a. For each fault, the number of output edges are determined randomly
  - b. For each output edge of each fault, a node without input from the same fault is randomly determined

Steps 2 and 3 are repeated until a system that satisfies the constraints is achieved. After performing the algorithm for each sub-system, sub-systems are randomly cross-connected as per  $N_{ce}$  number without overlapping edges. For each cross-connection, one node in each corresponding sub-systems are randomly chosen and the direction of the edge is chosen as random.

The main drawback of this algorithm is that finding appropriate sub-system that satisfies the constraints gets harder and harder for larger number of nodes and lower number of edges. Therefore, a second algorithm is introduced when a system is not found within a reasonable number of iterations. The algorithm is as follows:

1. Randomly choose two nodes from the pool of available nodes and connect them.  
Mark the node at the end of the directed edge as current node and place it in the pool of visited nodes
2. Define probability parameter  $\beta$  for each sub-system:
  - a. With chance of  $\beta$ , connect the current node to a randomly chosen node from the pool of available nodes. Mark the chosen node as current node and place it in the pool of visited nodes
  - b. Otherwise, randomly choose a node from pool of visited nodes and connect it to a randomly chosen node from the pool of available nodes and place the second node in the pool of visited nodes

It should be noted that step 2 is performed until the  $N_e$  number of connections are made. Despite that, the second algorithm is faster and another advantage of it lies in the choice of value for parameter  $\beta$ . Higher values of  $\beta$  result in systems analogous to recycle process systems while lower values result in systems analogous to spanning tree systems.

#### **5.1.1.3 Initial Response Table Calculation**

After generating the random sub-systems with fault nodes and cross-connecting the sub-systems, the overall system is achieved. The total DG matrix that includes the fault nodes for the overall system can be obtained by augmenting the fault DG matrices with augmented system DG matrices. As shown below, the total DG matrix contains four blocks. The zero blocks are due to the assumptions that faults have no input edges. The FDG block is made by augmenting the fault adjacency matrices of all sub-systems. Similarly, DG block is made by augmenting the adjacency matrix of all sub-system DGs. After calculating the logical reachability matrix of the total DG matrix, the FDG block of the logical reachability matrix will represent the IRT.

$$\begin{matrix} F & X \\ F \begin{bmatrix} [0] & \text{FDG} \end{bmatrix} \\ X \begin{bmatrix} [0] & \text{DG} \end{bmatrix} \end{matrix}$$

### 5.1.2 Fault Detection in Decomposed System

While performing the fault detection for each sub-system, one can either ignore that there are any faults outside the sub-system (in other sub-systems) and assume they cannot affect the sub-system through the inward cross-connection, or, we can find a simple way to bring those into consideration and mitigate their effects. Clearly, the former will cause some information loss, while the latter will add more information to the system and may improve the fault detection. The latter can be realized by simply assuming all the inward cross-connections as a pseudo-fault inside the sub-system. This way all the inward cross-connections are assumed to be coming from a single node marked as pseudo-fault. While one may argue that each inward cross-connection can act as a single pseudo-fault and add more information to the system, the drawback to this assumption is that a large number of pseudo-faults can further complicate fault detection and may compromise the speed for little to no additional information. Therefore, the approach taken in this work is based on assuming all the inward cross-connections from other sub-systems as coming from a single pseudo-fault. The pseudo-fault is then added to the system as a node and considered in the fault detection. Figure 5-2 shows an example of how the pseudo-fault is considered in a sub-system. In this example, red nodes indicate the faults while black nodes indicate the graph nodes. The effect of faults F1 and F2 in Sub-system 1 are passed to Sub-system 2 through the dashed edges, which represent the cross-connection between the sub-systems. The cross-connections in Figure 5-2 are then replaced by a pseudo-fault (yellow node) and the pseudo-fault is connected to the same nodes, marked as SP1 and SP2 in Sub-system 2.

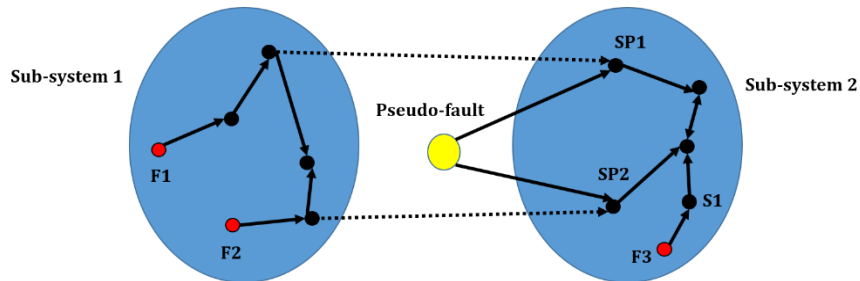


**Figure 5-2. Pseudo-fault representation for two sub-systems.**

The main issues that arise in the pseudo-fault approach are the existence of multiple solutions in fault detection and the information loss due to decomposition. As an example, consider performing the fault detection for Sub-system 2 where we want to resolve between fault F3 and the pseudo-fault. The multiple solutions which are available for fault resolution are S1, SP1 and SP2 nodes. Assume the cost of placing sensors on all the nodes are the same, thus, placing a sensor on each of the nodes can be the solution to our sensor placement problem. However, due to information loss by decomposition, each solution can have different impact on fault detection of the overall system. If S1 is picked as the solution and implemented on the overall system, fault pairs (F3,F1) and (F3,F2) can be resolved. If SP1 is picked as the solution and implemented on the overall system, although fault pair (F3,F1) can be resolved, fault pair (F3,F2) cannot be resolved. Similarly, if SP2 is picked as the solution and implemented on the overall system, although fault pair (F3,F2) can be resolved, fault pair (F3,F1) cannot be resolved. Therefore, since no extra information is available about the overall system, multiple solutions with different overall fault resolutions may exist. One way to overcome this issue is to pick the nodes affected by the faults but not the pseudo fault, for example, S1 in Figure 5-2. This ensures total resolution from the faults out of the sub-system.

In the original fault detection method, fault resolution is based on the set difference of the nodes affected by the fault that are being resolved. If  $A$  is a set of nodes affected by fault  $f_1$  and  $B$  is set of nodes affected by  $f_2$ , then, set difference  $S$  is defined as:  $S = A \cup B - A \cap B$ . In the new approach, when resolving between a fault (as set  $A$ ) and the pseudo-fault (as set  $B$ ), the set difference is replaced by  $S_{new} = A - A \cap B$ . This ensures that the fault is resolved from all other faults outside the sub-system. However, there may be cases when resolving between a fault and the pseudo-fault where  $S_{new} = \emptyset$  and  $S \neq \emptyset$ . In this case,  $S$  contains at least a solution and can be used over  $S_{new}$ .

## 5.2 Results

Here, we study the effect of different system and decomposition parameters on the fault detection and computation speed. The results in this section are based on a Monte Carlo simulation analysis where a pool of systems are considered and the presented results are either the probability of occurring (fault detection results) or the mean average over the

pool of systems (computation speed results). The sensitivity analysis of system parameters include the effect of number of nodes, sub-systems, and cross-connections on the computation speed, fault resolution capability and sensor network cost. For computation speed, the average computation time for fault detection of overall system ( $T_O$ ) is compared with the average sum of computation times of sub-systems ( $T_D$ ). For comparison, the average percent reduction in computation time by decomposition ( $T_R$ ) is also presented ( $T_R = (1-T_D/T_O) \times 100$ ). For fault resolution capability, the solutions obtained from sub-systems are augmented to form the decomposition solution. The decomposition solution is implemented in the overall system to check the resolution, which is how many of the faults cannot be resolved using the decomposition solution. The optimal resolution is always achieved by considering the overall system and counting the number of unresolvable faults. For comparison, the percentage of the systems in the pool where their decomposition have resolution greater than that of optimal resolution is presented ( $P_F$ ). For sensor network cost, the cost of sensor networks for all sub-systems are summed up and compared with the sensor network cost of the overall system. For comparison, the percentage of the systems in the pool that have sensor network cost different than the cost of sensor network of their overall system is presented ( $P_C$ ). It should be noted that cost of placing sensor on all nodes are assumed equal with the value of 1.

Table 5.1 shows the sensitivity analysis of number of sub-systems. In this analysis, total number of nodes, edges, fault nodes, fault edges and cross-connections are fixed for the overall systems at 3600,  $1.2 \times 3600$ , 60, 60 and 60, respectively. In all of the subsequent studies, the numbers of edges are chosen to be 20% more than the number of nodes in order to have feedback/recycle edges similar to process systems; and the numbers of fault edges are chosen equal to the number of faults in order to ensure each fault has single outward edge. Also, the values for number of nodes, edges, fault, fault edges and cross-connections in all subsequent tables represent the parameters of each sub-system in an overall system. The random systems in each pool are generated with a specified number of sub-systems. In Table 5.1, for each system in each pool, numbers of sub-systems are fixed and the mentioned fixed parameters are divided equally among the sub-systems. For example in Table 5.1, pool 1 has systems where each system consists of 2 sub-systems, where each sub-system has 1800, 2160, 30, 30 and 30 number of nodes, edges, faults, fault edges and

cross-connections, respectively. Only for pool 6, the number of cross-connections cannot be divided equally among the sub-systems, therefore, number of cross-connections between each sub-system are chosen randomly for each sub-system with summation equal to 60. It should be noted that it is assumed that each pair of sub-systems has at least 1 cross-connection. In order to be consistent, the maximum number of cross-connections is 16 for Pool 6.

**Table 5.1. Sensitivity analysis of number of sub-systems**

<b>Parameters</b>	<b>Pool 1</b>	<b>Pool 2</b>	<b>Pool 3</b>	<b>Pool 4</b>	<b>Pool 5</b>	<b>Pool 6</b>
Sub-Systems	2	3	4	5	6	10
Nodes	1800	1200	900	720	600	360
Edges	2160	1440	1080	864	720	432
Faults	30	20	15	12	10	6
Fault Edges	30	20	15	12	10	6
Cross-Connections	30	20	10	6	4	1-16
$T_O$ (s)	1.6587	1.6587	1.6587	1.6587	1.6587	1.6587
$T_D$ (s)	0.4372	0.2404	0.1818	0.1439	0.1186	0.0819
$T_R$	74%	86%	89%	91%	93%	95%
$P_F$	0%	0%	<1%	2%	2%	3%
$P_C$	44%	59%	73%	85%	90%	100%

In Table 5.1, the computation time of the overall system,  $T_O$ , is averaged over all 6 pools as all the overall systems have similar properties. As the number of sub-systems increase, the reduction in computation time increases, meaning that it takes much less time to perform fault detection for all the sub-systems than performing on the overall system. This can be seen as the average of sum of sub-systems' computation time,  $T_D$ , reduces due to fault detection of smaller systems. One of the major reasons behind the computation time reduction is the amount of time required to perform fault resolution (set difference) in

a system. For the overall system, the number of computations required for fault resolution is equal to the number of non-repetitive fault pairs in the overall system, which is  $60 \times 59 / 2 = 1770$ . If the system is decomposed to 10 sub-systems, the total number of computations required for fault resolution is  $10 \times 6 \times 5 / 2 = 150$ . This means that the total number of computations, which is directly related to the computation time, has been reduced by approximately 92%. As the number of sub-systems increase, the probability of systems with more faults being unresolved is slightly increasing due to the reason that the probability of presence of nodes that can resolve those faults in the corresponding sub-system gets lower as the number of sub-systems increase. Moreover, as the number of sub-systems increase, resolving the faults in sub-systems require more number of sensors to be placed due to the reason that sensors which could resolve multiple faults, now are not available to use in different sub-systems. Therefore, there is high probability that decomposition results in higher sensor network cost. In summary, choosing the appropriate number of sub-systems for decomposition is a trade-off between computation speed and fault resolution and sensor network cost. Increasing the number of sub-systems reduces the computation time significantly while it may result in lower fault resolution and different sensor network cost.

Table 5.2 shows the sensitivity analysis of number of nodes and fault nodes. The number of sub-systems is fixed at 4 in this study. In pools 1-3 in Table 5.2, the number of nodes increase from 10 to 1000 while the number of faults are fixed at 4. Although the computation time for both overall and decomposed systems increases by increasing the number of nodes, the amount of reduction in computation time is actually increasing, meaning that decomposition efficiently reduces the computation time as the size of the system increases. Moreover, while the numbers of faults are fixed, as the number of nodes increase, more number of sensors are available for fault resolution, therefore, the probability of systems with more number of unresolved faults due to decomposition is reducing. Similarly, the probability of systems with different sensor network cost increases as the number of nodes increase due to more availability of sensors for fault resolution. However, the sensor network cost maybe greater or less than in the case of overall system design depending on the fault resolution. For example, fault resolution maybe achieved by using more number of sensors while if some faults cannot be resolved in the sub-systems,

therefore, less number of sensors will be involved in the fault resolution, thus, resulting in less sensor network cost. In pools 4-6, the number of nodes is fixed at 1000 while the number of faults increases from 40 to 80. Pools 4 and 5 show that at higher number of faults compared to pool 3, computation time reductions are significant, however, the impact of increasing the number of fault nodes on both overall and decomposed systems' computation time is significantly larger than the effect of increasing the number of nodes. This effect can also be explained by the number of computations as in the study of number of sub-systems. The probability of systems with higher number of unresolved faults increases at higher number of faults. However, compared to pool 3, we can see that this probability has remained approximately the same for larger number of faults. An explanation is that since the number of faults is large, many faults remain unresolved in the overall system and system decomposition has little effect on the fault resolution. For the same reason, the probability of systems with different sensor network cost for pools 4 and 5 are lower compared to the pool 3. For pool 6, the number of faults are too high that exceeds the computation memory of the computer, while it is still possible to perform the fault detection on the decomposed system. Therefore, no comparison can be made for pool 6. This interesting result justifies the need for system decomposition for fault detection of large systems and large number of faults.

**Table 5.2. Sensitivity analysis of number of nodes and fault nodes**

<b>Parameters</b>	<b>Pool 1</b>	<b>Pool 2</b>	<b>Pool 3</b>	<b>Pool 4</b>	<b>Pool 5</b>	<b>Pool 6</b>
Sub-Systems	4	4	4	4	4	4
Nodes	10	100	1000	1000	1000	1000
Edges	12	120	1200	1200	1200	1200
Faults	4	4	4	40	50	80
Fault Edges	4	4	4	40	50	80
Cross-Connections	4	4	4	4	4	4
$T_O(s)$	0.0257	0.0349	0.1251	14.3853	26.4105	Out of memory
$T_D(s)$	0.0158	0.0182	0.0288	1.3469	2.6569	4.8287
$T_R$	37%	48%	77%	91%	90%	

P <sub>F</sub>	9%	3%	<1%	1%	1%
P <sub>C</sub>	100%	98%	97%	66%	63%

Table 5.3 shows the sensitivity analysis of number of cross-connections while other parameters remained the same. Although in a decomposed system an edge can either be inside a sub-system or between a pair of sub-systems, the following sensitivity analysis shows the effect of number of cross-connections, for example in a highly interconnected system, on computation time and fault detection when the system is decomposed. As seen in Table 5.3, the number of cross-connections has very little effect on the computation time reduction, although still the decomposition has resulted in significant time reduction of approximately 90%. The probability of systems with higher number of unresolved faults in the decomposed system is at a minimum when there is only one cross-connection between the sub-systems. As can be predicted, the less the interaction between the sub-systems, the more the probability of achieving optimal resolution with system decomposition. At higher number of cross-connections, although not highly probable, it is possible that the decomposition can cause some faults to be unresolved. Moreover, as the number of cross connections increase, the probability of system decomposition resulting in sensor network cost higher than the optimal cost gets higher. This is due to the reason that when a system is more interconnected, it is possible that a single sensor can resolve multiple faults. Therefore, decomposing systems with more connections can result in sensor network with higher cost for achieving the optimal resolution.

**Table 5.3. Sensitivity analysis of number of cross-connections**

Parameters	Pool 1	Pool 2	Pool 3	Pool 4	Pool 5	Pool 6
Sub-Systems	4	4	4	4	4	4
Nodes	1000	1000	1000	1000	1000	1000
Edges	1200	1200	1200	1200	1200	1200

Faults	40	40	40	40	40	40
Fault Edges	40	40	40	40	40	40
Cross-Connections	1	5	10	20	40	80
$T_O$ (s)	10.28	15.81	16.15	16.93	16.95	16.47
$T_D$ (s)	1.26	1.44	1.50	1.55	1.3317	1.59
$T_R$	88%	91%	91%	91%	92%	90%
$P_F$	0%	2%	3%	3%	2%	2%
$P_C$	70%	70%	84%	93%	99%	100%

---

### 5.3 Conclusion

The system decomposition for fault detection is promoted by a series of sensitivity analysis that promises computation time reduction while achieving, with a high probability, optimal resolution using the decomposed system. However, it is likely that the decomposed system will result in higher sensor network cost compared to the optimal cost. The optimal resolution and sensor network cost can be obtained by the fault detection of the original system before decomposition.

The system decomposition promises significant computation time reduction as the number of sub-systems and the system size, which includes number of nodes and fault nodes, increases. The larger the system, the more appealing the system decomposition is. It is more likely for system decomposition to achieve the optimal resolution as the size of the system increases, and when system decomposition has lower number of sub-systems and lower number of cross-connections. It is highly probable that system decomposition will result in higher sensor network cost while the probability is lower for larger systems, when the system is decomposed to lower number of sub-systems, and when sub-systems' interaction through cross-connections are lower.

An appropriate graph partitioning algorithm for fault detection must trade-off between the computation speed and sensor network cost. Minimizing the number of cross-connections promises higher chance of achieving optimal resolution while the number of sub-systems is a tradeoff between computation speed, fault resolution and sensor network cost. Maximizing the number of nodes in each sub-system ensures highest computation time reduction, which can be achieved by equally dividing the nodes in the sub-systems as much as possible. Also, when the number of fault nodes in each sub-system is less, computations will also be less, which again means equal number of fault nodes in each sub-system will be an appropriate choice.

## Chapter 6

### Component-Level Sensor Placement

#### 6.1 State Estimation Development

##### 6.1.1 Introduction

Differential-algebraic equation (DAE) systems often arise in modeling of physical and mechanical systems, such as robotics, chemical processes, electrical circuits and so on. DAE systems, which are also called descriptor systems, can be viewed as ordinary differential equations (ODEs) that are constrained by the algebraic equations. In general, both the differential and algebraic equations can be linear or nonlinear. Although the dynamic behavior is modeled by ODEs, the presence of algebraic constraints results in some complications while solving the DAE systems. State estimation of linear and nonlinear ODEs have been studied thoroughly in literature and several techniques are present for state estimation including but not limited to Kalman filter (KF), extended Kalman filter (EKF) Unscented Kalman filter (UKF), Ensemble Kalman filter(EnKF), particle filters and etc.<sup>108</sup> The Kalman filter is an estimator of linear stochastic ODEs where the term “stochastic” represents the presence of process and measurement noises. Kalman filter is optimal when the noise is assumed as Gaussian white noise. Although the Kalman filter is optimal for linear systems, an extension of KF is sub-optimal when applied to non-linear systems.<sup>109</sup> The idea of extended Kalman filter (EKF) is based on local linearization of the non-linear equations and application of the linear Kalman filter framework. At first glance, it seems that by converting the DAE to an implicit ODE, state estimation can be performed using the KF or EKF framework as it is done for implicit ODE systems. However, unlike ODE systems, there is a necessity for generation of consistent initial guesses that respect the algebraic constraints. Further, DAEs are characterized by the index of the system, which is the number of differentiations that are required to convert a DAE system into fully implicit ODEs. As a result, state estimation techniques for ODEs cannot be directly extended to DAE systems.<sup>110</sup>

The index of a DAE represents the difficulty in the numerical treatment of such systems. DAEs of index- zero and one are considered to be the easiest for numerical treatment compared to higher index systems. The systems considered in this work are all assumed to be index-1 DAEs.<sup>111</sup> A literature search indicates extensive work on applying KF to linear DAEs, see<sup>112-117</sup>, though there is very little work on implementation of EKF on non-linear DAEs.<sup>108,118</sup>

For applying EKF to DAE systems, Becerra et al.<sup>118</sup> proposed a modified EKF for DAE systems. In their approach, the DAE is converted to implicit ODE and the non-linear equations are linearized locally, then, the Kalman filter is performed at each sampling time while the error covariance matrix is updated for differential states. A disadvantage of this approach is that the effect of prior algebraic state estimates and measurements from algebraic states are ignored and updated algebraic state estimates are obtained by solving the algebraic equations after updated differential state estimates are computed.<sup>108</sup> Further, measurements of the algebraic states cannot be directly included in this framework. To address these disadvantages, in our previous work, an approach was proposed that takes into consideration the effect of prior algebraic states and accommodates the measurements from the algebraic states in the framework.<sup>108</sup>

One of the difficulties in state estimation of DAEs is that derivative of white noise may show up in state estimates. However, derivative of white noise is not well-defined.<sup>119</sup> For linear systems, researchers have proposed different approaches to address this problem. For instance, Campbell<sup>120</sup> suggested the use of band limited noise filter and in turn compromised the optimality of the Kalman filter. Schon et al.<sup>121</sup> explained the transformation of the DAE into a state space form and the conditions under which derivative of white noise in algebraic equations can be avoided in state-space form. Darouach et al.<sup>114</sup> avoided the presence of white noise derivative by decomposing the filtering problem into two subproblems: (i) computing the estimates and error covariance of differential states, and (ii) using them in computation of estimates and error covariance of algebraic states.

In almost all of the works that consider the EKF for non-linear DAEs, the algebraic equations are noise-free and the process noise is considered only in the differential

equations. The reason is that when differentiating the algebraic equations to convert the DAE to an implicit ODE, white noise will be differentiated, if present in the algebraic equations. Therefore, algebraic equations must be certain for differentiation to be meaningful. However, in practice, algebraic equations are not always exact and they might themselves be uncertain equations. This is particularly true when simplifying correlations are used in the modeling framework. Moreover, when extra information such as exact state equality constraints are available for the system, current EKF formulation cannot handle such information. Thus, EKF must be modified to include such constraints. In this work, we address these issues by proposing a modification to the EKF to handle constrained DAEs of index-1 with uncertainties in both differential and algebraic equations.

In the proposed work, the error covariance matrix is written as a 4-block matrix with separate square blocks for differential and algebraic variables, respectively. Since the DAE is of index-1, the algebraic equations are written in terms of the differential variables and the error covariance in the corresponding covariance matrix are updated by linear or non-linear transformation of the error covariance of the differential equations. This avoids the differentiation of algebraic equations and makes the filter practical.

### 6.1.2 State Estimation of DAE Systems

#### 6.1.2.1 Problem Formulation

Consider the following stochastic nonlinear discrete-time DAE system with discrete measurements sampled at intervals of  $\Delta t$

$$\begin{aligned} x_{k+1} &= x_k + \int_{k \Delta t}^{(k+1) \Delta t} f(x(t), z(t)) dt + \omega_{k+1} \\ g(x_{k+1}, z_{k+1}) &= 0 \\ y_{k+1} &= h(x_{k+1}, z_{k+1}) + v_{k+1} \\ \omega &\sim N(0, Q) \quad v \sim N(0, R) \end{aligned} \tag{6.1}$$

where  $x_{k+1} \in \mathbb{R}^{m \times 1}$  and  $z_{k+1} \in \mathbb{R}^{p \times 1}$  are the differential and algebraic states at interval  $(k+1)$ , respectively; and  $Q \in \mathbb{R}^{m \times m}$  and  $R \in \mathbb{R}^{p \times p}$  are known covariance matrices.

### 6.1.2.2 Propagation

Let  $\hat{x}_{k|k}$  and  $\hat{z}_{k|k}$  be the updated differential and algebraic states estimates at time  $t = k\Delta t$  using the information available up to and including  $k^{\text{th}}$  measurement sample, respectively. The predicted states,  $\hat{x}_{k+1|k}$  and  $\hat{z}_{k+1|k}$ , are obtained by integrating the DAE system in Eqn. (6.1). Let  $P_{k|k}$  be the error covariance matrix of updated estimates, the predicted error covariance,  $P_{k+1|k}$ , is obtained by first linearizing the nonlinear system in Eqn. (6.1) around the updated differential and algebraic states ( $\hat{x}_{k|k}$  and  $\hat{z}_{k|k}$ ) and second, differentiating the algebraic equations in Eqn. (6.1) to convert the DAE into a continuous implicit ODE. Therefore, augmenting the resulting system as:

$$\begin{bmatrix} \dot{x} \\ \dot{z} \end{bmatrix} = \begin{bmatrix} A & B \\ -D^{-1}CA & -D^{-1}CB \end{bmatrix} \begin{bmatrix} x \\ z \end{bmatrix} = A^{\text{aug}}x^{\text{aug}} \quad (6.2)$$

where superscript ‘*aug*’ represents the augmented form (i.e.  $x^{\text{aug}} = \begin{bmatrix} x \\ z \end{bmatrix}$ ) and the Jacobian matrix around the  $\hat{x}_{k|k}$  is evaluated as

$$J = \begin{bmatrix} A & B \\ C & D \end{bmatrix} = \begin{bmatrix} \frac{\partial f}{\partial x} & \frac{\partial f}{\partial z} \\ \frac{\partial g}{\partial x} & \frac{\partial g}{\partial z} \end{bmatrix}_{\hat{x}_{k|k}, \hat{z}_{k|k}} \quad (6.3)$$

The transition matrix, calculated as  $\Phi = \exp(J\Delta t)$ , is used to obtain the predicted error covariance by

$$P_{k+1|k} = \phi P_{k|k} \phi^T + \Gamma Q_{k+1} \Gamma^T \quad (6.4)$$

where

$$\Gamma = \begin{bmatrix} I \\ -D^{-1}C \end{bmatrix} \quad (6.5)$$

### 6.1.2.3 Correction

In the update step of EKF, the augmented states are updated as

$$\hat{x}_{k+1|k+1}^{aug} = \hat{x}_{k+1|k}^{aug} + K_{k+1} \left( y_{k+1} - h(\hat{x}_{k+1|k}^{aug}) \right) \quad (6.6)$$

Only the differential part of the estimated augmented states are retained and the algebraic part is obtained by solving

$$g(\hat{x}_{k+1|k+1}, \hat{z}_{k+1|k+1}) = 0 \quad (6.7)$$

The updated covariance matrix is obtained by

$$P_{k+1|k+1} = (I - K_{k+1} H_{k+1}) P_{k+1|k} \quad (6.8)$$

where in the update step,  $H_{k+1}$  is the linearized measurement model evaluated at  $\hat{x}_{k+1|k}^{aug}$  and  $K_{k+1}$  is the Kalman gain matrix calculated by

$$\begin{aligned} K_{k+1} &= P_{k+1|k} H_{k+1}^T (H_{k+1} P_{k+1|k} H_{k+1} + R_{k+1})^{-1} \\ &= (P_{k+1|k}^a)^{-1} + C^T R^{-1} C \end{aligned} \quad (6.9)$$

Note that these equations are written for augmented system except for Eqn. (6.7) where the algebraic part is only calculated.

### 6.1.3 Equality Constrained State Estimation of Uncertain Nonlinear DAEs

In practice, not all the algebraic equations that describe the behavior of a physical system are exact and additional information about the dynamic system may be available. If the algebraic equations are not exact, uncertainties must be considered in these equations to more closely represent the real behavior. Therefore, one could model uncertainties in the algebraic equations also as Gaussian random variables with known statistical properties. Moreover, if additional information about the system represents an equality constraint, which the system variables must satisfy, then this information must be incorporated into the estimation framework. To the best of our knowledge no work exists for estimation of such systems in the literature. In this section, we propose enhancements to the EKF approach for DAE systems to address this class of problems. We believe this class of

systems is quite common in all engineering disciplines and particularly in chemical engineering, where the DAE models are likely to be uncertain in addition to the presence of exact equality constraints arising out of flow balances and summation of mole fractions.

Most efforts in constrained Kalman filtering involves linear systems with optimal filtering while non-linearities in the system result in sub-optimal and complicated filtering.<sup>109</sup> Therefore, approximation is inevitable in filtering non-linear systems while they remain sub-optimal. Although there is no extensive investigation on constrained Kalman filtering of non-linear models due to their sub-optimal nature and complications, we make the assumptions that handling constraints in Kalman filtering of non-linear models can be done similar to their linear counterparts due to their linear approximations. There are several ways in which equality constraints can be incorporated into the linear Kalman filter. An attractive approach is to substitute the constraints into the model equations. This approach has an advantage of reducing the constrained problem to a simpler unconstrained problem with lower computational load of the Kalman filter. However, a major disadvantage is that this method will sacrifice the physical meaning of the variables, especially in systems expressing the detail phenomenon taking place in a process. Study on constrained filtering have shown that projecting the unconstrained estimates of the Kalman filter on the constraint surface accommodates ease of implementation, low computational cost and flexibility compared to other approaches for both linear and non-linear systems.<sup>109</sup> In this work, constraints are handled by approaching the problem using the same state estimates projection approach.

#### 6.1.3.1 Problem Formulation

The system of interest in this section is as shown in Eqn. (6.10).

$$\begin{aligned}
 x_{k+1} &= x_k + \int_{k \Delta t}^{(k+1) \Delta t} f(x(t), z(t)) dt + G\omega_{k+1} \\
 g(x_{k+1}, z_{k+1}) + \gamma_{k+1} &= 0 \\
 y_{k+1} &= h(x_{k+1}, z_{k+1}) + v_{k+1} \\
 \omega &\sim N(0, Q) \quad v \sim N(0, R) \quad \gamma \sim N(0, W) \\
 \text{subject to: } &Ex_{k+1}^{aug} = b
 \end{aligned} \tag{6.10}$$

where in addition to the assumptions for system described in Eqn. (6.1),  $G \in \mathbb{R}^{m \times m}$  is a known matrix with  $\text{rank}(G) = l < m$ ,  $E \in \mathbb{R}^{l \times m+n}$  is the equality constraint with  $\text{rank}(E) = l$  which can be split into  $E = [E_x \quad E_z]$  where  $E_x \in \mathbb{R}^{l \times m}$  satisfies  $E_x G = 0_{l \times m}$  and  $E_z = 0_{l \times n}$ ,  $b \in \mathbb{R}^{l \times 1}$  is a vector of equality constraint values and  $W \in \mathbb{R}^{n \times n}$  is a known covariance matrix. The estimation algorithm described previously is not a valid framework for the defined system. The main issue is that the white noise is not differentiable; therefore, the system cannot be converted into an implicit ODE as shown in Eqn. (6.2).

**Remark 2.1:** Assume  $\text{rank}(E) = m+n$ , then for all  $k \geq 1$  the system is fully constrained and the updated states are calculated as  $x_{k+1} = E^{-1}b$ .

**Proof:** If  $\text{rank}(E) = m+n$ , then  $E$  is square and invertible. Therefore, the constraint equation has unique answer as  $x_{k+1} = E^{-1}b$ .

### 6.1.3.2 Propagation

Let  $\hat{x}_{k|k}$  and  $\hat{z}_{k|k}$  be updated differential and algebraic state estimates, respectively, at  $k^{\text{th}}$  time instant and  $P_k$  be the error covariance of the states. States are propagated by solving the DAE from  $k^{\text{th}}$  time instant to  $k+1^{\text{th}}$  time instant to get  $\hat{x}_{k+1|k}$  and  $\hat{z}_{k+1|k}$ . In what follows, the superscripts ‘*c*’ and ‘*st*’ represent the corrected and standard form, respectively. In order to propagate the covariance matrix, the DAE system is linearized around the  $\hat{x}_{k|k}$  and  $\hat{z}_{k|k}$  as

$$\dot{x} = Ax + Bz \quad (6.11)$$

$$Cx + Dz = 0 \quad (6.12)$$

where the coefficient matrix of linearized form is simply the Jacobian evaluated at the operating point,  $\hat{x}_{k|k}, \hat{z}_{k|k}$ , similar to Eqn. (6.3). Solving Eqn. (6.12) in terms of  $z$  and rewriting the Eqn. (6.11) results

$$z = -D^{-1}Cx \quad (6.13)$$

$$\dot{x} = (A - BD^{-1}C)x \quad (6.14)$$

Based on differential and algebraic variables, the error covariance matrix can be split into

$$P_{k+1|k} = \begin{bmatrix} P_{k+1|k}^{xx} & P_{k+1|k}^{xz} \\ P_{k+1|k}^{zx} & P_{k+1|k}^{zz} \end{bmatrix} \quad (6.15)$$

The error covariance of differential states is calculated as

$$P_{k+1|k}^{xx} = \phi P_{k|k}^{xx} \phi^T + G Q G^T \quad (6.16)$$

where  $\phi$  is the transition matrix of differential states and is obtained as

$$\phi = e^{(A-BD^{-1}C)\Delta t} \quad (6.17)$$

The error covariance of algebraic states is propagated as

$$P_{k+1|k}^{zz} = (D^{-1}C)P_{k+1|k}^{xx}(D^{-1}C)^T + D^{-1}WD^{-1} \quad (6.18)$$

Since the algebraic states are linear transformation of the differential states, the error covariance between differential and algebraic states is propagated as a linear transformation of the error covariance of differential states as

$$P_{k+1|k}^{xz} = P_{k+1|k}^{xx}(D^{-1}C)^T \quad (6.19)$$

$$P_{k+1|k}^{zx} = (D^{-1}C)P_{k+1|k}^{xx} \quad (6.20)$$

### 6.1.3.3 Correction

The updated augmented state estimates are obtained by solving the following minimization problem

$$\begin{aligned} \min_{\hat{x}_{k+1|k+1}^{a,c}} & \left( \hat{x}_{k+1|k+1}^{aug,c} - \hat{x}_{k+1|k}^{aug} \right)^T P_{k+1|k}^{-1} \left( \hat{x}_{k+1|k+1}^{aug,c} - \hat{x}_{k+1|k}^{aug} \right) \\ & + \left( y_{k+1} - C \hat{x}_{k+1|k+1}^{aug,c} \right)^T R^{-1} \left( y_{k+1} - C \hat{x}_{k+1|k+1}^{aug,c} \right) \end{aligned} \quad (6.21)$$

subject to the state constraints

$$E \hat{x}_{k+1|k+1}^{aug,c} = b \quad (6.22)$$

where  $\hat{x}_{k+1|k+1}^{aug,c}$  is the augmented updated state estimates (i.e.  $\hat{x}_{k+1|k+1}^{aug,c} = \begin{bmatrix} \hat{x}_{k+1|k+1}^c \\ \hat{z}_{k+1|k+1}^c \end{bmatrix}$ ) that

satisfies the state constraints.

**Remark 2.2:** In the absence of any constraints, the optimization problem is similar to the problem investigated in the work of Vachhani et al.<sup>122</sup> and the solution to the optimization problem for all  $k \geq 1$  is given by standard KF.

**Proof:** The proof is described in the work of Vachhani et al.<sup>122</sup>

The optimization problem is solved using the standard Lagrange multiplier technique, where the Lagrangian is defined as

$$\begin{aligned} L\left(\hat{x}_{k+1|k+1}^{aug,c}, \lambda\right) &= \left(\hat{x}_{k+1|k+1}^{aug,c} - \hat{x}_{k+1|k}^{aug}\right)^T P_{k+1|k}^{-1} \left(\hat{x}_{k+1|k+1}^{aug,c} - \hat{x}_{k+1|k}^{aug}\right) \\ &\quad + \left(y_{k+1} - H\hat{x}_{k+1|k+1}^{aug,c}\right)^T R^{-1} \left(y_{k+1} - H\hat{x}_{k+1|k+1}^{aug,c}\right) \\ &\quad + \lambda^T \left(E\hat{x}_{k+1|k+1}^{aug,c} - b\right) \end{aligned} \quad (6.23)$$

The necessary conditions for  $\hat{x}_{k+1|k+1}^{aug,c}$  minimizing Eqn. (6.23) are

$$\begin{aligned} \frac{\partial L}{\partial \hat{x}_{k+1|k+1}^{aug,c}} &= 2P_{k+1|k}^{-1} \left(\hat{x}_{k+1|k+1}^{aug,c} - \hat{x}_{k+1|k}^{aug}\right) - 2H^T R^{-1} \left(y_{k+1} - H\hat{x}_{k+1|k+1}^{aug,c}\right) \\ &\quad + E^T \lambda = 0 \end{aligned} \quad (6.24)$$

$$\frac{\partial L}{\partial \lambda} = E\hat{x}_{k+1|k+1}^{aug,c} - b = 0 \quad (6.25)$$

Solving Eqn. (6.24) for  $\hat{x}_{k+1|k+1}^{aug,c}$  after some manipulations yields

$$\begin{aligned} \hat{x}_{k+1|k+1}^{aug,c} &= \hat{x}_{k+1|k}^{aug} + \left(P_{k+1|k}^{-1} + H^T R^{-1} H\right)^{-1} C^T R^{-1} \left(y_{k+1} - H\hat{x}_{k+1|k}^{aug}\right) \\ &\quad - \frac{1}{2} \left(P_{k+1|k}^{-1} + H^T R^{-1} H\right)^{-1} E^T \lambda \end{aligned} \quad (6.26)$$

Following the definition of Kalman gain matrix,  $K_{k+1}$ , in Eqn. (6.9) and matrix inversion lemma<sup>123</sup> we have

$$\left[P_{k+1|k}^{-1} + H^T R^{-1} H\right]^{-1} \quad (6.27)$$

$$\begin{aligned}
 &= P_{k+1|k} - [P_{k+1|k}^{-1} + H^T R^{-1} H]^{-1} H^T R^{-1} H P_{k+1|k} \\
 &= P_{k+1|k} - K_{k+1} H P_{k+1|k} \\
 &= P_{k+1|k+1}
 \end{aligned}$$

Substituting Eqn. (6.27) into Eqn. (6.26) and using the state update in Eqn. (6.6) we have

$$\hat{x}_{k+1|k+1}^{aug,c} = \hat{x}_{k+1|k+1}^{aug} - \frac{1}{2} P_{k+1|k+1} E^T \lambda \quad (6.28)$$

Substituting Eqn. (6.28) into Eqn. (6.25) and solving for Lagrangian multiplier,  $\lambda$ , we get

$$\lambda = 2(E P_{k+1|k+1} E^T)^{-1} (E \hat{x}_{k+1|k+1}^{aug} - b) \quad (6.29)$$

Substituting the value of Lagrangian multiplier from Eqn.(6.29), the states are updated in the presence of equality constraints as

$$\hat{x}_{k+1|k+1}^{aug,c} = F \hat{x}_{k+1|k+1}^{aug} + b' \quad (6.30)$$

where

$$F = \left( I - P_{k+1|k+1} E^T (E P_{k+1|k+1} E^T)^{-1} E \right) \quad (6.31)$$

$$b' = P_{k+1|k+1} E^T (E P_{k+1|k+1} E^T)^{-1} b \quad (6.32)$$

where  $P_{k+1|k+1}$  is the KF covariance matrix calculated similar to Eqn. (6.8). Using the state propagation matrix, for covariance matrix update we have

$$\begin{aligned}
 &P_{k+1|k+1}^c \\
 &= F P_{k+1|k+1} F^T \\
 &= \left( I - P_{k+1|k+1} E^T (E P_{k+1|k+1} E^T)^{-1} E \right) P_{k+1|k+1} \left( I - P_{k+1|k+1} E^T (E P_{k+1|k+1} E^T)^{-1} E \right)^T \\
 &= P_{k+1|k+1} - P_{k+1|k+1} \left[ P_{k+1|k+1} E^T (E P_{k+1|k+1} E^T)^{-1} E \right]^T \\
 &\quad - P_{k+1|k+1} E^T (E P_{k+1|k+1} E^T)^{-1} E P_{k+1|k+1} \\
 &\quad + P_{k+1|k+1} E^T (E P_{k+1|k+1} E^T)^{-1} E P_{k+1|k+1} \left[ P_{k+1|k+1} E^T (E P_{k+1|k+1} E^T)^{-1} E \right]^T \\
 &= P_{k+1|k+1} - P_{k+1|k+1} E^T (E P_{k+1|k+1} E^T)^{-1} E P_{k+1|k+1}
 \end{aligned}$$

$$\begin{aligned} & -P_{k+1|k+1}E^T(E P_{k+1|k+1}E^T)^{-1}EP_{k+1|k+1} \\ & +P_{k+1|k+1}E^T(E P_{k+1|k+1}E^T)^{-1}(EP_{k+1|k+1}E^T)(EP_{k+1|k+1}E^T)^{-1}EP_{k+1|k+1} \end{aligned}$$

**Remark 2.3:** Assume that equality constraint,  $E$ , in Eqn. (6.10) can be split into  $E = \begin{bmatrix} E_x \\ E_z \end{bmatrix}^T$

where  $E_x \in \mathbb{R}^{l \times m}$  is left eigenvector(s) of  $\Phi$  that satisfies  $E_x G = 0_{l \times m}$ ,  $E_x f_x = 0_{m \times 1}$  and  $E_z = 0_{l \times n}$  where  $f_x$  is the differential equations of the DAE system represented by Eqn. (6.10). Also assume that for a given  $k = 1$ ,  $E \hat{x}_{k+1|k+1}^{aug,c} = b$  and  $EP_{k+1|k+1}^c = 0_{l \times m+n}$ . Then, for all  $k \geq 2$ ,  $x_{k+1|k+1}^{aug,c} = \hat{x}_{k+1|k+1}^{aug}$  and  $P_{k+1|k+1}^c = P_{k+1|k+1}$ .

**Proof:** By multiplying the differential equations in DAE system of Eqn. (6.10) by  $E$  we get

$$\begin{aligned} Ex_{k+1}^{aug} &= E_x x_k + \int_{k \Delta t}^{(k+1) \Delta t} E_x f_x(x(t), z(t)) dt + E_x G \omega_{k+1} + E_z z_{k+1} \\ &= b + 0_{l \times 1} + 0_{l \times 1} + 0_{l \times 1} \\ &= b \end{aligned} \tag{6.34}$$

Since  $E_x$  is the left eigenvector(s) of  $\Phi$ , then we can write  $E_x \Phi = \lambda E_x$  where  $\lambda$ s are the eigenvalues of the corresponding eigenvectors. Multiplying Eqn. (6.15) by  $E$  then yields

$$\begin{aligned} EP_{k+1|k} &= \begin{bmatrix} E_x P_{k+1|k}^{xx} + E_z P_{k+1|k}^{zx} \\ E_x P_{k+1|k}^{xz} + E_z P_{k+1|k}^{zz} \end{bmatrix}^T \\ &= \begin{bmatrix} (E_x \phi P_{k|k}^{xx} \phi^T + E_x G Q G^T) + E_z (D^{-1} C) P_{k+1|k}^{xx} \\ E_x P_{k+1|k}^{xx} (D^{-1} C)^T + (E_z (D^{-1} C) P_{k+1|k}^{xx} (D^{-1} C)^T + E_z M) \end{bmatrix}^T \\ &= \begin{bmatrix} (\lambda E_x P_{k|k}^{xx} \phi^T + 0_{l \times m}) + 0_{l \times m} \\ 0_{l \times n} + (0_{l \times n} + 0_{l \times n}) \end{bmatrix}^T \\ &= 0_{l \times (m+n)} \end{aligned} \tag{6.35}$$

**Lemma 2.1:** let  $v$  be a left eigenvector of the square matrix  $U$  with a corresponding eigenvalue  $\lambda$ . Then,  $v e^{U \Delta t} = e^{\lambda \Delta t} v$ .

**Proof:** To prove this, we can write  $U \Delta t = U \Delta t - \lambda I \Delta t + \lambda I \Delta t$ , therefore

$$\begin{aligned}
 \nu e^{U\Delta t} &= \nu e^{U\Delta t - \lambda I \Delta t + \lambda I \Delta t} \\
 &= \nu e^{(U - \lambda I)\Delta t + \lambda I \Delta t} \\
 &= \nu e^{(U - \lambda I)\Delta t} e^{\lambda \Delta t} \\
 &= \nu \left( I + (U - \lambda I)\Delta t + \frac{(U - \lambda I)^2 \Delta t^2}{2!} + \dots \right) e^{\lambda \Delta t} \\
 &= \left( \nu I + \nu(U - \lambda I)\Delta t + \frac{\nu(U - \lambda I)^2 \Delta t^2}{2!} + \dots \right) e^{\lambda \Delta t} \\
 &= (\nu I + 0 + 0 + \dots) e^{\lambda \Delta t} \\
 &= e^{\lambda \Delta t} \nu
 \end{aligned} \tag{6.36}$$

Therefore, in Eqn. (6.35)  $E_x$  is already the left eigenvector(s) of  $(A - BD^{-1}C)$ . Multiplying Eqn. (6.30) and (6.33) by  $E$  yields

$$\begin{aligned}
 E\hat{x}_{k+1|k+1}^{aug,c} &= EF\hat{x}_{k+1|k+1}^{aug} + Eb' \\
 &= E \left( I - P_{k+1|k+1}E^T (EP_{k+1|k+1}E^T)^{-1}E \right) \hat{x}_{k+1|k+1}^{aug} \\
 &\quad + EP_{k+1|k+1}E^T (EP_{k+1|k+1}E^T)^{-1}b \\
 &= (E - E)\hat{x}_{k+1|k+1}^{aug} + b \\
 &= b
 \end{aligned} \tag{6.37}$$

$$\begin{aligned}
 EP_{k+1|k+1}^c &= EP_{k+1|k+1} \\
 &= E \left( I - P_{k+1|k+1}E^T (EP_{k+1|k+1}E^T)^{-1}E \right) P_{k+1|k+1} \\
 &= (E - E)P_{k+1|k+1} \\
 &= 0_{l \times (m+n)}
 \end{aligned} \tag{6.38}$$

Giving Eqn. (6.37)-(6.38), from Eqn. (6.34)-(6.35) we have  $x_{k+1|k+1}^{aug,c} = \hat{x}_{k+1|k+1}^{aug}$  and  $P_{k+1|k+1}^c = P_{k+1|k+1}$ . Therefore, if the assumptions hold, the correction step in Eqn. (6.30) and (6.33) has to be performed only once at  $k = 1$  and for all  $k \geq 2$  the corrected states given by Eqn. (6.6) already satisfies  $E\hat{x}_{k+1|k+1}^{aug} = b$ .<sup>124</sup>

## 6.2 Problem Formulation

### 6.2.1 Introduction

In the past decades, process monitoring for safety and optimal operation has been a vast area for researchers to develop techniques for control, optimization, fault detection, condition monitoring, etc. With growing scale and complexity of the processes, mathematical models cannot be solely used and information from sensors as an alternate source of information is necessary. The problem of sensor placement is defined as finding optimal locations throughout the process such that if sensors are placed in those locations then maximum possible information about the process could be acquired. Most important constraints involved are the feasibility of placing sensors, cost and redundancy of the sensors. For example, in a fixed-bed reactor, it is not feasible to directly measure the temperature of the catalyst and not economical to place sensors at every possible location. Also, sensor redundancy, which means placing multiple sensors at same location due to probability of the sensor failure, can cause clustering of sensors in an area, which may result in achieving significantly less information as if they were distributed. Therefore, optimizing sensor placement is crucial to maximizing the profit of the process and reducing the risk of health and environmental issues.

Sensor placement has been applied in different tasks such as parameter estimation<sup>125-132</sup>, state estimation<sup>133-144</sup> and fault detection<sup>145</sup> that deals with distributed parameter systems (DPS). Distributed systems are dynamical systems governed by partial differential equations (PDE). A most common technique in sensor placement is by optimizing a performance criterion. Many contributions in literature can be found that consider the steady-state behavior of the systems<sup>95</sup>, including the sensor placement by qualitative analysis<sup>9,98,105,146</sup>. Although many efforts on sensor placement belong to linear DPS, various optimality criteria have either been developed or adopted from linear systems to account for nonlinear systems. A common metric used in sensor placement involves the use of empirical observability Gramian proposed by Muller and Weber<sup>147</sup>. This includes evaluation of different aspects of the observability matrix (observability Gramian) such as smallest eigenvalue, determinant, trace of the inverse, condition number, spectral norm and smallest singular value<sup>133,144,148-153</sup>. Different criteria in sensor placement has been also

proposed based on the geometric approach<sup>134,154</sup>, measurement cost<sup>143,155</sup>, sensor failure<sup>156-157</sup>, max-min optimization<sup>158</sup>, posterior Cramer-Rao lower bound<sup>157</sup> and so on.

Despite the information from common observability matrix, efforts in state estimation have been made in defining metrics for sensor placement that considers trace, determinant, variance and norm of the error covariance matrix of the Kalman filter.<sup>138-142,152-153,159-161</sup> Colantuoni and Padmanabhan<sup>141</sup>, Kumar and Seinfeld<sup>142</sup> and Omatsu et al.<sup>138</sup> considered minimization of the trace of the error covariance as the metric in their sensor placement work and proposed an iterative optimization procedure for sensor placement for a tubular reactor. Harris et al.<sup>140</sup> performed the sensor placement for a tubular reactor while minimizing the trace and determinant of the error covariance matrix. Alvarez et al.<sup>152</sup> approached the problem by developing a variable measurement structure for the tubular reactor with minimum variance as the optimality index. Morari and O'Dowd<sup>160</sup> considered optimality criteria as minimization of the error caused by the unobservable subspace and Morari and Stephanopoulos<sup>161</sup> extended the criteria to also include the minimization of the estimation error.

In most of the works mentioned above, the sensor placement is performed at steady state condition. In the cases where dynamical systems are considered, sensor placement is performed by linearizing the nonlinear equations around the steady-state point. This reduces the complexity of the nonlinear equations to linear form and the sensor placement can be performed as if the system is linear. This is due to the reason that solving the nonlinear equations in the sensor placement frameworks is cumbersome and makes the sensor placement intractable. However, this is not always applicable for two reasons. First, since the previous works on sensor placement always consider the system is represented by ODE/PDE, it is not always possible to have the system as fully implicit PDE (or ordinary differential equations, ODE). For example, as the system in this work is represented by differential and algebraic equations (DAE), it is not possible to differentiate the equations to get ODE since the white Gaussian noise in algebraic equations cannot be differentiated. Second, in terms of fault detection, if a fault occurs in the process it will significantly deviate the system from steady-state condition and result in the system to go to a new steady-state condition, therefore, the linearized system or the assumption of the dynamics around the initial steady-state condition is no longer valid. These drawbacks of the classical

sensor placement approaches necessitate the use of nonlinear models in the sensor placement framework.

The most important drawback of using nonlinear models in sensor placement is the computational burden and tractability of the calculations caused by nonlinear models in state estimation. A most recent work in use of nonlinear model in extended Kalman filter (EKF) is reported in the work of Olanrewaju and Al-Arfaj<sup>139</sup> in which the sensor placement problem is not extensively addressed. One way to address the tractability of the use of detailed nonlinear models is to use simplified or reduced models. However, it is not clear how much this will affect the computational burden and how close are the sensor placement results to that of detailed models. To our best knowledge, no one has investigated the suitability of the simplified models in sensor placement.

In this section, a sensor placement framework is developed that makes use of EKF for state estimation. For simplicity, the optimality index is chosen as the accuracy of the state estimates by minimizing the error between the true solution and the state estimates. The infinite dimensional model of the reactor is discretized along the reactor axis by finite element method and the discrete points on the reactor are assumed to be the locations at which sensors can be placed. The sensor placement is performed by genetic algorithm (GA) where the genes are assumed to be measurement models and each measurement model represents a vector of binary decision variables in which if a sensor is placed, the decision variable will take a value of "1" and a value of "0" otherwise. The GA evolves while minimizing the objective function and the optimal measurement model as the result of the optimization is obtained. The optimal measurement model is then the optimal sensor placement when projected on the discretized locations.

### **6.2.2 Summary of Simplified WGS Model**

The detailed reactor model represent complex equations that must be solved. A simplified model of the reactor has been developed in section 3.1. Model simplification retains the most important phenomena occurring in the reactor by means of scaling analysis. In the scaling analysis, dimensionless groups are formed using the parameters and inlet condition values. The decision on retaining or discarding the phenomenon in the reactor is made by analyzing the values of the dimensionless groups where the phenomenon

with least values can be discarded from model equations. Through this simplifications, it is observed that the model can be represented by only by a single partial differential equation while the rest of the equations are represented by ordinary differential equations. Further it is observed that for the species balance in the simplified model, it is enough to solve only for one of key species and the simulation results for other species can be easily be calculated using stoichiometric relations. Following the simplifications from the scaling analysis and from stoichiometric relations and considering only water gas shift reaction, following forms the simplified model of WGS reactor:

Mass balance:

$$\frac{dy_{H_2O}}{dz} = \left( \frac{r_{WGS,H_2O}}{G} \right) \frac{1 - \varepsilon}{\varepsilon} \quad (6.39)$$

Energy balance:

$$\frac{\partial T}{\partial t} = \frac{1}{\rho_{cat} C_{p,cat}} \left( -\frac{G\varepsilon C_p}{1 - \varepsilon} \frac{\partial T}{\partial z} + r_{CO} \Delta H_{R,WGS} \right) \quad (6.40)$$

Momentum balance:

$$\frac{dP}{dz} = \frac{\rho u^2}{d_{cat}} \left( \frac{1 - \varepsilon}{\varepsilon} \right) \left( 1.75 + \frac{150}{Re} \right) \quad (6.41)$$

Total equations of simplified model are derived in Section 3.1.9 with the exception that here we only consider the sweet WGS reaction and COS and H<sub>2</sub>S components are present in the system.

### 6.2.3 EKF for Simplified Model

In mathematical view of the simplified model, part of differential equations are decoupled from the original system and assumed to be algebraic through the scaling analysis shown in Chapter 3. Although the corresponding states represent the states of the original system, they have no effect on the internal states of the simplified model and can be treated as exogenous states with corresponding exogenous equations. In view of DAEs, these exogenous equations can be either part of the DAE system as algebraic equations or be used outside the DAE model and computed independently. A simple drawback of

assuming the exogenous equations as part of the DAE is that while exogenous equations do not impose a constraint on the system, they still have to be solved at each integration step in the propagation step of the filter. Therefore, this poses a burden on the DAE solvers and hence complicating the computations. Another drawback is that in the propagation step of the filter, the updated states at the next time step are only required while the path that these states take to the final states can be neglected. For these reasons, the decoupled algebraic equations are treated as independent exogenous equations. The overall simplified system is presented by

$$\begin{aligned}
 DAE \left\{ \begin{array}{l} x_{k+1} = x_k + \int_k^{(k+1)\Delta t} f(x(t), z(t)) dt + \omega_{2,k} \\ g(x_{k+1}, z_{k+1}) = \gamma_{k+1} \\ s_{k+1} = Ux_{k+1}^A + Js_k + \Gamma_{k+1} \\ y_{k+1} = h(x_{k+1}, z_{k+1}, s_{k+1}) + v_{k+1} \end{array} \right. \\
 \omega \sim N(0, Q_2) \quad v \sim N(0, R) \quad \gamma \sim N(0, W) \quad \Gamma \sim N(0, \Omega) \\
 \text{subject to: } Ex_{k+1}^{aug} = b
 \end{aligned} \tag{6.42}$$

where  $s_{k+1}$  is the vector of exogenous states and  $U$  and  $J$  are the coefficient matrices of the linearized exogenous equations around the state updates,  $x_{k+1}^A$  and  $s_k$ , respectively. Here,  $x_{k+1|k}^A$  is the augmented internal states,  $x_{k+1|k}^A = \begin{bmatrix} x_{k+1} \\ z_{k+1} \end{bmatrix}$ , and  $x_{k+1}^{aug}$  is the augmented internal and exogenous states,  $x_{k+1}^{aug} = \begin{bmatrix} x_{k+1}^A \\ s_k \end{bmatrix}$ . Also, here, the exogenous states do not depend on their initial states, therefore,  $J = \mathbf{0}$ . Note that  $\omega_{2,k}$  is assumed uncorrelated with  $v$ ,  $\gamma$  and  $\Gamma$ ; and since the exogenous equations are decoupled from the differential equations,  $G$  matrix that correlates the noise in mole fractions is omitted, however, a white noise term,  $\Gamma_{k+1}$ , is assumed in the exogenous equations. Although omitting  $G$  may have effect on the quality of the state estimates, it is not easy mathematically to account for the correlated noise in the mole fractions when considering the simplified model.

The modifications made to the original system require modifications of the filter equations as well. The new filter formulation follows the same process as for DAEs while adding the presence of the exogenous states. In the propagation step, the DAE model can be solved again by the DAE solvers from instant  $k$  to  $k + 1$ , while the exogenous states

are computed using the updated internal states to obtain the updated exogenous states. The updated error covariance matrix is calculated by splitting the matrix for internal and the exogenous states as

$$P_{k+1|k}^{aug} = \begin{bmatrix} P_{k+1|k}^{x^A x^A} & P_{k+1|k}^{x^A s} \\ P_{k+1|k}^{s x^A} & P_{k+1|k}^{ss} \end{bmatrix} \quad (6.43)$$

where  $P_{k+1|k}^{x^A x^A}$  is the error covariance matrix of the simplified DAE and is derived using general derivation explained in section 6.1.3. This results in equations similar to equations derived in section 6.1.3 with the exception that the simplified model has now modified process noise covariance ( $\omega \sim N(0, Q_2)$ ). The other blocks in  $P_{k+1|k}^{aug}$  can be calculated by

$$P_{k+1|k}^{x^A s} = P_{k+1|k}^{x^A x^A} U^T \quad (6.44)$$

$$P_{k+1|k}^{s x^A} = U P_{k+1|k}^{x^A x^A} \quad (6.45)$$

$$P_{k+1|k}^{ss} = U P_{k+1|k}^{x^A x^A} U^T + \Omega \quad (6.46)$$

Eqn. (6.44)-(6.46) can be proved simply by taking similar approach as for filtering of the DAE systems. Therefore, for the sake of brevity we have omitted the mathematical proofs. In the correction step of the filter, the corrected states can be calculated similar to the Eqn. (6.30)-(6.33).

Although considering noise in exogenous equations may results in better quality estimates since the original states are not noise free, it raises the need for the presence of constraint in the formulation. However, another approach would then be to remove the noise from the exogenous equations. Since the exogenous equations automatically satisfy the constraint, therefore, the constraint in Eqn. (6.42) can be removed and the correction step reduces to the use of standard EKF correction step. It is not clear to what extent this can affect the quality of state estimates and the SP results. Removing the noise term from exogenous equations may or may not be compensated by tuning the error covariance matrix  $Q_2$  in the filtering. This will be further studied in a later section.

#### 6.2.4 Genetic Algorithm

In the genetic algorithm (GA), the genes represent the binary measurement models that can be used by EKF for state estimation. The fixed population of GA evolves by the elitist selection strategy where a portion of the population is considered as the elite genes and carry over to the next generation. The rest of the population are obtained based on the tournament selection where fitness values of 2 randomly chosen genes are compared against each other and the gene with highest fitness is considered as the winner. This selection is repeated until two winner genes are selected for crossover and mutation- the GA operators for obtaining the two children from parent genes. Since in our work the number of measurements (sensors) is fixed for a particular study, the crossover and mutation on the winner genes are repeated until at least one of the children has the same number of fixed measurements. The tournament selection results in obtaining two children per each run, therefore, this process must be repeated until a new population is generated. The objective of the GA is to minimize the error between actual data and the state estimates and the objective function is given by

$$\min \sum_{i=2}^{k_T} \sum_{j=1}^{n_T} \left( \frac{x_{actual,(i,j)} - \hat{x}_{estimated,(i,j)}}{x_{actual,(i,j)}} \right)^2 \quad (6.47)$$

subject to: EKF of WGSR for  $k_T$  time instants and  $n_T$  variables

It should be noted that the summation in Eqn. (6.47) is over all the estimated values for all time instants while the initial state estimates are discarded and summation start from  $i = 2$ . This assumption will be justified later when we study the effect of initial error covariance of the states.

#### 6.2.5 State Estimation Validation

In this section, the performance of the proposed state estimation technique is demonstrated on two examples. The first example is a nonlinear system that is akin to a batch reactor and the second example is the water gas shift reactor (WGSR), where a catalytic reaction is performed in a plug-flow reactor. The performance of the filter is demonstrated by comparison of root mean square error (RMSE) of the data and the estimated states calculated as

$$RMSE = \sqrt{\frac{\sum_{i=1}^s (x_{i,k} - \hat{x}_{i,k}^c)^2}{s}} \quad (6.48)$$

where  $x_{i,k}$  is the actual value that is specific to the simulation study and  $\hat{x}_{i,k}^c$  is the constrained state estimates. In order to calculate the RMSE of the measurement data,  $\hat{x}_{i,k}^c$  in Eqn. (6.48) is replaced by the measured value  $y_{i,k}$ . Another metric that is used in the following analysis is the normalized sum of squared errors (SSE) of all state estimates over the total time instance and is calculated as

$$SSE = \sum_{t=1}^T \sum_{i=1}^X \left( \frac{x_i(t) - \hat{x}_i(t)}{x_i(t)} \right)^2 \quad (6.49)$$

where  $T$  is the number of time instances,  $X$  is the number of variables and  $x_i(t)$  and  $\hat{x}_i(t)$  are  $i^{\text{th}}$  actual and estimated states at  $t^{\text{th}}$  time instance, respectively. It should be noted that in the following studies, SSE values are calculated by averaging over 100-run Monte Carlo simulations.

### 6.2.5.1 Example 1: Non-linear synthetic system

Our synthetic example is comprised of two differential equations and an algebraic equation. The aim of this example is to show the filter performance when the assumptions in Remark 2.3 is valid. The system under study is given as

$$\begin{bmatrix} \dot{x}_1 \\ \dot{x}_2 \end{bmatrix} = \begin{bmatrix} 8.69 \times 10^{-4}z(0.6 - x_1) - z \times 10^{-3} \left( x_1 - \frac{x_2}{2} \right) \\ 8.69 \times 10^{-4}z(0.4 - x_2) + z \times 10^{-3} \left( x_1 - \frac{x_2}{2} \right) \end{bmatrix} + G \begin{bmatrix} \omega_1 \\ \omega_2 \end{bmatrix} \quad (6.50)$$

$$g(x) = z^{0.3} + 0.5x_1^3z - 10 \frac{x_2}{z} = \gamma \quad (6.51)$$

where  $G = \begin{bmatrix} 0.5 & -0.5 \\ -0.5 & 0.5 \end{bmatrix}$  and true initial state of  $x_0 = [0.431 \quad 0.569 \quad 3.546]^T$ . The sampling time is chosen as  $\Delta t = 5$  s and the state estimator is initialized with

$$\begin{aligned}
 Q &= \begin{bmatrix} 2.5 \times 10^{-5} & 0 \\ 0 & 2.5 \times 10^{-5} \end{bmatrix} \\
 W &= 2.5 \times 10^{-3} \\
 R &= \begin{bmatrix} 2.5 \times 10^{-5} & 0 & 0 \\ 0 & 2.5 \times 10^{-5} & 0 \\ 0 & 0 & 2.5 \times 10^{-3} \end{bmatrix} \\
 P_0 &= \begin{bmatrix} 10^{-4} & 0 & 0 \\ 0 & 10^{-4} & 0 \\ 0 & 0 & 10^{-4} \end{bmatrix} \\
 x_{0|0} &= [0.555 \quad 0.456 \quad 2.822]^T
 \end{aligned} \tag{6.52}$$

The constraint given for this system is

$$E = [1 \quad 1 \quad 0], \quad b = 1 \tag{6.53}$$

Note that the initial estimate does not satisfy the constraint. From the constraint, it can be seen that  $E_x = [1 \quad 1]$ ,  $E_z = 0_{1 \times 1}$ ,  $E_x G = 0_{1 \times 2}$  and  $E_x f_x = 0_{1 \times 1}$ . The Jacobian matrix is calculated analytically as

$$\begin{aligned}
 &\begin{bmatrix} A & B \\ C & D \end{bmatrix} \\
 &= \begin{bmatrix} (-0.869z - z) \times 10^{-3} & -\frac{z}{2} \times 10^{-4} & \left(0.869(0.6 - x_1) - \left(x_1 - \frac{x_2}{2}\right)\right) \times 10^{-3} \\ z \times 10^{-3} & \left(-0.869z - \frac{z}{2}\right) \times 10^{-3} & \left(0.869(0.4 - x_2) + \left(x_1 - \frac{x_2}{2}\right)\right) \times 10^{-3} \\ 1.5x_1^2z & \frac{-10}{z} & 0.3z^{-0.7} + 0.5x_1^3 + \frac{10x_2}{z^2} \end{bmatrix} \tag{6.54}
 \end{aligned}$$

Multiplying  $E_x$  by  $(A - BD^{-1}C)$  yields

$$\begin{aligned}
 &E_x(A - BD^{-1}C) \\
 &= [1 \quad 1] \begin{bmatrix} -8.69z \times 10^{-4} - z \times 10^{-3} + z \times 10^{-3} & -\frac{z}{2} \times 10^{-3} \\ z \times 10^{-3} & -8.69z \times 10^{-4} + \frac{z}{2} \times 10^{-3} \end{bmatrix} \tag{6.55} \\
 &= [-86.9z \times 10^{-4} \quad -86.9z \times 10^{-4}] \\
 &= -86.9z \times 10^{-4} \times [1 \quad 1]
 \end{aligned}$$

From Eqn. (6.53), it is known that  $x_1 + x_2 = 1$  after the first iteration of the filter, therefore,  $E_x BD^{-1}C = 0$ . From Eqn. (6.55),  $E_x$  is a left eigenvector of  $\Phi$ . Since the assumptions in Remark 2.3 hold, state estimates are obtained as explained in Remark 2.3. Figure 6-1 to 6-3 show the actual, measured and estimated values of each variables for 100 time

instances. Initially, states do not satisfy the constraint, however, after the first iteration of the filter, estimated states satisfy the constraints for all time instances.

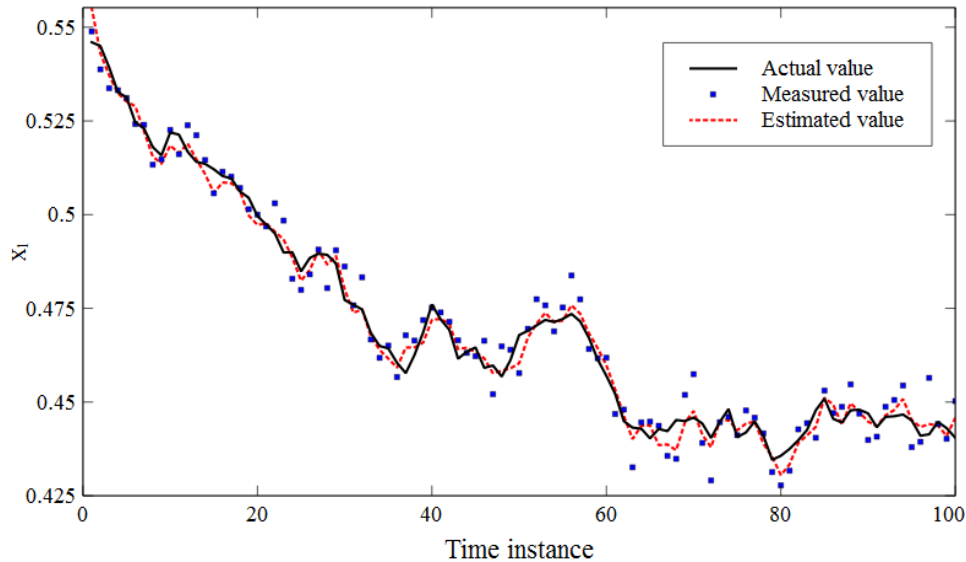


**Figure 6-1. Actual, measured and estimated values of differential variable  $x_1$ .**

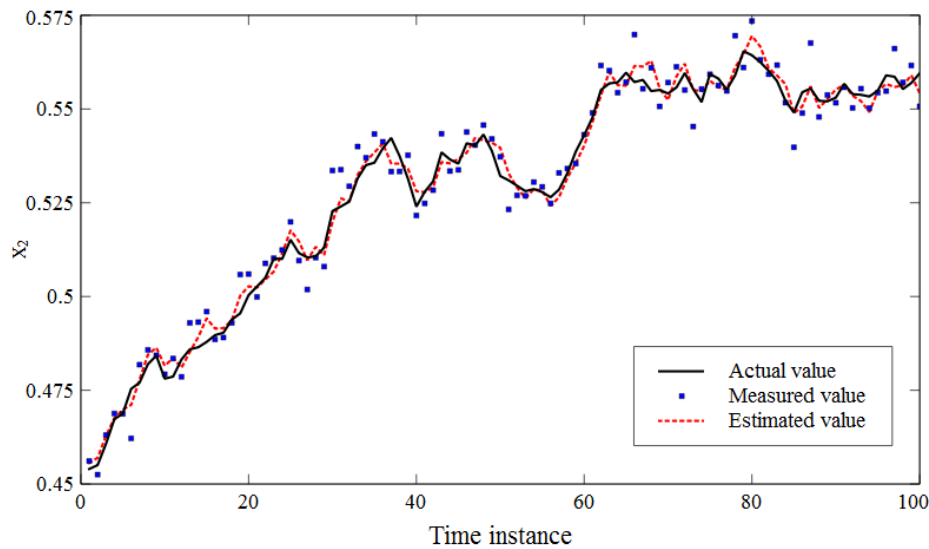


**Figure 6-2. Actual, measured and estimated values of differential variable  $x_2$ .**

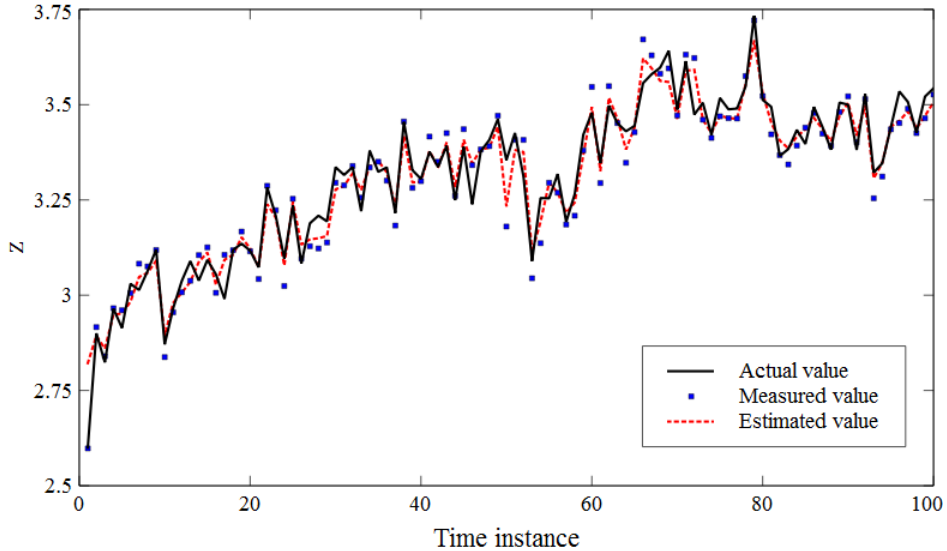


**Figure 6-3. Actual, measured and estimated values of algebraic variable z**

Table 6.1 shows the RMSE and SSE values of measured and estimated variables. In Table 6.1, RMSE and SSE are compared for Filter I, filter with certain algebraic equation assumption as described in Section 5.1, and Filter II, the proposed filter. It should be noted that the propagation step in Filter I is modified to include the state constraints as shown in Eqn. (6.21). As seen in Table 6.1, RMSE of differential variables  $x_1$  and  $x_2$  using Filter II are slightly reduced over using Filter I although both filters result in better estimates compared to the measurements. The RMSE of the algebraic variable  $z$  for Filter I is greater than that of the measurement due to underestimation of noise in its corresponding equation. This suggests that measuring the algebraic variable would result in more accurate values than using Filter I. However, the reduced RMSE of the algebraic variable for Filter II compared to the RMSE of the measurement justifies the correct assumption of uncertain algebraic equation. Also, the SSE value of Filter II indicates significant improvement over Filter I, which means the estimates are closer to the actual values. These improvements show that the proposed filter can mitigate the effect of uncertain algebraic equations and result in better estimates.

**Table 6.1. Comparison of RMSE and SSE values for measured and estimated values**

	RMSE			SSE
	$x_1$	$x_2$	$z$	
Measurement (data)	0.0050	0.0050	0.0501	
Filter I	0.0029	0.0029	0.0684	0.0479
Filter II	0.0027	0.0027	0.0417	0.0215

### 6.2.5.2 Example 2: Water gas shift reactor

State estimation of reactors has been the focus of many researchers for control and fault diagnosis. The next example is the system of interest, water gas shift reactor (WGSR), in which carbon monoxide (CO) reacts with steam (H<sub>2</sub>O) to produce hydrogen (H<sub>2</sub>) and carbon dioxide (CO<sub>2</sub>), through the water gas shift reaction. A non-linear DAE model of the sour water gas shift reactor (SWGSR) has been developed in section 2.1 where in addition to the water gas shift reaction, carbonyl sulfide (COS) reacts with H<sub>2</sub>O (i.e., COS hydrolysis), and CO<sub>2</sub> and hydrogen sulfide (H<sub>2</sub>S) are produced. For simplicity, here, the sulfur content of the feed is assumed negligible and only the water gas shift reaction is considered. In addition to the reactor model, feed and product stream flowrates are controlled by valves (V<sub>1</sub>, V<sub>2</sub> and V<sub>3</sub>) as shown in Figure 6-4. The corresponding equation for calculation of flows through the valves is  $F_{V_i} = \left( \frac{d_{V_i} S_{V_i}}{M_{V_i}} \right) \sqrt{\rho_{V_i} \Delta P_{V_i}}$ , where  $d_{V_i}$ ,  $S_{V_i}$ ,  $M_{V_i}$ ,

$\rho_{V_i}$  and  $\Delta P_{V_i}$  are flow coefficient, valve opening, average molecular weight, average density and pressure drop across the valve, respectively. Syngas and steam are passed through valves V<sub>1</sub> and V<sub>2</sub>, respectively, and it is assumed that these streams are well mixed in an ideal mixer before entering the reactor. The presence of the valve adds an additional algebraic equation to the system model as described by Eqn. (6.56)-(6.60). Table 6.2 shows the summary of the equations used to represent the system with parameters shown in Table 6.3. Some of the parameters in our previous work are changed for simplicity and reduced computations. For example, the reactor size and correspondingly the number of grid points in discretization are reduced. These parameters are shown in Table 6.3.

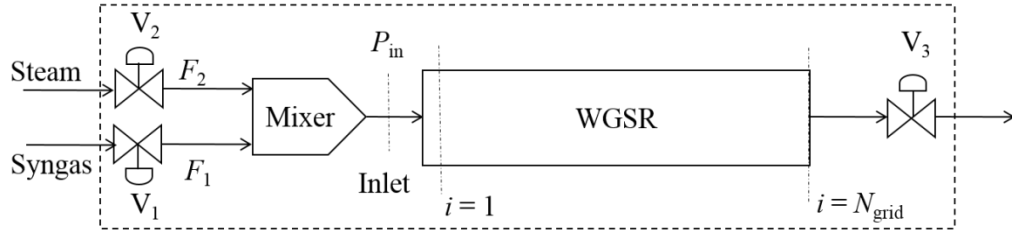


Figure 6-4. Schematic of the WGSR system

Table 6.2. Summary of equations of water gas shift reactor

$$\frac{\partial y_i}{\partial t} = \frac{RT}{P} \left( -F_{MF} \frac{\partial y_i}{\partial z} + r_{WGS,i} \frac{1-\varepsilon}{\varepsilon} \right) + G \omega_{1,i} \quad i = \text{CO, H}_2\text{O, CO}_2 \text{ and H}_2 \quad (6.56)$$

$$\frac{\partial T_g}{\partial t} = \frac{1}{\rho_{gas} C_p} \left[ -C_p F_{MF} \frac{\partial T_g}{\partial z} + \frac{h_f a_c}{\varepsilon} (T_{cat} - T_{gas}) \right] + \omega_2 \quad (6.57)$$

$$\begin{aligned} \frac{\partial T_{cat}}{\partial t} = \frac{1}{\rho_{cat} C_{p,cat}} & \left[ K_{cat} \frac{\partial^2 T_{cat}}{\partial z^2} - \frac{h_f a_c}{1-\varepsilon} (T_{cat} - T_{gas}) + r_{WGS} \rho_{cat} \Delta H_{R,WGS} \right] \\ & + \omega_3 \end{aligned} \quad (6.58)$$

$$\frac{dP}{dz} = \frac{\rho u^2}{D_{cat}} \left( \frac{1-\varepsilon}{\varepsilon^3} \right) \left( 1.75 + \frac{150}{Re} \right) + \gamma_1 \quad (6.59)$$

$$\Delta P_{V_3} = \frac{1}{\rho_{V_3}} \left( \frac{F_{V_3} M_{V_3}}{d_{V_3} S_{V_3}} \right)^2 + \gamma_2 \quad (6.60)$$

Table 6.3. Summary of the parameters of the WGSR model used in this work

Parameter	Value
Length	1 m
Diameter	0.5 m
Number of grids ( $N_{\text{grid}}$ )	25
Valve $V_1$ (syngas)	Opening
Flow Coefficient	$6 \times 10^{-5}$
Valve $V_2$ (steam)	Opening
	50%

	Flow Coefficient	$2 \times 10^{-5}$
Valve V <sub>3</sub> (products)	Opening	50%
	Flow Coefficient	$10^{-4}$
Inlet temperature		580 K
Feed pressure (steam and syngas)		5626121 Pa
Outlet pressure		$4.5 \times 10^6$ Pa
Catalyst diameter		0.1 mm

---

The state vector consists of 176 states including mole fractions of CO, H<sub>2</sub>O, CO<sub>2</sub>, and H<sub>2</sub>, temperature and pressure at each grid-point and pressure at the inlet of the reactor ( $P_{in}$ ). The constraint for this system is imposed as the summation of mole fractions at each grid-point is equal to one. Since the actual mole fraction values must sum up to one for consistency, in simulating the actual mole fraction values, the process noise is introduced in the mole fractions in such a way that the summation of the process noises at each grid-point and time instance are equal to zero. To do this, random process noises generated for each mole fractions at a particular grid-point are corrected by subtracting the mean average of the process noises from each. Therefore,  $G$  in system of Eqn. (6.10) is written such the diagonal elements are  $+\frac{3}{4}$  and the elements corresponding to mole fractions of the other components at the same grid-point are  $-\frac{1}{4}$ . The process covariance,  $Q$ , of each equation type is assumed the same and chosen as  $10^{-4}$  and  $2.5 \times 10^{-5}$  for mole fraction and temperature equations, respectively. The covariance matrix of algebraic equations (pressure) is also fixed at  $4 \times 10^{-4}$ . The measurement covariance,  $R$ , is also assumed in the same manner with  $6.4 \times 10^{-5}$ ,  $2.5 \times 10^{-5}$  and  $4 \times 10^{-6}$  for mole fraction, temperature and pressure measurements, respectively. It should be mentioned that temperature and pressure variables are normalized using 580 K and 55 atm, respectively. The sampling time is chosen as  $\Delta t = 5$  s and the state estimation is performed for 100 time instances. The error covariance is  $P_0 = 10^{-6} I_{176 \times 176}$ . The condition in Remark 2.3 applies here also and the correction step for constraint is applied only once in the beginning. Note that since a large portion of the reactant is consumed in the first half of the reactor, it is more desirable to accurately estimate the states

in this zone. Therefore, a random grid-point in the first half of the reactor is chosen to show the performance of the proposed filter. Figure 6-5 and Figure 6-6a show the actual, measured and estimated states at 9<sup>th</sup> grid-point using Filter II with all the states measured. The corresponding RMSE are shown in the figure captions where  $\text{RMSE}_{\text{data}}$  and  $\text{RMSE}_{\text{est}}$  represent RMSE in measured and estimated values, respectively. Clearly, estimated values have smaller errors compared to the measurements, thus, the proposed filter performs reasonably. It should be mentioned that for better visualization, Figure 6-5 and Figure 6-6 are shrunk for the first 30 time instances although the calculations of RMSE and SSE values are based on 100 time instances. In order to avoid comparing the RMSE of large number of variables for Filter I and Filter II in this example, the superiority of the proposed filter, Filter II, is shown by comparing SSE values and also RMSE values at 9<sup>th</sup> grid-point for the algebraic variable P. The SSE values are 10.312 and 6.819 for Filter I and Filter II, respectively. Comparing the SSE values, the proposed filter results in estimated values significantly closer to the actual values as the squared error is reduced approximately by 33%. Moreover, higher  $\text{RMSE}_{\text{est}}$  for Filter I than  $\text{RMSE}_{\text{data}}$  shows that the filter fails to outperform the measurements and produce unreliable estimates while Filter II results in estimates with lower errors than that of measurements. The state estimation results are presented in Figure 6-6a and Figure 6-6b for Filter II and Filter I, respectively. From Figure 6-6, it can be seen how accurately Filter II tracks the changes in algebraic state compared to Filter I. As mentioned before, this is due to the fact that Filter II correctly accounts for the presence of noise in the algebraic state. Consequently, this is reflected in the quality of the state estimates.

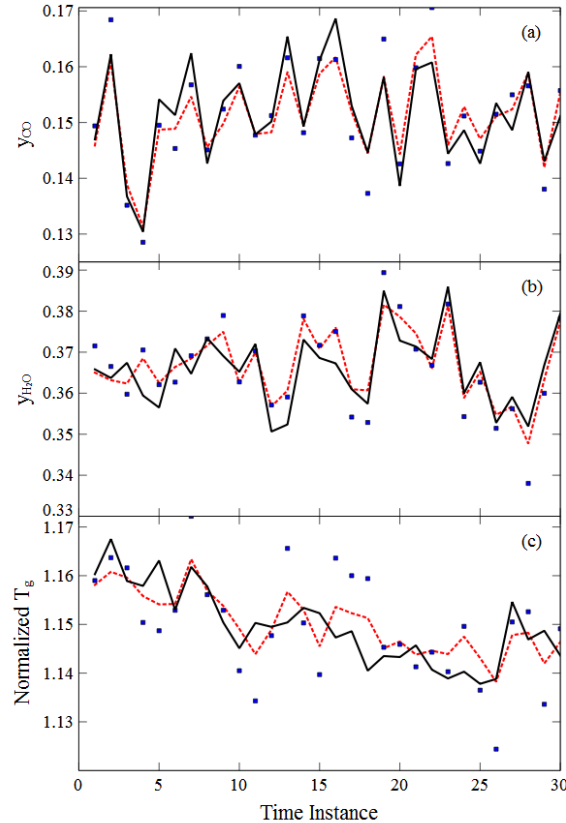


**Figure 6-5. Actual (-), measured (\*) and estimated (---) value at 9<sup>th</sup> grid-point on the reactor for (a)  $y_{CO}$  ( $\text{RMSE}_{\text{data}} = 5.005 \times 10^{-3}$ ,  $\text{RMSE}_{\text{est}} = 3.852 \times 10^{-3}$ ) (b)  $y_{H_2O}$  ( $\text{RMSE}_{\text{data}} = 5.003 \times 10^{-3}$ ,  $\text{RMSE}_{\text{est}} = 3.827 \times 10^{-3}$ ) (c)  $T_g$  ( $\text{RMSE}_{\text{data}} = 7.978 \times 10^{-3}$ ,  $\text{RMSE}_{\text{est}} = 4.945 \times 10^{-3}$ )**

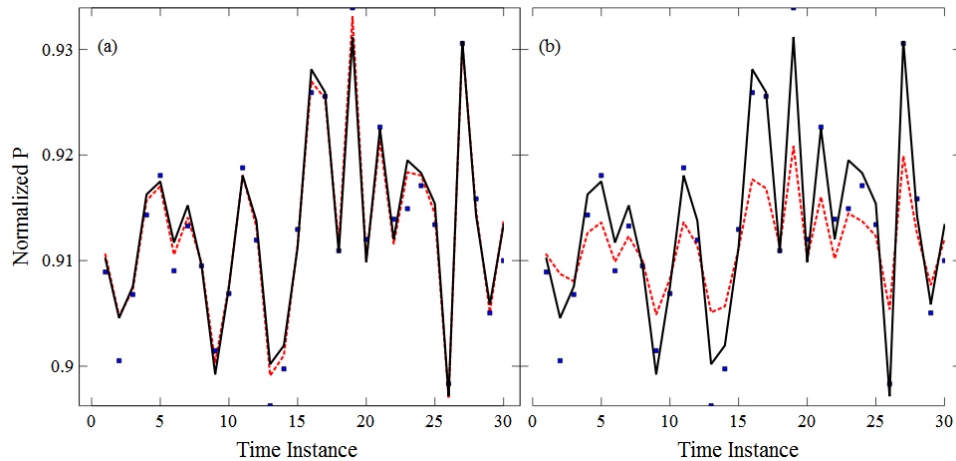


**Figure 6-6. Actual (-), measured (\*) and estimated (---) value at 9<sup>th</sup> grid-point on the reactor for (a)  $P$  ( $\text{RMSE}_{\text{data}} = 1.998 \times 10^{-3}$ ,  $\text{RMSE}_{\text{est}} = 0.894 \times 10^{-3}$  using Filter II) (b)  $P$  ( $\text{RMSE}_{\text{est}} = 5.312 \times 10^{-3}$  using Filter I).**

### 6.2.5.3 Discussion

In the previous section, our proposed filter which accurately estimates the states, especially the algebraic states, was used to estimate the states in the WGSR example. In the WGSR example, however, all the states are measured for the purpose of filtering. Practically, it is neither possible nor economical to measure all the states in the WGSR. In operating plants, as the budget and integrity of the equipment items limit the number and type of sensors that can be used for monitoring the process, state estimation becomes a challenge. Increasing the number of sensors results in more accurate estimates of the variables. On the other hand, reducing the number of sensors requires identifying the most important variables that, if measured, will lead to accurate state estimates. However, the following questions arise. What should be the type and location of the sensors? How much does each measurement type and location contribute to the accuracy of the state estimates especially when using a rigorous filter for state estimation? To answer these questions, we begin by evaluating the case where only a few measurements are available. First, it is assumed that measurements are mutually exclusive and only available at fixed locations for similar states (i.e. only mole fractions of CO,  $y_{CO}$ , or, only gas temperature,  $T_g$ , at fixed locations). The fixed grid-points are assumed to be 1<sup>st</sup>, 5<sup>th</sup>, 9<sup>th</sup>, 13<sup>th</sup>, 17<sup>th</sup> and 21<sup>st</sup> grid-points. For satisfying product specification, product concentration, temperature and pressure are usually monitored at the reactor outlet. Therefore, in subsequent studies it is assumed that all the states except the catalyst temperature,  $T_{cat}$ , are always measured at the outlet of the reactor (25<sup>th</sup> grid-point). Table 6.4 shows the SSE values for the corresponding available measurements with  $T = 100$ . As seen in Table 6.4, the lowest estimation error is achieved if the measurements of CO mole fraction ( $y_{CO}$ ) are available. In contrast, if measurements of only pressure ( $P$ ) are available, estimation error is comparatively higher than others in Table 6.4. Therefore, it can be concluded that the type of the variable that is being measured contributes to the accuracy of the estimation, and if identified, it can result in better estimation accuracy.

**Table 6.4. Sum of squared errors value when fixed points measure the same type of states**

SSE value	Measured state type					
	$y_{CO}$	$y_{H_2O}$	$y_{CO_2}$	$y_{H_2}$	$T_g$	P
	31.889	35.522	34.626	35.500	36.077	37.790

Next, we investigate how informative are each of the fixed measurement locations when only  $y_{CO}$  is measured. Therefore, six independent cases are considered, where in each case it is assumed that one of the measurement locations is unavailable and information from only 5 other measurement locations are used for state estimation. Table 6.5 shows the SSE values for each of these state estimations with  $T = 100$ . Table 6.5 shows that the 13<sup>th</sup>, 17<sup>th</sup>, and 21<sup>st</sup> grid-points have the highest impact on the accuracy of the estimates with approximately minimum 3% increase in the overall squared estimation error in absence of measurements from each of these grid-points individually. Moreover, even with one less measurement of  $y_{CO}$ , measurement of  $y_{CO}$  results in better estimation accuracy in comparison to the cases where temperature or pressure are measured. Next, we investigate if measurements from other variables at different locations combined with measurements of  $y_{CO}$  can actually improve the accuracy of the estimates while the total number of locations are still six. For this study,  $y_{CO}$  measurements from the 13<sup>th</sup> and 17<sup>th</sup>, and 21<sup>st</sup> grid-points, which have highest impact on the accuracy, are combined with a measurements of temperature and  $y_{H_2O}$ . Table 6.6 shows SSE values when combinations of variables are measured at different locations. Since the number of combinations of the type and locations is large, only a few combinations are considered and shown in Table 6.6. Interestingly, combinations 2, 8 and 11 show improvement over when only  $y_{CO}$  is measured. Moreover, in practice, if a measurement of  $y_{CO}$  can be replaced by a temperature measurement that is significantly cheaper, a considerable reduction in cost can be achieved. This means that not only the type of the measured variable contributes to the accuracy of the state estimates, the location where each of these variables are measured also contributes to the accuracy of the estimated values. However, if one were to consider all of the grid-points on the WGSR as candidate locations and pick the location and type of the variables with fixed total number of variables, a large number of combination need to be evaluated. This motivates

further research on the development of systematic ways to answer the question: what are the best types and locations of sensors on WGSR in order to generate the most accurate estimates with limited budget?

**Table 6.5. Sum of squared errors with one missing measurement**

SSE value	Removed measurement location						
	None	1 <sup>st</sup>	5 <sup>th</sup>	9 <sup>th</sup>	13 <sup>th</sup>	17 <sup>th</sup>	21 <sup>st</sup>
31.889	32.119	32.171	32.439	32.982	33.315	33.572	

**Table 6.6. SSE values with measurement combination**

Iteration	Locations	SSE value
1	$T_g[21]$ $y_{CO_2}[13]$ $y_{H_2O}[5]$	32.160
2	$T_g[5]$ $y_{CO_2}[9]$ $y_{H_2O}[5]$	31.685
3	$T_g[13]$ $y_{CO_2}[5]$ $y_{H_2O}[21]$	32.087
4	$T_g[9]$ $y_{CO_2}[13]$ $y_{H_2O}[21]$	31.966
5	$T_g[5]$ $y_{CO_2}[13]$ $y_{H_2O}[17]$	31.906
6	$T_g[9]$ $y_{CO_2}[17]$ $y_{H_2O}[1]$	32.035
7	$T_g[5,13]$ $y_{CO_2}[17]$	31.964
8	$T_g[13]$ $y_{CO_2}[5,9]$	31.493
9	$T_g[21]$ $y_{CO_2}[1,17]$	32.003
10	$T_g[17]$ $y_{CO_2}[5,21]$	32.325
11	$T_g[5]$ $y_{CO_2}[1,21]$	31.432
12	$T_g[17]$ $y_{CO_2}[9,21]$	31.931

### 6.2.6 Optimal Distributed Sensor Placement

For simplicity, it is assumed that gas temperature, species mole fractions and pressure variables are available for measurements at each grid points and the measured values for all type of measurements are available at the same time. However, it may be difficult to make concentration measurements in practice and availability of all measured values at the same time may not be practically feasible. But, this work can be considered with the assumptions that the most easiest and rapid measurements are from temperature

and perform the sensor placement for the case that only temperature measurements can be made. Also, the EKF can be tailored for the case when there are delayed measurements and so on.

### 6.2.6.1 Steady-state solution

Table 6.7 shows the parameters considered in the WGSR reactor. The system of equations are consist of 176 equations which are solved in MATLAB using 'fsolve' function; and the steady-state solution for the parameters shown in Table 6.7 is obtained.

**Table 6.7. Water gas shift reactor model parameters**

Parameter	Value	Parameter	Value
Inlet steam and gas pressure (Pa)	5,626,121	Inlet steam and gas temperature (K)	580
Diameter (mm)	0.1	Syngas Valve Opening (%)	50
Density (g/cm <sup>3</sup> )	0.65	Syngas Valve coefficient	$6 \times 10^{-5}$
Catalyst Thermal conductivity (W/m-K)	35	Steam Valve Opening (%)	50
Porosity	0.38	Steam Valve coefficient	$2 \times 10^{-5}$
tortuosity	5	Syngas mole fractions	CO      0.31 H <sub>2</sub> O    0.26 CO <sub>2</sub> 0.13 H <sub>2</sub> 0.30
Specific heat (J/Kg-K)	880	Reactor Length (m)	1
		Reactor diameter (m)	0.5
		Number of grid points	25

### 6.2.6.2 Actual data

The actual data used in the GA's objective function is obtained by simulating the WGSR over a certain period of operation time and the actual data is stored at each sampling time. Noise simulation in the actual data is performed in two steps: (i) Noise with known variance in differential state are added after the states are integrated from  $k$  to  $k+1$  using DAE solver (ii) after integration and obtaining noisy differential states, noise in algebraic states are introduced by solving algebraic equations with presence of algebraic noise with known variance. Random noise terms with known variances are added to the initial states and the initial noisy data along with the stored data at each time instant are considered as the actual data. In our work, process time is assumed as 200 seconds with a sampling time of 5 seconds. Therefore, a total of 41 set of data are obtained for use in GA. The measured values are obtained by adding the random noise with known variance to the corresponding actual values.

### 6.2.6.3 Sensor placement results

Based on the model descriptions explained in the previous sections, five different models are formulated and the performances of these models in the sensor placement framework are compared. The result of these comparisons will be a recommendation of an appropriate model that can be used for study of the effect of different parameters on the sensor placement results. The models that are evaluated are as follows: (1) *Model I*: In this model, both state and error propagations are performed using the detailed model shown in Eqn. (6.10) (2) *Model II*: In this model, state propagation is performed by integrating the simplified model, but, the error propagation is performed by computing the numerical Jacobian matrix around the current state estimates using the detail model (3) *Model III*: This model has both state and error propagations performed using the simplified model. In this model, the covariance of the noise in the simplified model is assumed to be equal to the covariance of the noise in the detail mode (i.e.  $10^{-3}$  for both  $T_g$  and H<sub>2</sub>O mole fractions) and the exogenous equations are assumed to be noise free ( $\Gamma_{k+1} = \mathbf{0}$ ), consequently, no state constraints) (4) *Model IV*: This model is similar to *Model III* except that here the error covariance matrix is tuned to account for the lost information due to the model simplification, i.e. absence of assuming correlated noise in mole fractions. (5) *Model V*: In

this model, as shown in Eqn. (6.42), it is assumed that the exogenous algebraic states are not noise free ( $\Gamma_{k+1} \neq \mathbf{0}$ ) and a corresponding error covariance matrix is added in the error propagation step as in Eqn. (6.46) to account for the noise in CO<sub>2</sub>, CO, H<sub>2</sub> mole fractions and  $T_{cat}$ . Since it is theoretically difficult to account for the correlated noise while the equations are decoupled, therefore, the error covariance matrices are tuned to account for such information loss. Table 6.8 shows the parameters used in each model for state estimation.

**Table 6.8. Process noise variance values for different models**

Noise Term	Model				
	I	II	III	IV	V
$\omega$	$y: 10^{-3}$	$y: 10^{-3}$			
	$T_g: 10^{-3}$	$T_g: 10^{-3}$			
$\nu$	$y: 10^{-3}$	$y: 10^{-3}$	$y: 10^{-3}$	$y: 10^{-3}$	$y: 10^{-3}$
	$T_g: 10^{-3}$	$T_g: 10^{-3}$	$T_g: 10^{-3}$	$T_g: 10^{-3}$	$T_g: 10^{-3}$
$\gamma$	$P: 5 \times 10^{-3}$	$P: 5 \times 10^{-3}$	$P: 5 \times 10^{-3}$	$P: 5 \times 10^{-3}$	$P: 5 \times 10^{-3}$
	$P: 10^{-3}$	$P: 10^{-3}$	$P: 10^{-3}$	$P: 10^{-3}$	$P: 10^{-3}$
$\omega_2$		$y_{H_2O}: 10^{-3}$	$y_{H_2O}: 2.5 \times 10^{-3}$	$y_{H_2O}: 3.7 \times 10^{-4}$	
		$T_g: 10^{-3}$	$T_g: 9 \times 10^{-4}$	$T_g: 8 \times 10^{-4}$	
$\Gamma$				$y_{CO}: 10^{-3}$	
				$y_{CO_2}: 10^{-3}$	
				$y_{H_2}: 10^{-3}$	
				$T_{cat}: 10^{-3}$	

Sensor placement is explored for a fixed number of sensors (50) by running GA for each model separately. Figure 6-7 shows normalized fitness values for each model as the GA searches for the optimal sensor placement. It should be noted that the fitness values are normalized by the fitness value that is obtained if all available states are measured. In Figure 6-7, *Model I* has the highest fitness as the sensor placements are obtained using the detailed model that has no information loss. *Model II* shows interesting results in terms of

fitness value compared to *Model III* and *Model IV* as the only difference is that *Model II* uses Jacobian matrix computed from the detailed model. This shows that more accurate Jacobian matrix for error propagation can compromise for loss of information due to use of less accurate model for state propagation. *Model V* provides higher fitness compared to *Model III* and *IV* although it is fully based on the simplified model. This shows the importance of considering presence of noise in algebraic states while considering a DAE system.

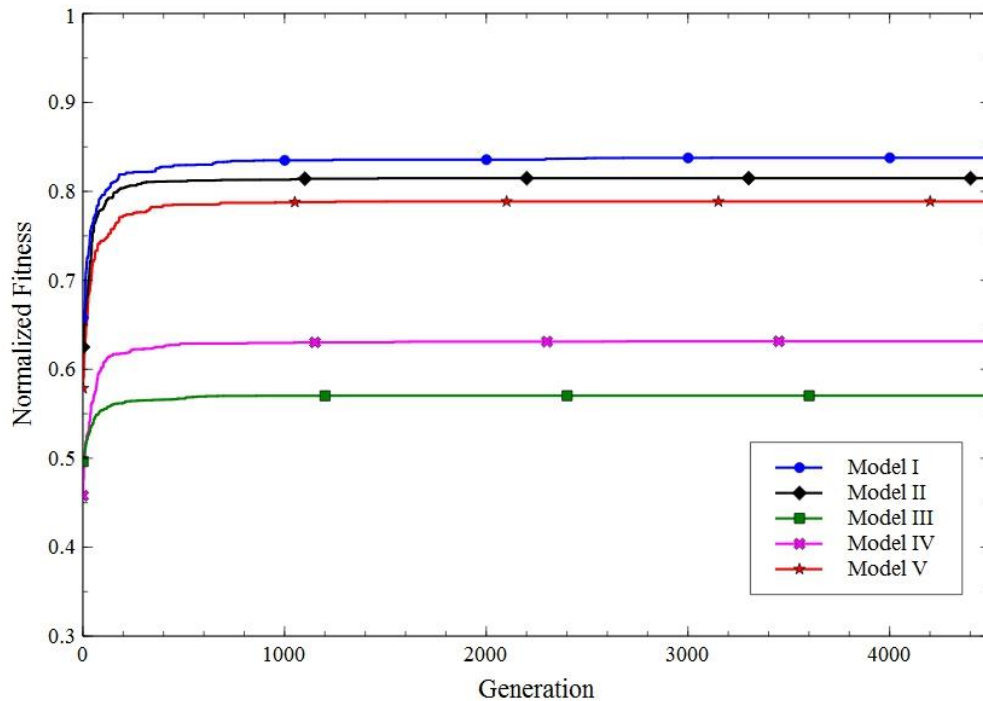


**Figure 6-7. Normalized fitness evolution for each model**

The main incentive for considering the simplified model is to achieve reduction in computation time. Although the fitness values of each model in Figure 6-7 shows the performance of each model for state estimation, the final sensor placement results of each model must be checked against the detailed model, therefore, the reduction in computation time and sensor location of each final results will be compared. Table 6.9 shows the detailed analysis of the final solution of each model. In Table 6.9, *Model I* is the benchmark as it represents the full use of detailed model and therefore, other models are compared

against *Model I*. The first 6 columns of Table 6.9 show the number of sensors picked after 4500 generations of the GA optimization for each type of variables out of 25 available candidate locations on the reactor. Values in the parenthesis represent the number of sensors that have similar location as the sensors picked using *Model I*. As can be seen in Table 6.9, none of the models except *Model III* pick any pressure sensors (*P*) mainly because the system pressure is very high and therefore, slight variation in the system pressure due to the process noise has very little effect on the accuracy of the state estimates. The best solution, *Model I*, has selected only a temperature sensor ( $T_g$ ). It is also observed that through optimal placement of sensors, it is possible to achieve 84% of accuracy compared to the case where all states are measured. However, the average time to achieve the optimal solution is relatively high when compared to the simplified models. For example, the average time can be reduced up to approximately one-fifth of the original time when considering *Model V*. Number of temperature sensors picked by simplified models are relatively higher compared to *Model I*, this is because that gas temperature is the only differential variable in the simplified models and accurate estimation of the only differential variable can affect the accuracy of the state estimates. However, as *Model III* and *Model IV* assume the exogenous algebraic equations are exact, considering the existence of noise in these equations (*Model V*) resulted in elimination of the temperature sensor due to uncertainty in exogenous algebraic states compared to *Model III* and *IV*. *Model II* shows significant reduction in computation time while maintaining high fitness (0.83) in comparison to *Model I*. Although *Model III* and *IV* show significant computation time reduction, neglecting the process noise has resulted in significant information loss and therefore results in lower fitness value calculated by both GA and the detailed model. Among all simplified models, *Model V* shows the least computation time. Moreover, *Model V* results in reasonably good estimates when compared to *Model I*. This is due to fact that *Model V* accounts for process noise in algebraic variables, and therefore results in better estimates in comparison to other models. Therefore, *Model V* is a very good compromise between estimation accuracy and computation time.

**Table 6.9. Sensor placement results and computation time for each model**

Model	Number of sensors (Number of sensors similar to <i>Model I</i> )						Fitness	Average CPU time per generation (s)	
	CO	H <sub>2</sub> O	CO <sub>2</sub>	H <sub>2</sub>	T <sub>g</sub>	P		in GA	in detail
<i>I</i>	17	6	17	9	1	0	0.84	0.84	16.69
<i>II</i>	16 (16)	6 (5)	17 (17)	6 (6)	5 (1)	0 (0)	0.81	0.83	7.03
<i>III</i>	20 (15)	10 (3)	13 (11)	4 (2)	2 (0)	1 (0)	0.57	0.78	3.84
<i>IV</i>	20 (15)	5 (1)	15 (12)	8 (4)	2 (0)	0 (0)	0.63	0.78	3.83
<i>V</i>	19 (17)	6 (2)	18 (16)	7 (7)	0 (0)	0 (0)	0.79	0.82	3.63

#### 6.2.6.4 Study of Number of Sensors

From the perspective of installation and maintenance, it is more desirable to reduce the number of sensors while achieving reasonable state estimates. Therefore, sensor placements are evaluated for different number of candidate sensors and the results are tabulated. Different number of candidate sensors involves the assumption that all the candidate locations are available but restricts the total number of sensors that can be placed. This means that, for example, placing temperature and pressure sensors at a same candidate location is considered as two sensors. In Table 6.10, the sensor placement results of *Model V* is compared against the detailed model to study the effect of number of sensors on the performance of the *Model V* and amount of information loss due to reducing the number of sensors. Obviously when the number of sensors is increased, the difference in normalized fitness values of *Model V* and *I* reduces. However, this difference in accuracy can be compensated by the computation burden reduction that is gained by simplified model. For all cases, *Model V* appears to select the H<sub>2</sub>O composition sensors more than the detailed model. This is because H<sub>2</sub>O state has direct effect on the overall estimation accuracy since the exogenous algebraic states are calculated based on the H<sub>2</sub>O state in the simplified model. As the number of sensors increases, more number of composition sensors are chosen while the number of temperature sensors remain fairly the same for both models.

These results are interesting in the sense that the simplified model follows the same trend in picking candidate sensors as the detailed model and maintains good performance while reducing the computation time. It should be noted that the normalized fitness of *Model V* in Table 6.10 and all the subsequent tables represent the normalized fitness of the solution evaluated in the detailed model, *Model I*.

**Table 6.10. Sensor placement results comparison of *Model I* and *Model V* for different number of sensors**

Number of sensors	Normalized fitness		Sensor placement $\left\{ \begin{array}{l} \text{Model } I \\ \text{Model } V \text{ (similar to Model } I) \end{array} \right\}$					
			CO	H <sub>2</sub> O	CO <sub>2</sub>	H <sub>2</sub>	T <sub>g</sub>	P
	Model I	Model V						
10	0.60	0.56	8	0	0	0	2	0
			6 (6)	4 (0)	0 (0)	0 (0)	0 (0)	0 (0)
20	0.69	0.66	13	2	2	2	1	0
			10 (10)	5 (0)	4 (1)	1 (0)	0 (0)	0 (0)
30	0.74	0.71	15	2	9	3	1	0
			15 (14)	4 (0)	9 (6)	2 (1)	0 (0)	0 (0)
40	0.79	0.75	15	3	15	6	1	0
			16 (14)	5 (0)	14 (12)	5 (5)	0 (0)	0 (0)
50	0.84	0.82	17	6	17	9	1	0
			19 (17)	6 (2)	18 (16)	7 (7)	0 (0)	0 (0)

#### 6.2.6.5 Study of Effect of Process Noise Covariance

Process noise covariance has high impact on the accuracy of the state estimates. However, it is not evident how sensor placement is affected and how much of information is lost when process noise covariance is not chosen properly. Table 6.11 shows the sensor placement comparison for *Model I* and *V* for different process noise covariance. In Table 6.11, *Model V-c* has the same parameters as *Model V* in Table 3. Underestimating and

overestimating the process noise covariance, as in *Model V-a* and *V-e*, significantly reduces the performance of the obtained solution. This can be seen as the normalized fitness of the solution obtained using these models has low normalized fitness compared to the other models when evaluated by the detailed model. In addition, for models *V-a*, and *V-e*, the SP algorithm selects significantly more number of temperature sensors than *Model I* while only *Model V-e* selects more number of pressure sensors than *Model I*. In these models, since the accuracy in estimation of H<sub>2</sub>O state has direct effect on the overall estimation accuracy, therefore, more number of H<sub>2</sub>O sensors compared to *Model I* are chosen to increase the normalized fitness and thus the overall accuracy.

**Table 6.11. Effect of process noise covariance on the sensor placement results**

Model	Process noise covariance	Normalize d fitness	Number of sensors (Number of sensors similar to Model I)					
			CO	H <sub>2</sub> O	CO <sub>2</sub>	H <sub>2</sub>	T <sub>g</sub>	P
<i>I</i>	$Q = 10^{-6}$	0.84	17	6	17	9	1	0
	$Q_{H_2O} = 10^{-8}$							
<i>V-a</i>	$Q_{T_g} = 10^{-8}$	0.68	16 (10)	18 (5)	6 (5)	5 (1)	5 (0)	0 (0)
	$Q_{alg} = 10^{-8}$							
	$Q_{H_2O} = (3.7 \times 10^{-4})^2$							
<i>V-b</i>	$Q_{T_g} = (8 \times 10^{-4})^2$	0.78	18 (15)	14 (5)	11 (9)	6 (3)	1 (0)	0 (0)
	$Q_{alg} = 10^{-8}$							
	$Q_{H_2O} = (3.7 \times 10^{-4})^2$							
<i>V-c</i>	$Q_{T_g} = (8 \times 10^{-4})^2$	0.81	19 (17)	6 (2)	18 (16)	7 (7)	0 (0)	0 (0)
	$Q_{alg} = 10^{-6}$							

	$Q_{H_2O} = 10^{-6}$							
<i>V-d</i>	$Q_{Tg} = 10^{-6}$	0.81	17 (16)	5 (1)	18 (16)	9 (6)	1 (0)	0 (0)
	$Q_{alg} = 10^{-6}$							
	$Q_{H_2O} = 10^{-4}$							
<i>V-e</i>	$Q_{Tg} = 10^{-4}$	0.67	7 (7)	16 (5)	9 (8)	8 (4)	4 (0)	6 (0)
	$Q_{alg} = 10^{-4}$							

---

### 6.2.6.6 Study of Effect of Initial Error Covariance

In this part, we examine the effect of initial error covariance of *Model V* on the SP results and compare it with the SP results of *Model I* as shown in Table 6.12. After simulating the process for obtaining the actual data, additive white Gaussian noise with known variance is added to the initial states to represent the noisy initial states. The effect of initial error covariance is studied by varying the noise covariance matrix of the initial states according to the values in Table 6.12. In all models, *Model V-a* through *c*, no temperature and pressure sensors are selected while more H<sub>2</sub>O sensors are selected in comparison to the detailed model. Overall, the sensors that are similar to the detailed model are relatively high for all three models. In addition, in all three models, the normalized fitness of the solution remains reasonably high and confirms their reliability for not only state estimation, but also for SP. It is worth mentioning once again that in calculating the fitness of these models, the first set of state estimates are ignored and the corresponding fitness and its normalizing fitness are calculated without considering the quality of the initial estimates. It can be seen from Table 6.12 that the choice of initial error covariance has minor effect on the SP results.

**Table 6.12. Effect of initial error covariance on the sensor placement results**

Model	Initial error covariance matrix	Normalized fitness	Number of sensors (Number of sensors similar to <i>Model I</i> )					
			CO	H <sub>2</sub> O	CO <sub>2</sub>	H <sub>2</sub>	T <sub>g</sub>	P
<i>I</i>	P <sub>0</sub> = 10 <sup>-6</sup>	0.84	17	6	17	9	1	0
V-a	P <sub>0</sub> = 10 <sup>-4</sup>	0.81	18 (17)	8 (2)	17 (16)	7 (6)	0 (0)	0 (0)
V-b	P <sub>0</sub> = 10 <sup>-6</sup>	0.82	19 (17)	6 (2)	18 (16)	7 (7)	0 (0)	0 (0)
V-c	P <sub>0</sub> = 10 <sup>-8</sup>	0.82	19 (17)	7 (0)	17 (16)	7 (6)	0 (0)	0 (0)

### 6.3 Conclusion

Previous EKF frameworks for DAE systems published in the literatures assume that algebraic equations are exact. However, in practice, algebraic equations could be describing a physical state and derived using modeling assumptions which introduces uncertainties in these process equations. Therefore, stochastic algebraic equations cannot be handled in the previous EKF formulations due to differentiation of white noise which is not well-defined. Moreover, extra information about the process may be present in the form of implicit equality constraints, such as mole balance in a reactor, which cannot be handled by previous EKF frameworks. A modification to the EKF approach that addresses these difficulties by avoiding the differentiation of the algebraic equations is proposed. The error covariances of algebraic variables are propagated as linear and non-linear combinations of error covariance of differential variables. The performance of the proposed filter is demonstrated through two examples. In the simple example, it is shown that estimates are improved over the measurements as RMSE of estimated states are considerably reduced in comparison to the RMSE of the measured data. In the WGSR example, the filter also shows considerably higher estimation accuracy of the states over the measurements when all states are measured. In both examples, the proposed filter shows superiority over the previous filtering framework by returning estimates with lower RMSE and closer to the actual values. Application of the proposed filter to the WGSR revealed that the type and

location of the sensors used on the WGSR have important role in the accuracy of the state estimates.

A framework for sensor placement of water gas shift reactor is also described in this chapter. The proposed framework combines the state estimation technique with an evolutionary algorithm to obtain the optimal sensor locations (and types) that return most accurate estimates of the process states for a fixed number of sensors. The state estimation technique used in this work has been developed in our previous work for the models that are described by the differential and algebraic equations (DAE). The developed extended Kalman filter (EKF) for DAE is suitable for implementation on the reactor. The 1-D detailed model of the reactor is discretized along the reactor axis to convert partial differential equations to ordinary differential equations (ODE). This results in solving the complex mathematical equation of the reactor model at each discretization point while the discretization points pose as available locations for measurement for EKF. However, number of discretization points and number of equations that must be solved at each point result in high computation time and gives rise to a need for simpler models. A common way to reduce the computational complexity of detailed models is to linearize the model around the operating point. However, since a main future application of this work is to come up with sensor placements for fault detection and identification, linearized models are ruled out due to severe drift of these model from normal operating condition as a consequence of process faults; and also linearized form of highly non-linear models carry much less information of the process and causes difficulties in tracking crucial process variables. A simplified model through scaling analysis developed in previous sections that is promising in effective reduction of complexity of the system while maintaining reasonable accuracy is used in sensor placement. The EKF for DAE is briefly re-derived for simplified reactor model. As a result, different state estimation formulations of the system can be derived based on the model simplifications. A genetic algorithm (GA) is used to generate measurement models for use in the state estimations which represent the sensor placements. GA searches over possible measurement models to obtain an optimal sensor placement that result in most accurate state estimates. The GA is performed for different EKF formulation and the results are compared. A significant reduction in computation time is observed by using the simplified model. However, the accuracy of

each model seems not only affecting the quality of state estimates, but, different sensor placements are obtained by these model. Model V seems superior to the other models as it has lowest computation time, relatively high state estimates accuracy and closest SP results to the detailed model.

As a brief summary, the goal in this chapter was to develop a novel framework for component-level sensor placement and address issues of using comprehensive models that gives rise to computational complexities. Our analysis has shown that using an appropriate simplified model can be an advantage in terms of reducing computational complexity while achieving reasonable sensor placements that can result in performance as good as the detailed model. This analysis has shown that using simplified model in both state and error propagation can further reduce the computational load; and when appropriately tuned, it can replace the complex detailed model as the study of process noise covariance suggests. Study of the initial error covariance has shown insignificant change of the placement and performance of the solution.

An application of the proposed framework is to obtain optimal sensor placements that can help in estimation of the faults in a system. Take catalyst deactivation in a reactor due to thermal cycling, ash decomposition and etc. as an example. One is interested in locating such abnormality in a lengthy reactor by optimally placing sensors on the reactor that not only identifies that somewhere catalyst is being/has deactivated, but, also interested in locating such abnormality and prepare for preventive/corrective action. In economical viewpoint, since reactors' catalyst are usually removed and replaced by fresh catalyst after certain time, locating the area with deactivated catalyst reduce the catalyst replacement cost. In process viewpoint, an optimal sensor placement can help in better monitoring the process and asses the estimation of faults that can degrade the process or drive the system to hazardous conditions. Therefore, for 2-tier sensor placement, we will focus on designing a sensor network that can help in estimating the possible fault that can harm the process operation and/or production.

## Chapter 7

# Implementation of 2-Tier Sensor Placement on Gasification Island Process

### 7.1 Fault Simulation

For the fault simulation on the SELEXOL side of the gasification island, different faults are selected as compared to Section 4.7.4. The new faults simulated are as follows.

- CO<sub>2</sub> Absorber fault: Fault is simulated by reducing the 15<sup>th</sup> tray area as syngas enters from bottom.
- H<sub>2</sub>S absorber fault: Fault is imulated by reducing the 26<sup>th</sup> tray area. This tray is in the vicinity of stream coning from SWGSR, stream rich with H<sub>2</sub>S coming from SELST and gas turbine outlet containing CO<sub>2</sub> and H<sub>2</sub>. Possible reasons for this fault can be sulfur deposition or ash/soot carried along SWGSR.
- H<sub>2</sub>S concentrator fault: Fault is simulated by reducing the 5<sup>th</sup> tray area. N<sub>2</sub> stream enters at this tray. Possible reason for this fault can be due to particulate matter entrained in it.
- SELEXOL stripper fault: Fault is simulated by reducing the 6<sup>th</sup> tray area. This is the feed tray for stream coming from H<sub>2</sub>S concentrator. Deposit of particulate matters or other degradation products can lead to this fault.
- H2SSTRBT heat exchanger: Fault is simulated by considering the fouling in this heat exchanger. H2SSTRBT is an important heat exchanger that heats the stream coming from the bottom of the H<sub>2</sub>S absorber and sends it to the H<sub>2</sub>S concentrator using the lean solvent stream.
- The heat exchanger PRCRE: Fault is simulated by considering the fouling in this heat exchanger. PRCRE is a heat exchanger that is used to cool down the solvent stream to the CO<sub>2</sub> absorber.

Multiple severities of the above faults are considered as shown in Table 7.1.

**Table 7.1. Faults simulated on the SELEXOL side of the integrated model**

Fault	Description
F <sub>1-3</sub>	Reduction in the area of the bottom (15 <sup>th</sup> ) tray of the CO <sub>2</sub> absorber × 3
F <sub>4-6</sub>	Reduction in the area of the bottom(26 <sup>th</sup> ) tray of the H <sub>2</sub> S absorber × 3
F <sub>7-9</sub>	Reduction in the area of the bottom(5 <sup>th</sup> ) tray of the H <sub>2</sub> S concentrator × 3
F <sub>10-12</sub>	Reduction in the area of the bottom (6 <sup>th</sup> ) tray of the SELEXOL stripper × 3
F <sub>13-15</sub>	Leakage fault at start of heat exchanger H2SSTRBT × 3
F <sub>16-18</sub>	Leakage fault at end of heat exchanger H2SSTRBT × 3
F <sub>19-21</sub>	Fouling fault simulated in heat exchanger H2SSTRBT × 3
F <sub>22-24</sub>	Fouling fault simulated in heat exchanger PRCRE × 3

A more detailed approach to simulate a fault at different locations within the same equipment is developed while simulating Faults F<sub>13-15</sub> and F<sub>16-18</sub>. Both faults are simulated in the HE H2SSTRBT, however, the configurations are different. Faults F<sub>13-15</sub> and Fault F<sub>16-18</sub> are simulated in the following manner as shown in Figure 7-1 and Figure 7-2, respectively.

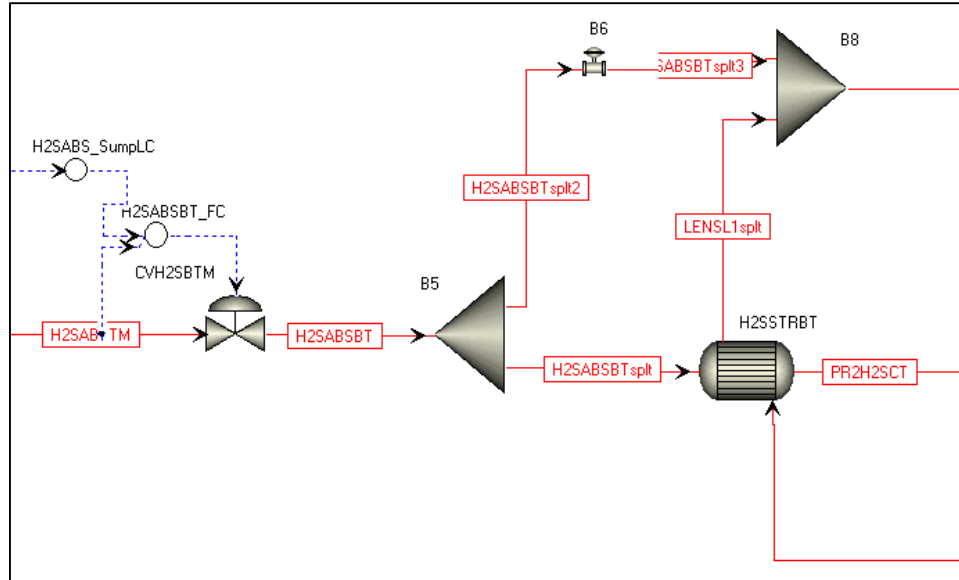


**Figure 7-1. HE configuration 1: leak simulated as mixing of inlet high pressure stream into outlet low pressure stream**

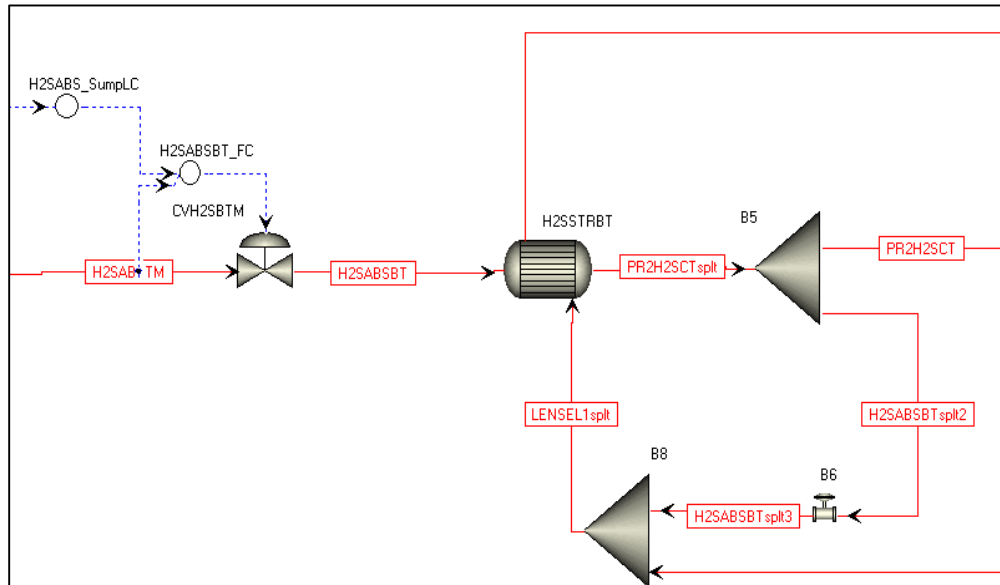


**Figure 7-2. HE configuration 2: leak simulated as mixing of outlet high pressure stream into inlet low pressure stream**

The purpose of simulating the leakage fault in two separate ways is to assess whether the sensor network can give information of the location of the leakage within the heat exchanger. In fault F<sub>13-15</sub>, the leakage has taken place closer to the entrance of the

tubes while in fault F<sub>16-18</sub> it is simulated as if the leakage has taken place towards the outlet of the tube side. This would bring key information into the sensor placement study if it can detect the location within single equipment while considering plant wide faults. Fault F<sub>22-24</sub> is to see whether a sensor network can be found that can distinguish between a leakage fault and a fouling fault within the same equipment.

On the sour WGS reactor side of the integrated model a total of 17 faults, which represent the most common faults that occur in the reactor, are considered. These faults include reduction in porosity, activity and surface area of the catalyst as discussed in earlier chapters. Each type of faults is simulated for three different severities. However, due to technical difficulties, activity reduction, F<sub>31-32</sub>, has only two instances rather than three as other faults. These faults and their corresponding fault number for each severity are shown in Table 7.2. It should be noted that the faults are simulated after five minutes of normal operation.

**Table 7.2. Faults simulated on the sour WGS reactor side of the integrated model**

Fault #	Description	Fault type	Duration	Severity
F <sub>25-27</sub>	Porosity reduction (1 <sup>st</sup> reactor)	Ramp	25min	2%, 5%, 10%
F <sub>28-30</sub>	Porosity reduction (both reactors)	Ramp	25min	2%, 5%, 10%
F <sub>31-32</sub>	Activity reduction (1 <sup>st</sup> reactor)	Ramp	25min	2%, 5%
F <sub>33-35</sub>	Surface area reduction (1 <sup>st</sup> reactor)	Ramp	25min	2%, 5%, 10%
F <sub>36-38</sub>	Surface area reduction (both reactors)	Ramp	25min	2%, 5%, 10%

### 7.1.1 Study of Fault Effects

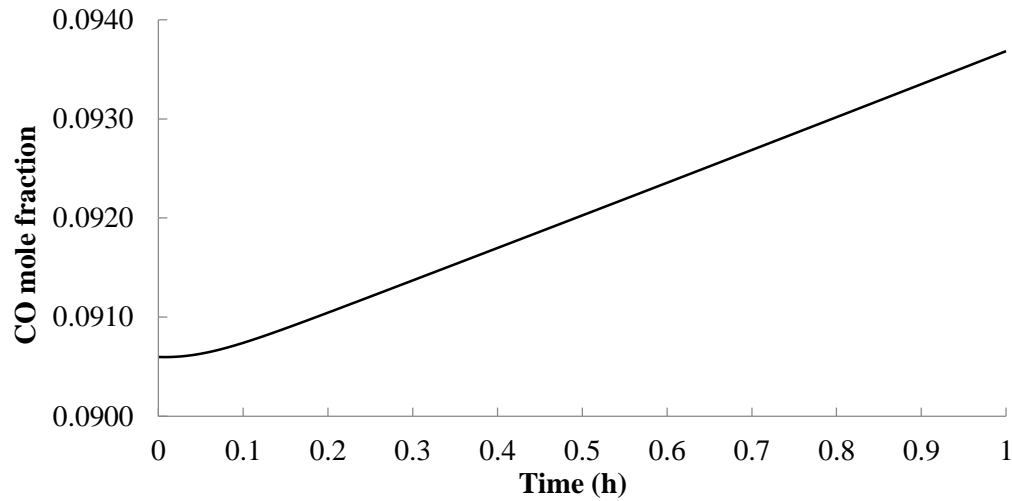
Before simulating the faults in the gasification island, it is important to implement the control configuration as would be expected in an actual operating plant. In the sour WGS reactor system, the syngas flowrate is maintained for producing the desired amount of power by the IGCC plant. In addition, the CO/H<sub>2</sub>O ratio at the inlet of the WGS reactor system is maintained by manipulating the steam flowrate to the reactors. These two

controllers have been coded in MATLAB for manipulating valves  $V_1$  and  $V_2$ . The controllers were then tuned for satisfactory response.

The integrated system is used to simulate some typical faults. The responses of process variables to faults are necessary for both system- and component-level sensor placement. Although detailed explanations of faults considered in the gasification island for 2-tier sensor placement are given in Chapter 7, here, we study the effect of different faults on the key process variables. As an example, the results due to change in porosity of reactor  $R_1$ , will be studied here. This fault is expected to happen in a sour WGS reactor system as part of an IGCC plant since tar or soot that are generated in the gasifier can escape the scrubber and could enter the reactor and clog the pores of the catalyst. As a result of this, the reaction rate reduces and yield could suffer. For this fault, it is assumed that the unwanted material is captured by the first reactor alone, and thus only the porosity of  $R_1$  is ramped down. This is done at a rate of 25% decrease in catalyst porosity over a period of 12 hours. The responses of different process variables to this fault are then investigated. It should be noted that in real-life, such faults can happen over much longer period of time, but here a much faster rate is considered in order to study the capability of the integrated models.

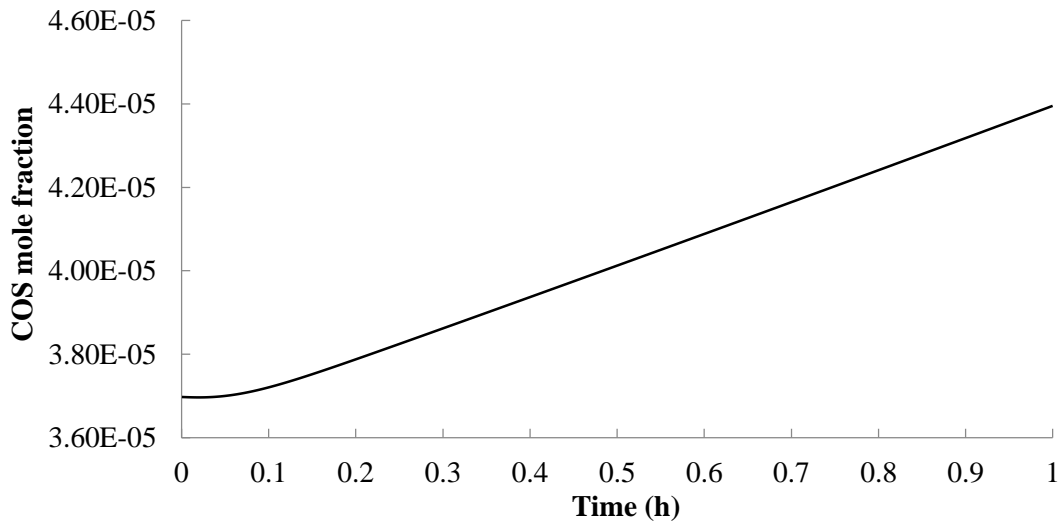
#### **7.1.1.1 Effects on Reactor $R_1$**

Figure 7-3 shows the CO mole fraction at the end of reactor  $R_1$  as the time progresses. As the catalyst pores get clogged and the porosity decreases, the extent of WGS reaction reduces, and thus the amount of CO consumed reduces.



**Figure 7-3.** CO mole fraction transient at reactor R<sub>1</sub> outlet for a ramp decrease in catalyst porosity

The rate of COS hydrolysis also gets affected due to the fault. The amount of COS converted reduces due to the reduction in porosity. Therefore, the COS mole fraction at the end of the reactor R<sub>1</sub> increases. This can be seen in Figure 7-4.



**Figure 7-4.** COS mole fraction transient at reactor R<sub>1</sub> outlet for a ramp decrease in catalyst porosity

Since the WGS reaction is an exothermic reaction, the reaction does not reach equilibrium in the first reactor due to the fault. As the extent of reaction decreases in reactor R<sub>1</sub>, the temperature at the outlet also reduces. This can be seen in Figure 7-5.

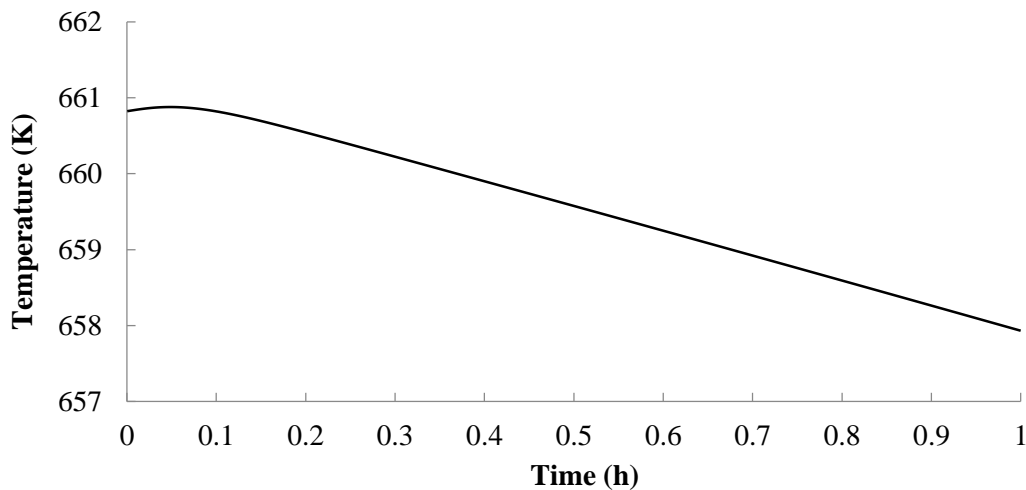
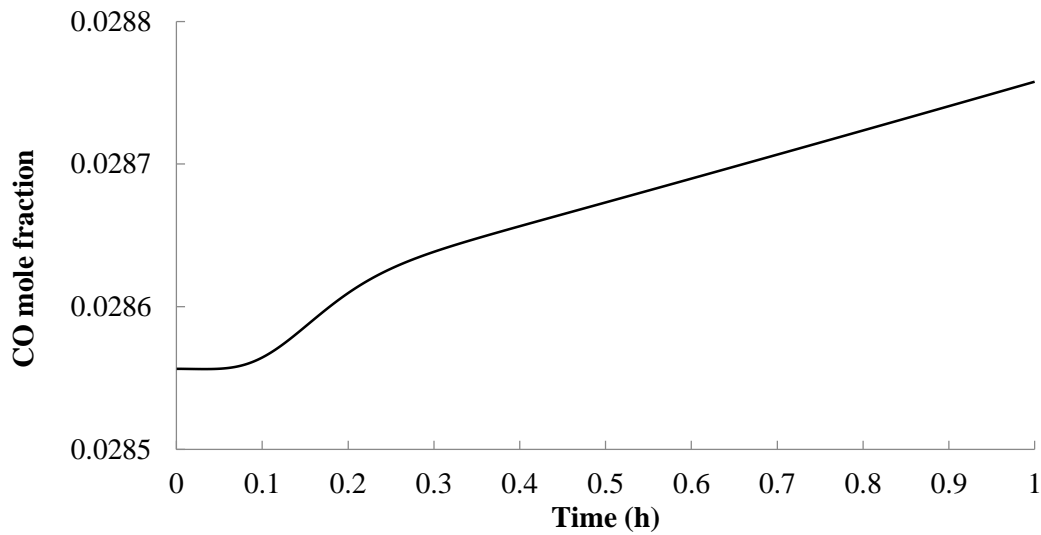


Figure 7-5. Temperature transient at reactor R<sub>1</sub> outlet for a ramp decrease in catalyst porosity

### 7.1.1.2 Effects on Reactor R<sub>2</sub>

Overdesign has been considered in the design of the second reactor, R<sub>2</sub>, to accommodate acceptable deterioration in the performance of reactor R<sub>1</sub>. Due to lower extent of WGS reaction in reactor R<sub>1</sub>, the mole fraction of CO at the inlet of reactor R<sub>2</sub> increases. As a result, higher conversion of CO takes place in R<sub>2</sub>. The WGS reaction in reactor R<sub>2</sub> still approaches the equilibrium, but, it does so at different conditions as compared to condition it had prior to the fault, which is due to the changes in the inlet conditions. From Figure 7-6, it can be seen that the effect of the fault in reactor R<sub>1</sub> has slight impact on the overall conversion at the outlet of reactor R<sub>2</sub>.



**Figure 7-6. CO mole fraction transient at reactor R<sub>2</sub> outlet for a ramp decrease in catalyst porosity**

As seen in Figure 7-7, COS mole fraction seems to show stronger response than CO but the overall change in COS conversion is still negligible.

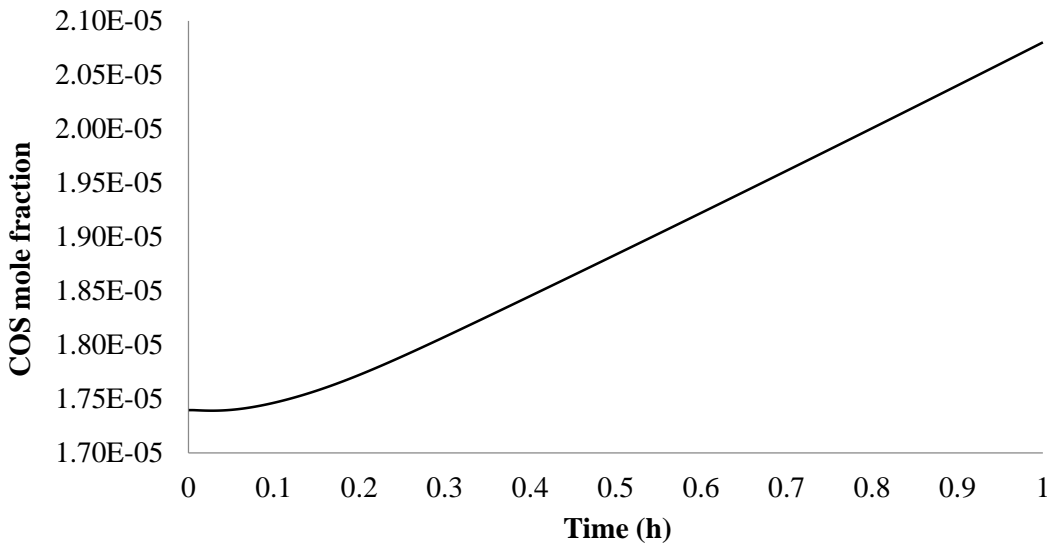


**Figure 7-7. COS mole fraction transient at reactor R<sub>2</sub> outlet for a ramp decrease in catalyst porosity**

Due to the increase in inlet CO mole fraction, more reaction takes place in the reactor R<sub>2</sub>. Due to the exothermic nature of the WGS reaction, as more reaction takes place, the temperature at the exit of the reactor increases. This can be seen in Figure 7-8.

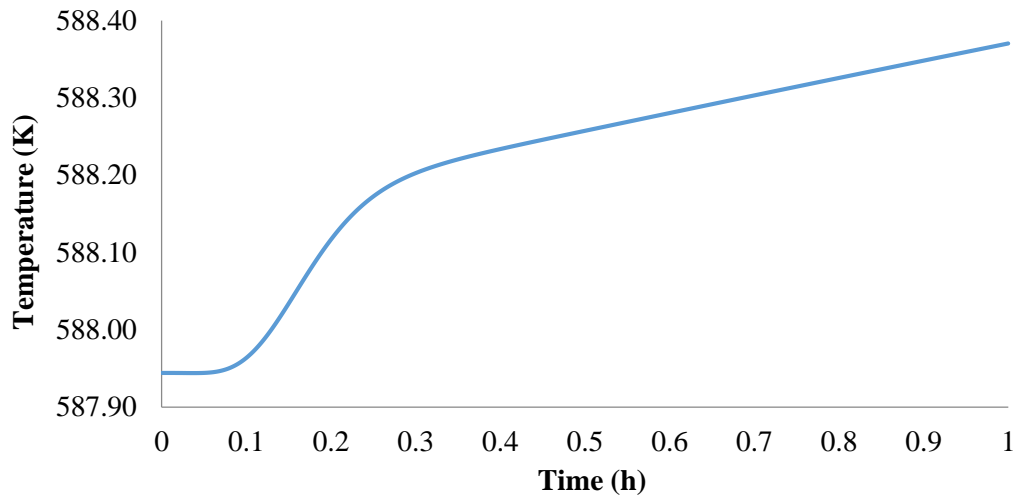


**Figure 7-8. Temperature response at the exit of R<sub>2</sub> as a result of ramp change in porosity.**

The increase in CO mole fraction as a result of the ramp change in catalyst porosity is also reflected at the end of the SELEXOL plant. Figure 7-9 is shows CO mole fraction increases due to this fault. However, it takes around 12 to 13 minutes for this effect to be seen. The changes in the mole fractions of other components are very small to be detected clearly by a measuring device.

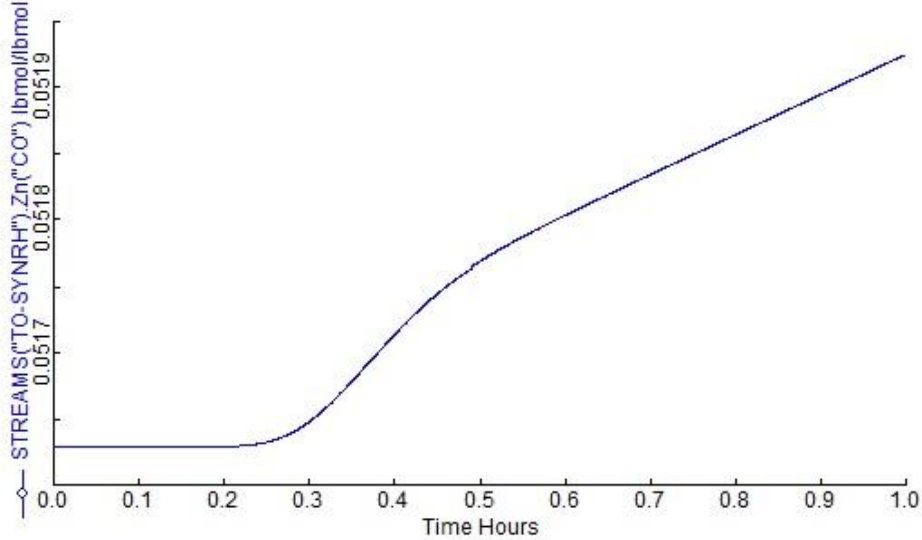


**Figure 7-9. CO response at the exit of the SELEXOL unit as a result of ramp change in porosity.**

## 7.2 Results

### 7.2.1 System-Level: Gasification Island

The system-level sensor placement algorithms are implemented on the gasification island and the results are presented in the Table 7.3. From the case studies in previous sections we have learned that the optimal results are obtained from the combination algorithm (FES & MR). Here, since the magnitude of the faults considered in the gasification island is low (maximum 10% change as a fault), therefore, we can predict that low level MR threshold should be chosen. This can be verified by the results in Table 7.3. The FES & MR algorithm with low MR threshold level has the lowest number of unresolvable faults and sensor network cost. The results of SDG and FES individual algorithm are shown for the sake of comparison. In order to save space, the sensors and unresolved faults of different algorithms are avoided and are shown only for FES & MR with low MR threshold level in Table 7.4. Note that almost all of the sensors picked for resolution are temperature sensors except for a concentration sensor on the first stage sour WGS reactor. Since the temperature sensors are the least expensive sensors in this study, system-level fault resolution has been achieved with a significantly cost effective sensor network. Out of 703 pair of fault sets, only 25 of which, as shown in Table 7.4, cannot be

resolved. This implies that more than 96% of the faults considered in the system can be resolved by a cost effective network of sensors.

**Table 7.3. System-level sensor placement results of gasification island**

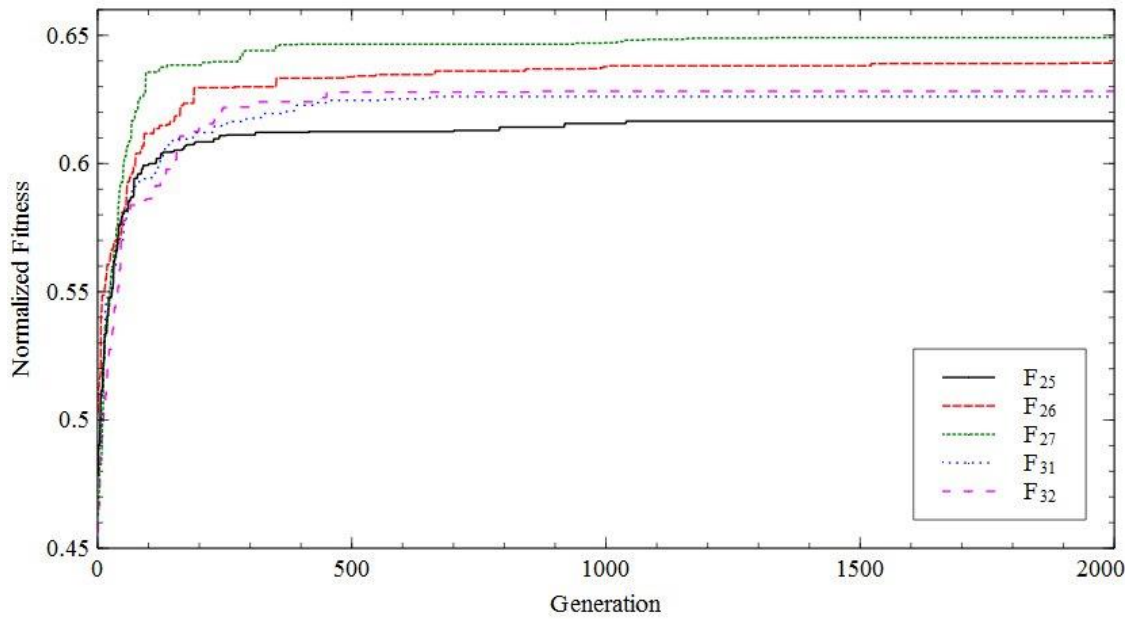
<b>Algorithm(s)</b>	<b>MR threshold level</b>	<b>Number of sensors</b>	<b>Sensor network cost</b>	<b>Number of unresolvable fault sets</b>
SDG		11	2	29
FES		9	0.9	28
MR	Low	10	11.8	28
	Medium	11	2	29
	High	11	2	29
	Low	8	0.8	28
FES & MR	Medium	9	0.9	28
	High	9	0.9	28

**Table 7.4. List of sensors for FES & MR algorithm with low MR threshold level**

<b>Sensor number</b>	<b>Sensor location</b>	<b>Sensor Type</b>
1	Outlet stream of water from 2 <sup>nd</sup> HE before H2S absorber	Temperature
2	Cooled syngas stream from outlet of 3 <sup>rd</sup> HE before H2S absorber	Temperature
3	Syngas stream inlet T to HE right before H2S absorber	Temperature
4	SELEXOL stream after H2SSTRBT fed to H2S concentrator	Temperature
5	Bottoms stream of H2S concentrator	Temperature
6	9 <sup>th</sup> tray in CO <sub>2</sub> absorber	Temperature
7	Temperature sensor at 40% length of R <sub>1</sub>	Temperature
8	Temperature sensor at grid 68% length of R <sub>1</sub>	Temperature

### 7.2.2 Component-Level: First-Stage Sour Water Gas Shift Reactor

The distributed sensor placement is performed on the first stage sour WGS reactor. The actual data for the optimization problem is obtained by simulating the faults in the integrated system for each faults individually. The noise in the data are assumed as additive noise, where white Gaussian noise with known mean and variance is added to each state. The model in the state estimation is chosen as the simplified model where noise in the differential, algebraic and exogenous algebraic states are tuned due to the use of simplified model as explained in Chapter 6. The faults considered in the component-level are  $F_{25}$ ,  $F_{26}$  and  $F_{27}$  for catalyst activity reduction; and  $F_{31}$  and  $F_{32}$  for catalyst porosity reduction. Each fault is assumed as a state and is augmented with other states in the system. Since the faults are modeled as a reduction in the catalyst activity, each fault state is assumed to be associated with a process noise which is also tuned for in the EKF. Table 7.5 shows the reactor and EKF parameters. Figure 7-10 shows the progress of the GA for different faults. As seen in Figure 7-10, with only 30 sensors optimally placed on the reactor, more than 60% accuracy of measuring all the states (201 sensors on CO, H<sub>2</sub>O, CO<sub>2</sub>, H<sub>2</sub>, COS and H<sub>2</sub>S mole fractions, temperature and pressure states) has been achieved. Table 7.6 shows the optimal solution, sensor type and location, for each fault. The numbers in Table 7.6 show the grid-point number out of 25 total available grid-points of the corresponding sensor type at which measurement must be made. The grid-point numbers represent the location of the sensors on the reactor and the variable names represent the sensor type in Table 7.6. Using the optimal sensor placements, each corresponding fault state is estimated and plotted in Figure 7-11. Figure 7-11 shows that the fault severities are estimated with reasonable accuracy.

**Figure 7-10. GA progress for different faults****Table 7.5. Reactor and state estimation parameters**

Parameter	Value
<b>Reactor parameters</b>	
Length	7 m
Diameter	3 m
Inlet temperature	487.5 K
Inlet pressure	6093 kPa
<b>Inlet Composition</b>	
CO mole fraction	0.25711
H <sub>2</sub> O mole fraction	0.37753
CO <sub>2</sub> mole fraction	0.11025
H <sub>2</sub> mole fraction	0.24960
COS mole fraction	0.00014
H <sub>2</sub> S mole fraction	0.00534
<b>EKF parameters</b>	
Number of grids	25
Sampling time	5.4 s
<b>Mole fraction process noise covariance</b>	
CO, H <sub>2</sub> O, CO <sub>2</sub> , H <sub>2</sub>	10 <sup>-6</sup>

COS, H <sub>2</sub> S	$2.5 \times 10^{-11}$
<b>Mole fraction measurement noise covariance</b>	
CO, H <sub>2</sub> O, CO <sub>2</sub> , H <sub>2</sub>	$10^{-6}$
COS, H <sub>2</sub> S	$10^{-12}$
<b>Noise covariance</b>	
Temperature process noise covariance	$2.5 \times 10^{-7}$
Temperature measurement noise covariance	$10^{-6}$
Pressure process noise covariance	$10^{-6}$
Pressure measurement noise covariance	$2.5 \times 10^{-7}$
Fault state process noise covariance	$2.5 \times 10^{-5}$
<b>Initial error covariance</b>	
COS, H <sub>2</sub> S	$10^{-12}$
Other states	$10^{-6}$

**Table 7.6. Optimal location and type of sensors for different faults**

Sensor Type	Sensor Location				
	F <sub>25</sub>	F <sub>26</sub>	F <sub>27</sub>	F <sub>31</sub>	F <sub>32</sub>
T <sub>g</sub>	21,22,24	17,21	15,17	10,21	13,14,24
P					
P <sub>in</sub>					
CO	13,16,21, 22,23,24,25	11,14,21, 22,23,24,25	13,20,21,22, 23,24,25	12,13,15,19, 20,21,22,23, 24,25	19,20,21, 22,23,24,25
COS	25	23,24,25	22,23,24,25	22,24,25	19,20,21,22, 23,24,25
H <sub>2</sub> O	13	14	13	12	
CO <sub>2</sub>	2,7,8,9, 10,11,12,14, 15,23,24,25	4,6,8,10, 11,12,13, 15,16,22, 23,24,25	5,14,15,17, 19,20,21, 22,23,24,25	3,5,14,17, 18,22,23, 24,25	3,13,14, 16,21,23,24, 25
H <sub>2</sub>	10,11,12, 14,15,16	12,13,15,16	14,15,17, 19,21	14,15,16, 17,18	13,14,15,16, 17
H <sub>2</sub> S					

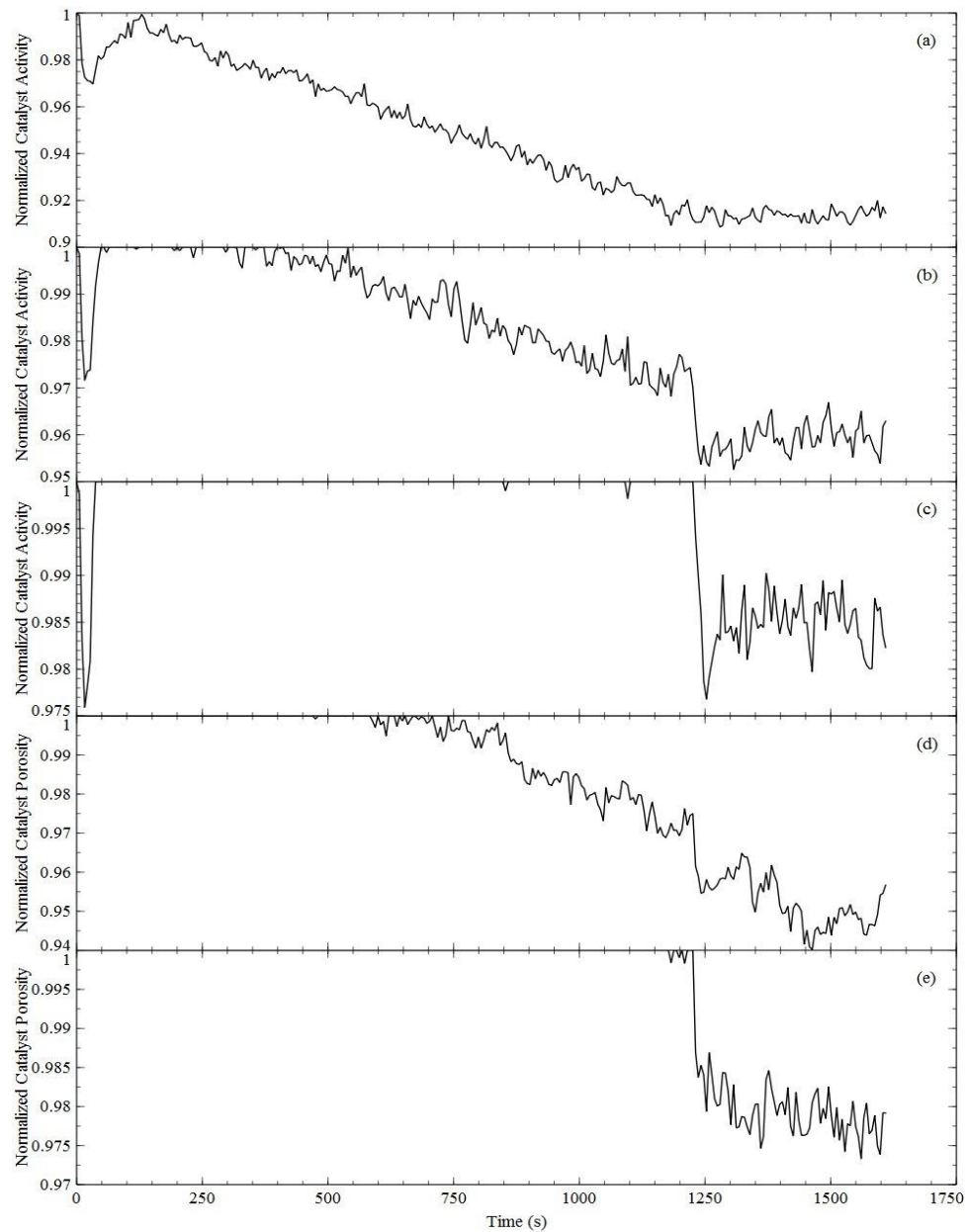


**Figure 7-11. Fault severity estimation in reactor  $R_1$  using optimal solution for fault (a)  $F_{25}$  (b)  $F_{26}$  (c)  $F_{27}$  (d)  $F_{31}$  (e)  $F_{32}$**

### 7.3 Conclusion

The system-level sensor placement resulted in a set of sensors that help in fault resolution to a great extent although some fault sets remain unresolved. For each fault in the sour WGS reactor at component-level, type and location of set of sensors with fixed

quantities are obtained by solving the optimization problem where each set can be used to estimate the severity of the corresponding fault with reasonable accuracy.

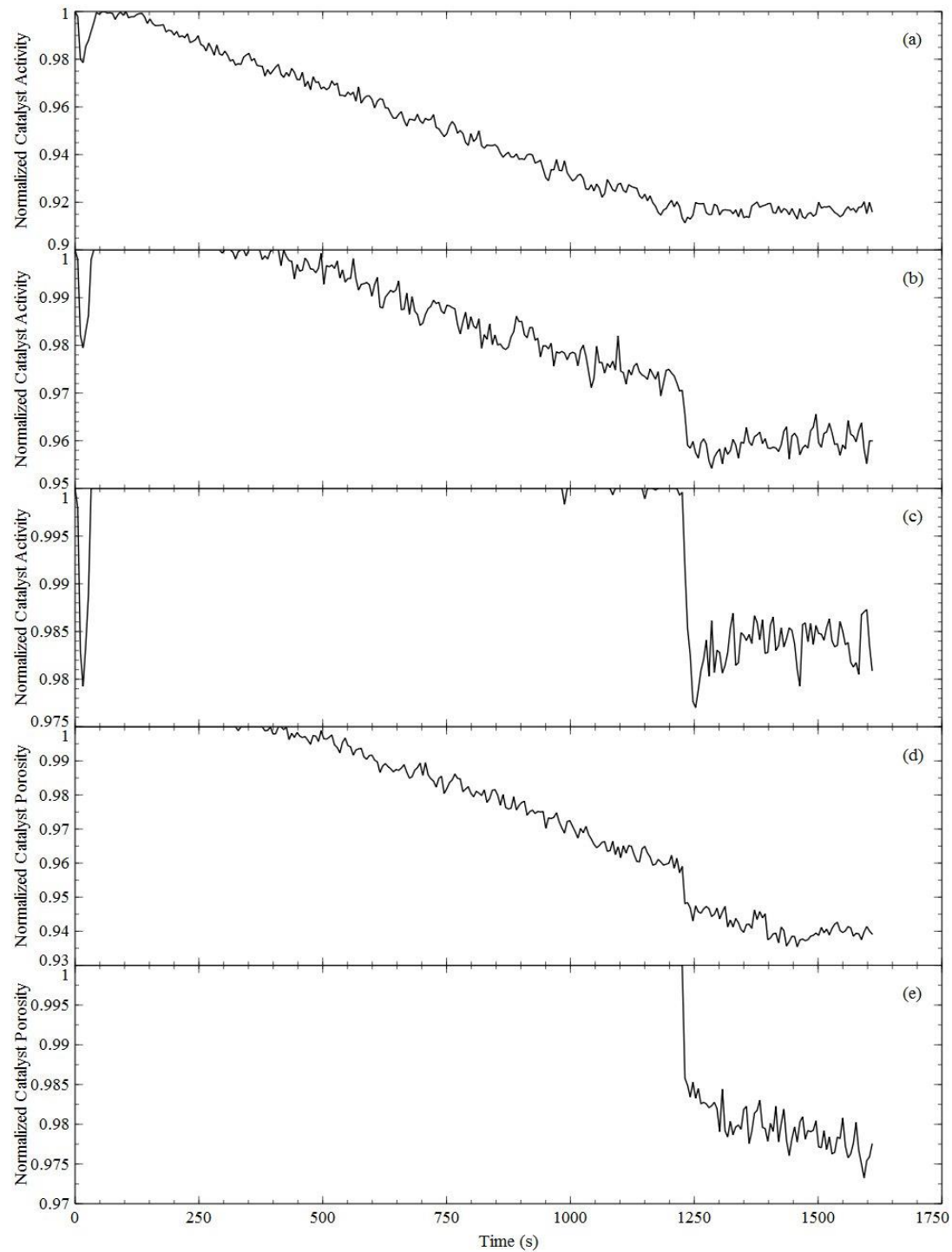
A few sensors obtained by system-level sensor placement are placed on the sour WGS reactor. These sensors along with all the sensors obtained by distributed sensor placement are combined to make up the total sensors for the component monitoring and fault severity estimation. Although for each fault 30 sensors are chosen to be placed on the reactor. While some sensor type and locations are similar for each fault, there are 66 unique sensors when the sensor sets are combined. These 66 sensors are combined with the sensors obtained in system-level sensor placement. Also, since usually the states at the outlet of the reactor are measured for control and product specification purposes, 8 more sensors are placed at the reactor outlet to measure the mole fractions, temperature and pressure. This results in a set of 78 unique sensors. Therefore, in the integrated sensor placement, which is the combination of the sensors obtained in the system- and component-level sensor placement, a network of 78 sensors is used for state monitoring and fault severity estimation.

Figure 7-12 shows the fault severity estimation for each fault using the final sensor network. Table 7.7 compares the normalized fitness values using the optimal sensor placements and the final integrated sensor network. Although more number of sensors can help in improved estimation of the states, the improvement in quality of the fault severity estimation is not significant. The slight improvement can hardly be seen by comparing Figure 7-12 with Figure 7-11. This is due to the reason that the improvement in the normalized fitness values represents slight improvement in the estimation quality of each state rather than significant improvement in the fault state.

Figure 7-13 to 7-17 show the actual, measured and estimated states at the outlet of the reactor for mole fractions, temperature and pressure in the presence of different faults using the final sensor network. Figure 7-13 to 7-17 show that using the final network the filter can greatly estimate the states. States at different locations can be estimated using the final sensor network, thus, the reactor can be monitored efficiently using the sensor network.

**Table 7.7. Comparison of normalized fitness values for GA solution and final sensor network**

Fault	GA solution normalized fitness	Final sensor network normalized fitness
F <sub>25</sub>	0.6168	0.7561
F <sub>26</sub>	0.6391	0.7716
F <sub>27</sub>	0.6491	0.7751
F <sub>31</sub>	0.6261	0.7800
F <sub>32</sub>	0.6282	0.7749



**Figure 7-12. Fault severity estimation in reactor R<sub>1</sub> using final sensor network for fault (a) F<sub>25</sub> (b) F<sub>26</sub> (c) F<sub>27</sub> (d) F<sub>31</sub> (e) F<sub>32</sub>**

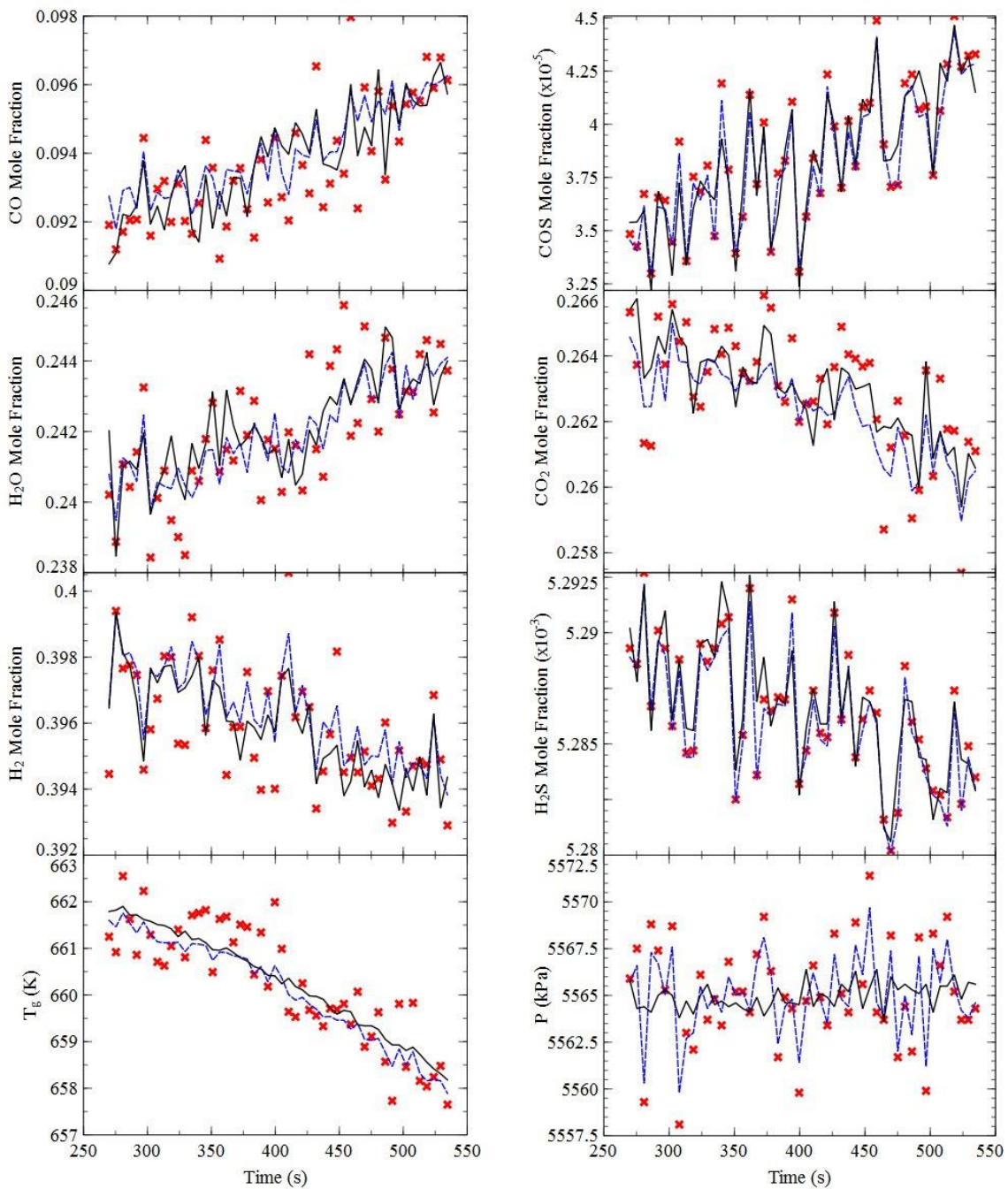


**Figure 7-13. Actual (-), measured (\*) and estimated (--) value of different states at the outlet of the reactor R<sub>1</sub> for fault F<sub>25</sub>**

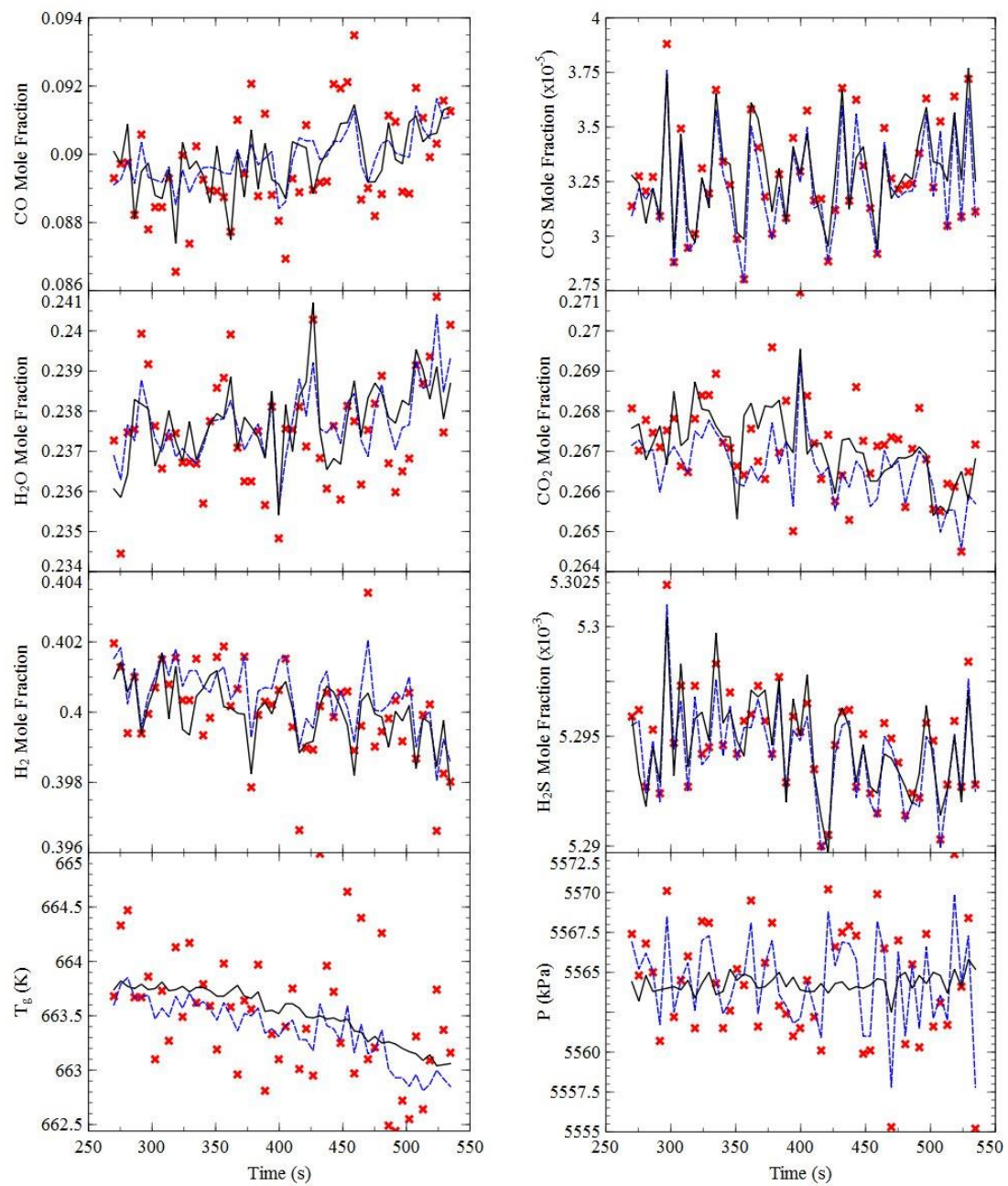


**Figure 7-14. Actual (-), measured (\*) and estimated (--) value of different states at the outlet of the reactor R<sub>1</sub> for fault F<sub>26</sub>**

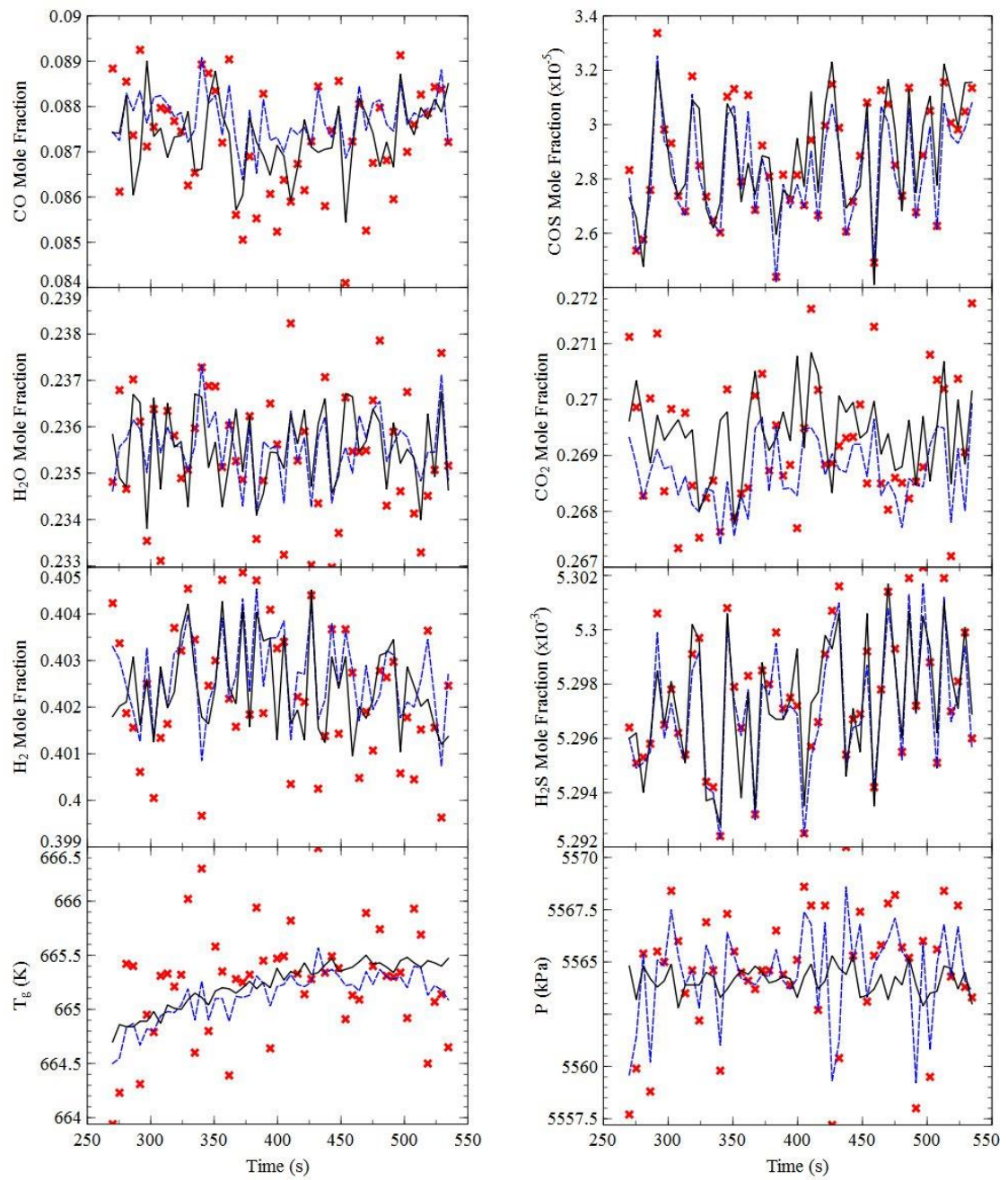


**Figure 7-15. Actual (-), measured (\*) and estimated (--) value of different states at the outlet of the reactor R<sub>1</sub> for fault F<sub>27</sub>**

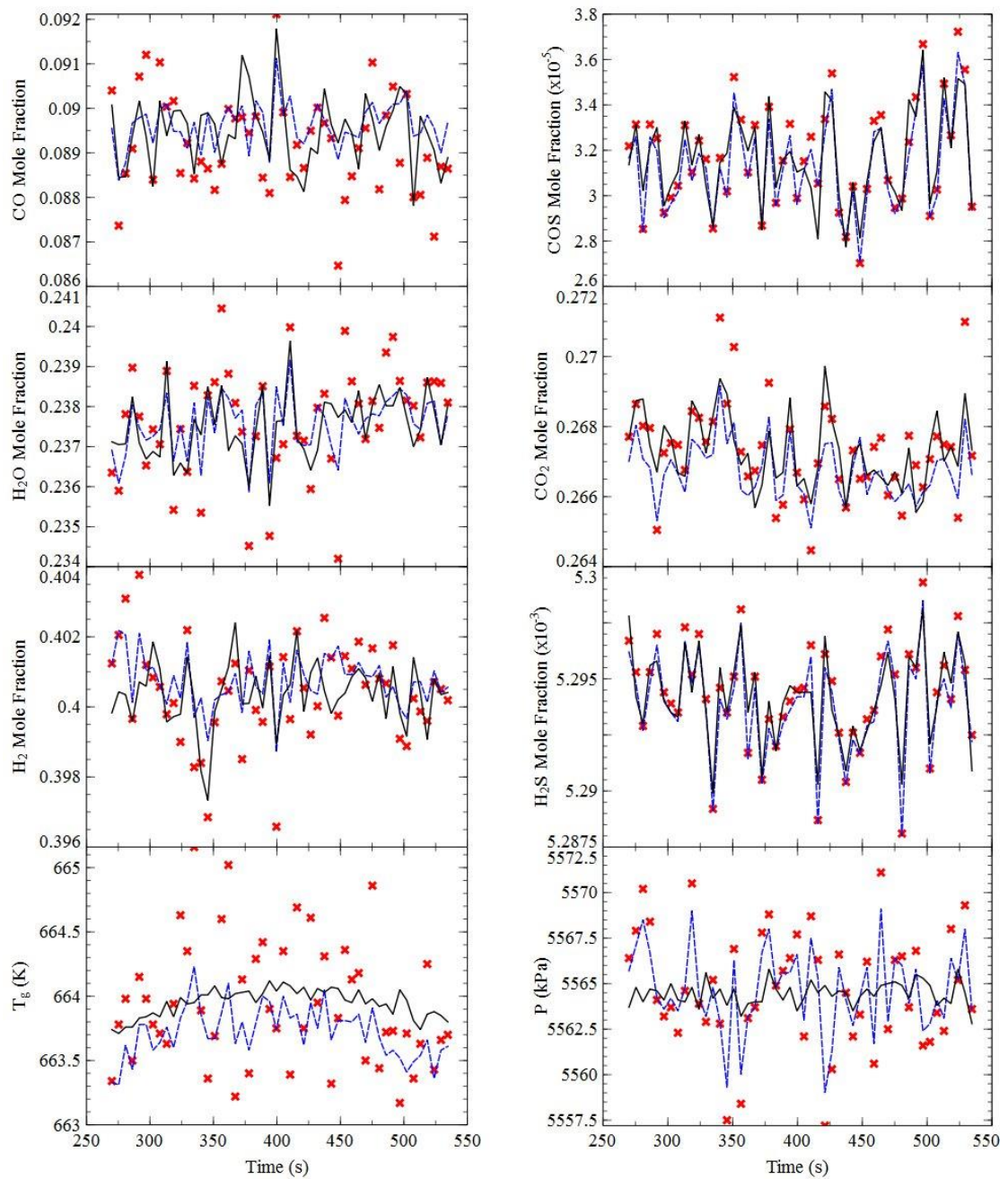


**Figure 7-16. Actual (-), measured (\*) and estimated (--) value of different states at the outlet of the reactor R<sub>1</sub> for fault F<sub>31</sub>**

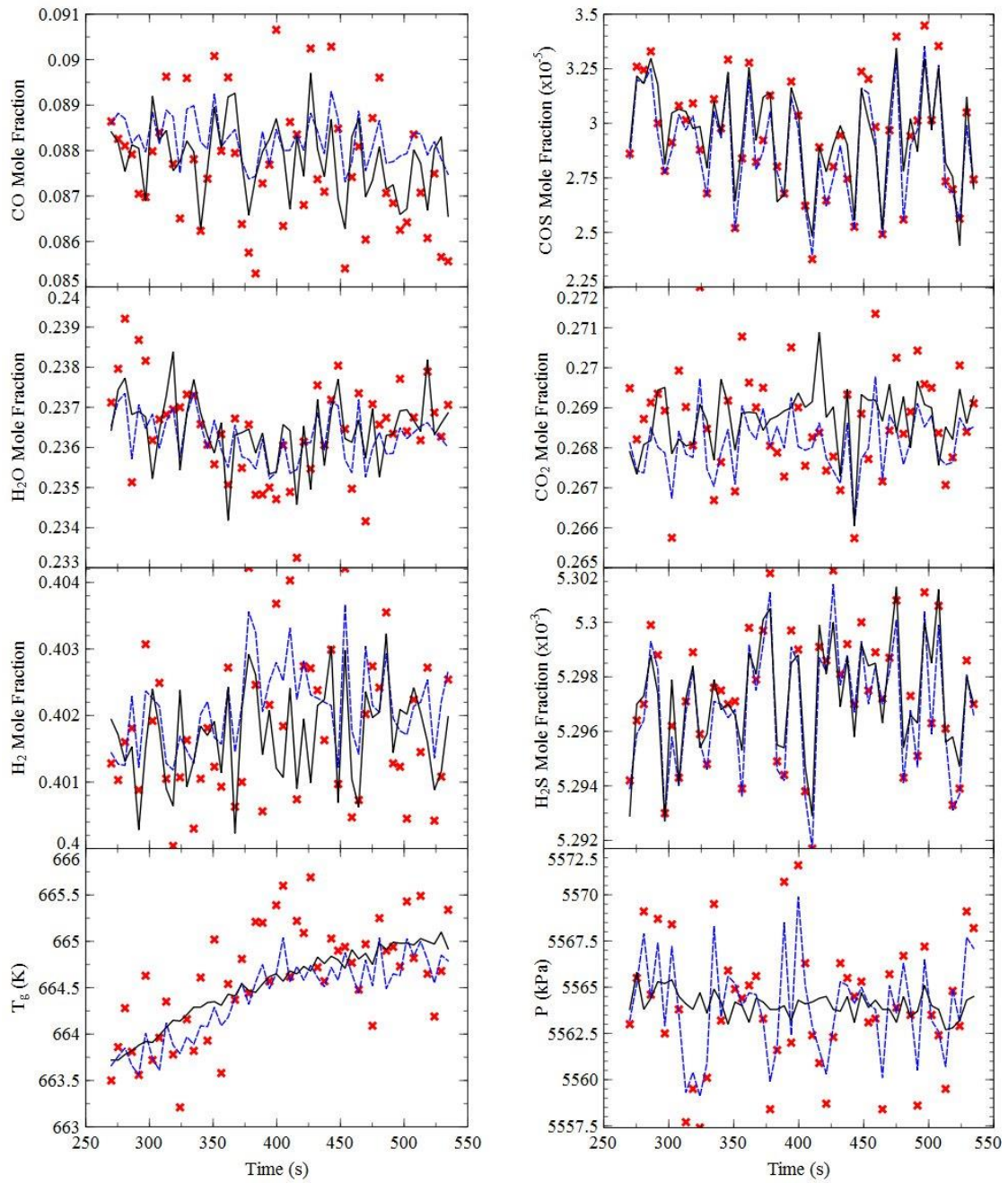


**Figure 7-17. Actual (-), measured (\*) and estimated (--) value of different states at the outlet of the reactor R<sub>1</sub> for fault F<sub>32</sub>**

## Chapter 8

### Summary and Future Work

#### 8.1 Summary

A 2-tier sensor placement framework is introduced. The framework consists of system- and component-level sensor placement approaches. The system-level sensor placement is based on the model-based qualitative analysis combined with the numerical solution. The system-level sensor placement is enhanced by introducing the magnitude ratio and fault evolution sequence algorithms. The network of the sensors obtained in the system-level helps in observation and identification of the faults in the system with an optimum cost. The distributed sensor-placement is based on solving an optimization problem that minimizes the error in estimated states of an extended Kalman filter and results in optimal location and type of the sensors. The optimization problem is solved by genetic algorithm. The resulting sensors not only help in better estimation of the states, but, the fault severities can also be estimated using the filter.

Each of the system- and component-level algorithms are mathematically derived and implemented on different case studies. The integrated algorithm is then implemented on the gasification island of the IGCC plant. The sensors required for fault detection and identification in gasification island are obtained by the system-level sensor placement; and the sensors required for monitoring and fault severity estimation of the gasification island are obtained by distributed sensor placement. The sensors obtained in system-level that are also present in the component level are then combined with sensors obtained in the component-level for monitoring and state estimation.

#### 8.2 Future Work

The sensor placement approach developed in this thesis can easily be used for different processes. This requires availability of the mathematical model of the process and an appropriate state estimation. When the process model is available, fault simulations and

system-level sensor placement can be performed. A major drawback would be the implementation of system-level sensor placement on very large processes. For large processes, future research on network decomposition can help in reducing the complexity of the problem and make the system-level sensor placement easier to be implemented. Through the use of process model and a state estimation technique, the component-level sensor placement is performed. The main drawback of the component-level sensor placement is the complexity of detailed process models that increases the computations in state estimation and, thus, the optimization problem. In this thesis, we have shown that this issue can be approached by use of simplified models. An avenue for future research in this area would be the exploration of order reduction methods for process models to be used in distributed sensor placement for fault detection, diagnosis and estimation.

## References

1. Black, J. Cost and performance baseline for fossil energy plants Volume 1: Bituminous coal and natural gas to electricity. DOE/NETL-2010/1397: **2010**.
2. Gray, D., Plunkett, J., Salerno, S., White, C., Tomlinson, G. Current and future IGCC technologies—A pathway study focused on non–carbon capture advanced power systems r&d using bituminous coal, DOE/NETL-2008/1337, *National Energy Technology Laboratory (NETL)*, Pittsburgh: **2008**.
3. Bhattacharyya, D., Turton, R., Zitney, S. E. Steady-state simulation and optimization of an integrated gasification combined cycle power plant with CO<sub>2</sub> capture. *Ind. Eng. Chem. Res.* **2010**, 50 (3), 1674–1690.
4. Bhushan, M., Rengaswamy, R. Design of sensor network based on the signed directed graph of the process for efficient fault diagnosis. *Ind. Eng. Chem. Res.* **2000**, 39 (4), 999–1019.
5. Bhushan, M., Rengaswamy, R. Comprehensive design of a sensor network for chemical plants based on various diagnosability and reliability criteria. 1. Framework. *Ind. Eng. Chem. Res.* **2002**, 41 (7), 1826 – 1839.
6. Bhushan, M., Rengaswamy, R. Comprehensive design of a sensor network for chemical plants based on various diagnosability and reliability criteria. 1. Applications. *Ind. Eng. Chem. Res.* **2002**, 41 (7), 1840 – 1860.
7. Bhushan, M., Narasimhan, S., Rengaswamy, R. Robust sensor network design for fault diagnosis, *Comput. Chem. Eng.* **2008**, 32, 1067–1084.
8. Han, X., Xie, K. Fault diagnosis based on artificial immune and principal component analysis, *Lect. Notes ARTIF Int.* **2009**, 5589, 429.
9. Raghuraj R., M. Bhushan, R. Rengaswamy. Locating sensors in complex chemical plants based on fault diagnostic observability criteria. *AIChE J.* **1999**, 45 (2), 310–322.
10. Thambirajah, J., Benabbas, L., Bauer, M., Thornhill N. Cause–and–effect analysis in chemical processes utilizing XML, plant connectivity and quantitative process history, *Comp. & Chem. Eng.* **2009**, 33, 503.
11. Allende, H., Bravo, D., Canessa, E. Robust design in multivariate systems using genetic algorithms, *Quality & Quantity* **2010**, 44, 315.
12. Duarte, E., Pozo, A., Nassu, B. Fault diagnosis of multiprocessor systems based on genetic and estimation of distribution algorithms: A performance evaluation, *Int. J. Art. Int. tools* **2010**, 19 (1), 1–18.
13. He, Z., Chiang, H., Li, C., Zeng, Q. Fault–section estimation in power systems based on improved optimization model and binary particle swarm optimization, *IEEE power & energy society general meeting* **2009**, 1–8.

14. Sumana, C., Venkateswarlu, C. Genetically tuned decentralized proportional–integral controllers for composition control of reactive distillation, *Ind. Eng. Chem. Res.* **2010**, 49 (3), 1297–1311.
15. Upreti, S., A new robust technique for optimal control of chemical engineering processes, *Comp. & Chem. Eng.* **2004**, 28 (8), 1325–1336.
16. Woods, M. C., Capicotto, P., Haslbeck, J. L., Kuehn, N. J. Matuszewski, M., Pinkerton, L. L., Rutkowski, M. D., Schoff, R. L., Vaysman, V., Cost and performance baseline for fossil energy plants, Volume 1: Bituminous coal and natural gas to electricity, [www.netl.doe.gov](http://www.netl.doe.gov), Aug, **2007**
17. McDaniel J. E., Hornick, M. POLK power station IGCC – 5<sup>th</sup> year of commercial operation, *Gasification Technologies Conference*, San Francisco, California, October 8–10, **2001**.
18. McDaniel J.E. The Tampa electric integrated gasification combined cycle project: An update, DOE Topical Report No. 19,  
<http://www.netl.doe.gov/technologies/coalpower/cctc/cctdp/bibliography>, **2000**.
19. McDaniel J. E., Hornick, M. Polk power station IGCC – 6<sup>th</sup> year of commercial operation, *Gasification Technologies Conference*, San Francisco, California, October 27–30, 2002.
20. McDaniel J.E. Tampa electric Polk power station integrated gasification combined cycle project, Final Technical Report,  
<http://www.netl.doe.gov/technologies/coalpower/cctc/cctdp/bibliography>, **2002**.
21. Tampa electric company IGCC project, DOE Annual Technical Report, DOE/MC/27363–29, [www.netl.doe.gov](http://www.netl.doe.gov), **1996**.
22. Tampa electric company IGCC project, A DOE Assessment, DOE/NETL–2004/1207, **2004**.
23. Cornils B., Hibbel J. Langhoff J. and Ruprecht P. Stand der Texaco–Kohlevergasung in der Ruhrchemie/Ruhrkohle–Variante, *Chem. Ing. Tech.* **1980**, 52, 12–19.
24. Cornils B., Specks R. Experiences with the Texaco process of coal–dust Pressure Gasification using the Ruhrchemie/Ruhrkohle Technical Version, *EPRI Conference on Synthetic Fuels*, San Francisco, California, October **1980**.
25. Koog W. The Texaco coal gasification process status and outlook, *8<sup>th</sup> Annual WATTEc Energy Conference and Exhibition*, Knoxville, Tennessee, February **1981**.
26. Schlinger W. G. Coal gasification development and commercialization of the Texaco coal gasification process, *Energy Research* **1980**, 4 (2), 127–136.
27. Grol, E. Assessment of power plants that meet proposed greenhouse gas emission performance standards. DOE/NETL–401/110509, **2009**.
28. Hou, P., Meeker, D., Wise, H. Kinetic studies with a sulfur–tolerant water gas shift catalyst. *J. Catal.* **1983**, 80 (2), 280–285.
29. Newsome, D. S. The water–gas shift reaction. *Catal. Rev.* **1980**, 21 (2), 275–318.

30. Beavis, R., Forsyth, J., Roberts, E., Song, B., Combes, G., Abbott, J., Macleod, N., Vass, E., Davies, M., Barton, P. I. A Step-change sour shift process for improving the efficiency of IGCC with CCS. *Energy Procedia*, **2013**, 37. 2256–2264.
31. Carbo, M. C., Jansen, D., Boon, J., Dijkstra, J. W., Van den Brink, R. W., Verkooijen, A. H. M. Staged water–gas shift configuration: Key to efficiency penalty reduction during precombustion decarbonisation in IGCC. *Energy Procedia*, **2009**, 1 (1), 661–668.
32. Carbo, M. C., Boon, J., Jansen, D., Van Dijk, H. A. J., Dijkstra, J. W., Van den Brink, R. W., Verkooijen, A.H.M. Steam demand reduction of water–gas shift reaction in IGCC power plants with pre–combustion CO<sub>2</sub> capture. *Int. J. Greenh. Gas Con.*, **2009**, 3 (6), 712–719.
33. Botha, F. J. Simulation of a syngas from coal production plant coupled to a high temperature nuclear reactor. Stellenbosch University, **2012**.
34. Park, J. N., Kim, J. H., Lee, H. I. A study on the sulfur–resistant catalysts for water gas shift reaction iii. modification of Mo/g–Al<sub>2</sub>O<sub>3</sub> catalyst with iron group metals. *Bull. Korean Chem. Soc.* **2000**, 21 (12), 1233–1238.
35. Li, Y., Wang, R., Chang, L. Study of reactions over sulfide catalysts in CO–CO<sub>2</sub>–H<sub>2</sub>–H<sub>2</sub>O system. *Catal. Today* **1999**, 51 (1), 25–38.
36. Kim, J. H., Lee, H. I. A study on the sulfur–resistant catalysts for water gas shift reaction, II. Effect of alkali metal salt on the activity of CoMo catalyst. *J. Korean Chem. Soc.* **1998**, 42 (6), 696–702.
37. Maurstad, O. An overview of coal based integrated gasification combined cycle (IGCC) technology. MIT, **2005**.
38. Bell, N. H., Edgar, T. F. Modelling of a fixed–bed water–gas shift reactor: 1. Steady–state model verification. *J. Process Control* **1991**, 1 (1), 22–31.
39. Mondal, P., Dang, G. S., Garg, M. O. Syngas production through gasification and cleanup for downstream applications — Recent developments. *Fuel Process. Technol.* **2011**, 92 (8), 1395–1410.
40. Bell, N. H., Edgar, T. F. Modelling of a fixed–bed water–gas shift reactor: 2. Variable catalyst activity effects and dynamic testing. *J. Process Control* **1991**, 1 (2), 59–67.
41. Ding, O. L., Chan, S. H. Water–gas shift reaction – A 2–D modeling approach. *Int. J. Hydrogen Energy* **2008**, 33 (16), 4325–4336.
42. Adams II, T. A., Barton, P. I. A dynamic two–dimensional heterogeneous model for water gas shift reactors. *Int. J. Hydrogen Energy* **2009**, 34 (21), 8877–8891.
43. Francesconi, J. A., Mussati, M. C., Aguirre, P. A. Analysis of design variables for water–gas–shift reactors by model–based optimization. *J. Power Sources* **2007**, 173 (1), 467–477.
44. Giunta, P., Amadeo, N., Laborde, M. Simulation of a low temperature water gas shift reactor using the heterogeneous model/application to a PEM fuel cell. *J. Power Sources* **2006**, 156 (2), 489–496.

45. Choi, Y., Stenger, H. G. Water gas shift reaction kinetics and reactor modeling for fuel cell grade hydrogen. *J. Power Sources* **2003**, 124 (2), 432–439.
46. Chen, W. H., Lin, M. R., Jiang, T. L., Chen, M.H. Modeling and simulation of hydrogen generation from high-temperature and low-temperature water gas shift reactions. *Int. J. Hydrogen Energy* **2008**, 33 (22), 6644–6656.
47. Gunawardana, P. V. D. S., Lee, H. C., Kim, D. H. Performance of copper–ceria catalysts for water gas shift reaction in medium temperature range. *Int. J. Hydrogen Energy* **2009**, 34 (3), 1336–1341.
48. Levent, M. Water–gas shift reaction over porous catalyst: temperature and reactant concentration distribution. *Int. J. Hydrogen Energy* **2001**, 26 (6), 551–558.
49. Lim, S., Bae, J., Kim, K. Study of activity and effectiveness factor of noble metal catalysts for water–gas shift reaction. *Int. J. Hydrogen Energy* **2009**, 34 (2), 870–876.
50. Sun, J., DesJardins, J., Buglass, J., Liu, K. Noble metal water gas shift catalysis: Kinetics study and reactor design. *Int. J. Hydrogen Energy* **2005**, 30 (11), 1259–1264.
51. Amadeo, N. E., Laborde, M. A. Hydrogen production from the low–temperature water–gas shift reaction: Kinetics and simulation of the industrial reactor. *Int. J. Hydrogen Energy* **1995**, 20 (12), 949–956.
52. Hla, S. S., Duffy, G. J., Morpeth, L. D., Cousins, A., Roberts, D. G., Edwards, J. H. Investigation into the performance of a Co–Mo based sour shift catalyst using simulated coal–derived syngases. *Int. J. Hydrogen Energy* **2011**, 36 (11), 6638–6645.
53. de la Osa, A. R., De Lucas, A., Valverde, J. L., Romero, A., Monteagudo, I., Sánchez, P. Performance of a sulfur–resistant commercial WGS catalyst employing industrial coal–derived syngas feed. *Int. J. Hydrogen Energy* **2011**, 36 (1), 44–51.
54. Andreev, A. A., Kafedjiysky, V. J., Edreva–Kardjieva, R. M. Active forms for water–gas shift reaction on NiMo–sulfide catalysts. *Appl. Catal. A Gen.* **1999**, 179 (1), 223–228.
55. Hakkarainen, R., Salmi, T., Keiski, R. L. Water–gas shift reaction on a cobalt–molybdenum oxide catalyst. *Appl. Catal. A Gen.* **1993**, 99 (2), 195–215.
56. Berispek, V. Studies of an alkali impregnated cobalt–molybdate catalyst for the water–gas shift and the methanation reactions. Virginia Polytechnic Institute and State University, **1975**.
57. Jakobsen, H. A. Chemical reactor modeling: multiphase reactive flows. Springer, **2008**.
58. Fiedorow, R., Léauté, R., Lana, I. G. D. A study of the kinetics and mechanism of COS hydrolysis over alumina. *J. Catal.* **1984**, 85 (2), 339–348.
59. George, Z. M. Kinetics of cobalt–molybdate–catalyzed reactions of SO<sub>2</sub> with H<sub>2</sub>S and COS and the hydrolysis of COS. *J. Catal.* **1974**, 32 (2), 261–271.
60. Hoggan, P. E., Aboulayt, A., Pieplu, A., Nortier, P., Lavalley, J. C. Mechanism of COS Hydrolysis on Alumina. *J. Catal.* **1994**, 149 (2), 300–306.

61. Overstreet, A. D. *A screening study of a new water gas shift catalyst*. Virginia Polytechnic Institute and State University, **1974**.
62. Aspen Technology *Aspen Physical Property System*, v7.1, **2009**.
63. Aldridge, C. L. *Shift process for new catalyst*. Google Patents: **1974**.
64. Svoronos, P. D. N., Bruno, T. J. Carbonyl Sulfide: A review of its chemistry and properties. *Ind. Eng. Chem. Res.* **2002**, 41 (22), 5321–5336.
65. Satterfield, C. N. *Mass transfer in heterogeneous catalysis*. RE Krieger Publishing Company: **1981**.
66. Fogler, H. S. Elements of chemical reaction engineering. Prentice–Hall, **1999**.
67. Thoenes Jr, D., Kramers, H. Mass transfer from spheres in various regular packings to a flowing fluid. *Chem. Eng. Sci.* **1958**, 8 (3), 271–283.
68. Ergun, S. Fluid flow through packed columns. *Chem. Eng. Prog.* **1952**, 48, 89–94.
69. Moe, J. Design of water–gas shift reactors. *Chem. Eng. Prog.* **1962**, 58 (3).
70. Singh, C. P. P., Saraf, D. N. Simulation of high–temperature water–gas shift reactors. *Ind. Eng. Chem. Proc. Des. Dev.* **1977**, 16 (3), 313–319.
71. Bartholomew, C. H. Mechanisms of catalyst deactivation. *Appl. Catal. A Gen.* **2001**, 212 (1), 17–60.
72. Rase, H. F., Holmes, J. R. *Chemical reactor design for process plants*. Wiley New York: **1977**, Vol. 2.
73. Romagnoli, J., Sanchez, M. C. Data processing and reconciliation for chemical process operations. Academic Press, **1999**.
74. Renganathan, T., Narasimhan, S. A strategy for detection of gross errors in nonlinear processes. *Ind. Eng. Chem. Res.* **1999**, 38 (6), 2391–2399.
75. Narasimhan, S., Jordache, C. Data reconciliation and gross error detection: An intelligent use of process data. Gulf Professional Publishing, **1999**.
76. Levy, A. The accuracy of the bubble meter method for gas flow measurements. *J. Sci. Instrum.* **1964**, 41 (7) 449.
77. Haggstrom, C. Synthesis gas from black liquor – trace components and methanol synthesis. Lulea University of Technology, Lulea, Sweden, **2011**.
78. Mobed, P., Maddala, J., Rengaswamy, R., Bhattacharyya, D., Turton, R. Data reconciliation and dynamic modeling of a sour water gas shift reactor. *Ind. Eng. Chem. Res.* **2014**, 53 (51), 19855–19869.
79. Dahl, J.K., Weimera, A.W. and Krantz, B.W. Sensitivity analysis of the rapid decomposition of methane in an aerosol flow reactor. *Int. J. Hydrogen Energy* **2004**, 29 (1), 57–65.
80. Kopaygorodsky, E.M., Guliant, V.V. and Krantz, B.W. Predictive dynamic model of single–stage ultra–rapid pressure swing adsorption. *AIChE J.* **2004**, 50 (5), 953–962.

81. Kaisare, N.S., Lee, J.H. and Fedorov, A.G. Hydrogen generation in a reverse-flow microreactor: 1. Model formulation and scaling. *AICHE J.* **2005**, 51 (8), 2254–2264.
82. Balaji, S., Lakshminarayanan, S. and Krantz, B.W. Scaling and sensitivity analysis of a reverse flow reactor. *Chem Eng. Sci.* **2008**, 63 (2), 342–355.
83. Rao, V.R., Farooq, S. and Krantz, W. B. Design of a two-step pulsed pressure-swing adsorption-based oxygen concentrator. *AICHE J.* **2009**, 56 (2), 354–370.
84. Rezvanpour, A., Krantz, B.W. and Wang, C.H. Scaling analysis of the electrohydrodynamic atomization (EHDA) process or pharmaceutical particle fabrication. *Chem Eng. Sci.* **2012**, 80, 81–90.
85. Baldea, M., Daoutidis, P. Dynamics and control of autothermal reactors for the production of hydrogen. *Chem Eng. Sci.* **2007**, 62 (12), 3218–3230.
86. Krantz, W.B. Scaling analysis in modeling transport and reaction processes. Wiley, New York, **2007**.
87. Kramer, M., Mah, R. Model-based monitoring, *Proc. Int. Conf. On Foundations of Computer Aided Process Operations (FOCAPO)*, **1993**, 45–68.
88. Bagajewicz, M. A review of techniques for instrumentation design and upgrade in process plants. *Can. J. Chem. Eng.* **2002**, 80 (1), 3–16.
89. Frank, P., Ding, S., Marcu, T. Model-based fault diagnosis in technical processes. *T. I. Meas. Control* **2000**, 22 (1), 57–101.
90. Venkatasubramanian, V., Rengaswamy, R., Yin, K., Kavuri, S. A review of process fault detection and diagnosis: Part I: Quantitative model-based methods. *Comput. Chem. Eng.* **2003**, 27 (3), 293–311.
91. Iri, M., Aoki, K., O'Shima, E., Matsuyama, H. An algorithm for diagnosis of system failures in the chemical process. *Comp. Chem. Eng.* **1979**, 3 (1), 489–493.
92. Tsuge, Y., Shiozaki, J., Matsuyama, H., O'Shima, E. Fault diagnosis algorithms based on signed directed graph and its modifications. *Ind. Chem. Eng. Symp. Ser.* **1985**, 92, 133–144.
93. Kramer, M., Palowitch, B. A rule-based approach to fault diagnosis using the signed directed graph. *AICHE J.* **1987**, 33 (7), 1067–1078.
94. Lambert, H. Fault trees for locating sensors in process systems. *Chem. Eng. Prog.* **1977**, 81.
95. Madron, F., Veverka, V. Optimal selection of measuring points in complex plants by linear models. *AICHE J.* **1992**, 38 (2), 227–236.
96. Chang, C., Mah, K., Tsai, C. A simple design strategy for fault monitoring systems. *AICHE J.* **1993**, 39 (7), 1146–1163.
97. Bhushan, M., Rengaswamy, R. Design of sensor location based on various fault diagnostic observability and reliability criteria. *Comput. Chem. Eng.* **2000**, 24 (2), 735–741.

98. Bagajewicz, M. Design and retrofit of sensor networks in process plants. *AICHE J.* **1997**, 43 (9), 2300–2306.
99. Yang, F., Xiao, D., Shah, S. Optimal sensor location design for reliable fault detection in presence of false alarms. *Sensors* **2009**, 9 (11), 8579–8592.
100. Chen, J., Chang, C. Development of an optimal sensor placement procedure based on fault evolution sequences. *Ind. Eng. Chem. Res.* **2008**, 47 (19), 7335–7346.
101. Liptak, B. Process measurement and analysis. CRC Press: **1995**, Vol. I.
102. Maurya, M. R., Rengaswamy, R., Venkatasubramanian, V. A systematic framework for the development and analysis of signed digraphs for chemical processes. 1. Algorithms and analysis. *Ind. Eng. Chem. Res.* **2003**, 42 (20), 4789–4810.
103. Mavrovouniotis, M., Stephanopoulos, G. Formal order-of-magnitude reasoning in process engineering. *Comput. Chem. Eng.* **1988**, 12 (9–10), 867–880.
104. Raiman, O. Order of magnitude reasoning. *Artif. Intell.* **1991**, 51 (1), 11–38.
105. Mobed, P., Maddala, P., Pednekar, P., Bhattacharyya, D., Rengaswamy, R. Optimal sensor placement for fault diagnosis using magnitude ratio. *Ind. Eng. Chem. Res.* **2015**, 54 (38), 9369–9381.
106. Downs, J., Vogel, E. A plant-wide industrial process control problem. *Comput. Chem. Eng.* **1993**, 17 (3), 245–255.
107. Ricker, N., Lee, J. Nonlinear model predictive control of the Tennessee Eastman challenge process. *Comput. Chem. Eng.* **1995**, 19 (9), 961–981.
108. Kumar Mandela, R., Rengaswamy, R., Narasimhan, S., Sridhar, L. N. Recursive state estimation techniques for nonlinear differential algebraic systems, *Chem. Eng. Sci.* **2010**, 65 (16), 4548–4556.
109. Simon D. Kalman filtering with state constraints: A survey of linear and nonlinear algorithms, *IET Control Theory Appl.* **2010**, 4 (8), 1303–1318.
110. Petzold', L. Differential/Algebraic equations are not ODE's, *SIAM J. Sci. STAT. Comput.* **1982**, 3 (3), 367–384.
111. Takamatsu, M., Iwata, S. Index reduction for differential-algebraic equations by substitution method, *Linear Algebra Appl.* **2008**, 429 (8), 2268–2277.
112. Chisci, L., Zappa, G. Square-root Kalman filtering of descriptor systems, *Syst. Control Lett.* **1992**, 19 (4), 325–334.
113. Darouach, M., Boutayeb, M., Zasadzinski, M. Kalman filtering for continuous descriptor systems, *Proc. 1997 Am. Control Conf. (Cat. No.97CH36041)* **1997**, 3, 0–4.
114. Darouach, M., Bassong Onana, A., Zasadzinski, M. State estimation of stochastic singular linear systems: convergence and stability, *Int. J. Syst. Sci.* **1993**, 24 (5), 1001–1008.
115. Dai, L. State estimation schemes for singular systems, *Preprints of the 10th IFAC World Congress*, **1987**.

116. Deng Z. L., Liu, Y. M. Descriptor Kalman estimators, *Int. J. Syst. Sci.* **1999**, 30 (11), 1205–1212.
117. Nikoukhah, R. Willsky, A. S., Levy, B. C., Member, S. Kalman filtering and Riccati equations for descriptor systems, *IEEE Trans. Automat. Contr.* **1992**, 37 (9), 1325–1342.
118. Becerra, V. M., Roberts, P. D., Gri, G. W., Park, C., Oax, C. C. B. Applying the extended Kalman filter to systems described by nonlinear differential-algebraic equations, *Control Eng. Pract.* **2001**, 9 (3), 267–281.
119. Åström, K. J. *Introduction to stochastic control theory*. Courier Corporation, **2012**.
120. Campbell, S. L. Descriptor systems in the 90's, **1990**.
121. Schon, T., Gerdin, M., Glad, T., Gustafsson, F. A modeling and filtering framework for linear differential-algebraic equations, *42nd IEEE Int. Conf. Decis. Control (IEEE Cat. No.03CH37475)* **2003**, 1 (3).
122. Vachhani, P., Rengaswamy, R., Gangwal, V., Narasimhan, S. Recursive estimation in constrained nonlinear dynamical systems, *AICHE J.* **2005**, 51 (3), 946–959.
123. Bernstein, D. S. *Matrix mathematics: theory, facts, and formulas*. Princeton University Press, **2009**.
124. Teixeira, B. O. S., Chandrasekar, J., Tôrres, L. A. B., Aguirre, L. A., Bernstein, D. S. State estimation for linear and non-linear equality-constrained systems, *Int. J. Control* **2009**, 82 (5), 918–936.
125. Korbicz, J. Discrete-scanning observation problem for stochastic non-linear discrete-time distributed parameter systems, *Int. J. Syst. Sci.* **1991**, 22 (9), 1647–1662.
126. Alaña, J. E., Theodoropoulos, C. Optimal location of measurements for parameter estimation of distributed parameter systems, *Comput. Chem. Eng.* **2011**, 35 (1), 106–120.
127. Alaña, J. E., Theodoropoulos, C. Optimal spatial sampling scheme for parameter estimation of nonlinear distributed parameter systems, *Comput. Chem. Eng.* **2012**, 45, 38–49.
128. Mehra, R. Optimal inputs for linear system identification, *IEEE Trans. Automat. Contr.* **1974**, 19 (3).
129. Walter, E., Pronzato, L. Qualitative and quantitative experiment design for phenomenological models—A survey, *Automatica* **1990**, 26 (2) 195–213.
130. Nahor, H. B., Scheerlinck, N., Van Impe, J. F., Nicolaï, B. M. Optimization of the temperature sensor position in a hot wire probe set up for estimation of the thermal properties of foods using optimal experimental design, *J. Food Eng.* **2003**, 57 (1), 103–110.
131. Papadimitriou, C. Optimal sensor placement methodology for parametric identification of structural systems, *J. Sound Vib.* **2004**, 278 (4), 923–947.

132. Joshi, S., Boyd, S. Sensor Selection via Convex Optimization, *IEEE Trans. Signal Process.* **2009**, 57 (2), 451–462.
133. Waldruff, W., Dochain, D., Bourrel, S., Magnus, A. On the use of observability measures for sensor location in tubular reactor, *Journal of Process Control* **1998**, 8 (5), 497–505.
134. López, T., Alvarez, J. On the effect of the estimation structure in the functioning of a nonlinear copolymer reactor estimator, *J. Process Control* **2004**, 14 (1), 99–109.
135. Vande Wouwer, A., Point, N., Porteman, S., Remy, M. An approach to the selection of optimal sensor locations in distributed parameter systems, *J. of Process Control* **2000**, 10 (4), 291–300.
136. El Jai, A. Distributed systems analysis via sensors and actuators, *Sens. Act. A-Phys.* **1991**, 29 (1), 1–11.
137. Kubrusly, C. S., Malebranche, H. Sensors and controllers location in distributed systems—A survey, *Automatica* **1985**, 21 (2), 117–128.
138. Omatsu, S., Koide, S. Soeda, T. Optimal sensor location problem for a linear distributed parameter system, *IEEE Trans. Automat. Contr.* **1978**, 23 (4).
139. Olanrewaju, M. J., Al-Arfaj, M. A. Estimator-based control of reactive distillation system: Application of an extended Kalman filtering, *Chem. Eng. Sci.* **2006**, 61 (10), 3386–3399.
140. Harris, T. J., Macgregor, J. F., Wright, J. D. Optimal sensor location with an application to a packed bed tubular reactor, *AICHE J.* **1980**, 26 (6), 910–916.
141. Colantuoni, G., Padmanabhan, L. Optimal sensor locations for tubular-flow reactor systems, *Chem. Eng. Sci.* **1977**, 32 (9), 1035–1049.
142. Kumar, S., Seinfeld, J. H. Optimal location of measurements in tubular reactors, *Chem. Eng. Sci.* **1978**, 33 (11), 1507–1516.
143. Musulin, E., Benqlilou, C., Bagajewicz, M. J., Puigjaner, L. Instrumentation design based on optimal Kalman filtering, *J. Process Control* **2005**, 15 (6), 629–638.
144. Sumana, C., Venkateswarlu, C. Optimal selection of sensors for state estimation in a reactive distillation process, *J. Process Control* **2009**, 19 (6), 1024–1035.
145. Watanabe, K., Sasaki, M., Himmelblau, D. M. Determination of optimal measuring sites for fault detection of non-linear systems, *Int. J. Syst. Sci.* **1985**, 16 (11), 1345–1363.
146. Ali, Y., Narasimhan, S. Sensor network design for maximizing reliability of linear processes, *AICHE J.* **1993**, 39 (5), 820–828.
147. Müller, P. C., Weber, H. I. Analysis and optimization of certain qualities of controllability and observability for linear dynamical systems, *Automatica* **1972**, 8 (3), 237–246.
148. Singh, A. K., Hahn, J. Sensor location for stable nonlinear dynamic systems: Multiple sensor case, *Ind. Eng. Chem. Res.* **2006**, 45 (10), 3615–3623.

149. Brewer, J., Huang, Z., Singh, A. K., Misra, M., Hahn, J. Sensor network design via observability analysis and principal component analysis, *Ind. Eng. Chem. Res.* **2007**, 46 (24), 8026–8032.
150. Dochain, D., Tali-Maamar, N., Babary, J. P. On modelling, monitoring and control of fixed bed bioreactors, *Comput. Chem. Eng.* **1997**, 21 (11), 1255–1266.
151. Van Den Berg, F. W. J., Hoefsloot, H. C. J., Boelens, H. F. M., Smilde, A. K. Selection of optimal sensor position in a tubular reactor using robust degree of observability criteria, *Chem. Eng. Sci.* **2000**, 55 (4), 827–837.
152. Alvarez, J., Romagnolit, J. A., Stephanopoulos, G. Variable measurement structures for the control of a tubular reactor, *Chem. Eng. Sci.* **1981**, 36 (10), 1695–1712.
153. Romagnoli, J., Alvarez, J., Stephanopoulos, G. Variable measurement structures for process control, *Int. J. Control* **1981**, 33 (2), 269–289.
154. Hermann, R., Krener, A. Nonlinear controllability and observability, *IEEE Trans. Automat. Contr.* **1977**, 22 (5), 728–740.
155. Athans, M. On the determination of optimal costly measurement strategies for linear stochastic systems, *Automatica* **1972**, 8 (4), 397–412.
156. Fahroo, F., Demetriou, M. A. Optimal actuator/sensor location for active noise regulator and tracking control problems, *J. Comput. Appl. Math.* **2000**, 114 (1), 137–158.
157. Punithakumar, K., Kinrubarajan, T., Hernandez, M. Multisensor deployment using PCRLBS, incorporating sensor deployment and motion uncertainties, *IEEE Trans. Aerosp. Electron. Syst.* **2006**, 42 (4), 1474–1485.
158. Alonso, A. A., Kevrekidis, I. G., Banga, J. R., Frouzakis, C. E. Optimal sensor location and reduced order observer design for distributed process systems, *Comput. Chem. Eng.* **2004**, 28 (1), 27–35.
159. Jørgensen, S. B., Goldschmidt, L., Clement, K. A sensor location procedure for chemical processes, *Comput. Chem. Eng.* **1984**, 8 (3), 195–204.
160. Morari, M., O'Dowd, M. J. Optimal sensor location in the presence of nonstationary noise, *Automatica* **1980**, 16 (5), 463–480.
161. Morari, M., Stephanopoulos, G. Studies in the synthesis of control structures for chemical processes: Part III: Optimal selection of secondary measurements within the framework of state estimation in the presence of persistent unknown disturbances, *AICHE J.* **1980**, 26 (2), 247–260.